Solar Water Splitting on Low-Dimensional Semiconductor Nanostructures

by

Yongjie Wang

A dissertation submitted in partial fulfillment
of the requirements for the degree of
Doctor of Philosophy
(Electrical and Computer Engineering)
in The University of Michigan
2019

Doctoral Committee:

Professor Zetian Mi, Chair
Professor L. Jay Guo
Professor Jennifer Ogilvie
Professor Zhaohui Zhong

Yongjie Wang

yjiewang@umich.edu

ORCID iD: 0000-0002-9268-837X

DEDICATION

To my loved Xinghan Liu and my family

ACKNOWLEDGEMENTS

At first, I would like to thank my research advisor, Professor Zetian Mi, for his constant support during my PhD studies. The hard-working style of Professor Mi has encouraged all my group colleagues to stay focused on our research work. Professor Mi is such a brilliant and knowledgeable advisor to guide my research area and provide support at almost any time. This dissertation would not be possible without his supervision. Beyond the dissertation research achievements, I have learnt much more about the motivation, attitude, personality, willing, etc., which is really appreciated.

I am sincerely grateful to my committee members, Professor Jennifer Ogilvie, Professor L. Jay Guo, and Professor Zhaohui Zhong. Without their encouragement, careful reviews, and valuable suggestions, this dissertation research would not be improved and completed on time. I would also like to thank my qualifying examiners, Professor Pallab Bhattacharya, Professor Wei Lu, Professor L. Jay Guo, and Professor Stephen Forrest. Without their evaluation and recommendation, I would not have the chance to conduct this dissertation research here.

I acknowledge all the support from our research group members at both McGill University and the University of Michigan, Dr. Songrui Zhao, Dr. Yichen Wang, Dr. Yong-Ho Ra, Dr. Sheng Chu, Dr. Fei Chen, Dr. Xianhe Liu, Dr. Huy Binh Le, Dr. Renjie Wang, Dr. Bandar AlOtaibi, Dr. Shizhao Fan, Dr. Md Golam Kibria, Srinivas Vanka, Roksana Tonny Rashid, Yuanpeng Wu, Yazhou Zhang, Ronglei Fan, David Arto Laleyan, Ayush Pandey, Eric Reid, Kishwar Mashooq, Nick Pant, and Walter Jin Shin. Special thanks to Yuanpeng Wu and Yazhou Zhang for some valuable co-work. Their cooperation, help, suggestion, and friendship have made my graduate life easier toward the successful thesis work.

I would like to thank all the collaborators for the extended research and achievements, Tomoya Asaba and Professor Lu Li at the Department of Physics, Dr. Pengfei Song, Dr. Bin Ouyang, Dr. Xianghua Kong, Pengfei Ou, Professor Hong Guo, and Professor Jun Song at McGill University, and Yumin He and Professor Dunwei Wang at Boston College. The collaboration with them have greatly promoted my dissertation research work.

I would like to thank all the staff of the Lurie Nanofabrication Facility (LNF) and Michigan Center for Materials Characterization ($(MC)^2$) laboratories for their valuable training and support on fabrication processing and materials characterizations. Special acknowledgement to Pilar Herrera-Fierro, Terre Briggs, Brian Armstrong, Nadine Wang, Kai Sun, and Haiping Sun for their close support on my projects.

I give sincerely gratitude to my girlfriend, Xinghan Liu, and my family in China, who have always supported, encouraged, and motivated me to complete this dissertation work.

This dissertation work would not be successfully completed without the support, help, encouragement, and supervision from all the people above. I really want to express my sincere appreciation to every individual supporting my graduate studies.

PREFACE

This presented research work covers the molecular beam epitaxial growth, material characterizations, and solar water splitting performance of low-dimensional III-nitride and transition metal dichalcogenide nanostructures. The manuscripts included in this dissertation are listed below.

1. Yongjie Wang, Yuanpeng Wu, Kai Sun, and Zetian Mi. Quadruple-band metal-nitride nanowires for high efficiency photocatalytic overall solar water splitting. *In preparation*. (Chapter III)
2. Yongjie Wang, Srinivas Vanka, Jiseok Gim, Yuanpeng Wu, Ronglei Fan, Yazhou Zhang, Jinwen Shi, Mingrong Shen, Robert Hovden, and Zetian Mi. An $In_{0.42}Ga_{0.58}N$ tunnel junction nanowire photocathode monolithically integrated on a nonplanar Si wafer. *Nano Energy*, 57, 405-413, 2019. (Chapter IV)
3. Yongjie Wang, Yuanpeng Wu, Jonathan Schwartz, Suk Hyun Sung, Robert Hovden, and Zetian Mi. A single junction cathodic approach for stable unassisted solar water splitting. *Under review*. (Chapter V)
4. Yongjie Wang, Jonathan Schwartz, Robert Hovden, and Zetian Mi. High efficiency, stable unassisted solar water splitting on semiconductor photocathodes protected by multi-functional GaN nanostructures. *In preparation*. (Chapter VI)
5. Yongjie Wang, Songrui Zhao, Yichen Wang, David Arto Laleyan, Yuanpeng Wu, Bin Ouyang, Pengfei Ou, Jun Song, and Zetian Mi. Wafer-scale synthesis of monolayer WSe_2: A multi-functional photocatalyst for efficient overall pure water splitting. *Nano Energy*, 51, 54-60, 2018. (Chapter VII)

TABLE OF CONTENTS

LIST OF FIGURES

Figure

LIST OF TABLES

Table

ABSTRACT

Mimicking the natural photosynthesis process, the direct conversion of solar energy into hydrogen fuel via unassisted water splitting process is one of the key sustainable technologies for future clean, storable, and renewable source of energy. An essential step of artificial photosynthesis is solar water splitting, which can be achieved by either photocatalytic or photoelectrochemical approach. A theoretical solar-to-hydrogen (STH) conversion efficiency ~27% has been predicted for a double-junction photoelectrode consisting of a 1.70 eV top junction and a 1.05 eV bottom junction (*e.g.* silicon) under AM 1.5G one-sun illumination. To date, however, there has been no demonstration of such efficient and stable device for photocatalytic or photoelectrochemical water splitting, which has been largely limited by the lack of semiconductor photoelectrodes that can operate efficiently and stably under visible light and can be directly integrated onto Si wafers.

III-nitride semiconductors, including GaN, InN, and $In_xGa_{1-x}N$ compounds, have recently emerged as highly promising materials for solar fuel conversion due to the tunable bandgaps from 0.65 to 3.4 eV by varying the indium compositions, which can cover nearly the entire solar spectrum. Moreover, the band edges of InGaN compounds can straddle the required chemical potentials for water reduction and water oxidation reactions with indium incorporation up to 50% (bandgap ~1.7 eV). In addition, III-nitride semiconductor nanostructures grown by molecular beam epitaxy can exhibit N-termination, which is highly stable in harsh photocatalysis condition, protecting photoelectrode surfaces against photocorrosion, which is one major issue for practical solar water splitting devices and systems.

In this dissertation, we investigate the MBE growth, electronic and optical properties, and photocatalytic and photoelectrochemical performance of low-dimensional III-nitride and transition metal dichalcogenide (TMDC) nanostructures. Relatively high STH efficiency (>5%) photocatalytic water splitting has been demonstrated on monolithically integrated multi-band InGaN nanowires grown on nonplanar Si wafers. We also report on the demonstration of an InGaN nanowire photocathode for efficient proton reduction reaction, demonstrating a maximum applied bias photon-to-current efficiency (ABPE) ~4%, which is nearly one order of magnitude higher than the previously reported values for III-nitride photocathodes in solar water splitting. With the incorporation of an InGaN tunnel junction structure, we have achieved an improved unassisted solar water splitting in two-electrode configuration, demonstrating a true STH efficiency ~3.4% with ~300 hours stability, which is the highest efficiency value ever achieved in a single-junction photocathode for unbiased photoelectrochemical water splitting. To achieve solar water splitting with both high efficiency and long-term stability, we have further developed GaN-protected $GaInP_2$/GaAs/Ge triple-junction (GaN/3J) photocathode, which can exhibit an STH efficiency ~12.6%. The monolithic GaN/3J photocathode exhibits relatively good stability (>50 hours) in unassisted solar water splitting, which is the best reported stability for multi-junction photocathodes with >10% STH efficiency for true unassisted solar water splitting. In addition, two-dimensional TMDC materials, *e.g.* tungsten diselenide (WSe_2), have been recently reported as potentially low-cost and bi-functional photocatalysts for solar water splitting. Wafer-scale synthesis of monolayer WSe_2 is demonstrated in this work by molecular beam epitaxial growth, which can exhibit multi-functionality in overall solar water splitting, including extraordinary capacities for efficient light harvesting, water oxidation reaction, and proton reduction reaction. Work presented in this thesis provides a new approach for achieving high efficiency and highly stable solar water splitting using the commonly used semiconductors, *e.g.* silicon and gallium nitride.

CHAPTER I

Introduction

1.1 Background of Solar Water Splitting

Fossil fuels, such as coal, oil, and natural gas, have been used for decades to provide the majority of global primary energy.[1] However, it takes millions of years to gradually form such resources and there is only a limited amount on earth. In recent years, such non-renewable fuels start challenging our steady and dependable supply of energy due to the difficult mining and rising price. Moreover, carbon dioxide and other harmful gases excreted from consuming conventional fossil fuels lead to the depletion of ozone and irreversible pollution of environment.[2] Therefore, it is of critical importance to develop renewable and environment-friendly energy systems. Solar and hydrogen energies can potentially address such issues, since solar is abundant and free and hydrogen has no negative effect on environment. Solar water splitting is an artificial photosynthesis process to provide chemical fuels from solar energy to solve future energy and environmental issues.[3, 4] The dissociation of water molecules to H_2 and O_2 provides a simple approach to solar-to-fuel conversion with using only sunlight. Extensive efforts have been devoted to designing low-cost and stable solar water splitting cells, which are still far from the commercial target, *i.e.* 10% solar-to-hydrogen (STH) efficiency and 2000 hours stability.[5]

Semiconductor photoelectrode, as an artificial leaf, plays a significant role in the transduction of energy from solar irradiation to chemical fuels.[6] The semiconductor captures solar energy to generate free electrons and holes with sufficient potentials to accomplish the chemical reactions of water splitting. Transition metal oxides[7-10], *e.g.*

TiO_2, ZnO, Cu_2O, and CoO_x, and Group III-V[11-15], *e.g.* InP, GaInP, and GaAs, semiconductors have been extensively studied for solar water splitting. Unfortunately, these semiconductors have detrimental drawbacks and cannot met the requirements of solar water splitting in large scale for long duration. Transition metal oxides are usually stable in solar-to-fuel conversion but its efficiency is much below 1% because it is generally active only under ultraviolet (UV) radiation due to the large energy gap.[16] As for III-V semiconductors, small and direct bandgap materials could provide high solar-to-hydrogen efficiency in the range of 5-20%.[17] However, their stability is extremely poor, due to photo-corrosion which prevents any practical large-scale production.[18]

Recently, III-nitride semiconductors, including GaN, InN, and their ternary alloys ($In_xGa_{1-x}N$), have attracted intensive attention for solar water splitting due to their direct bandgaps, tunable band edge positions, and extreme chemical stability.[19] As shown in Figure 1.1, the conduction band minimum (CBM) of GaN is more negative than the proton reduction potential, and its valence band maximum (VBM) is more positive than water oxidation potential, making GaN one of the very few materials that can drive overall water splitting without any external bias.[4] More importantly, it is possible to form InGaN ternary semiconductors with tunable band diagram. High-quality InGaN crystal can be synthesized with excellent photon absorption and large carrier mobility to realize high-efficiency solar-to-hydrogen conversion via water splitting under solar irradiation.[20]

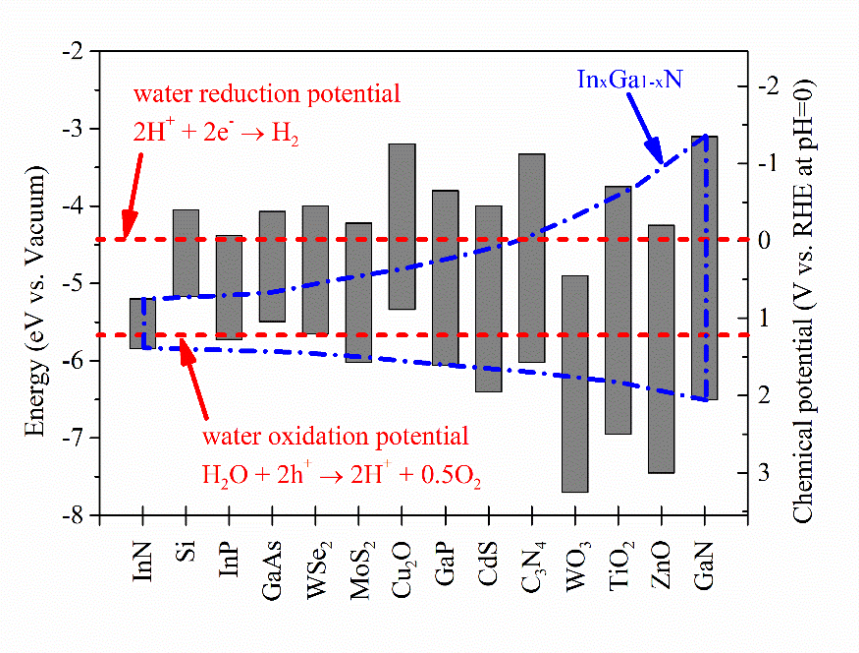

Figure 1.1 Band edge positions of III-nitrides, WSe_2, and other widely used semiconductors for solar water splitting.

Long term stability is essential for reliable solar water splitting devices, which has been elusive due to detrimental corrosion and decomposition issues of semiconductor photocatalysts and photoelectrodes in harsh solar water splitting environment.[21] TiO_2 or metal films as surface protection layers have been deposited on high efficiency III-V photocathodes,[17, 22, 23] achieving improved stability performance in three-electrode measurement, but not for unassisted water splitting. Therefore, novel surface protection layer is urgently required for long-term unassisted solar water splitting. Molecular beam epitaxy (MBE) grown III-nitride semiconductors with N-terminated surface have demonstrated to be stable in harsh water splitting environment,[24-26] which can potentially protect high efficiency photoelectrodes against corrosion.

In addition, cocatalyst nanoparticles at semiconductor surface play an important role in extracting photo-generated charge carriers and driving efficient solar water splitting reactions, by suppressing surface charge recombination, reducing potential losses, and improving overall efficiency.[24, 27] Noble metal (oxide) nanoparticles are currently best-reported cocatalysts for water splitting reactions, *e.g.* Pt and Ru for water reduction reaction; IrO_x and RuO_x for water oxidation reaction.[11, 17, 21, 22, 25] However, they have high price and insufficient reserve on earth, whereas low cost and earth abundant

catalyst is essentially required for scalable solar hydrogen conversion systems. Recently, two-dimensional (2D) transition metal dichalcogenide (TMDC) materials have emerged as efficient and stable photocatalysts for solar water splitting.[28, 29] The challenges include the limiting area of TMDC 2D layers grown by conventional chemical vapor deposition (CVD) or mechanical/chemical exfoliation.[30] In this research, wafer-scale synthesis of monolayer WSe_2 is demonstrated using MBE growth,[31] enabling the studies on TMDC photocatalysts for solar water splitting.

1.2 Mechanisms of Solar Water Splitting

1.2.1 Photocatalytic (PC) water splitting

Photocatalytic water splitting requires the separation and extraction of photo-generated electrons and holes, to drive water oxidation reaction, equation (1-1), and water/proton reduction reaction, equation (1-2), simultaneously,[21, 32] as illustrated in Figure 1.2. Therefore, such semiconductors need to have large bandgaps ($E_{fc} - E_{fv} > 1.23$ eV) for driving water reduction and water oxidation reactions and show less charge carrier recombination for efficient extraction and transfer to semiconductor/electrolyte interface.[32] Wide bandgap metal oxide semiconductors, *e.g.* TiO_2,[33] can drive photocatalytic overall water splitting, but with very low efficiency due to large bandgap only absorbing high energy ultraviolet light. To absorb as much solar energy as possible the semiconductor should have relatively small energy gap. The tradeoff between strong light absorption and large photo-voltage needs to be considered. Therefore, advanced semiconductor photocatalyst systems with tunable energy bands are urgently required for high efficiency wireless solar water splitting. In addition, the chosen semiconductors should be catalytically active for water redox reactions or additional cocatalysts, *e.g.* Rh/Cr_2O_3, CoO_x, and IrO_x, are generally required to facilitate water splitting reactions.[7, 19, 34]

$$2H_2O + 4h^+ \rightarrow 4H^+ + O_2, \text{ -5.68 eV vs. vacuum at pH=0} \quad (1\text{-}1)$$

$$2H^+ + 2e^- \rightarrow H_2, \text{ -4.45 eV vs. vacuum at pH=0} \quad (1\text{-}2)$$

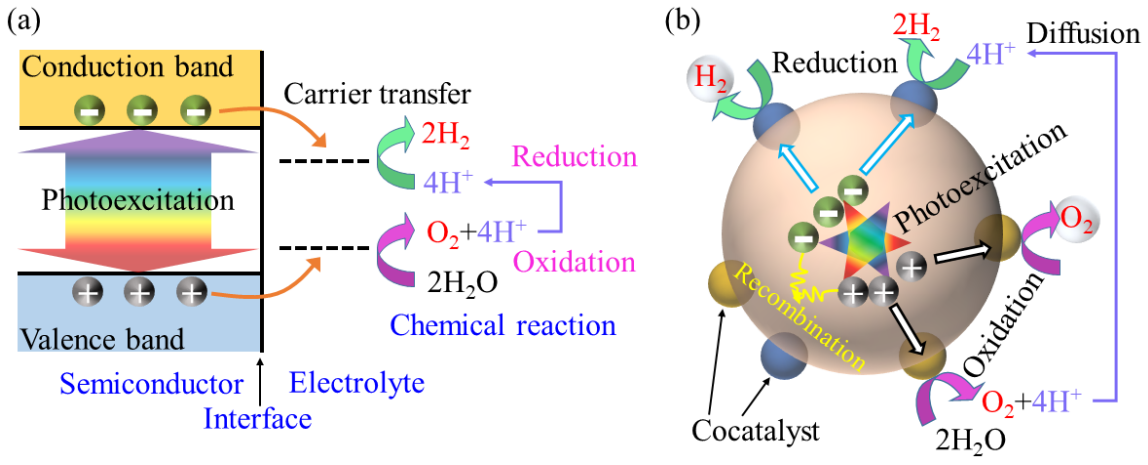

Figure 1.2 The principle of photocatalytic water splitting. (a) Fundamental steps for water splitting by solid-state photocatalysts. (b) Important factors in cocatalyst-loaded powder photocatalysts.

1.2.2 Photoelectrochemical (PEC) water splitting

Different from photocatalytic water splitting, photoelectrochemical water splitting separates water reduction reaction and water oxidation reaction that can occur on the surfaces of two different materials.[35, 36] Figure 1.3 illustrates three widely used configurations for PEC water splitting: (a) Water oxidation reaction occurs on an n-type semiconductor (photoanode) with surface band bending up for holes transferring towards the semiconductor/electrolyte interface, which is connected to a platinum wire (counter electrode) for water reduction reaction. (b) Water reduction reaction occurs on a p-type semiconductor (photocathode) with surface band bending down for electron diffusion into the interface, which is connected to a metal wire (counter electrode) for water oxidation reaction. And if integrating (a) and (b) together, (c) water oxidation and reduction reactions can occur simultaneously on the surface of an n-type semiconductor (photoanode) with surface band bending up and on the surface of a p-type semiconductor (photocathode) with surface band bending down, respectively. Configurations (a) and (b) have similar bandgap requirements to photocatalytic water splitting, but it only requires each semiconductor to be catalytically active for a single reaction, either water reduction or water oxidation, which makes more materials, with simple cocatalyst deposition, suitable for solar hydrogen production. For configuration (c), the requirements of large photovoltage depending on bandgaps can be divided into two parallel semiconductors with a smaller photovoltage. This allows for the utilization of small bandgap

semiconductors, which can produce higher photocurrent due to more light absorption, as an alternative to achieve high-efficient solar-to-hydrogen conversion.

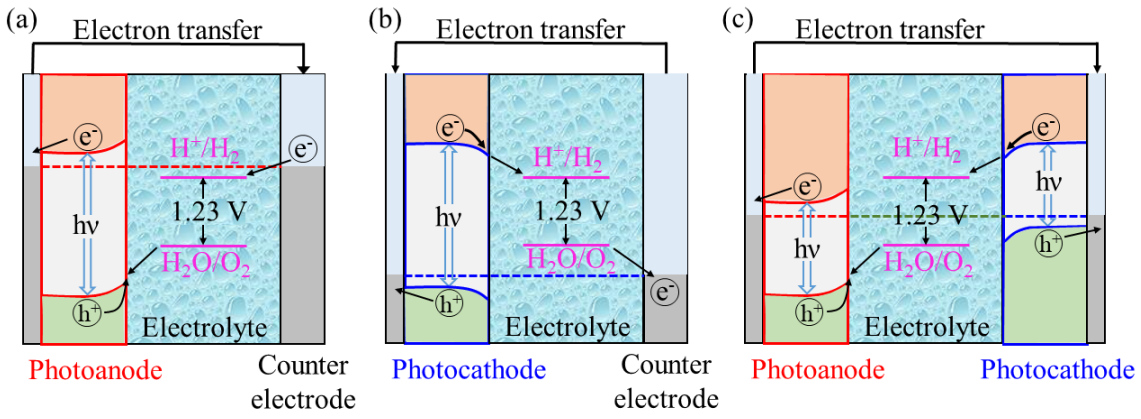

Figure 1.3 Energy diagrams of photoelectrochemical water splitting using (a) a photoanode, (b) a photocathode, and (c) both photoanode and photocathode connected in series. The band gaps are depicted smaller in (c) to emphasize that semiconductors with a narrow band gap can be employed.

1.2.3 Cocatalyst

Separation and extraction of photogenerated charge carriers with low recombination is an important step for solar water splitting in both photocatalytic and photoelectrochemical configurations. To accelerate the utilization of energetic photocarriers to drive solar water splitting at the semiconductor/electrolyte interface before annihilation by surface recombination, a thin layer of cocatalyst, usually composed of noble metal (oxide) nanoparticles, is often deposited at semiconductor surface to facilitate water redox reactions. In addition, cocatalysts can reduce potential losses at semiconductor/electrolyte interface. For example, Pt and Rh/Cr_2O_3 nanoparticles are widely used for water reduction reaction,[34, 37] and IrO_x is frequently deposited for water oxidation reaction.[19] However, current cocatalysts are generally derived from noble metals that are very expensive. Moreover, their catalytic performance is still unideal, especially for water oxidation reaction.[19, 38] Recently, two-dimensional (2D) transition metal dichalcogenide (TMDC) layers have shown to exhibit highly catalytic performance to facilitate the extraction of photo-generated charge carriers for water splitting reaction.[29] But the lack of large-area growth of atomic TMDC layers impedes their applications for solar water splitting.[30] Compared to conventional chemical vapor

deposition or mechanical/chemical exfoliation methods, MBE has shown promising potential to grow TMDC 2D layers on a wafer scale as an emerging photocatalyst for solar water splitting.

1.3 Challenges for Solar Water Splitting

1.3.1 Energy band requirements and light absorption

Overall solar water splitting has stringent requirements on the electronic energy band structures, shown in Figure 1.1. Significantly, the energy band structure of photoelectrode/photocatalyst semiconductors is required to straddle water redox potentials thermodynamically.[21] The conduction band edge should be more negative than water reduction potential (0 V vs. RHE in pH ~0 solutions), providing the chemical overpotential, 0.1~0.3 eV, to drive proton reduction reaction for H_2 gas production.[39-41] The valence band edge should locate more positive than water oxidation potential (1.23 V vs. RHE in pH ~0 solutions), providing the chemical overpotential, 0.4~0.7 eV, to drive water oxidation reaction for O_2 gas production, which is normally a bottleneck for water splitting.[41-43]

The energy band and light absorption requirements pose serious limitations on selecting semiconductor materials for achieving efficient unassisted solar water splitting. Wide bandgap semiconductors can satisfy the requirements on band edge positions and enough chemical overpotential. However, only high energy ultraviolet light can be absorbed, which generally exhibit very low energy conversion efficiency <1%. On the other hand, semiconductor materials with small energy gap cannot straddle the water redox reaction potentials, even though strong light absorption can take place. Therefore, it is urgently required to modify the electronic bands of conventional photoelectrode semiconductors or explore novel semiconductors with tunable energy bands, such as Group III-V and III-nitride materials.[4, 35, 44] In addition, the required chemical overpotential could be reduced by using the most active cocatalyst deposited on electrode/electrolyte interface.[41] For proton reduction reaction on photocathode, small size Pt nanoparticles reduce its chemical overpotential below 0.1 eV.[39] For photoanode

driving water oxidation reaction, the reported cocatalyst, IrO_x, RuO_x, and NiO_x, still requires chemical overpotential >0.3 eV,[41] which is the limit for efficient overall water splitting. Moreover, the deposition of such cocatalyst nanoparticles requests extra complex processing, wherein the uniformity, distribution, and stability may not be precisely controlled.

For realistic solar fuel conversion, it is urgently required to drive unassisted solar water splitting under visible light.[35] Due to the stringent requirements on electronic bands of photocatalysts and photoelelctrodes, there have been intensive studies on modifying the electronic band structures for improved solar water splitting. For example, black TiO_2 has been reported for significantly improved optical absorption properties. Metal doping, dye sensitization, and forming metal organic frame have been used to prepare black TiO_2.[44] However, there has no demonstration on black TiO_2 for efficient unassisted solar water splitting, mainly due to strong surface pinning and charge carrier recombination. For comparison, Group III-nitride semiconductors with tunable energy gap and band edge positions are ideally suited for unbiased solar water splitting in pH ~7 electrolyte solutions with an indium incorporation up to ~40%.[45, 46] In addition, MBE-grown III-nitride nanostructures, with N-terminated surface, has been demonstrated to be stable in harsh water splitting environment and can protect photoelectrode against corrosion.[24, 25]

1.3.2 Charge carrier separation and extraction

Charge carrier separation and extraction is another important factor determining the energy conversion efficiency of solar water splitting systems.[27] The process involves the separation of photo-excited electron-hole pairs and efficient charge carrier transfer to the semiconductor/electrolyte interface, shown in Figure 1.4. To date, there have been very few reports achieving the light-limited photocurrent for unassisted solar water splitting.[22, 23] To overcome such an efficiency bottleneck, bulk and surface charge recombination should be suppressed. For example, charge carrier separation can be facilitated by the build-in electric field, which can enable efficient water splitting reaction.

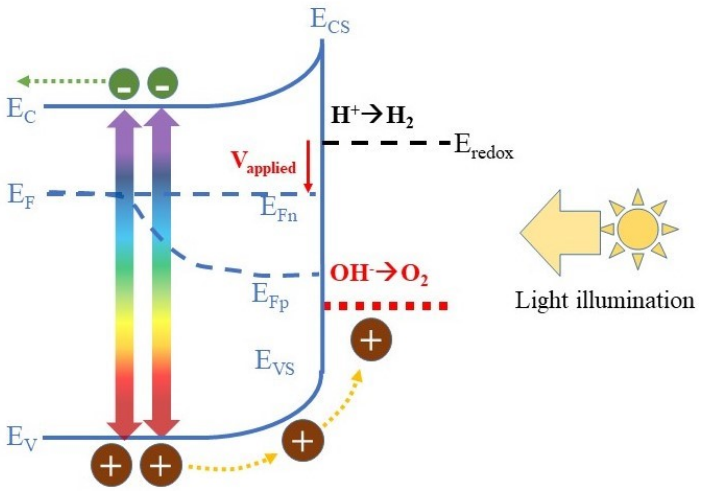

Figure 1.4 Schematic illustration on an n-type semiconductor photoanode of charge carrier photo-excitation, transfer, extraction for water oxidation reaction.

Cocatalyst nanoparticles have been often deposited on the photoelectrode surface for driving water splitting reactions efficiently. Noble metal (oxide) generally demonstrates the best catalytic performance, which, however, is very expensive and unfeasible for low cost solar hydrogen production on a large scale. There have been intensive studies on non-noble transition metals, *e.g.* NiO_x, FeO_x, CoO_x, MoS_2, $MoSe_2$, and CdS,[29, 40, 41, 47] as potential low cost cocatalysts. Nevertheless, their catalytic performance has not surpassed noble metals and their long-time stability has remained elusive. In addition, multi-functional surface passivation layer can be deposited to reduce the surface charge recombination. For example, n-type GaN nanofilm has been demonstrated on n^+p-Si photocathode for efficient charge carrier transfer and reduced surface charge recombination.[25]

1.3.3 Long term stability

Long term stability is the necessity of realistic solar hydrogen conversion devices,[18, 48] which, however, has not been demonstrated, mainly due to serious photocorrosion of semiconductor materials in harsh electrolyte solution. GaInP/GaInAs tandem photocathodes can exhibit STH efficiency >15%.[17, 22] However, there is no stability demonstration on such high efficiency photoelectrodes. On the other hand, although TiO_2 can protect Si, InP, and GaAs photoelectrodes[18, 48, 49] by demonstrating long-term

stable operation, these photoelectrodes cannot drive unassisted solar water splitting. Therefore, it is very urgent to address the stability issue by exploring new materials with chemical inert property as the photoelectrodes or as the surface protection layer for high efficiency photoelectrodes. MBE-grown GaN nanostructures have N-terminated surface,[24, 26] which has been demonstrated to be stable in harsh water splitting environment and can protect the buried junctions effectively against corrosion.

1.4 Solar Water Splitting Performance Evaluation

1.4.1 Photocatalytic water splitting

1.4.1.1 Solar-to-hydrogen conversion efficiency

For overall water splitting, STH conversion efficiency is defined as the chemical energy of generated H_2 gas divided by the solar energy of incident light.[50] The STH efficiency for photocatalytic water splitting devices can be calculated by Eqn. (1-3) using the Gibbs free energy (237 kJ mol^{-1}) of H_2. In addition, the incident light spectra should be close to the standard AM 1.5G solar spectra. To obtain STH efficiency correctly, it is required to demonstrate stoichiometric H_2 and O_2 gas evolution, without adding any sacrificial reagents.

$$\mathrm{STH} = \left[\frac{H_2\ generation\ rate\ (\mu mol\ h^{-1}\ cm^{-2}) \times 237\ kJ\ mol^{-1}}{incident\ solar\ power\ (mW\ cm^{-2}) \times time\ (3600\ s\ h^{-1})}\right]_{AM1.5G} \qquad (1\text{-}3)$$

where the energy density of H_2 gas is represented by its Gibbs free energy (237 kJ mol^{-1}), the incident solar power should be measured using light power meter or calibrated by the manufactory.

For the currently reported photocatalytic devices, the incident light used in the experiments may vary from AM 1.5G spectrum to single-wavelength laser or ultraviolet (UV) light using different short-pass filters and from one sun intensity to concentrated illumination, which have significant effect on the reported efficiency values. Therefore, it is important to compare any efficiency values under comparable conditions, *e.g.* solar spectra, light intensity, and electrolyte solutions. As demonstrated in Table 1.1, III-nitride

semiconductors have shown an STH efficiency >3%. However, metal oxide photocatalyst systems generally have a limited efficiency <1.5%.

Table 1.1 STH efficiency of previously reported photocatalytic systems for overall water splitting.

Materials	**Cocatalyst**	**Electrolyte**	**Light**	**STH (%)**	**Stability (hours)**	**Year [Ref.]**
Double-band $In_{0.22}Ga_{0.78}N$/GaN	Rh/CrO_x	Pure water	32 suns	3.3	2	2018 [51]
$SrTiO_3$:Al	Rh/CrO_x	Pure water	300W Xe lamp	0.4	4	2018 [52]
TiO_2:Ta/N	Ru - RuO_2	1 mM $NaIO_3$	One sun	0.02	15	2017 [53]
$SrTiO_3$:Rh		1 mM $FeCl_3$				
$SrTiO_3$:La, Rh/C /$BiVO_4$:Mo	Ru - RuO_x	Pure water	One sun	1.2	6	2017 [54]
Bi_4NbO_8Cl $SrTiO_3$:Rh	Pt - RuO_x	Fe^{3+}/Fe^{2+} redox	300W Xe lamp	<0.4	24	2016 [55]
$SrTiO_3$:La, Rh/Au /$BiVO_4$:Mo	Ru/Cr_2O_3/a-TiO_2	Pure water	One sun	1.1	10	2016 [56]
GaN nanowires	Rh/CrO_x	Pure water	27 suns	<1	22	2015 [57]
$SrTiO_3$: Rh, Sb $BiVO_4$:Mo	IrO_2/CoO_x	1 mM H_2SO_4	300W Xe lamp	0.01	30	2014 [58]
Si/TiO_2	Pt - IrO_x	0.5 M H_2SO_4	1.5 suns	0.12	4.5	2013 [59]

1.4.1.2 Apparent quantum yield

Apparent quantum yield (AQY) is an extension from the STH efficiency to evaluate and compare the photocatalytic performance of different photocatalysts or under different experimental conditions. AQY is defined by the number of reacted electrons, equal to two times number of evolved H_2 molecules, divided by the number of incident photons using Eqn. (1-4).[60] Unlike the H_2 gas production measured by a gas chromatograph machine, it is usually difficult to obtain the number of incident photons, since real-time spectrum of a lamp is not easy to measure. Generally, we can measure the power density of incident light, which is divided by the photon energy to estimate the number of incident photons.

$$AQY\ (\%) = \frac{2 \times n(H_2)}{n_{in}} \times 100\% \quad (1\text{-}4)$$

where $n(H_2)$ is the number of evolved H_2 gas production and n_{in} is the number of incident photons, which can be estimated by integrating the photon flux.

1.4.1.3 Photocatalytic stability

High efficiency and stable solar water splitting is one significant step of artificial photosynthesis for solar fuel conversion to solve the energy and environment crisis in future. Stabilized photocatalytic water splitting needs to generate stable and stoichiometric H_2 and O_2 gas production. In photocatalytic water splitting experiment, both H_2 and O_2 should be monitored for a desired time to evaluate its stability. The observed linear gas production can confirm the photocatalyst is stable for overall water splitting. In addition, to avoid heating effect, multiple cycles of solar water splitting experiments can be conducted, instead of continuous measurement.

1.4.2 Photoelectrochemical water splitting

1.4.2.1 Solar-to-hydrogen conversion efficiency

STH conversion efficiency is a critical parameter to evaluate the performance of solar water splitting devices, including photocatalytic overall water splitting and photoelectrochemical unassisted water splitting. For photoelectrodes, STH efficiency for unassisted water splitting needs to be measured in two-electrode configuration without any sacrificial reagents, by using Eqn. (1-5), at zero bias vs. a counter electrode.[21, 31]

$$\mathrm{STH} = \left[\frac{J_{ph}\ (mA\ cm^{-2}) \times 1.23V}{P_{in}\ (mW\ cm^{-2})}\right]_{AM1.5G} \quad (1\text{-}5)$$

where J_{ph} is the measured photocurrent at zero bias in a two-electrode configuration, and P_{in} is the power density of incident light illumination. As demonstrated in Table 1.2, multi-junction III-V materials have demonstrated very high STH efficiencies for unassisted solar water splitting. However, they are highly unstable in harsh photocatalysis environment, which is impossible for any practical application.

Table 1.2 STH efficiency of previously reported high efficiency photoelectrodes for unassisted solar water splitting.

Materials	STH efficiency (%)	Unbiased stability (h)	Protection layer	Year [Ref.]
Rh-TiO_2-AlInP/GaInP-/GaInAs/GaAs-RuO_x	19.3	0.5	TiO_2	2018 [22]
PtRu-GaInP/AlInP/GaInP-GaInP/GaInAs	16.2	0.4	n-GaInP	2017 [17]
Pt-metal/n^+p-GaAs & IrO_x-metal/p^+n-GaAs	13.1	N/A	ohmic metal layer	2017 [11]
Pt-TiO_2-3J-SUS-IrO_2	11.2	2	TiO_2	2017 [61]
Pt-TiO_2-Dye cDBR/ITO| Pt-$BiVO_4$/WO_3	7.1	10	TiO_2	2016 [62]
Rh/AlInP-GaInP/GaInAs-RuO_2	14	0.04	N/A	2015 [23]
Pt/$GaInP_2$/GaAs	12.4	10	N/A	1998 [15]

1.4.2.2 Applied-bias photon-to-current efficiency

Many PEC experiments are measured in three-electrode configuration, wherein STH conversion efficiency cannot be derived. In this regard, applied-bias photon-to-current efficiency (ABPE) is defined to evaluate the performance for solar water half reactions, either water reduction reaction for a photocathode or water oxidation reaction for a photoanode, which can be calculated using Eqn. (1-6) and Eqn. (1-7), respectively. It is of importance to note that ABPE measurement is not the true solar water splitting efficiency, even though it is an important diagnostic tool. Regardless the values of ABPE, the measured results under dark should be negligible compared to that under light.

$$\text{ABPE}\ (\%) = \frac{J_{ph}\left(mA{\cdot}cm^{-2}\right) \times V_{app}\ (V\ vs.\ RHE)}{P_{in}\ (mW{\cdot}cm^{-2})} \times 100\% \qquad (1\text{-}6)$$

where J_{ph} is the measured photocurrent of a photocathode in a three-electrode configuration, V_{app} represents the external electric bias (V vs. RHE), and P_{in} is power density of the incident light (100 mW cm^{-2} in this work).

$$\text{ABPE}\ (\%) = \frac{J_{ph}\left(mA{\cdot}cm^{-2}\right) \times \left(1.23 - V_{app}\right)(V\ vs.\ RHE)}{P_{in}\ (mW{\cdot}cm^{-2})} \times 100\% \qquad (1\text{-}7)$$

where J_{ph} is the measured photocurrent of a photoanode in a three-electrode configuration, V_{app} represents the external electric bias (V vs. RHE), and P_{in} is power density of the incident light (100 mW cm^{-2} in this work).

1.4.2.3 Incident photon-to-current efficiency

Another important merit for photoelectrochemical devices is the incident photon-to-current efficiency (IPCE), which can be integrated to provide an estimation of the STH maximum limiting value under ideal conditions. The IPCE includes effects such as photon absorption on photoelectrode semiconductors, charge carrier separation and transfer, and water splitting reactions on the electrode/electrolyte interface. In the measurement, the photocurrent is measured under monochromatic light, with or without external electrical bias. We can divide the measured photocurrent by incident photon flux, using following Eqn. (1-8), for IPCE calculation. Since IPCE provides the performance at a specific wavelength, it is very important to design complex photoelectrodes, by integrating multiple semiconductors with different bandgaps, to improve the overall energy conversion efficiency.

$$\text{IPCE}\ (\lambda) = \frac{J_{ph}\ (mA{\cdot}cm^{-2}) \times 1239.8\ (V{\cdot}nm)}{P_{mono}\ (mW{\cdot}cm^{-2}){\times}\lambda\ (nm)} \times 100\% \qquad (1\text{-}8)$$

where J_{ph} is the measured photocurrent of a photoelectrode in two-/three-electrode configuration, 1239.8 (V·nm) represents the multiplication of Planck's constant and light speed in vacuum, P_{mono} stands for the power intensity of incident monochromatic light, and λ is the wavelength of incident monochromatic light.

1.4.2.4 Faradaic efficiency

H_2 gas production during solar water splitting experiments can be measured by using a gas chromatograph. In addition, the ideal gas production can be predicted using Eqn. (1-9) based on the Faraday's law of water electrolysis.[63, 64] Therefore, we can calculate the theoretical H_2 gas production by assuming the unity faradaic efficiency (η = 1), compared to the measured values. When the measured H_2 production and the calculated values are in agreement, the faradaic efficiency is confirmed to be nearly unity.

$$H_2 \text{ production} = 0.5 \times \frac{\int_0^t J_{ph} dt}{F} \times \eta \quad (1\text{-}9)$$

where J_{ph} is the measured photocurrent during solar water splitting experiments, t is the experiment time for solar water splitting, F represents the Faraday constant (96485 C mol^{-1}), and η is the faradaic efficiency.

1.4.2.5 Photoelectrochemical stability

Long-term stability is the necessity of realistic solar hydrogen conversion devices, which, however, has not been demonstrated, mainly due to serious photocorrosion of conventional semiconductor materials in harsh electrolyte solution that is more preferred for efficient water redox reactions. Ideally, the photoelectrode can drive unassisted solar water splitting in two-electrode configuration, wherein chronoamperometry (CA) measurement should be conducted for the photocurrent at zero bias versus the counter electrode. However, most semiconductor photoelectrodes are not able to drive unassisted solar water splitting, wherein the CA measurement can be performed at the point of highest output power (P_{max}). It also requires to use stable lamp for light illumination and consistent testing environment especially the heating effect under light for long time. As demonstrated in Table 1.3, currently reported high efficiency photoelectrodes for unassisted solar water splitting have very limited stability <0.5 hours even with surface protection layer. TiO_2, MoS_2, and metal films have demonstrated some improved stability in three-electrode measurements, shown in Table 1.4, which, however, cannot drive unassisted solar water splitting without external bias.

Table 1.3 Summarized stability of previously reported high-efficiency photocathodes measured in three-electrode (3E) configuration for half-cell water reduction reaction and in two-electrode (2E) configuration for unassisted solar water splitting, and the comparison with the multifunctional GaN/3J photocathode presented in this work. All measurements were performed under AM 1.5G one-sun illumination.

Materials	STH efficiency	Electrolyte	3E stability	2E stability	Surface protection	Ref.
Inverted metamorphic PtRu-GaInP/GaInAs	16.2%	H_2SO_4	10 hours	0.5 hour	TiO_2	[17]
Pt-$AlInPO_x$/AlInP/	14%	$HClO_4$	16 hours	<0.5 hour	Rh film/	[23]

GaInP/GaInAs					$AlInPO_x$	
Pt-metal/n^+p-GaAs cathode & IrO_x/metal/p^+n-GaAs anode	13.1%	H_2SO_4	10 hours	<0.5 hour	Metal film	[11]
Ru-TiO_2/oxide/AlInP/GaInP/ GaInAs/GaAs	19.3%	KH_2PO_4/K_2HPO_4	50 hours	0.5 hour	TiO_2	[22]

Table 1.4 Summarized stability of previously reported stable photocathodes for half-cell water reduction reaction, but unable to perform unassisted solar water splitting. The stability measurement was performed in three-electrode (3E) configuration.

Materials	**Type**	**Electrolyte**	**ABPE**	**3E stability**	**Surface protection**	**Ref.**
Pd/TiO_2/b-Si	photocathode	H_2SO_4	0.24%	100 hours	TiO_2	[65]
Pt/GaN/n^+p-Si	photocathode	H_2SO_4	10.5%	120 hours	GaN	[25]
Pt/metal/n^+p-GaAs	photocathode	H_2SO_4	17%	8 days	Metal	[11]
MoS_2/$GaInP_2$	Photocathode	K_2SO_4	1%	70 hours	MoS_2	[66]
$NiCrO_x$/TiO_2/p^+n-Si	Photoanode	KOH	0.2%	2200 hours	TiO_2	[48]
Ni/TiO_2/p^+n-Si	Photoanode	KOH	5.6%	100 hours	TiO_2	[18]

1.5 Overview of the Dissertation

The focus of this dissertation research is on MBE growth of III-nitride nanowires and transition metal dichalcogenide (TMDC) two-dimensional nanostructures and their applications towards high efficiency and stable solar water splitting.

Chapter I introduces the background and importance of solar water splitting on semiconductors to meet the increasing demand of clean, renewable energy on a global scale. Different configurations, including photocatalytic and photoelectrochemical, to achieve solar water splitting are described. Stringent requirements and challenges for high efficiency and stable solar water splitting are discussed, together with the performance evaluation methods.

Chapter II presents an overview of the unique advantages of MBE, including heterostructure formation, abrupt doping profile, impurity-free interface, and the formation of N-terminated surface in N-rich environment. Advanced techniques for material characterizations, optical properties, and photocatalytic measurements of low-dimensional III-nitride and TMDC nanostructures are briefly discussed.

Chapter III reports monolithically integrated quadruple-band InGaN nanowire arrays for photocatalytic overall water splitting, which achieves a record STH efficiency of ~5.2%. To our best knowledge, it is the first time for metal nitride nanostructures demonstrating such high efficiency for direct photocatalytic water splitting. The monolithic multi-band $In_{0.35}Ga_{0.65}N/In_{0.27}Ga_{0.73}N/In_{0.20}Ga_{0.80}N/GaN$ nanowire arrays are integrated on a nonplanar silicon wafer for enhanced light absorption. Moreover, a doping gradient is introduced along the lateral dimension of the nanowires, which forms a built-in electric field and promotes efficient charge carrier separation and extraction for water redox reactions. This work demonstrates a novel strategy using multi-band semiconductor nanostructures for artificial photosynthesis and solar fuel conversion with significantly improved performance.

Chapter IV presents a relatively efficient p-type $In_{0.42}Ga_{0.58}N$ nanowire photocathode, which is monolithically integrated on an n-type nonplanar Si wafer through a GaN nanowire tunnel junction. The open pillar design, together with the nonplanar Si wafer can significantly maximize light trapping, whereas the tunnel junction reduces the interfacial resistance and enhances the extraction of photo-generated electrons. The nanowire photocathode exhibits a photocurrent density of 12.3 mA cm^{-2} at 0 V vs. RHE and an onset potential of 0.79 V vs. RHE under AM 1.5G one-sun illumination. The maximum applied bias photon-to-current efficiency reaches 4% at ~0.52 V vs. RHE, which is nearly one order of magnitude higher than the previously reported values for III-nitride photocathodes. Significantly, no performance degradation was measured for over 30 hours solar water splitting with a steady photocurrent density ~12 mA cm^{-2} without using any extra surface protection, which may be attributed to the spontaneous formation of N-terminated surfaces of InGaN nanowires to protect against photocorrosion.

In Chapter V, we show that a single junction approach of p-type $In_{0.25}Ga_{0.75}N$ nanowires monolithically integrated on an n-type Si wafer through an n^{++}/p^{++}-InGaN tunnel junction can drive relatively efficient and stable unassisted water splitting under AM 1.5G one-sun illumination. A photocurrent density of 2.8 mA cm^{-2} is measured at zero bias vs. platinum counter electrode in a two-electrode configuration, which corresponds to a true STH efficiency of 3.4%. Of importance, no performance degradation has been observed for ~300 hours unassisted solar water splitting without using any extra surface protection layers. Beyond this demonstration, such InGaN nanowire tunnel junction photocathode can be integrated with a narrow bandgap junction, *e.g.* Si or GaAs, to form a double-junction tandem photoelectrode to achieve further improved efficiency for long-term stable solar water splitting.

Chapter VI reports a multi-functional GaN nanostructure protected $GaInP_2$/GaAs/Ge triple-junction (GaN/3J) photocathode, demonstrating a 12.6% STH efficiency for solar water splitting without any external bias. The multi-functional GaN nanostructure not only significantly reduces the charge transfer resistance at semiconductor/electrolyte interface but also protects buried III-V materials against corrosion. Moreover, stable solar water splitting has been achieved for 80 hours in three-electrode configuration and 57 hours in two-electrode measurement at zero bias, requiring no extra surface protection layers, which is the best reported stability for multi-junction photocathodes with >10% STH efficiency. In future, such multi-functional GaN nanostructure proposes a new approach to further improve the STH efficiency, especially for tandem devices, for realistic unassisted solar water splitting at large scale.

Chapter VII reports the van de Waals epitaxy of crystalline monolayer WSe_2 on large area amorphous SiO_x substrates. We have demonstrated, for the first time, the multi-functionality of monolayer WSe_2 in solar water splitting, including extraordinary capacities for efficient light harvesting, water oxidation, and proton reduction. The absorbed photon conversion efficiency exceeds 12% for a single monolayer WSe_2. We have shown that wafer-scale WSe_2 monolayer sample could be directly grow on amorphous substrates by MBE with precise layer control and can exhibit superb optical properties and catalytic performance. This work provides a viable strategy for wafer-scale

synthesis of multi-functional photocatalysts for the development of efficient, low cost, and scalable solar fuel devices and systems.

Finally, Chapter VIII briefly summarizes the current work of solar water splitting on low-dimensional III-nitride and TMDC nanostructures presented in this dissertation. Possible future work is further proposed for achieving significantly improved efficiency for solar water splitting and carbon dioxide reduction.

Chapter II

Molecular Beam Epitaxial Growth and Characterizations of III-Nitride Nanowires and Transition Metal Dichalcogenide 2D Layers

2.1 Introduction

Molecular beam epitaxy (MBE) has been widely used for the growth/synthesis of high-purity, high-quality semiconductor nanostructures, with atomic level control of the interface and thickness. Compared to conventional metal-organic chemical vapor deposition (MOCVD) to grow III-V semiconductors or chemical vapor deposition (CVD) to deposit TMDC layers, MBE offers unique advantages of large-area growth, heterostructures, abrupt doping profile, and pristine interface.[67] Moreover, N-terminated surfaces can be formed for III-nitride nanostructures,[24] which makes it very stable in harsh photocatalysis conditions. In this chapter, we first provide an overview of the MBE systems to grow low-dimensional III-nitride and TMDC nanostructures, then discuss the state-of-the-art techniques used for crystal structures and optical properties. We will also review the experimental techniques of photocatalytic and photoelectrochemical water splitting measurements.

2.2 Overview of Plasma-Assisted Molecular Beam Epitaxy

MBE distinctly differs from other material growth/deposition systems due to its precise flux control for atomic layer growth and abrupt doping profiles.[67] MBE growth has been utilized in various materials systems, including III-nitride, III-V, and II-VI materials. The system discussed and used in this work is a nitrogen plasma-assisted

epitaxy system shown in Figure 2.1 and 2.2. Ultra-high vacuum conditions are maintained with a background vacuum level on the order of 1E-11 Torr. This ensures MBE grown materials to have far superior optical and electrical properties than previously used vacuum evaporation techniques. Unlike other vacuum evaporation techniques, the substrate heater can be heated to high temperatures (~1000^{o}C) which is ideal for the epitaxy of large bandgap (*e.g.* AlN and GaN) materials. Typically, liquid nitrogen is used to ensure efficient heat dissipation, and some source cells are cooled with chilled water. The MBE used in this work was equipped with different source effusion cells for gallium (Ga), indium (In), aluminum (Al), and selenium (Se), wherein a nitrogen plasma is derived from an ultra-purity (6N) nitrogen source. In addition, different dopant cells are integrated for n-type doing by silicon (Si) or germanium (Ge) and p-type doping by magnesium (Mg).

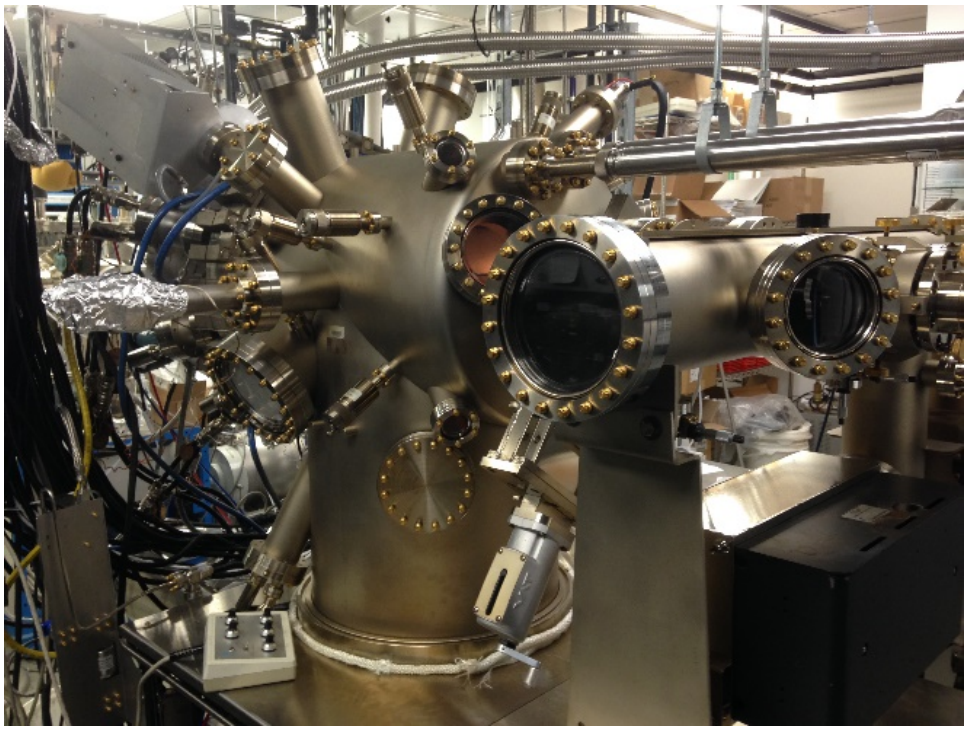

Figure 2.1 Veeco Gen II plasma-assisted molecular beam epitaxy system.

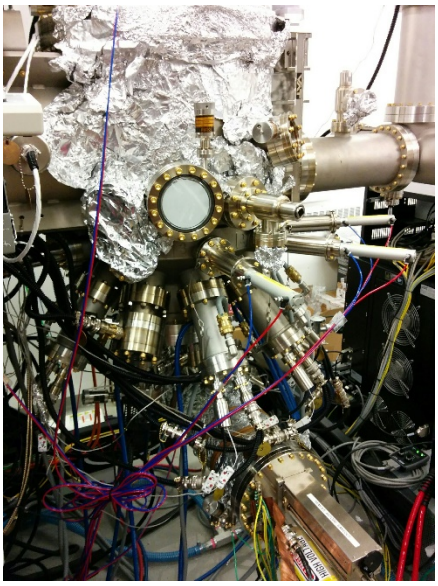

Figure 2.2 Veeco GenXplore plasma-assisted molecular beam epitaxy system equipped with a Telemark ebeam evaporator.

These MBE systems are capable of growing various types of materials. Even within the same material system, there is a considerable amount of diversity regarding structural characteristics. As an example, MBE can epitaxially grow different quantum structures like quantum wells, nanowires, or quantum dots. Each of such nanostructures has unique structural characteristics even if all of them are III-nitride-based. The presented work mainly focuses on III-nitride nanowires on planar or nonplanar Si wafers, and transition metal dichalcogenide 2D layers on amorphous SiO_x/Si or sapphire substrates.

2.3 Characterization Techniques

2.3.1 Photoluminescence

Photoluminescence (PL) spectroscopy is the measurement of light emission on semiconductor materials after photo-excitation process, which has been widely used to estimate the energy gap of semiconductor materials. In this work, we generally measure room-temperature PL spectrum of MBE-grown InGaN nanowires to estimate the energy gap and average indium compositions. In addition, PL characterization is widely used to identify the shallow impurities in semiconductors, wherein the linewidth of PL peak indicates the material crystallinity and interface quality.[68] PL spectroscopy, including

steady-state and time-resolved PL, can give information about the separation and recombination of photoinduced charge carriers, as PL essentially originates from the electron–hole recombination.[69] In general, high-intensity steady-state PL spectroscopy indicates efficient radiative recombination of electrons with holes.

2.3.2 Energy gap of InGaN alloys

Group III-nitride semiconductors have been intensively studied in electronic and optoelectronic devices due to the unique tunable energy band structures.[70] The direct bandgap of $In_xGa_{1-x}N$ ternary alloys can be estimated by using Vegard's law as described by Eqn. (2-1).

$$E_g(In_xGa_{1-x}N) = x \cdot E_g(InN) + (1-x) \cdot E_g(GaN) - b \cdot x \cdot (1-x) \qquad (2\text{-}1)$$

where b is the bowing parameter and its value typically varies between 1.3 and 1.4.[71, 72] In this study, the energy gap of InGaN nanowires was estimated from photoluminescence measurements. The indium compositions were then derived using Eqn. (2-1), correlating the energy bandgap values vs. In concentrations with a bowing parameter of 1.3 or 1.4. In this dissertation work, the indium composition of $In_xGa_{1-x}N$ ternary nanostructures can be accurately estimated in the range of 20% to 60% based on PL spectrum and Eqn. (2-1).

2.3.3 Raman spectroscopy

Using Raman spectroscopy we are able to differentiate between various phases of a material with the same chemistry or regions of different chemical composition of a sample.[73] It can be used to study the incorporation of impurities on a crystalline matrix, to measure stress distribution in a sample, or monitor phase transitions, with temperature or pressure. As previously reported,[74] Raman scattering can be correlated with the Mg doping level in GaN nanostructures, which helps to form n^{++}/p^{++}-GaN tunnel junction structure by quickly indicating the sufficient Mg doping or not. For two-dimensional materials,[31, 75] like graphene and WSe_2, Raman has been widely used to determine the number of deposited layers. It can also be used to image regions of different chemistry or structure. Its main limitation is that its intensity is very weak compared to the elastically scattered light and even to luminescence.[76]

2.3.4 X-ray photoelectron spectroscopy

X-ray photoelectron spectroscopy (XPS) is the technique to analyze emitted electrons of a specimen after X-ray bombardment, using an Mg K_α (1253.6 eV) or Al K_α (1486.6 eV) X-ray source. Generally, X-ray penetrates the specimen atom orbits and only the surface electrons can emit for analyzing the kinetic energy. Using XPS, different chemical bonding and electronic band structures can be determined. In addition, atomic composition can be measured using integrated area under the measured peaks in XPS spectrum.[31] XPS is one widely used non-destructive technique for surface analysis.[73] For example, XPS can be used to determine the surface Fermi level of III-nitride nanowires in photocatalytic water splitting research,[57] and the chemical bond and atomic composition in TMDC 2D materials.[31]

2.3.5 Scanning electron microscopy

By scanning the sample with high-energy electron beam (1-40 keV), sample and incident electrons interact to produce secondary electrons, backscattered electrons, and characteristic X-rays for analysis in scanning electron microscopy (SEM).[77]Therefore, SEM can image structural morphology and determine elemental compositions, with tunable magnification up to 1000K, corresponding to nanometer resolution. In this dissertation research, SEM is widely used to characterize the morphology of III-nitride nanostructures.

2.3.6 Transmission electron microscopy

Transmission electron microscopy (TEM) has been used to characterize materials at ultrahigh spatial resolution for morphology, elemental distribution, crystal structure, defects etc.[78] Ultrahigh energy (80-300 keV) electron beam passes through very thin sample specimen and forms images. Conventional (TEM) using a broad electron beam and scanning transmission electron microscope (STEM) with focused electron spot are two generally used modes for material characterization at atomic resolution.[73] High angle annually dark field scanning transmission electron microscope (HAADF-STEM) imaging collects incoherently scattered electrons at high angles, providing unique contrast with varied atomic number or specimen thickness. In this work, HAADF-STEM

imaging is used to determine the morphology, crystal structure, and elemental distribution of III-nitride and TMDC nanostructures.

2.4 Photocatalytic and Photoelectrochemical Measurements

2.4.1 Photocatalytic water splitting

Photocatalytic overall water or seawater splitting measurements were conducted in a vacuum chamber exposed to concentrated AM 1.5G solar spectrum with a measured intensity of 2339 mW/cm^2, which is about 23 suns. Such incident light of high intensity was applied in this work to mainly saturate the defect states in photocatalytic materials and enable the realistic photocatalytic device with low cost at large scale for solar hydrogen production in future artificial photosynthesis industry.[79] The measurement chamber is partially filled with 70 mL pure water or seawater electrolyte solution, with the immersed InGaN photocatalyst sample located at the bottom, was pumped down 20 minutes before exposing to light illumination. Pure water or seawater solution was purged ahead using argon gas flow for 30 minutes before any experiments. The production of H_2 and O_2 gases from solar water splitting on InGaN nanowires were analyzed by injecting the sampling into a gas chromatograph machine (GC-8A, Shimazdu) equipped with a thermal conductivity detector (TCD) with ultrahigh purity argon carrier gas. Seawater solution was artificially prepared by dissolving 27.2 g NaCl, 3.8 g $MgCl_2$, 1.6 $MgSO_4$, 1.4 g $CaSO_4$, 0.6 g K_2SO_4, 0.2 g K_2CO_3, and 0.1 $MgBr_2$ into 500 mL deionized pure water.

2.4.2 Photoelectrochemical water splitting

Photoelectrochemical (PEC) measurements were conducted in both three-electrode and two-electrode configuration in 0.1~0.5 M H_2SO_4 electrolyte solution equipped with a Newport solar simulator with AM 1.5G filter and one-sun intensity. The Ag/AgCl reference electrode was only used for three electrode measurements, and a platinum counter electrode for both configurations. Gamry and EC-Lab potentiostat device was used to perform all the PEC measurements including linear sweep voltammetry, chronoamperometry, electrochemical impedance spectroscope, chronopotentiometry, and

open circuit potential tests. H_2 gas production from solar water splitting on III-nitride based photocathodes was analyzed by injecting 1 mL gas sampling into a Shimazdu gas chromatograph (GC-8A). For long-term stability experiment over several days, the electrolyte was periodically refreshed to avoid accumulated heating effect.

2.5 Summary

This chapter provides an overview of the MBE system, with unique advantages including heterostructure formation, abrupt doping profile, impurity-free interface, relatively low growth temperature, and N-terminated surface for GaN nanostructures. Then, state-of-the-art characterization techniques, *e.g.* PL, Raman, XPS, SEM, and TEM are reviewed for characterizing the energy band structure, crystalline structure, and optical properties of low-dimensional III-nitride and TMDC nanostructures. In the last part, photocatalytic and photoelectrochemical measurements are described to perform solar water splitting experiments.

CHAPTER III

Quadruple-Band Metal-Nitride Nanowires for High Efficiency Photocatalytic Overall Solar Water Splitting

3.1 Introduction

Photocatalytic water splitting is a wireless approach to convert solar energy directly to hydrogen fuels, which is an essential step of artificial photosynthesis.[60, 80-82] Unlike photoelectrochemical water splitting that generally requires the integration of two (photo)electrodes in highly conductive electrolyte, water redox reactions can occur on the same surfaces of a light absorber in photocatalytic overall water splitting in nearly pH neutral solutions,[31, 82, 83] such as pure water or seawater, thereby promising large scale practical application. Direct photocatalytic water splitting has stringent requirements on the electronic band structure of the semiconductor light absorbers:[27, 31] the conduction and valence band edges must straddle water redox reactions with sufficient chemical overpotentials for proton reduction and water oxidation, respectively,[79, 84] while the energy bandgap should be sufficiently narrow for efficient sunlight harvesting. In spite of intensive studies on photocatalytic water splitting,[56, 83, 85-87] most of the semiconductor light absorbers reported to date do not possess suitable band edge positions for overall water splitting under visible light illumination.[16, 88] For example, metal oxides, such as TiO_2, $InNiTaO_4$, $SrTiO_3$, GaN/ZnO, and $LaMgTaO_2$,[52, 87, 89-91] can only absorb a small part of solar spectrum due to their large bandgap, whereas narrow band gap semiconductors, such as Si, GaAs, and InP,[92-94] do not possess suitable band edge positions to drive overall water splitting. Intensive studies have been performed to extend the energy bands of various wide bandgap

materials to enhance the efficiency of photocatalytic solar water splitting, such as black TiO_2 by metal doping, dye sensitization, or adding surface hydroxyl groups, but with limited success.[57, 95-97] To date, the solar-to-hydrogen conversion efficiency is generally limited to <0.5% for single-band metal-oxide photocatalysts (see Supplementary Table 3.1). Efficiency up to 5% has been reported with the use of CoO_x nanoparticles but the stability is limited to ~30 mins.[82] Z-scheme photocatalytic systems using two-step photo-excitation, in principle, can overcome the unsuitable energy band structure for water redox reactions. For example, $SrTiO_3/BiVO_4$ has been studied for improved photocatalytic performance.[54, 56] However, the energy conversion efficiency is still limited to ~1% (see Supplementary Table 3.1).

Recently, metal-nitride semiconductors, e.g. $In_xGa_{1-x}N$ (noted as InGaN), have drawn significant attention for photocatalytic water splitting.[51, 98-102] The energy bandgap of InGaN can be continuously varied from ultraviolet, through the visible, to the near-infrared, covering nearly the entire solar spectrum. Significantly, the energy band edge positions of InGaN can straddle water redox potentials for a large range of alloy compositions (up to indium compositions ~40-50%), which corresponds to an energy bandgap ~1.7-2 eV.[4, 46, 70] GaN-based materials have also been widely used in electronics and photonics industries, being the 2nd most produced semiconductor (next to only silicon).[103] Since the first demonstration of photocatalytic overall water splitting on GaN nanostructures, significantly improved performance has been reported by engineering the surface charge properties through p-type dopant incorporation and surface Fermi level tuning.[34, 57, 104] The wide bandgap (~3.4 eV) of GaN, however, greatly limits its light absorption capacity only in ultraviolet illumination. To enhance its visible light absorption, InGaN can be integrated forming the double-band structure as demonstrated previously.[26, 98] In addition, Mg doping gradient in III-nitride nanostructures can form the built-in electric field facilitating charge carrier separation and extraction.[4, 51] Recently, photocatalytic overall water splitting with an STH efficiency up to 3.3% has been demonstrated with the use of double-band InGaN/GaN nanowire structures.[51, 98] However, in these studies the indium composition is limited to ~22% or less, corresponding to an energy gap >2.6 eV, which can only absorb photons in the blue spectrum. Albeit photocatalytic water splitting with photon absorption up to

560 nm has been reported for InGaN nanowire photocatalyst,[105, 106] the reported efficiency is still very low, largely due to the inefficient separation and extraction of photo-generated charge carriers.

In this work, we have investigated the design and performance of multi-band InGaN/GaN nanowire arrays for photocatalytic overall solar water splitting. The monolithically integrated quadruple-band InGaN nanowire photocatalyst consists of Mg-doped (p-type) $In_{0.35}Ga_{0.65}N$ (E_g ~2.1 eV), $In_{0.27}Ga_{0.73}N$ (E_g ~2.4 eV), $In_{0.20}Ga_{0.80}N$ (E_g ~2.6 eV) and GaN (E_g ~3.4 eV) segments, which are grown on nonplanar silicon wafers by plasma-assisted molecular beam epitaxy (MBE) and can effectively absorb ultraviolet and visible portion of the solar spectrum. The use of a nonplanar Si wafer allows for the controlled formation of Mg doping gradient along the lateral dimension of the nanowire structures. The resulting built-in electric field steers photo-generated electrons and holes to the proton reduction and water oxidation sites, respectively, thereby leading to more efficient charge carrier separation and suppressed recombination and back reaction. An STH conversion efficiency of ~5.2% was achieved on such quadruple-band InGaN nanowire photocatalyst. The artificial photosynthesis device presented in this study offers a unique platform for achieving high efficiency, scalable solar-to-fuel conversion, including solar water splitting and reduction of carbon dioxide (CO_2) to hydrocarbon fuels.

3.2 Results and Discussions

3.2.1 Schematic designing of quadruple-band nanowires

Illustrated in Figure 3.1a is the schematic conduction and valence band edge positions of GaN, $In_{0.4}Ga_{0.6}N$, and InN, and their respective alignments to the water redox potentials, represented by hydrogen evolution reaction (HER) and oxygen evolution reaction (OER) in pH neutral water solution.[45, 107, 108] It is seen that InGaN alloys with indium compositions up to ~40% can meet the stringent electronic and thermodynamic requirements for overall water splitting and therefore have the potential to drive overall solar water splitting in pH neutral electrolyte solutions without sacrificial reagents.[45, 108] The overall photocatalytic water splitting system presented in this

study is illustrated in Figure 3.1b, showing the monolithic integration of InGaN nanowire arrays on a nonplanar silicon wafer. Schematic of the ideal quadruple-band InGaN nanowire structure and ideal light splitting diagram is further depicted in Figure 3.1c. Indium compositions in each band are 0%, 20%, 27%, and 35%, corresponding to energy bandgap of ~3.4 eV, ~2.6 eV, ~2.4 eV, and ~2.1 eV, respectively, which could absorb solar photons with wavelengths up to ~600 nm. For comparison, previously reported photocatalytic devices can only absorb high energy photons (2.8~3.5 eV) for overall water splitting,[4, 109, 110] which limits their energy conversion efficiency. In addition, the use of a nonplanar wafer in this work offers several benefits. It leads to enhanced light trapping and absorption,[111, 112] and allows for the direct exposure of lateral surfaces of nanowire arrays to normal sunlight illumination. As such, an inverted multi-band structure is studied, with the narrower bandgap light absorber placed atop. Schematically shown in Figure 3.1d is the monolithically integrated quadruple-band $In_{0.35}Ga_{0.65}N/In_{0.27}Ga_{0.73}N/In_{0.20}Ga_{0.80}N/GaN$ nanowire used for photocatalytic overall water splitting in this study. Such a stacking sequence was found to be easier to grow by plasma-assisted MBE (see Section 3.3.2).

Significantly, due to the use of a nonplanar Si wafer and the formation of nanowires vertically aligned to the local surfaces (Figure 3.1b), only one side of the nanowires is directly exposed to Mg flux during epitaxial growth, schematically shown in Figure 3.1d. As such, an Mg doping gradient is spontaneously formed along the nanowire lateral dimension, which introduces a built-in electric field, shown in Figure 3.1e.[51] It is seen that photo-generated electrons migrate towards the lightly Mg-doped side for proton reduction reaction, whereas photo-generated holes drift to the more heavily Mg-doped surface for water oxidation reaction. The rapid separation and extraction of photo-generated electrons and holes to the respective cathodic and anodic surfaces can significantly reduce charge carrier recombination and further suppress any back reaction, thereby leading to enhanced efficiency for solar water splitting.

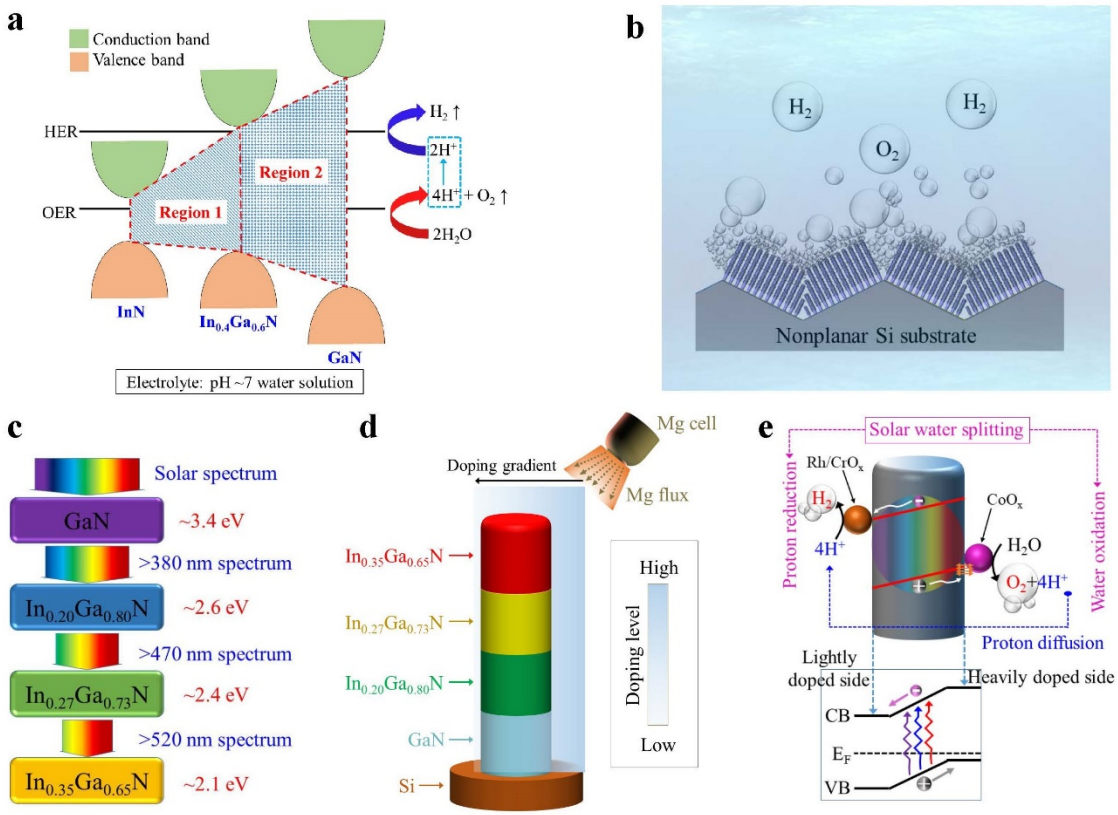

Figure 3.1 Schematic design and structural properties of monolithic multi-band metal nitride nanowire arrays for photocatalytic overall water splitting in nearly pH neutral electrolyte solution. (a) Band edge positions of GaN, InN, and their InGaN compounds. In pH ~7 liquid solution, InGaN alloy with indium incorporation up to 40% can straddle the water redox reaction, noted as Region 2. Higher indium incorporation (Region 1) makes InGaN compounds unsuitable for overall solar water splitting. (b) Schematic illustration of photocatalytic water splitting on InGaN nanowire arrays monolithically integrated on a nonplanar Si wafer. (c) Schematic illustration of ideal light absorption on the multi-band InGaN stacks with varied indium compositions. (d) Schematic of the quadruple-band InGaN nanowire. p-Type dopant originating from the tilted Mg effusion cell (relative to the nanowire orientation) leads to the Mg doping gradient profile in lateral direction of the nanowires, which can introduce a built-in electric field, illustrated in (e), for efficient charge carrier separation and extraction for water redox reactions.

3.2.2 Morphology and optical properties of InGaN nanowires

Scanning electron microscope (SEM) images of metal-nitride nanowires grown on planar and nonplanar Si wafers are shown in Figures 3.2a and 3.2b, respectively. InGaN nanowires grown on a nonplanar Si wafer improve the hydrophilic property, shown in Supplementary Figure 3.5, which may promote efficient mass diffusion during solar water splitting. Strong photoluminescence (PL) emission of InGaN nanowires with various indium compositions were measured at room temperature, shown in Figure 3.2c,

confirming the excellent material quality. By varying the growth conditions (see Section 3.3.2), their energy bandgaps can be tuned from ~3.4 eV to ~2.1 eV, corresponding to PL emission wavelengths from ~370 nm to ~580 nm, respectively.[70-72] For the PL emission at ~580 nm, the corresponding indium composition is ~35%.

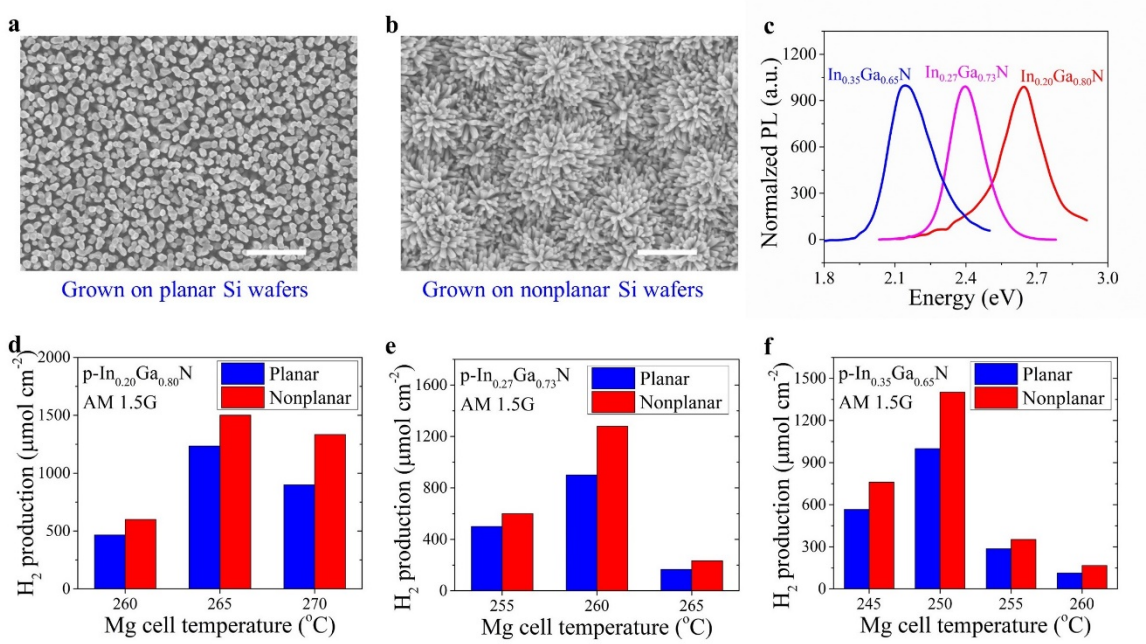

Figure 3.2 Properties and photocatalytic performance of single-band metal nitride nanowires grown on planar or nonplanar Si wafers, with different doping levels by varying the Mg effusion cell temperature. Electron microscope images of InGaN nanowires grown on planar and nonplanar Si wafers. (a) Scale bar: 1 μm. (b) Scale bar: 1 μm. (c) Room-temperature photoluminescence (PL) spectrum of single-band InGaN nanowires with varied indium compositions of ~20%, ~27%, and ~35%, corresponding to an energy gap of ~2.6 eV, ~2.4 eV, and ~2.1 eV, respectively. (d-f) Summarized H_2 gas production of photocatalytic pure water splitting on single-band p-$In_{0.20}Ga_{0.80}N$ (d), p-$In_{0.27}Ga_{0.73}N$ (e), and p-$In_{0.35}Ga_{0.65}N$ (f) nanowires with varied Mg effusion cell temperatures on planar and nonplanar Si wafers.

3.2.3 Photocatalytic performance of single-band nanowires

We have first performed photocatalytic water splitting studies on individual single-band InGaN nanowire arrays with various indium compositions and Mg-dopant incorporation (see Section 3.3). The photocatalytic water splitting performance of p-$In_{0.20}Ga_{0.80}N$, p-$In_{0.27}Ga_{0.73}N$, and p-$In_{0.35}Ga_{0.65}N$ nanowires are summarized in Figures 3.2d-f, respectively. Recent studies suggested that Mg doping plays a critical role on the photocatalytic performance of III-nitride materials for overall solar water splitting.[3, 57]

Therefore, we have first investigated and optimized the Mg doping effect on solar hydrogen production by varying Mg flux (controlled by the Mg effusion cell temperature). The optimum Mg cell temperatures were identified to be 265 ^{o}C, 260 ^{o}C, and 250 ^{o}C for $In_{0.20}Ga_{0.80}N$, $In_{0.27}Ga_{0.73}N$, and $In_{0.35}Ga_{0.65}N$, respectively. An optimum level of Mg dopant concentration is required to minimize the surface band bending for the efficient extraction of photo-generated charge carriers, as reported previously.[3, 51, 57] The optimum Mg doping levels, however, depend on indium composition and growth conditions. It is observed that 20-40% higher hydrogen production rate was measured for InGaN photocatalysts grown on nonplanar Si wafers compared to those on planar Si wafers under optimized conditions, due to, in part, the enhanced charge carrier separation and extraction (Figure 3.1e). The photocatalytic performance for InGaN nanowires under visible light irradiation has been further confirmed by utilizing various long-pass filters (see Supplementary Figure 3.6). Supplementary Figure 3.7 shows the effect of Mg doping of p-GaN nanowires on solar hydrogen production, which is consistent with previous reports.[57]

3.2.4 Overall pure water splitting of quadruple-band nanowires

We have subsequently studied quadruple-band metal-nitride nanowire photocatalyst by monolithically integrating p-$In_{0.35}Ga_{0.65}N$, p-$In_{0.27}Ga_{0.73}N$, and p-$In_{0.20}Ga_{0.80}N$ together on p-GaN segment (see Figure 3.1d), which can absorb incident light with wavelengths up to ~600 nm. Prior to the demonstration of quadruple-band structure, we first studied the photocatalytic performance of triple-band metal-nitride nanowires for overall solar water splitting (see Section 3.4.2.1 and Supplementary Figure 3.8). Shown in Figure 3.3a are the SEM images of quadruple-band InGaN nanowires grown on a nonplanar Si substrate. The flower-shaped morphology of InGaN nanostructures can maximize the side surface exposed to incident light illumination. The multi-band InGaN nanowires were further characterized by scanning transmission electron microscopy (STEM) and energy-dispersive X-ray spectroscopy (EDX). Shown in Figure 3.3b, the brighter contrast in the top region of the nanowire indicates more indium incorporation due to the atomic number contrast nature in high angle annular dark-field (HAADF) imaging. The InGaN nanowire becomes wider in diameter along the growth direction (indicated by the white

arrow). EDX line scans were performed along axial and lateral directions of the InGaN nanowire. Variations of Ga Lα, In Lα, and N Kα characteristic signals are presented in Figures 3.3c, 3.3d, 3.3e, and 3.3f for EDX scans along Line 1, Line 2, Line 3, and Line 4 in Figure 3.3b, respectively. Along the axial direction, In Lα signal intensity gradually decreases, indicating the reduced concentration of In incorporation from top to bottom of the InGaN nanowire, corresponding to the design shown in Figure 3.1d. There are four segments forming such quadruple-band InGaN nanowire, including (I) ~250 nm $In_{0.35}Ga_{0.65}N$, (II) ~200 nm $In_{0.27}Ga_{0.63}N$, (III) ~280 nm $In_{0.20}Ga_{0.80}N$, and (IV) ~290 nm GaN. For each InGaN segment, variations of Ga Lα and In Lα characteristic signal along the nanowire lateral dimensions are measured and shown in Figures 3.3d, 3.3e, and 3.3f. We have further performed atomic resolution HAADF-STEM imaging for InGaN crystals with various indium compositions, shown in Figures 3.3g-i. The periodic ordering of atoms further demonstrates the high crystallinity, which is critical to reduce the bulk recombination for efficient charge carrier extraction.

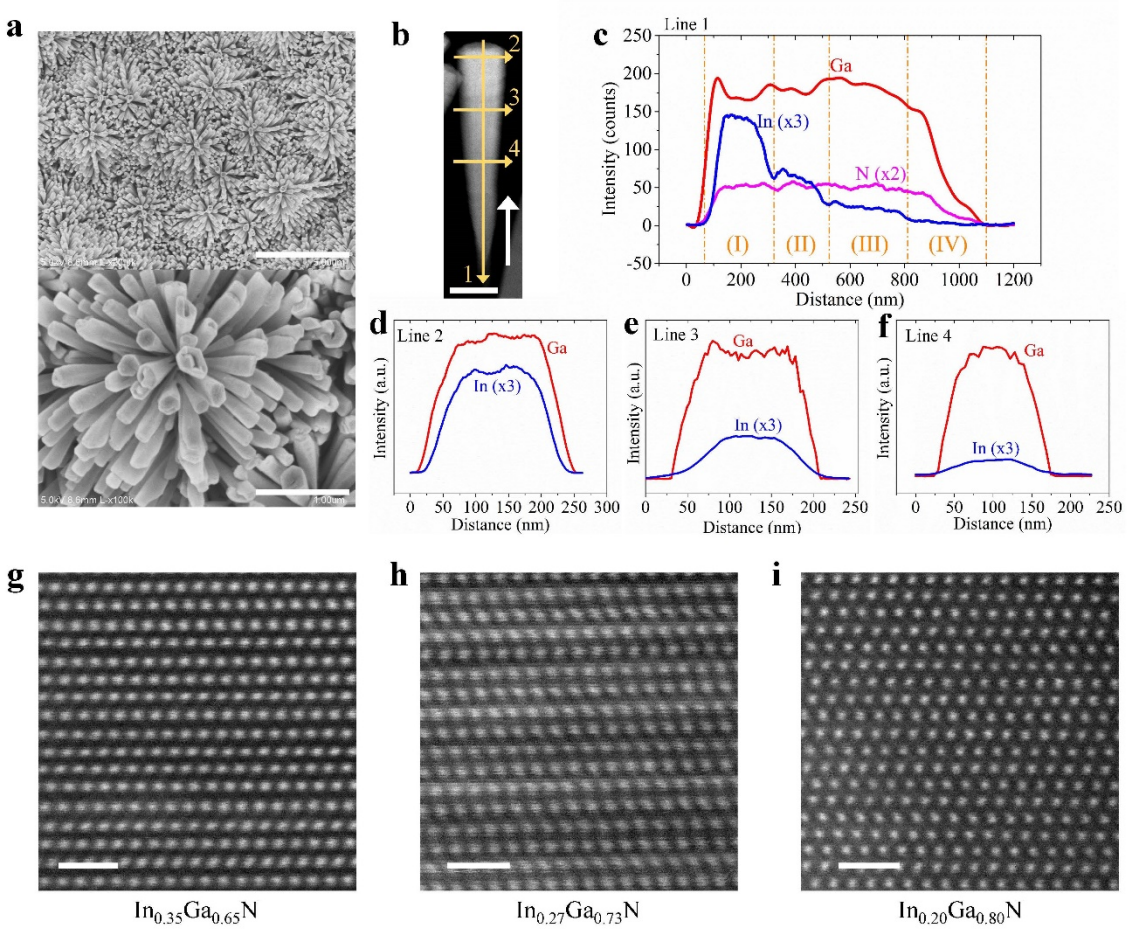

Figure 3.3 Structural characterization of the quadruple-band InGaN nanowire arrays monolithically integrated on a nonplanar Si wafer. (a) Top-view scanning electron microscope (SEM) images of flower-shaped InGaN nanowire structure grown on nonplanar Si substrates. Scale bar: 5 μm (top) and 1 μm (bottom). (b) Dark-filed scanning transmission electron microscope (DF-STEM) image of quadruple-band InGaN nanowire, with energy-dispersive X-ray spectroscopy (EDX) line scanning showing the variation of Ga Lα, In Lα, and N Kα characteristic signals along the axial and lateral directions. Scale bar: 200 nm. Spectrum of Line 1 (c), Line 2 (d), Line 3 (e), and Line 4 (f) are measured along Arrow 1, Arrow 2, Arrow 3, and Arrow 4 in (b), respectively. (g-i) Atomic resolution STEM images of InGaN crystals for (g) $In_{0.35}Ga_{0.65}N$, (h) $In_{0.27}Ga_{0.73}N$, and (i) $In_{0.20}Ga_{0.80}N$, respectively. Scale bar: 1 nm.

3.2.5 Overall pure water splitting of quadruple-band nanowires

Schematically illustrated in Figure 3.4a are the overall solar water splitting process on such quadruple-band InGaN nanowires under light illumination, including photon excitation in each single-band segment, charge carrier separation and extraction, and catalytic water splitting reaction. Due to the built-in electric field introduced by the Mg doping gradient profile, photo-generated electrons and holes are efficiently separated towards the cathodic surface driving water reduction reaction and anodic surface driving

water oxidation reaction, respectively. The rapid separation and extraction of photo-generated electrons and holes to the respective cathodic and anodic surfaces can significantly reduce charge carrier recombination and further suppress any back reaction. Shown in Figure 3.4b is the PL spectrum of quadruple-band InGaN nanowires measured at room-temperature. The very broad emission spectrum indicates its capability of absorbing solar photons across nearly the entire visible spectrum. PL emission spectrum of individual InGaN segments are also shown in Figure 3.4b for comparison.

Photocatalytic water splitting measurements of the quadruple-band nanowire arrays were performed in pH ~7 pure water solution under concentrated light illumination using an AM 1.5G filter (see Section 3.3.4). Shown in Figure 3.4c is the H_2 and O_2 gas evolution for 120 minutes continuous solar water splitting. Multiple cycles of photocatalytic experiments were further performed to confirm stable, continuous gas production. The calculated H_2 to O_2 production ratio is nearly 2:1, corresponding to the stoichiometric ratio in water molecules (H_2O), which is consistent with overall water splitting reaction occurring without other byproduct.[31] The H_2 generation rate is measured to be ~1840 μmol cm^{-2} h^{-1} corresponding to a STH efficiency ~5.2% (see Section 3.4.2.2).

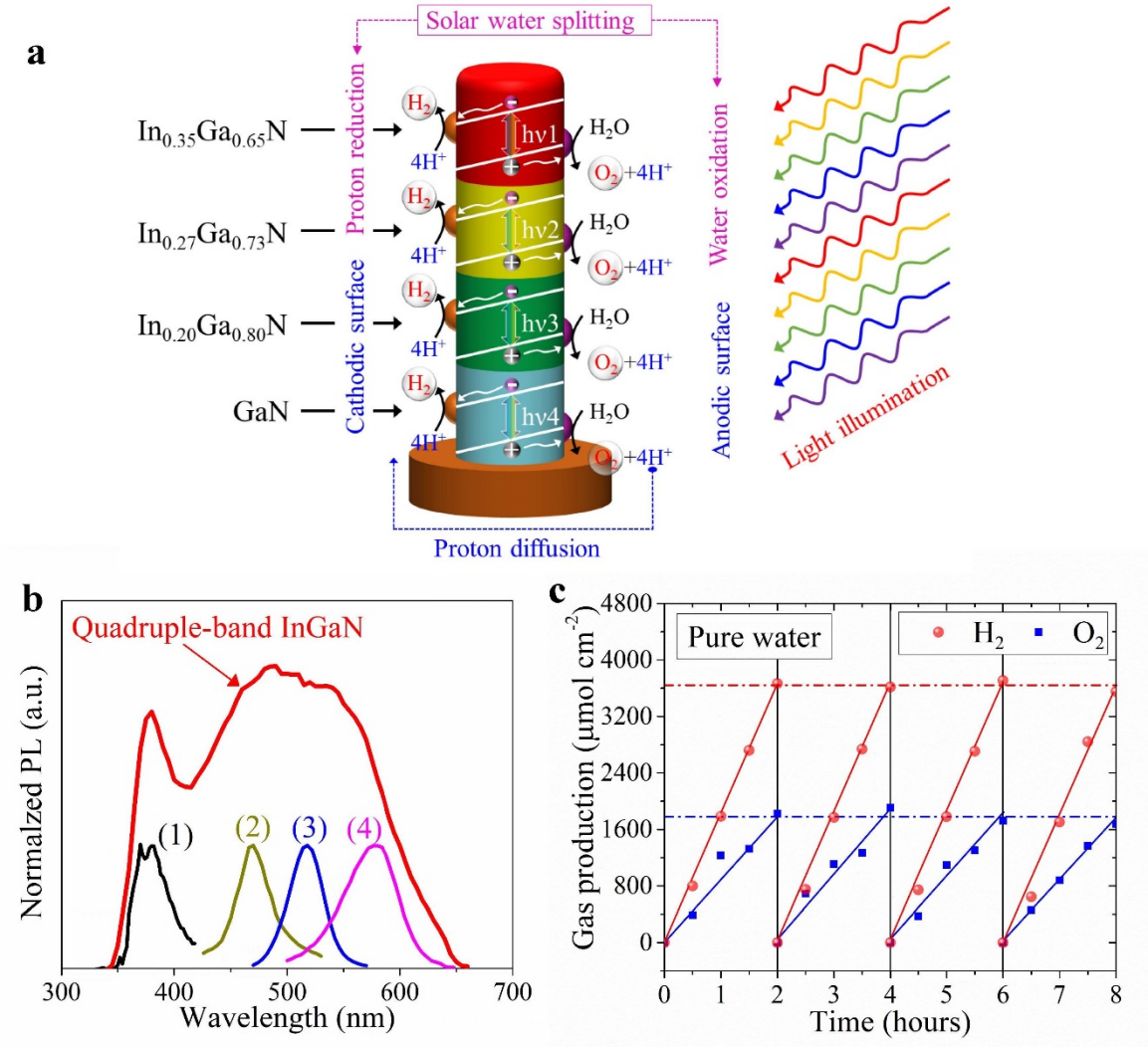

Figure 3.4 Photocatalytic performance of quadruple-band InGaN nanowire arrays measured in pure water under 300 W Xenon lamp equipped with an AM 1.5G filter. (a) Schematic illustration of overall water splitting process occurring on the quadruple-band nanowires under light illumination. (b) Room-temperature PL spectrum of the quadruple-band InGaN nanowires, compared to those of single-band nanowires, including (1) p-GaN, (2) p-$In_{0.20}Ga_{0.80}N$, (3) p-$In_{0.27}Ga_{0.73}N$, and (4) p-$In_{0.35}Ga_{0.65}N$. (c) H_2 and O_2 gas generation as a function of time measured in multiple experiment cycles.

3.2.6 Discussions

Summarized in Supplementary Table 3.1 is the performance comparison of some of the previously best-reported photocatalyst systems for overall solar water splitting, compared to quadruple-band InGaN nanowires demonstrated in this work. To date, for III-nitride semiconductors, the best reported STH efficiency is 3.3% on double-band $In_{0.22}Ga_{0.78}N$/GaN photochemical diode.[4, 26, 51] For metal oxide and other nitride

semiconductors showing comparable photocatalytic stability, e.g. $SrTiO_3$, $BiVO_4$, and C_3N_4,[53, 54, 56, 58, 85, 113] the highest STH efficiency has generally been limited to ~1% mainly due to insufficient light absorption and strong recombination. Compared to previously reported CoO_x particulate system with ~30 mins stability,[82] the presented quadruple-band metal-nitride nanowires demonstrate relatively good stability during overall solar water splitting, without showing any significant degradation of photocatalytic performance for ~8 hrs. Compared to previous reported III-nitride photocatalysts, the significantly improved performance is attributed to the following factors: 1) the use of quadruple-band structure to enhance visible light absorption and water redox reaction, 2) the use of nonplanar wafer to enhance light absorption and trapping, and 3) controlled p-type dopant incorporation to enhance charge carrier separation and extraction. Theoretically, the ideal multi-band photocatalytic system in the current design can reach an energy conversion efficiency ~16% if all the incident photons above the energy bandgap can be converted to charge carriers to drive water splitting reaction (see Supplementary Figure 3.9).[5, 114] Therefore, such multi-band nanostructures can be further optimized to achieve a possible STH efficiency >10%, which may include (1) optimization of the design by placing large energy gap materials on top, (2) optimization of the deposition of co-catalyst particles, (3) integration of such nanowire photocatalysts on reflective substrate surface to further enhance light absorption, and (4) minimization of surface recombination by surface treatment or passivation.

In summary, we have demonstrated wafer-level broadband InGaN nanowire photocatalysts that can significantly improve the efficiency of direct photocatalytic overall water splitting. Such photocatalyst materials can be directly synthesized on low cost, large area Si wafer utilizing industry standard manufacturing process. Therefore, their large scale manufacturability is unquestionable. Significantly, with the incorporation of suitable co-catalysts, such a unique structure can be exploited to achieve high efficiency, stable artificial photosynthesis including one-step CO_2 reduction to hydrocarbon fuels.

3.3 Methods

3.3.1 Nonplanar Si surface preparation

Two-inch prime-grade polished silicon wafer was etched in 80 °C KOH solution (1.8% KOH in weight with 20% isopropanol in volume) for 30 minutes to form the micro-textured surface with Si pyramids.[103] After being neutralized in concentrated hydrochloric acid, surface cleaning by acetone/methanol, and native oxide removal by 10% hydrofluoric acid, the nonplanar Si wafer was loaded into MBE chamber for the growth of InGaN nanowires.

3.3.2 Molecular beam epitaxial growth of multi-band InGaN nanowires

Mg doped (p-type) InGaN nanowires, single-band or multi-band structures, were grown on as-prepared nonplanar Si substrates by plasma-assisted molecular beam epitaxy (MBE) under N-rich conditions. The growth parameters include a gallium (Ga) beam equivalent pressure of ~7E-8 Torr, a nitrogen flow rate of 1 sccm, and a plasma power of 350 W. The substrate temperature, indium (In) beam equivalent pressure (BEP), and magnesium (Mg) cell temperature were tuned to synthesize different single-band or multi-band InGaN nanowires with various p-doping and alloy concentrations. For the single-band p-GaN nanowires, the substrate temperature was 685 ^{o}C, Ga BEP was ~7E-8 Torr, and the growth duration was 3 hours. p-Type doping level was tuned by using different Mg cell temperatures (265 ^{o}C, 270 ^{o}C, 275 ^{o}C, and 280 ^{o}C). For the single-band p-$In_{0.20}Ga_{0.80}N$ nanowires, the substrate temperature was 675 ^{o}C, Ga BEP ~7E-8 Torr, In BEP was ~7.3E-8, and growth duration was 3 hours. For single-band p-$In_{0.27}Ga_{0.73}N$ nanowires, the substrate temperature was 662 ^{o}C, Ga BEP was ~7E-8 Torr, In BEP was ~7.3E-8, and growth duration was 3 hours. For single-band p-$In_{0.35}Ga_{0.65}N$ nanowires, the substrate temperature was 640 ^{o}C with Ga BEP ~7E-8 Torr, In BEP ~3.5E-8, and growth duration of 3 hours. For quadruple-band InGaN nanowires, the growth conditions are nearly identical to those of the constituting single-band nanowires, including (along the growth direction)1.5 hours p-GaN, 1.5 hours p-$In_{0.20}Ga_{0.80}N$, 1.5 hours p-$In_{0.27}Ga_{0.73}N$, 1.5 hours p-$In_{0.35}Ga_{0.65}N$, and 0.5 hours p-GaN.

3.3.3 Cocatalyst nanoparticles deposition

Prior to photocatalytic water splitting experiments, metal nitride nanowires were decorated with hydrogen evolution reaction (HER) and oxygen evolution reaction (OER) cocatalyst nanoparticles for efficient water redox reactions using photo-deposition method. InGaN samples were put in a glass chamber with a quartz lid, which was first pumped down and then illuminated using a 300 W Xenon lamp for 20 minutes to deposit cocatalyst nanoparticles on InGaN nanowires. The deposition of Rh/CrO_x core/shell structures consists of two steps, including 1) the use of 55 ml deionized water, 11 mL methanol, and 2 μmol hexachlororhodate (Na_3RhCl_6, Sigma-Aldrich) for the formation of Rh core, and 2) the use of 55 mL deionized water, 11 mL methanol, and 4 μmol potassium chromate (K_2CrO_4, Sigma-Aldrich) for CrO_x shell. The deposition of CoO_x nanoparticles involves the use of 60 mL deionized water, 6 mL potassium iodate (KIO_3, 0.01 M, Sigma-Aldrich), and 4 μmol cobalt nitrate ($Co(NO_3)_2$, Alfa Aesar).

3.3.4 Photocatalytic water splitting measurements

Photocatalytic overall water splitting measurements were conducted in a vacuum chamber with a quartz lid. The measurement chamber was partially filled with 70 mL pure water solution (pH ~7), which covered the InGaN photocatalysts, and then was pumped down. After evacuating the chamber, the sample was illuminated with a Xenon lamp (PE300BUV, CERMAX) together with various optical filters. With the use of AM 1.5 G filter, the light intensity is ~2339 mW/cm^2, equivalent to ~23 suns, as measured at the sample position. The water solution was purged using argon gas for 30 minutes before any experiments. H_2 and O_2 gas was analyzed by sampling using a vacuum-tight syringe and evaluating using a gas chromatograph machine (GC-8A, Shimazdu) equipped with a thermal conductivity detector (TCD) and high purity argon as carrier gas. The sample size is in the range of 0.5~1 cm^2 for photocatalytic experiments.

3.3.5 Structural and optical characterization

Room-temperature photoluminescence measurements of InGaN nanowires were performed in a homemade setup with a He-Cd 325 nm laser as the excitation source, and the emission is spectrally resolved by a SPEX spectrometer equipped with a

photomultiplier tube. SEM images were recorded with a secondary electron detector using a Tescan MIRA3 system (15 kV) and a JEOL IT500 system (20 kV) with an EDX detector. High angle annular dark-field scanning transmission electron microscopy (HAADF-STEM) images were collected using a JEOL 3100R05 microscope operated at 300 keV in aberration corrected STEM mode with a beam convergence angle 22 mrad and detector collection angle 85 mrad.

3.4 Supporting Information

3.4.1 Supplementary figures

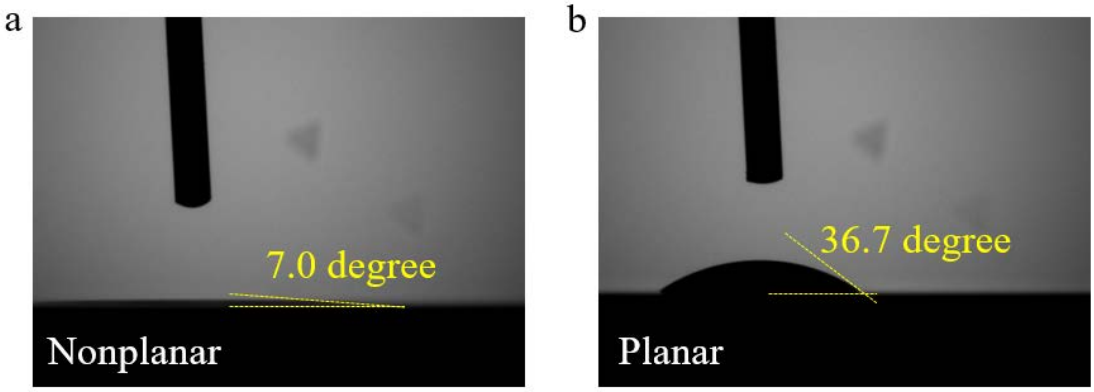

Figure 3.5 Contact angle measurements using pure water droplets on metal nitride nanowires grown on a nonplanar Si wafer (a) and a planar Si wafer (b). The water contact angle can be greatly reduced by using nonplanar substrates indicating the improved hydrophilic property.

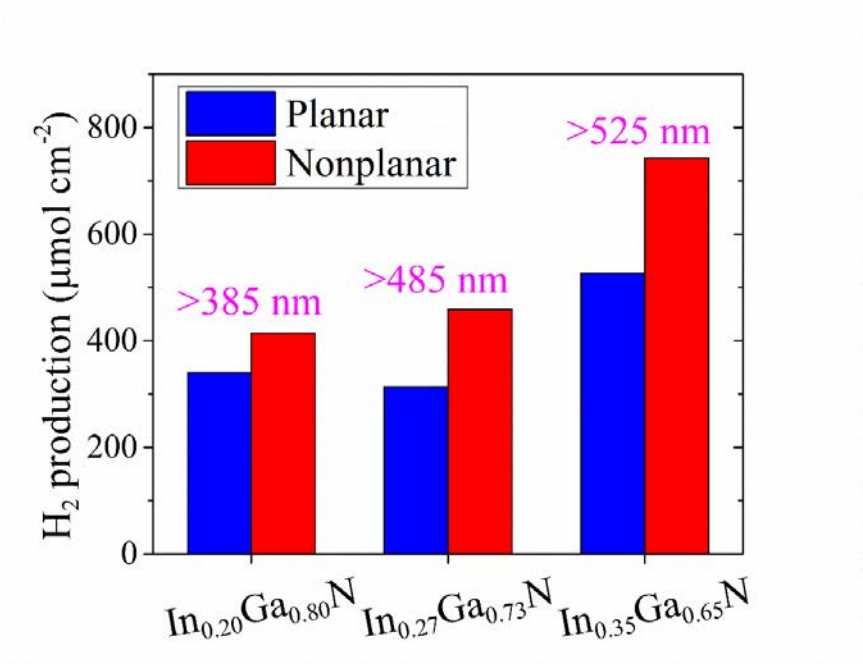

Figure 3.6 Visible light driven H_2 gas production of different InGaN nanowires with various indium compositions and optimized Mg doping for photocatalytic water splitting by using appropriate long-pass optical filters.

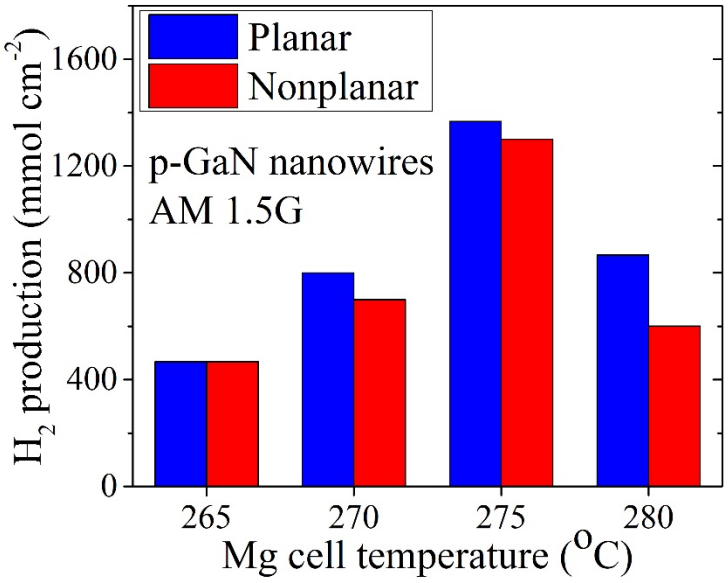

Figure 3.7 H_2 gas production of p-GaN nanowires with different Mg doping grown on planar and nonplanar substrates for photocatalytic water splitting. It is interesting to note that p-GaN nanowires shows nearly the same performance on nonplanar wafers, compared to that on planar wafers. The possible reason could be that the relatively small GaN nanowire size makes charge carrier transfer efficient so that gradient doping profile on nonplanar wafers may not play a significant role.

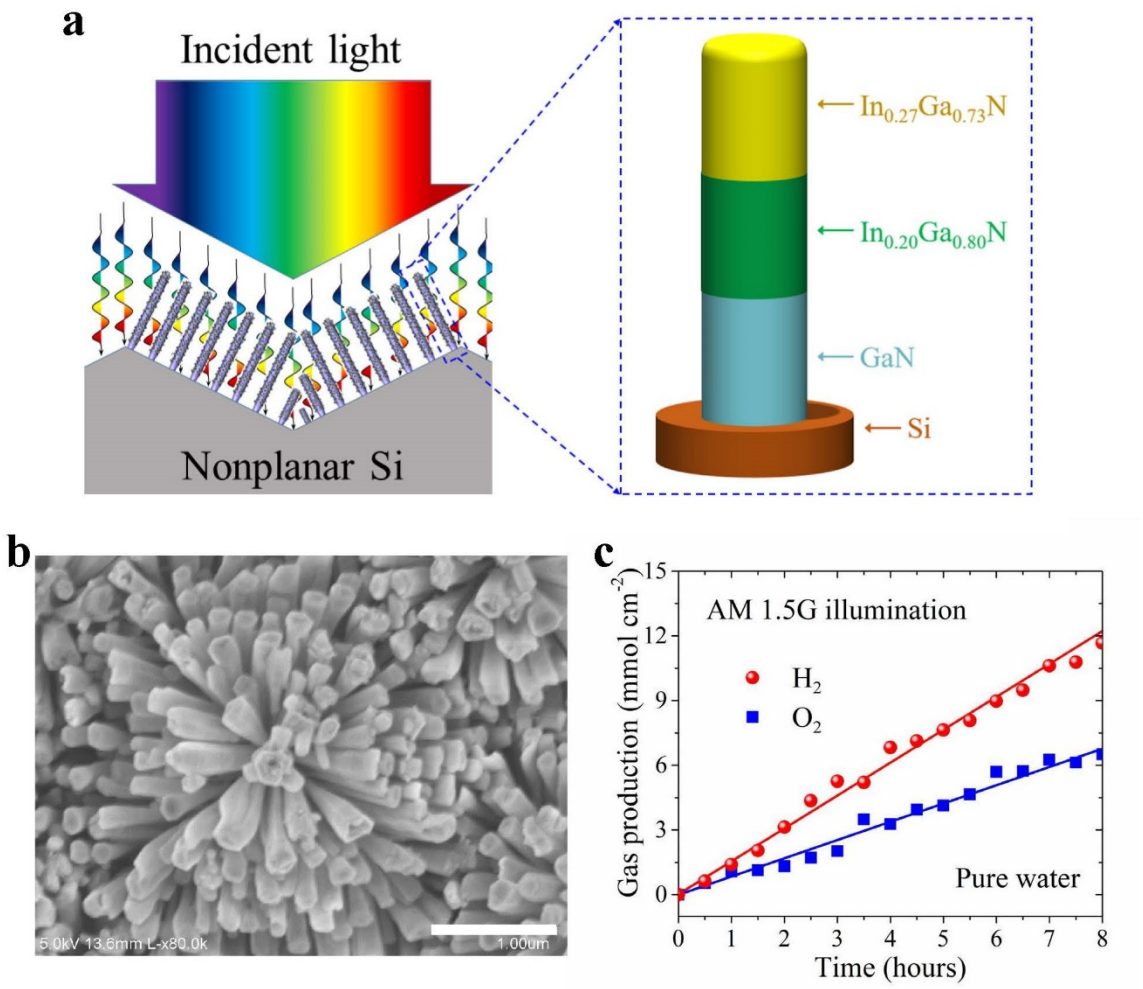

Figure 3.8 Structural properties and photocatalytic performance of triple-band InGaN nanowires arrays on nonplanar Si wafers under 300 W Xenon lamp equipped with an AM 1.5G filter. (a) Schematic illustration of photocatalytic water splitting of InGaN nanowires with triple-band nanostructure. (b) Electron microscope image of the triple-band InGaN nanowires integrated on a nonplanar Si substrate. Scale bar: 1 μm. (c) Overall photocatalytic pure water splitting on the triple-band InGaN nanowires for 8 hours, with a stoichiometric H_2 and O_2 gas production.

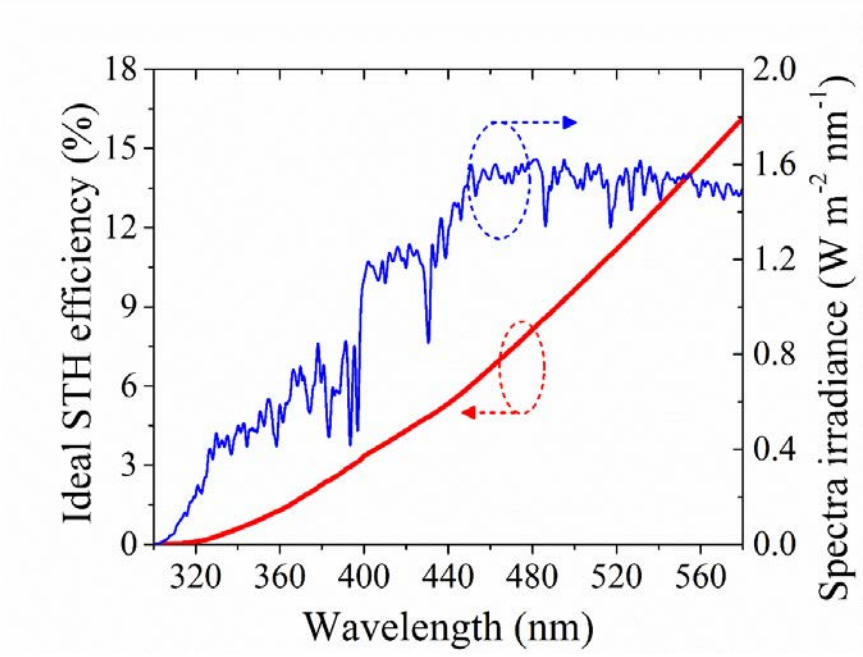

Figure 3.9 The theoretical maximum solar-to-hydrogen (STH) conversion efficiency for the ideal multi-band photocatalyst system absorbing photons with wavelengths up to 580 nm, wherein all the incident photons are assumed to drive water splitting reactions.[31]

3.4.2 Supplementary notes

3.4.2.1 Overall solar water splitting on triple-band InGaN nanowires consisting of p-$In_{0.27}Ga_{0.73}N$, p-$In_{0.20}Ga_{0.80}N$, and p-GaN segments

Schematically shown in Supplementary Figure 3.8a is the monolithically integrated triple-band metal-nitride nanowire arrays, consisting of p-$In_{0.27}Ga_{0.73}N$, p-$In_{0.20}Ga_{0.80}N$, and p-GaN segments grown on a nonplanar Si wafer. Shown in Supplementary Figure 3.8b is the SEM image of such triple-band $In_{0.27}Ga_{0.73}N$/$In_{0.20}Ga_{0.80}N$/GaN nanowire arrays grown on a nonplanar Si surface. InGaN nanowires are vertically aligned to the local Si surface, which forms the overall flower-shaped nanostructure due to the Si pyramid substrate. From the top view, there is no spatial gap to expose substrate surface, which, in turns, demonstrates the high nanowire density per projective area for improved light absorption. The tilted InGaN nanowires allow for a large surface exposure to incident illumination for enhanced light absorption and water redox reaction. The textured wafer surface, together with the nanowire arrays, also significantly enhances light trapping and absorption.

Photocatalytic measurement of the triple-band $In_{0.27}Ga_{0.73}N/In_{0.20}Ga_{0.80}N/GaN$ nanowire arrays was performed in pH ~7 pure water solution under concentrated AM 1.5G illumination. Shown in Supplementary Figure 3.8c is the H_2 and O_2 gas production of the triple-band InGaN nanowires for 8 hours overall solar water splitting. The observed linear H_2 and O_2 gas production indicates stable solar water splitting reaction occurring on InGaN nanowires.[104] Calculated H_2 to O_2 production ratio is nearly 2:1, corresponding to the stoichiometric ratio in water molecules (H_2O), which is consistent with overall water splitting reaction occurring without other byproduct.[31] H_2 generation rate is measured to be ~1450 μmol cm^{-2} h^{-1} corresponding to ~4.1% solar-to-hydrogen (STH) conversion efficiency (see Section 3.4.2.2). The continuous 8 hours photocatalytic overall pure water splitting on the triple-band $In_{0.27}Ga_{0.73}N/In_{0.20}Ga_{0.80}N/GaN$ nanowire arrays demonstrates its photocatalytic stability.

3.4.2.2 Solar-to-hydrogen conversion efficiency calculation

For overall water splitting, the solar-to-hydrogen (STH) conversion efficiency is defined as the chemical energy of generated H_2 gas divided by the solar energy of incident light. The STH efficiency for photocatalytic water splitting devices can be calculated by Eqn. (3-1) using the Gibbs free energy (237 kJ mol^{-1}) of H_2.[115] To obtain STH efficiency correctly, it is required to demonstrate the stoichiometric H_2 and O_2 gas evolution, without adding any sacrificial reagents.

$$\mathrm{STH} = \left[\frac{H_2\ generation\ rate\ (mmol\ s^{-1}) \times 237000\ J\ mol^{-1}}{Incident\ solar\ power\ (mW\ cm^{-2}) \times Area\ (cm^2)}\right]_{AM1.5G} \quad (3\text{-}1)$$

The incident solar power from Xenon lamp with AM 1.5G filter was measured to be 2329 mW cm^{-2} by a thermopile detector (919P, Newport).

(a) Triple-band InGaN nanowires for pure water splitting

$$\mathrm{STH} = \left[\frac{(1.45/3600\ mmol\ s^{-1}) \times 237000\ J\ mol^{-1}}{(2329\ mW\ cm^{-2}) \times (1\ cm^2)}\right]_{AM1.5G} = \sim 4.1\%$$

(b) Quadruple-band InGaN nanowires for pure water splitting

$$\mathrm{STH} = \left[\frac{(1.84/3600\ mmol\ s^{-1}) \times 237000\ J\ mol^{-1}}{(2329\ mW\ cm^{-2}) \times (1\ cm^2)}\right]_{AM1.5G} = \sim 5.2\%$$

3.4.3 Supplementary table

Table 3.1 STH efficiency and stability of previously reported photocatalyst systems for overall solar water splitting, compared to the multi-band InGaN nanowires presented in this work.

Materials	Cocatalyst	Electrolyte	Light	STH (%)	Stability (hours)	Year [Ref.]
Multi-band InGaN nanowires	Rh/CrO_x - CoO_x	Pure water	23 suns	5.2	10	This work
Double-band $In_{0.22}Ga_{0.78}N/GaN$	Rh/CrO_x	Pure water	32 suns	3.3	2	2018 [51]
$SrTiO_3$:Al	Rh/CrO_x	Pure water	300W Xe lamp	0.4	4	2018 [52]
CDs/CdS-S	N/A	Seawater	One sun	<0.1	90	2018 [116]
Double-band $In_{0.25}Ga_{0.75}N/GaN$	Rh/CrO_x - CoO_x	Seawater	27 suns	1.9	3	2018 [98]
MoS_2/TiO_2	N/A	Pure water methanol	One sun	<1	21	2018 [117]
TiO_2:Ta/N $SrTiO_3$:Rh	Ru - RuO_2	1 mM $NaIO_3$ 1 mM $FeCl_3$	One sun	0.02	15	2017 [53]
$SrTiO_3$:La, Rh/C /$BiVO_4$:Mo	Ru - RuO_x	Pure water	One sun	1.2	6	2017 [54]
Bi_4NbO_8Cl $SrTiO_3$:Rh	Pt - RuO_x	Fe^{3+}/Fe^{2+} redox	300W Xe lamp	<0.4	24	2016 [55]
$SrTiO_3$:La, Rh/Au /$BiVO_4$:Mo	$Ru/Cr_2O_3/a\text{-}TiO_2$	Pure water	One sun	1.1	10	2016 [56]
GaN nanowires	Rh/CrO_x	Pure water	27 suns	<1	22	2015 [57]
CDots/C_3N_4	N/A	Pure water	1 sun	2	200 days	2015 [85]
$SrTiO_3$: Rh, Sb $BiVO_4$:Mo	IrO_2/CoO_x	1 mM H_2SO_4	300W Xe lamp	0.01	30	2014 [58]
CoO nanoparticles	N/A	Pure water	One sun	5	0.5	2013 [82]
Si/TiO_2	Pt - IrO_x	0.5 M H_2SO_4	1.5 suns	0.12	4.5	2013 [59]

3.5 Summary

In this chapter, a benchmark STH efficiency of 5.2% is achieved on the quadruple-band InGaN nanowires for photocatalytic overall pure water splitting. Compared to previous reports, the significantly improved performance is attributed to the following factors: 1) the use of quadruple band structure to enhance water redox reaction without sacrificing photon absorption, 2) the use of nonplanar wafer to enhance light absorption and trapping, and 3) controlled p-type dopant incorporation to enhance charge carrier separation and extraction. Theoretically, however, the ideal multi-band photocatalytic

system in current design can reach an energy conversion efficiency ~16% if all the incident photons above the energy bandgap can be converted to charge carriers to drive water splitting reaction (Supplementary Figure 3.9).[5, 118] Therefore, such multi-band nanostructures can be further optimized to achieve a possible STH efficiency >10%, which may include (1) optimization of the design by placing large energy gap materials on top, (2) optimization of the deposition of co-catalyst particles, (3) integration of such nanowire photocatalysts on reflective substrate surface to further enhance light absorption, and (4) minimization of surface recombination by surface treatment or passivation layers. Significantly, with the incorporation of suitable co-catalysts, such a unique structure can be exploited to achieve high efficiency, stable artificial photosynthesis including one-step CO_2 reduction to hydrocarbon fuels.

CHAPTER IV

An $In_{0.42}Ga_{0.58}N$ Tunnel Junction Nanowire Photocathode Monolithically Integrated on a Nonplanar Si Wafer

4.1 Introduction

Solar water splitting and hydrogen generation is one important step of artificial photosynthesis to meet the increasing demand of clean, renewable energy.[17] An essential component of a solar water splitting device is a photocathode, often consisting of a p-type semiconductor, that can drive proton reduction efficiently and stably in acidic solution under sunlight illumination.[80, 119, 120] In the past decades, extensive efforts have been devoted to exploring various photocathode materials and structures. Illustrated in Figure 4.1 are the energy band diagrams of some commonly studied photocathode semiconductors.[4, 19, 35, 108, 121, 122] Metal oxide semiconductors typically have large energy bandgap values and, as a consequence, can only absorb a small portion of the solar spectrum.[20] To utilize the majority energy of sunlight, Group III-V and IV semiconductors, including GaP, $GaInP_2$, GaAs, InP, and Si photocathode materials have been intensively studied. Although relatively high photocurrent densities have been reported, e.g. ~22 mA cm^{-2} for GaAs (E_g ~1.4 eV)[11], ~25 mA cm^{-2} for InP (E_g ~1.3 eV)[123], and ~35 mA cm^{-2} for n^+/p-Si (E_g ~1.1 eV)[124], these materials are not stable in acidic electrolytes, which is kinetically preferred for proton reduction. An extra protection layer, e.g. TiO_2, is therefore required to protect against detrimental photocorrosion.[18, 125] In addition, there is an urgent need to develop a semiconductor photocathode with an energy bandgap ~1.7-2.0 eV, which, when integrated with a narrow

bandgap ~1.1 eV bottom light absorber, e.g. Si, promises solar water splitting cells with a solar-to-hydrogen (STH) efficiency up to 30%.[17, 114, 126, 127]

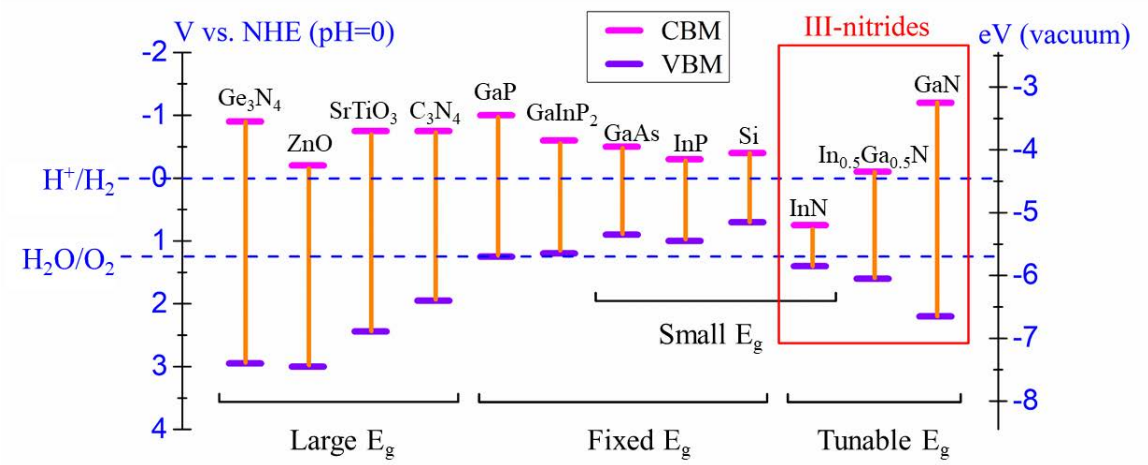

Figure 4.1. Schematic energy band diagram of some commonly studied single-junction photocathode materials, including metal oxides, III-V, Si, and III-nitride semiconductors, assuming in acidic solution (pH = 0). CBM and VBM represent the conduction band minimum and valence band maximum, respectively.

In the quest for a 1.7-2.0 eV semiconductor material that can function efficiently and stably as a photocathode in acidic electrolyte, group III-nitrides, e.g. GaN and its alloys, have drawn considerable attention.[19, 35, 126] GaN based semiconductors have been widely used in electronics and photonics industries, and they are the second most produced semiconductor material only next to Si. Significantly, InGaN with indium composition in the range of 40-50% exhibits a direct energy bandgap of 1.65-1.9 eV, whose band edges can straddle proton reduction and water oxidation potentials.[19] III-nitride semiconductors also exhibit large carrier mobility and a high absorption coefficient (~10^5 cm^{-1}),[128-132] and have demonstrated the capability to support current densities of hundreds of kA/cm^2 in power transistors[133-135] (e.g. six to seven orders of magnitude larger than that relevant for solar water splitting). To date, however, the best reported energy conversion efficiency for an InGaN photocathode in acidic electrolyte is still below 1% (see Supplementary Table 4.1).[136-138] Moreover, their long-term stability in an acidic electrolyte has remained largely unknown. The underlying challenges include the presence of large densities of defects and dislocations for conventional InGaN materials grown by metal-organic chemical vapor deposition (MOCVD) and the difficulty in achieving p-type doping of In-rich InGaN.[139-142]

In this work, we have performed a detailed investigation of the synthesis and photoelectrochemical properties of crystalline In-rich p-type InGaN nanowire arrays on industry-grade non-planar Si wafers that are commonly used for fabricating commercial Si solar cell modules. The nanowires are synthesized using a plasma-assisted molecular beam epitaxy (MBE) method under N-rich conditions to promote the formation of N-terminated surfaces,[24, 70, 143, 144] which can protect against photocorrosion and oxidation. p-Type InGaN nanowires are connected with the underlying n-type Si wafer through a tunnel junction, which provides low-resistivity connection and further serve as an electron blocking layer to enhance electron extraction. For the InGaN photocathode with indium composition ~42% (E_g ~1.9 eV), a short-circuit photocurrent density of 12.3 mA cm^{-2} and a large onset potential of 0.79 V vs. RHE were measured. The maximum applied bias photon-to-current efficiency (ABPE) is 4% at ~0.52 V vs. RHE, which is more than one order of magnitude larger than that of previously reported InGaN photocathodes.[136-138] Significantly, the photocathode shows no degradation for over 30 hrs solar wafer splitting at a steady current density of 12 mA cm^{-2} without adding any extra surface protection layer. Detailed studies were also performed to correlate the photoelectrochemical performance with indium composition of the InGaN nanowires. Further improvement in the device performance, together with the integration with a buried Si junction, promises stable unassisted solar water splitting.[114]

4.2 Results and Discussions

4.2.1 InGaN nanowire structure and optical property

Schematically shown in Figure 4.2a is the design of p-type InGaN nanowire photocathode formed on a non-planar Si wafer. Each nanowire consists of an n-type GaN segment (length ~160 nm), an n^{++}-GaN/InGaN/p^{++}-GaN tunnel junction, and a *p*-type InGaN segment (length ~800 nm). The top p-InGaN segment serves as the light absorber and photocatalytic reactor for proton reduction. Pt nanoparticles are deposited on the nanowire surfaces using a photodeposition process (see Section 4.4.3). The direct integration of p-type InGaN on Si wafer (whether n- or p-type) generally leads to high resistivity, due to the formation of extensive defects and impurity incorporation at the

heterointerface. To alleviate this issue, an n-type GaN nanowire segment is first grown on n-type Si wafer, schematically shown in the inset of Figure 4.2a, followed by the formation of an n^{++}/p^{++} GaN tunnel junction.[145, 146] A thin layer of InGaN is also incorporated between n^{++} and p^{++}-GaN, illustrated in the inset of Figure 4.2b. The piezoelectric field created by the InGaN segment can further reduce the depletion depth and resistivity of the tunnel junction, thereby enhancing the recombination of charge carriers (photo-generated holes from p-InGaN and electrons injected from n-Si).[147-149] Such tunnel junction design has been previously exploited to realize efficient light emitting diodes (LEDs) and photoelectrodes in HBr splitting, but has not been used in solar water splitting.[37, 146, 150] It is important to note, however, that in the present study the InGaN segments are not uniformly incorporated in all nanowires due to the use of non-planar Si wafer.

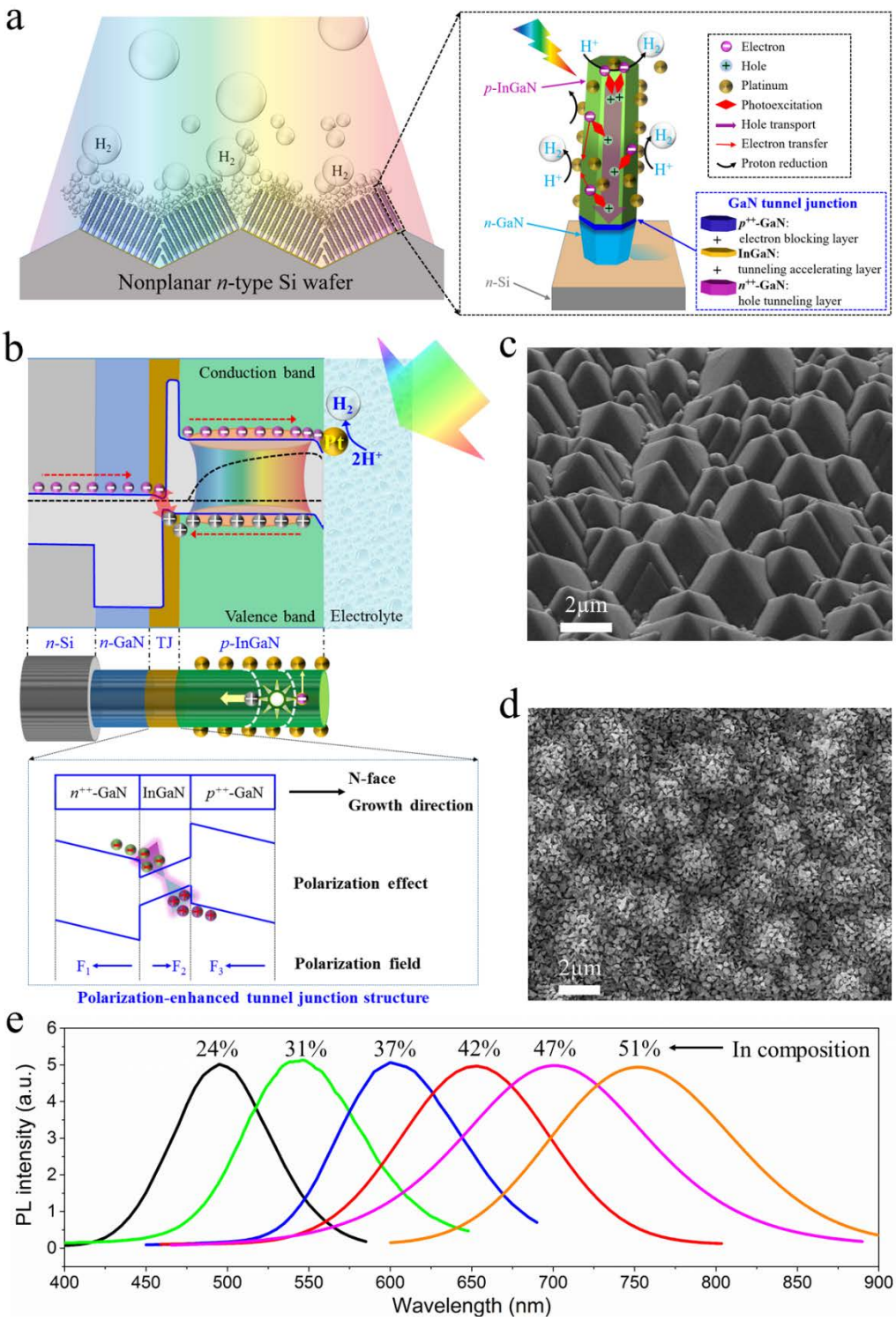

Figure 4.2 Illustration and characterization of p-InGaN tunnel junction nanowire photocathode. (a) Schematic of proton reduction on p-InGaN nanowires on a nonplanar Si wafer. The detailed tunnel junction heterostructure and the processes of photo-excitation, hole collection through the tunnel junction, electron extraction, and proton reduction on Pt co-catalyst nanoparticles are shown in the inset. (b) Schematic energy band diagram of InGaN tunnel junction

nanowires under illumination. The energy band diagram of a polarization-enhanced tunnel junction, n^{++}-GaN/InGaN/p^{++}-GaN, is shown in the inset. (c) SEM image of a non-planar silicon wafer surface. (d) Top-view SEM image of InGaN nanowires grown on non-planar Si wafer. (e) Room-temperature photoluminescence spectra of different InGaN nanowires, showing a large variation of the emission peaks from 500 to 750 nm.

Shown in Figure 4.2b is the schematic energy band diagram along the growth direction of an ideal p-InGaN tunnel junction nanowire under illumination. The photocathode is connected to a platinum (Pt) counter electrode where water oxidation takes place. Under light illumination, photo-excited holes are collected through tunnel junction, whereas photo-excited electrons migrate to the InGaN/liquid interface to drive proton reduction due to the downward surface band bending, shown in Figure 2b. The p^{++}-GaN also serves as an electron blocking layer to reflect photo-excited electrons, which can then readily migrate to InGaN nanowire surfaces, due to the downward surface band bending. Charge carrier extraction, which is often a bottleneck for conventional planar photoelectrodes, is no longer limited by carrier diffusion for the presented photocathode, due to the small size nanowires and large surface area.[128]

InGaN tunnel junction nanowires are grown on non-planar Si wafers using a Veeco Gen II MBE system equipped with a radio frequency plasma-assisted nitrogen source (see Section 4.4.2). The non-planar Si wafer, shown in Figure 4.2c, was created by using hot KOH solution (see Section 4.4.1). The growth was conducted in N-rich conditions to promote the formation of nanowires with N-terminated surfaces. The use of non-planar Si wafer, together with the light trapping effect of nanowire arrays, can significantly enhance light absorption.[35, 151, 152] The top-view scanning electron microscopy (SEM) image of InGaN nanowires grown on non-planar Si is shown in Figure 4.2d. More detailed SEM images are shown in Supplementary Figure 4.6. Photoluminescence (PL) spectra measured at room temperature for InGaN nanowires are shown in Figure 4.2e. By changing the growth conditions, the PL emission wavelengths can be varied from ~500 nm to ~750 nm, corresponding to an energy bandgap values of ~2.48 eV to ~1.65 eV, and indium compositions of ~24% to ~51%, respectively (see Supplementary Figure 4.7).[70-72] Significantly, the band edges of such InGaN nanowires can straddle the water redox potentials, which is essentially required for unassisted solar water splitting.[19] It is also observed that, with increasing indium composition, the PL intensity becomes weaker and

the linewidth becomes broader, indicating the reduced crystallinity and large compositional non-uniformity (see Supplementary Figure 4.8).[153] A detailed correlation between the PEC performance and indium composition is discussed next.

4.2.2 Electron microscope characterization

Energy dispersive X-ray (EDX) mapping on the top plane of $In_{0.42}Ga_{0.58}N$ nanowires shows that the nanowires are composed of Ga, In, and N with the presence of Pt nanoparticles, as demonstrated in Figure 4.3a and Supplementary Figure 4.9a. Displayed in Figure 4.3b is the cross-sectional high angle annular dark-field scanning transmission electron microscopy (HAADF-STEM) image of $In_{0.42}Ga_{0.58}N$ nanowires, which reveals the crystalline InGaN nanowires (width ~200 ± 40 nm, height ~800 nm, spacing ~800 ± 80 nm) extend atop an early growth of GaN nanowires. Using the characteristic X-rays obtained on pure GaN as a reference specimen, the elemental composition of InGaN was quantitatively estimated, showing that 62.7 ± 10.5% of Ga and 37.3 ± 10.5% of In are present in the InGaN nanowire. Figure 4.3c shows the atomic structure within a InGaN nanowire and a lattice spacing of 2.63 Å corresponding to the InGaN (002) wurtzite lattice planes along the preferred <0001> growth direction (*c*-axis).[19] Fast Fourier transform (FFT) patterns of the HAADF-STEM image exhibit InGaN (001) reflection peak which is a forbidden peak in electron diffraction pattern of wurtzite hexagonal symmetry (Supplementary Figure 4.10). The (001) reflection peak demonstrates the existence of periodic atomic ordering along the c-axis caused by a nonrandom atomic site occupancy of indium and gallium within the two unique cation sublattice positions ((0,0,0) and (1/3,2/3,1/2)) in a wurtzite unit cell.[154] This confirms the periodic ordering of In and Ga in the crystalline InGaN nanopillars.

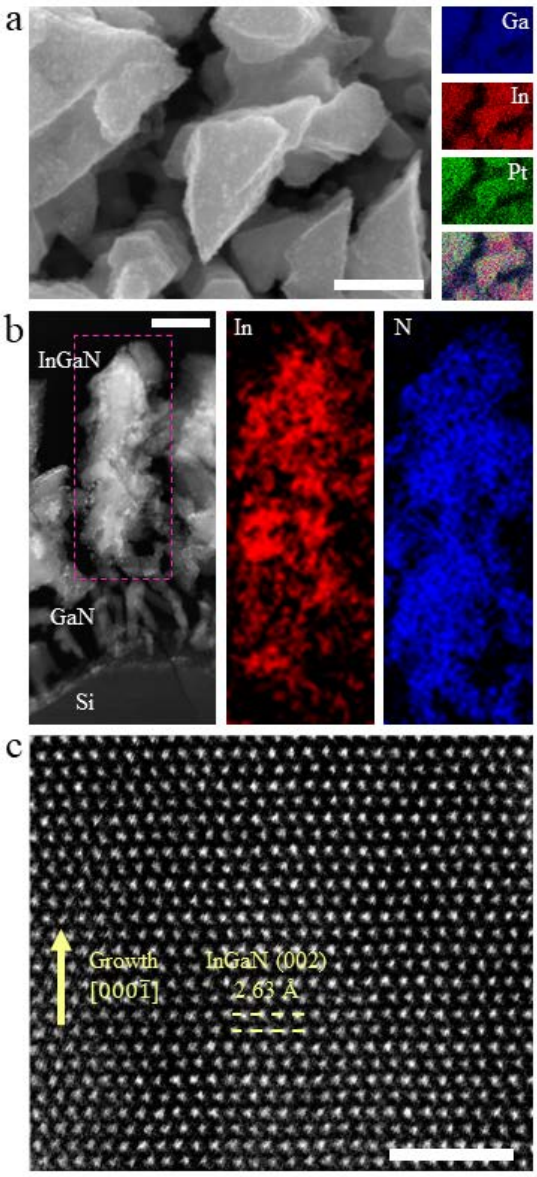

Figure 4.3 Electron microscope characterization of Pt-decorated $In_{0.42}Ga_{0.58}N$ nanowires. (a) Top-view SEM image with EDX elemental mapping, where Ga-L, In-L, and Pt-M characteristic X-ray spectra were measured. Scale bar: 200 nm. (b) HAADF-STEM image of cross-sectional InGaN nanowires with simultaneous EELS mapping images of In and N atoms. Scale bar: 200 nm. (c) Atomic resolution HAADF-STEM image highlighting the crystalline lattice spacing consistent with InGaN crystal. Scale bar: 2 nm.

In the low-dimensional geometry heteroepitaxy, increased In incorporation can occur due to the onset of strain relaxed growth.[70] The low substrate temperature (530-670 ºC) and relatively high N_2 flow rate (1 sccm) used for InGaN growth combined with 1D nanowire geometry allow for effective strain relaxation and reduce phase separation.

Furthermore, Pt co-catalysts with a size of 2-6 nm were uniformly loaded on InGaN nanowire surface to further enhance the performance, as demonstrated in Figure 4.3 and Supplementary Figure 4.9. In some cross-sectional GaN tunnel junction nanowires, an InGaN segment (~5 nm) was confirmed on the top of the GaN nanowire by the occurrence of additional superlattice spots (001) and higher HAADF intensity associated with the heavier atomic weight of Indium (Supplementary Figure 4.11). Our detailed studies further suggest that the thin InGaN segment is not uniformly incorporated in all GaN tunnel junction nanowires, which is likely due to the shadowing effects created by neighboring nanowires when grown on a non-planar Si wafer. This provides opportunities for further improving the device performance and yield. In addition, a thin SiN_x nanolayer is often formed at the Si and GaN interface, as previously reported by Eftychis et al.[155, 156]. Further studies are needed to understand its effect on charge carrier transport during solar water splitting.

4.2.3 Photoelectrochemical measurements

Photoelectrochemical measurements of p-InGaN tunnel junction nanowire photocathodes were performed in 0.5 M H_2SO_4 solution (pH ~0) under the illumination of 100 mW cm^{-2} simulated AM 1.5G solar spectrum (see Section 4.4.4). The photocathodic behavior of p-InGaN/TJ/Si nanowires was first confirmed by performing Mott-Schottky measurement (see Supplementary Figure 4.12).[157-159] Shown in Figure 4.4a is the linear sweep voltammetry measurement of p-$In_{0.42}Ga_{0.58}N$ tunnel junction photocathode. The performance of p-InGaN/Si (without tunnel junction) measured under identical conditions is also shown for comparison. p-InGaN/Si (without tunnel junction) structures exhibit poor onset potential, ~0 V vs. RHE, and low current density, due to inefficient charge carrier separation and extraction. The performance of p-InGaN/Si (without tunnel junction) photocathode is also severely limted by the large interfacial resistance between p-InGaN and the underlying n-type Si substrate. The p-$In_{0.42}Ga_{0.58}N$ tunnel junction nanowire photocathode, on the other hand, exhibits dramatically improved PEC performance. The onset potential is 0.79 V vs. RHE, and a significantly enhanced photocurrent density of 12.3 mA cm^{-2} is measured at 0 V vs. RHE. The dark current density is negligible compared to the photocurrent, confirming the measured

photocurrent comes from solar energy conversion. This is further confirmed under chopped light illumination (see Supplementary Figure 4.13). The substantially improved onset potential and photocurrent density of p-InGaN tunnel junction nanowire photocathode is directly related to the efficient charge separation, hole collection, and electron extraction enabled by the integration with GaN tunnel junction. In this study, we have only demonstrated InGaN tunnel junction nanowire integrated on a nonplanar Si wafer for efficient proton reduction reaction. However, planar Si wafer may also work to synthesize InGaN tunnel junction nanowire photocathode, by appropriate growth optimization.

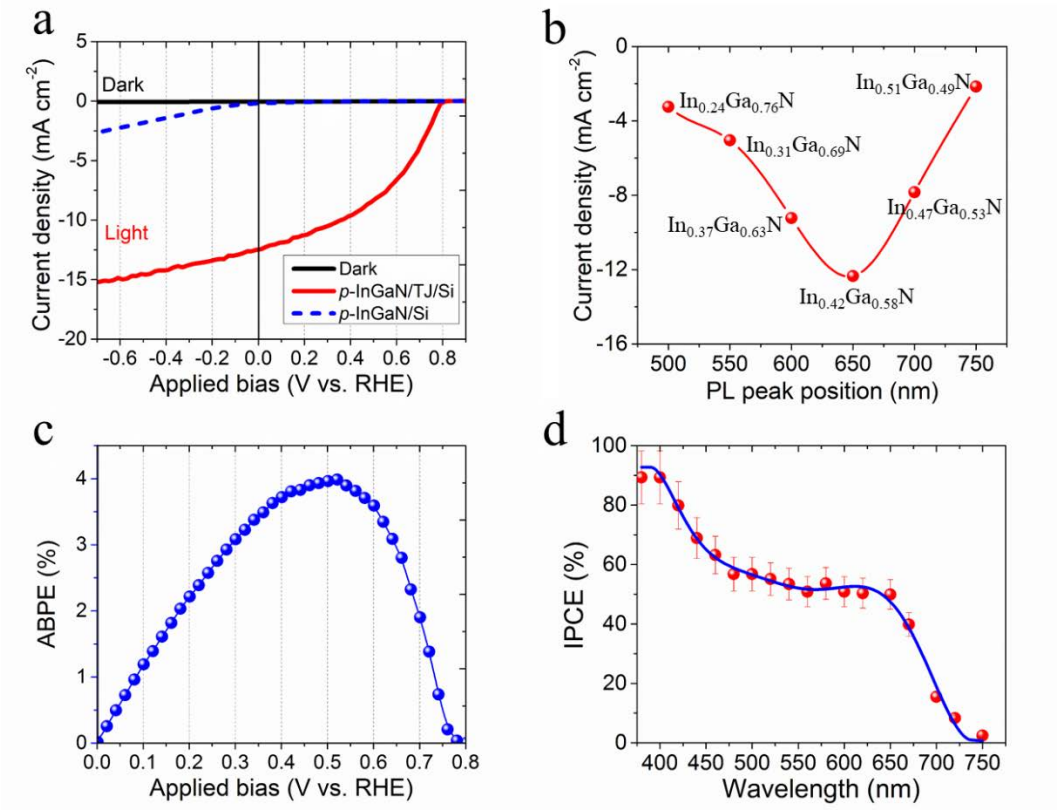

Figure 4.4 Photoelectrochemical performance of p-InGaN tunnel junction nanowire photocathode. (a) Linear sweep voltammetry measurements of p-$In_{0.42}Ga_{0.58}N$ tunnel junction nanowire (p-InGaN/TJ/Si) and p-$In_{0.42}Ga_{0.58}N$ without tunnel junction (p-InGaN/Si) in H_2SO_4 electrolyte (0.5 M, pH ~0) under stimulated AM 1.5G solar illumination of 100 mW cm^{-2}. (b) Variations of the photocurrent density (measured at 0 V vs. RHE) vs. indium composition of p-InGaN tunnel junction nanowire photocathodes. (c) Variations of the applied-bias photon-to-current conversion efficiency (ABPE) for p-$In_{0.42}Ga_{0.58}N$ tunnel junction nanowire photocathode vs. the applied bias voltage (vs. RHE). (d) The incident photon-to-current conversion efficiency (IPCE) of p-$In_{0.42}Ga_{0.58}N$ tunnel junction nanowire photocathode measured at 0 V vs. RHE in 0.5 M H_2SO_4 solution. The solid blue curve is a polynomial fitting.

We have further investigated the photoelectrochemical performance of p-InGaN tunnel junction nanowire photocathodes with indium compositions varying from ~24% to ~51%. The measured current densities at 0 V vs. RHE and onset potentials are plotted vs. the PL peak position of InGaN nanowires, shown in Figure 4.4b. It is seen that the measured photocurrent (absolute value) first shows an increasing trend with indium incorporation from 24% to 42%, due to the reduced bandgap and more efficient light absorption. A significant reduction of photocurrent, however, was observed for indium concentration >42%, which may be attributed to the increased defect formation and enhanced non-radiative recombination of In-rich InGaN. These observations are consistent with the degradation of the optical properties for In-rich InGaN nanowires (see Supplementary Figure 4.8). Moreover, the significant reduction of measured photocurrent for In-rich InGaN nanowires may also be related to the poor nanowire morphology, shown in Supplementary Figure 4.17. The highest photocurrent density ~12.3 mA cm^{-2} was measured for p-InGaN nanowires with In composition ~42% (E_g ~1.9 eV). Its photoelectrochemical performance is described in Figure 4.4a.

The ABPE for the InGaN tunnel junction nanowire photocathode was derived using the following equation:

$$\text{ABPE}\ (\%) = \frac{photocurrent\ density\ (mA{\cdot}cm^{-2}) \times applied\ bias\ (V\ vs.\ RHE)}{100\ mW{\cdot}cm^{-2}} \times 100\% \quad (4\text{-}1)$$

A maximum ABPE of 4% was measured at ~0.52 V vs. RHE, which is the highest value ever-reported for III-nitride semiconductor photocathodes (see Supplementary Table 4.1). Figure 4.4d shows the incident photon-to-current conversion efficiency (IPCE) of p-$In_{0.42}Ga_{0.58}N$ nanowire photocathode measured at 0 V vs. RHE in 0.5 M H_2SO_4 solution. IPCE reaches >90% for light illumination <400 nm, and then gradually decreases to 50-60% at 500-600 nm. Negligible IPCE is measured above 650 nm, which is consistent with the energy bandgap of $In_{0.42}Ga_{0.58}N$. The IPCE in the visible wavelength can be further improved by optimizing the epitaxy and properties of InGaN nanowires. By integrating the IPCE results with the standard AM 1.5G spectrum, a maximum photocurrent density of 14.4 mA cm^{-2} is predicted (see Supplementary Figure 4.14), which agrees reasonably well with the measured saturation current density shown in Figure 4.4a.

4.2.4 Stability test

We have further performed continuous solar water splitting measurements on p-InGaN tunnel junction nanowire photocathode. Shown in Figure 4.5a, the H_2 evolution in 0.5 M H_2SO_4 solution was measured as a function of time at a constant photocurrent density of ~12 mA cm^{-2} under AM 1.5G one-sun illumination. The applied bias stays nearly constant at ~0 V vs. RHE, illustrated in Figure 4.5a. The calculated H_2 evolution based on Faraday's law of electrolysis,

$$\text{Faradaic efficiency}\ (\%) = \frac{2 \times produced\ H_2\ (mol{\cdot}cm^{-2}) \times 96485\ (s{\cdot}A{\cdot}mol^{-1})}{photocurrent\ density\ (A{\cdot}cm^{-2}) \times time\ (s)} \times 100\% \quad (4\text{-}2)$$

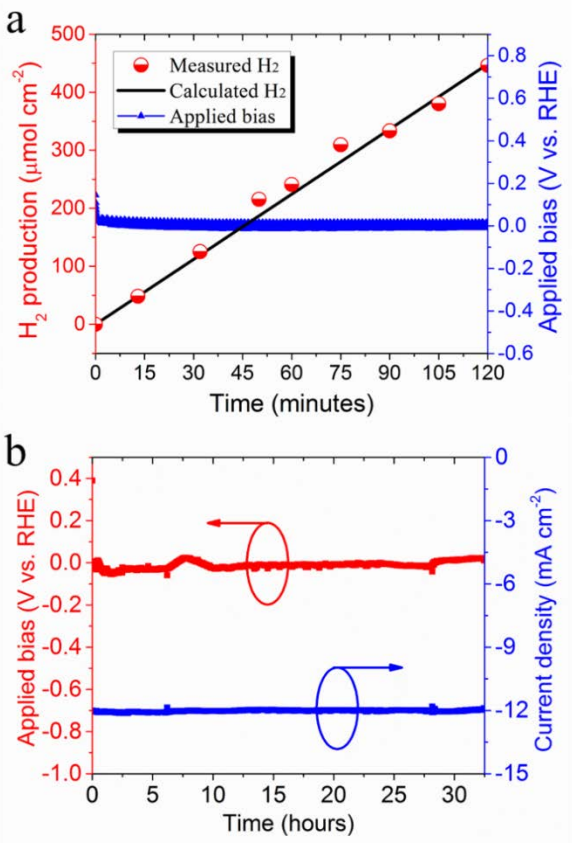

Figure 4.5 Long-term stability analysis of p-$In_{0.42}Ga_{0.58}N$ tunnel junction nanowire photocathode measured in 0.5 M H_2SO_4 under stimulated one-sun AM 1.5G illumination. (a) Hydrogen gas evolution under a constant photocurrent density of 12 mA cm^{-2}. The calculated H_2 production from photocurrent is also shown (solid black curve). (b) Chronopotentiometry measurement for over 30 hours solar water splitting with a steady photocurrent density of 12 mA cm^{-2} at a potential of ~0 V vs. RHE.

It is seen that the measured (446 μmol cm^{-2}) and calculated (448.5 μmol cm^{-2}) hydrogen evolution agrees well, confirming a nearly unity faradaic efficiency. The stability of p-$In_{0.42}Ga_{0.58}N$ tunnel junction nanowire photocathode was further evaluated by chronopotentiometry measurement, [160-162] shown in Figure 4.5b. A steady photocurrent density of 12 mA cm^{-2} is produced continuously at ~0 V vs. RHE without any noticeable degradation for over 30 hours, demonstrating good photoelectrochemical stability of p-InGaN tunnel junction nanowire photocathode. For comparison, conventional Si and III-V photocathodes generally require the use of extra surface protection layer to achieve enhanced stability (see Supplementary Table 4.1).[18, 48, 163]

4.3 Experiment Section

4.3.1 Non-planar Si surface preparation

Two-inch n-type silicon (100) wafer was etched in 80 °C KOH solution (1.8% KOH in weight with 20% isopropanol in volume) for 30 minutes to form the micro-textured surface. After the neutralization by hydrochloric acid, surface cleaning by acetone/methanol, and native oxide removal by 10% hydrofluoric acid, the non-planar n-Si wafer was then loaded into MBE chamber for nanowire growth.

4.3.2 InGaN nanowire growth

p-InGaN tunnel junction nanowires were grown on as-prepared nonplanar Si substrates by plasma-assisted molecular beam epitaxy (MBE) in nitrogen-rich environment. Silicon and magnesium are used as dopants for n-type and p-type nanowire growth, respectively. Firstly, n-GaN nanowires template was grown with a substrate temperature of 750 °C, a gallium (Ga) beam equivalent pressure (BEP) of 8E-8 Torr, a nitrogen flow rate of 1 sccm, and a plasma power of 350 W, as doped by silicon at 1250 °C. Then, the substrate temperature and Ga BEP were reduced to 645 °C and 3.5E-8 Torr, respectively, for the tunnel junction nanostructure, with 7 mins n^{++}-GaN doped by silicon at 1320 °C, 2 mins InGaN with an indium (In) BEP of 4E-8 Torr, and 10 mins p^{++}-GaN doped by magnesium at 210 °C. Subsequently, p-InGaN nanowires were grown

with Ga BEP of 2.5E-8 Torr and In BEP of 8E-8 Torr, with varied substrate temperatures and Mg doping for different indium incorporation.

4.3.3 Pt nanoparticle deposition

Platinum cocatalyst nanoparticles were photodeposited on p-InGaN nanowires in a vacuum chamber with 55 ml deionized water, 11 ml methanol, and 20 µl H_2PtCl_6 precursor solution (0.2 M conc.). InGaN nanowires were then irradiated by 300 W Xenon lamp through a quartz lid for 30 minutes.

4.3.4 PEC measurements

Photoelectrochemical measurements were conducted in a typical three-electrode configuration with a platinum counter electrode and an Ag/AgCl reference electrode in 0.5 M H_2SO_4 electrolyte solution equipped with a Newport solar simulator with AM1.5G filter and one-sun intensity. A BioLogic potentiostat device was used to perform the PEC measurements including linear sweep voltammetry, chronopotentiometry, and Mott-Schottky test. The production of hydrogen gas from solar water splitting on InGaN nanowires was analyzed by injecting 1 ml gas sampling into a Shimazdu gas chromatograph. The sample size is ~0.1 cm^2 for PEC measurements. It is important to note that large size samples should be demonstrated for practical solar water splitting devices in future, by further improving the growth uniformity on nonplanar Si wafers.

4.3.5 Structural and optical characterization

Room-temperature photoluminescence measurements of InGaN nanowires were performed in a homemade setup with a He-Cd 325 nm laser as the excitation source, and the emission is spectrally resolved by a SPEX spectrometer equipped with a photomultiplier detector. SEM images were recorded with a secondary electron detector using a Tescan MIRA3 system (15 kV) and a JEOL IT500 system (20 kV) with an EDX detector. High angle annular dark-field scanning transmission electron microscopy (HAADF-STEM) images were collected using a JEOL 3100R05 microscope with Cs aberration corrected STEM (300 keV, 29 mrad). STEM-EELS mapping and spectra were acquired by a Gatan quantum energy filter, at 0.25 eV per channel to capture the In and N edges simultaneously. Samples for STEM and EELS measurements were prepared in

cross-section by mechanical wedge polishing that provides a large and thin area for analyzing samples in nano- and atomic scale.

4.4 Supporting Information

4.4.1 Supplementary figures

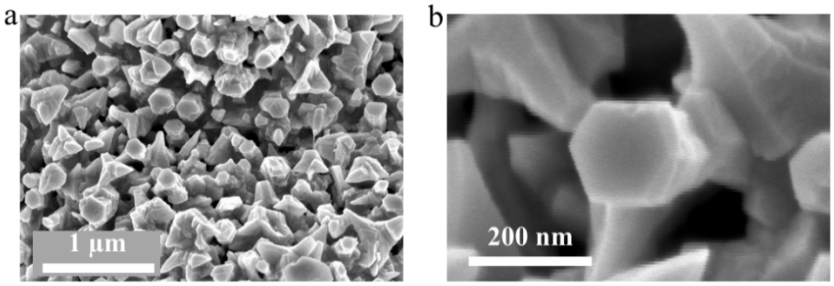

Figure 4.6 Top-view SEM images of p-InGaN nanowires at different magnifications.

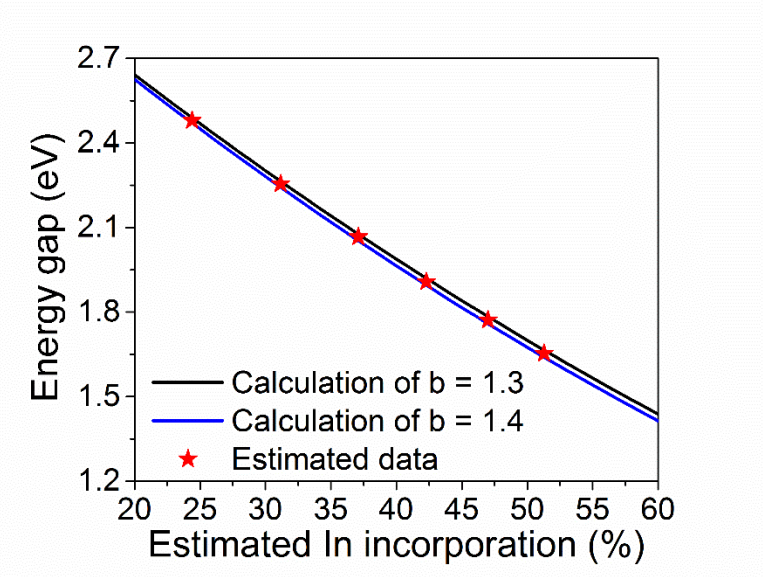

Figure 4.7 Estimated indium composition of various InGaN nanowires based on the Vegard's law with a bowing parameter b = 1.3~1.4.

For $In_xGa_{1-x}N$ alloy, the energy gap can be calculated by using Vegard's law as described by Equation (4-3).

$$E_g(In_xGa_{1-x}N) = x \cdot E_g(InN) + (1-x) \cdot E_g(GaN) - b \cdot x \cdot (1-x) \qquad (4\text{-}3)$$

where b is the bowing parameter and its value typically varies between 1.3 and 1.4.[71, 72] In this study, the energy gap of InGaN nanowires was estimated from photoluminescence measurements as shown in Figure 4.2e. The indium compositions were then derived using Equation (4-3). Shown in Figure 4.7 are the energy bandgap values vs. In concentrations calculated for a bowing parameter of 1.3 or 1.4. Based on these analyses, the indium composition of InGaN nanowires in this study are in the range of ~24% to ~51%.

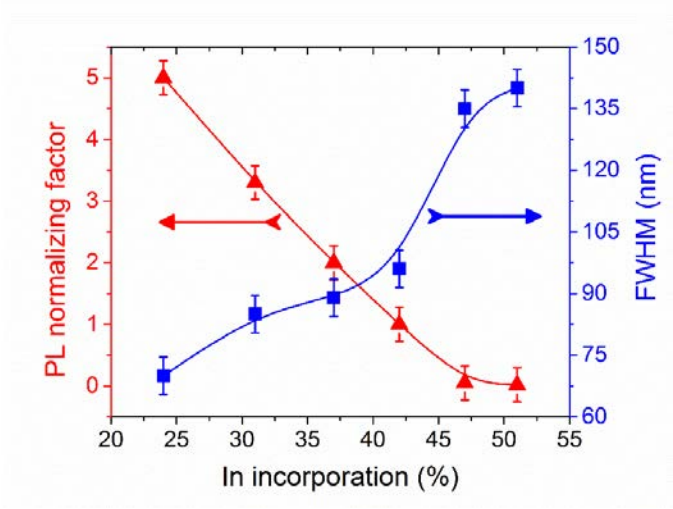

Figure 4.8 Variations of the integrated photoluminescence intensity and full-width-at-half-maximum (FWHM) of InGaN nanowires vs. indium compositions.

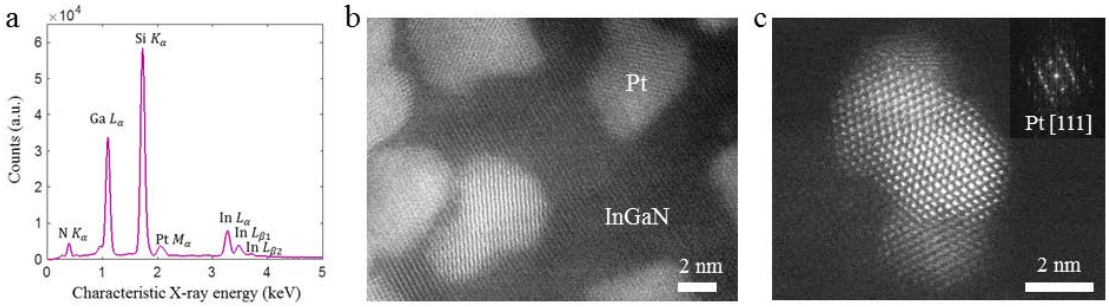

Figure 4.9 Characterization of InGaN nanowires after Pt nanoparticles deposition. (a) EDX spectrum demonstrating the presence of Ga, In, N, and Pt. (b,c) Atomic resolution HAADF-STEM images of Pt nanoparticles on the surface of InGaN nanowires. The inset is the FFT pattern of Pt nanocrystals.

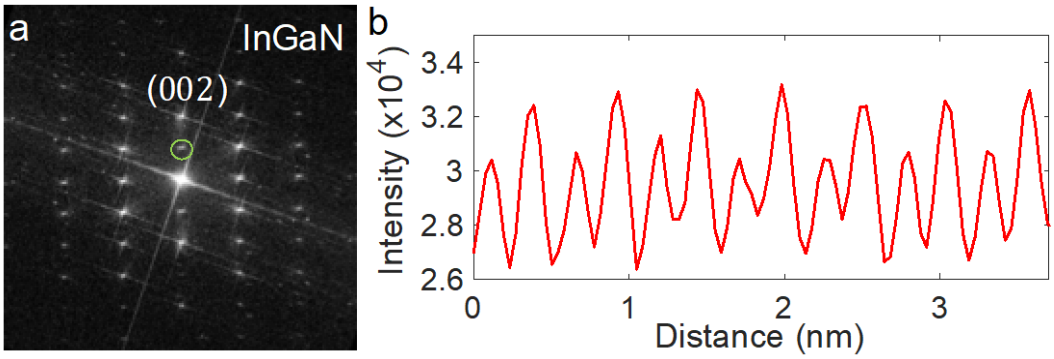

Figure 4.10 Atomic ordering of InGaN crystal. (a) Fast Fourier transform (FFT) of the InGaN nanowire in Figure 4.3c shows the superlattice peak (*circled*) associated with atomic ordering in wurtzite InGaN along *c*-plane direction. (b) Intensity profile along *c*-axis in HAADF-STEM image of InGaN nanowire.

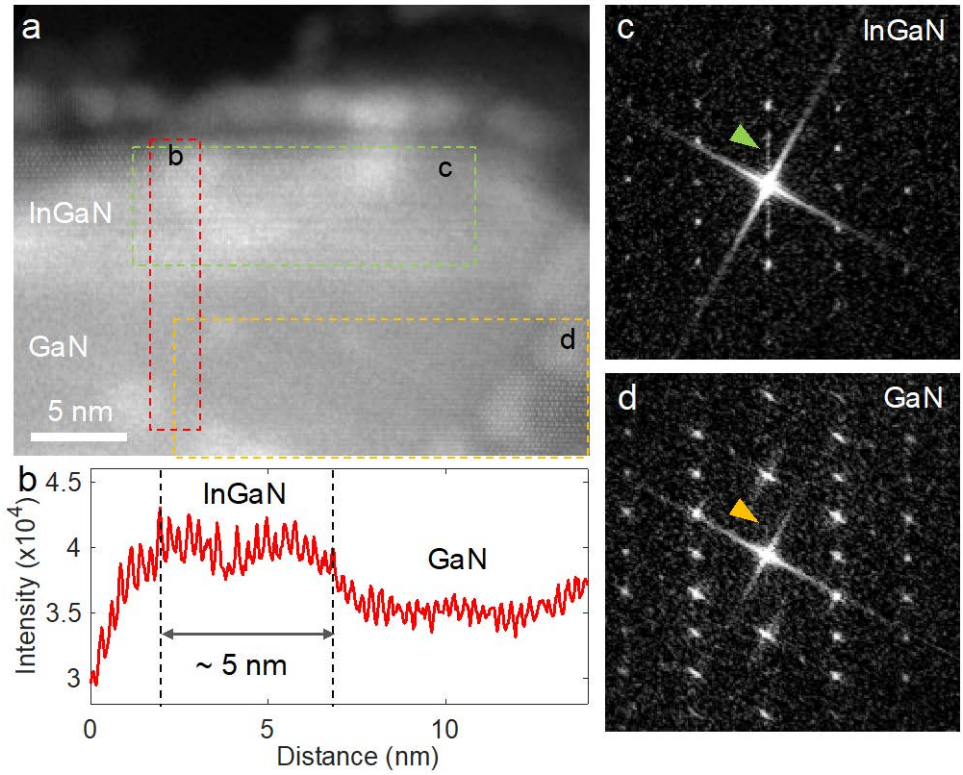

Figure 4.11 Characterization of InGaN tunnel junction on GaN nanowires. (a) HAADF-STEM image of the cross-sectional GaN nanowire. (b) HAADF line profile across the marked (red box) shows the increased intensity consistent with the heavier atomic weight of InGaN. (c,d) FFT of the region c and d within GaN nanowire in (a). A broad (001) reflection peaks caused by chemical ordering of In and Ga indicating InGaN phase grown on the top of the GaN nanowire.

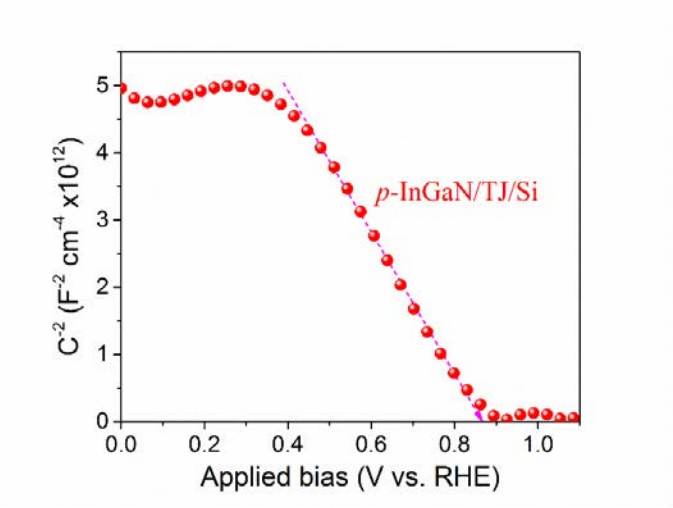

Figure 4.12 Mott-Schottky measurement of p-InGaN nanowire photocathode in 0.5 M H_2SO_4 solution, showing the p-type conduction of InGaN nanowire arrays.

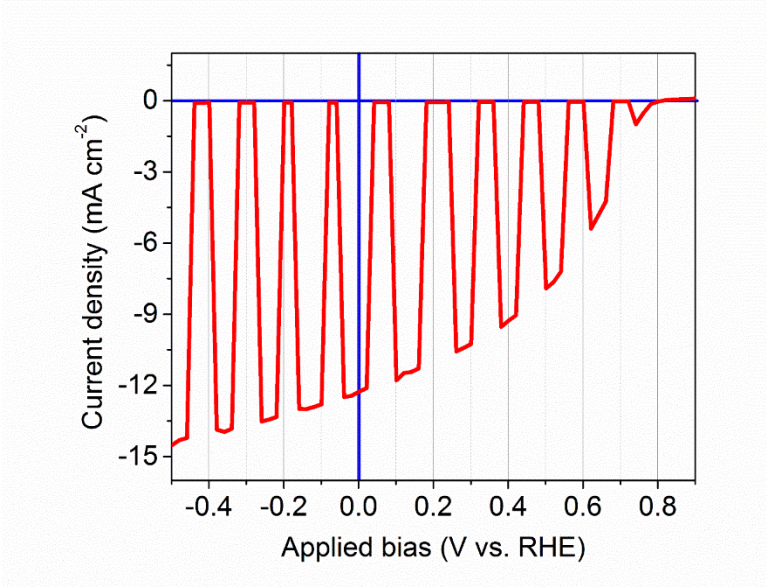

Figure 4.13 Linear sweep voltammetry measurement of p-$In_{0.42}Ga_{0.58}N$ tunnel junction nanowire photocathode under chopped illumination tested in 0.5 M H_2SO_4 solution.

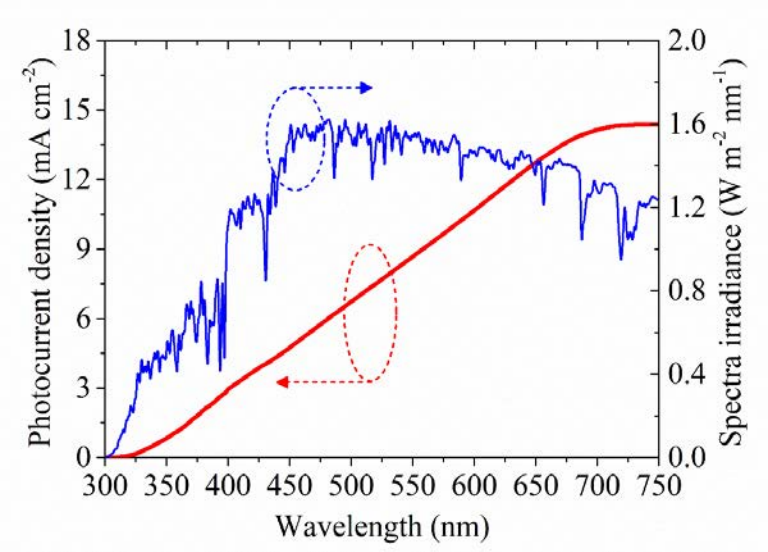

Figure 4.14 Theoretical maximum photocurrent density of $In_{0.42}Ga_{0.58}N$ nanowire photocathode, calculated by multiplying the photon flux with ideal light absorption using IPCE data in Figure 4.4d. The assumption is all the absorbed photons contribute to solar water splitting without any recombination.

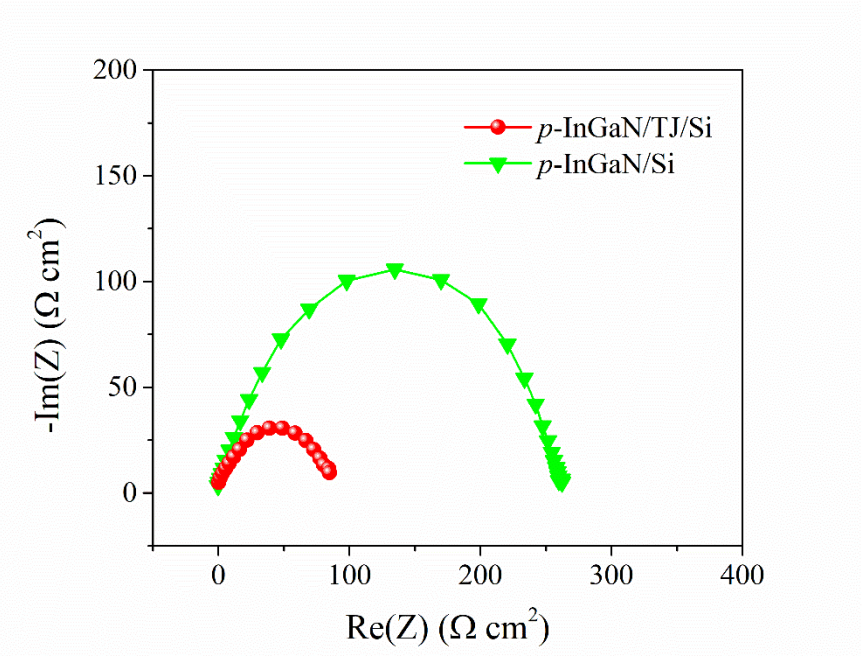

Figure 4.15 Photoelectrochemical impedance spectroscopy measurements of p-InGaN nanowires with and without tunnel junction (TJ) structure, measured in 0.5 M H_2SO_4 solution under illumination at the potential of 0 V vs. RHE.

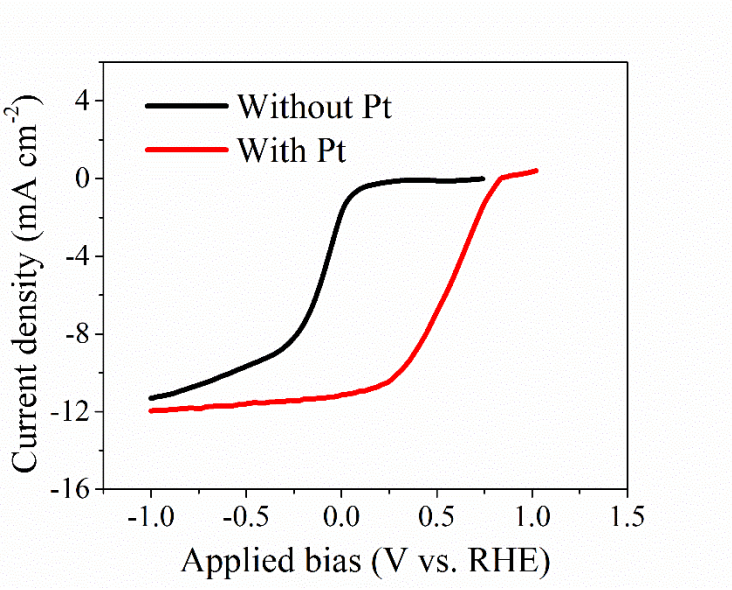

Figure 4.16. Linear sweep voltammetry measurement of p-InGaN tunnel junction nanowire photocathode with/without Pt nanoparticles in H_2SO_4 electrolyte (0.5 M, PH ~0) under stimulated AM 1.5G solar illumination of 100 mW cm^{-2}.

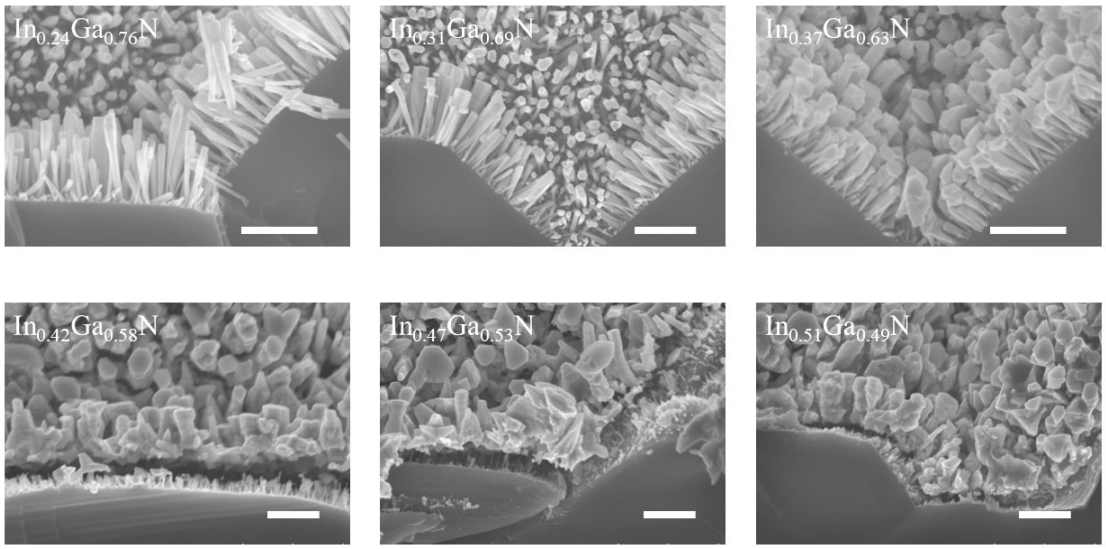

Figure 4.17 SEM images of p-InGaN tunnel junction nanowires, with varied indium incorporations, grown on nonplanar Si wafers. Scale bar: 500 nm.

4.4.2 Supplementary tables

Table 4.1 Summary of photoelectrochemical performance of previously reported III-nitride photocathodes in solar water splitting, and the comparison with p-InGaN tunnel junction (TJ) nanowire photocathode presented in this work. All the measurements are conducted under one-sun light intensity of simulated AM 1.5G solar spectrum.

Photocathode	**Electrolyte**	**Onset potential (V vs. RHE)**	**Current Density[1] (mA cm^{-2})**	**ABPE[2] (%)**	**IPCE[3] (at 400nm)**	**Stability**	**Ref.**
p-InGaN TJ nanowires	0.5 M H_2SO_4	0.78	12.3	4	93	>30 h	This work
InGaN/GaN MQW	N/A	-0.8	2 @ -1V	0	25%	2 h	[164]
p-InGaN NWs	0.5 M H_2SO_4	0.05	5 @ -0.5V	<0.1%	40%	>1 h	[130]
GaN/AlN/GaN	0.5 M H_2SO_4	0.9	1	0.28	--	--	[136]
EDT/p-GaN	1 M H_2SO_4	-0.1	0.1	<0.1%	7%	1.5 h	[165]
p-GaN	3 M H_2SO_4	0	0.05	<0.1%	--	14 h @-1.4V	[138]
InGaN/GaN MQW	0.1 M PBS	0.1	0.02	<0.1%	--	2 h	[137]

[1]: The current density was measured at 0V vs. RHE unless noted in the table.

[2]: ABPE refers to applied-bias photon-to-current efficiency.

[3]: IPCE refers to incident photon-to-current conversion efficiency.

Table 4.2 Stability performance of state-of-the-art high-efficiency single junction semiconductor photocathodes, and comparison with p-InGaN tunnel junction (TJ) nanowire photocathode presented in this work.

Photocathode	Electrolyte	ABPE (%)	Initial stability	Protection layer	Improved stability	Ref.
p-InGaN TJ nanowires	0.5 M H_2SO_4	4	>30 h	N/A	N/A	This work
n^+/p-Cu_2O	0.5M Na_2SO_4 0.1M KH_2PO_4	0.5	0.5 h	TiO_2	2 h	[166]
Sb_2Se_3 nanowires	0.1 M H_2SO_4	0.57		TiO_2	2 h	[82]
CdS/SnS	0.5 M H_2SO_4	0.2		TiO_2	3 h	[167]
CdS/CdTe	1 M KPi	3.7	70 mins			[120]
$GaInP_2$	0.5 M H_2SO_4	0.5	100 s	MoS_x/TiO_x	15 h	[163]

$GaInP_2$	pH = 13 solution		<2 mins	TiO_2-cobaloxime	20 mins	[125]
n^+/p-Si	1 M $HClO_4$	10	10 h	15nm TiO_2	168 h	[124]
Au-$CuInS_2$	0.5 M Na_2SO_4	4.29	1 h			[168]
p-InP	1 M $HClO_4$	2		MoS_x/Ti	2 h	[169]
InP nanowires	1 M HCl	4		TiO_2	10 h	[170]
p-Si	0.5 M H_2SO_4	2.5	1 h	TiO_2	40 h	[171]
p-InP	1 M $HClO_4$	14	unstable	10nm TiO_2	2 h	[123]
p-GaP nanowires	1 M $HClO_4$	1.4	5 h			[172]
p-InP	1 M $HClO_4$	11.6		30nm TiO_2	1 h	[173]
$CoSe_2$/Si	0.5 M Na_2SO_4 0.5 M H_2SO_4	0.5	20 mins			[174]
TiO_2/AZO/Cu_2O	0.5 M KPi	1.6	25 mins	RuO_2	8 h	[175]
p-GaP	1 M $HClO_4$	0.1	3 h	Nb_2O_3 TiO_2	9 h 24 h	[176]
MoS_3/InP	1 M $HClO_4$	6.4	10 mins	MoS_3	1 h	[14]
Amorphous Si	KPi buffer	6		TiO_2	12 h	[177]
p-InP nanopillars	1 M $HClO_4$	14	unstable	5nm TiO_2	4 h	[94]
Cu(In,Ga)Se_2	1 M NaPi	2.6	unstable	ZnO/TiO_2 CdS/TiO_2	30 cycles 30 cycles	[178]

4.5 Summary

The improved performance of p-InGaN tunnel junction nanowire photocathode, compared to previously reported InGaN photocathodes, is attributed to following factors: i) strongly enhanced light absorption for nanowire arrays grown on non-planar Si wafer; ii) crystalline nanowires with efficient p-type dopant incorporation; and iii) nanowire tunnel junctions that facilitate efficient collection of photo-excited holes and serve as an electron blocking layer to enhance the extraction of photo-excited electrons. Our recent studies have further suggested that Ga(In)N nanowire arrays grown by plasma-assisted MBE can exhibit N-terminated surfaces, not only for their top *c*-plane but also for the lateral nonpolar surfaces, which can effectively protect against photocorrosion and

oxidation and therefore ensures long-term stable operation without using any extra surface protection.[24]

In this chapter, we have investigated the fabrication and photoelectrochemical performance of a monolithically integrated p-InGaN tunnel junction nanowire photocathode on nonplanar Si wafer with relatively high indium composition (up to ~51%), which can drive relatively efficient and stable solar to hydrogen conversion. Factors that can further improve the photoelectrode performance, such as reduced defect densities, minimized surface recombination, and more controllable formation of tunnel junction nanowires, have been identified, which, together with the integration of a buried Si p-n junction and improved charge carrier transport, promise highly efficient, stable unassisted solar water splitting and hydrogen production.

CHAPTER V

A Single Junction Cathodic Approach for Stable Unassisted Solar Water Splitting

5.1 Introduction

In the past decades photoelectrochemical water splitting has been intensively studied, which has been considered as one of the most promising approaches to convert solar energy directly to chemical fuels.[21, 31] To date, however, there has been no demonstration of an efficient and stable solar water splitting device.[80, 179-184] Illustrated in Figure 5.1 are the schematic energy band diagrams of semiconductor photoelectrodes representing three commonly used approaches to achieve unassisted photoelectrochemical solar water splitting,[21] including the use of single-junction,[21, 80] double-junction,[114, 185] and multiple-junction semiconductor structures, which have also been referred to as single-photon, two-photon, and multi-photon approaches, respectively.[114, 186] Conventional single-junction semiconductor photoelectrodes often do not meet the stringent band edge positions and thermodynamic overpotentials required for photoelectrochemical water splitting[179] and, consequently, cannot drive unbiased water splitting under visible light.[14, 18, 93, 187] Therefore, double- or multi-junction structures, *i.e.* the so-called Z-scheme, have been proposed and intensively studied to achieve unassisted solar water splitting.[62, 185, 186] A theoretical solar-to-hydrogen conversion efficiency ~27% has been predicted for a double-junction photoelectrode consisting of a 1.70 eV top junction and a 1.05 eV bottom junction under AM 1.5G one-sun illumination.[17] While Si, given its narrow energy bandgap (~1.1 eV), scalable manufacturing and mature fabrication process, is ideally suited for the bottom light absorber, it has remained extremely challenging to identify a practical top light

absorber that is stable in photoelectrochemical reaction and can be monolithically integrated with Si. As such, there have been only few demonstrations of double-junction photoelectrodes, *e.g.* $GaInP_2/GaAs$ and $WO_3/BiVO_4$[180-182, 184] that can drive unbiased solar water splitting. The amount of solar energy converted to hydrogen of such devices is still exceedingly small due to either very low solar-to-hydrogen (STH) efficiency and/or extremely poor stability (see Supplementary Table 5.1 and Figure 5.5).[181]

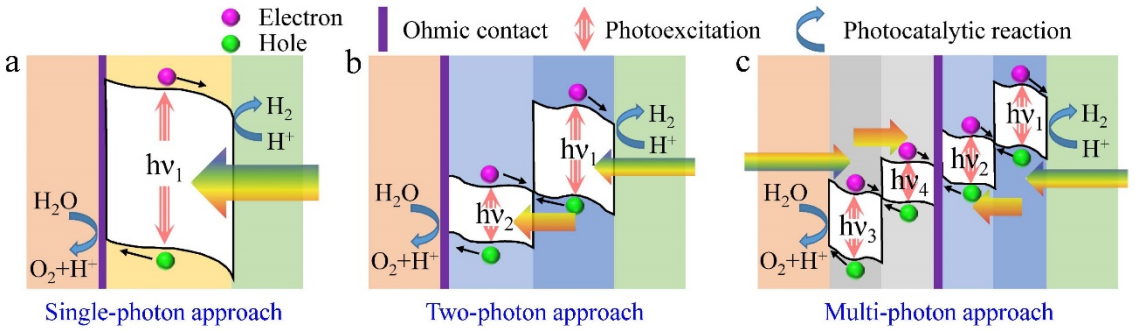

Figure 5.1 Schematic illustration of the energy band diagram of semiconductor photoelectrodes for unassisted solar water splitting on semiconductor photoelectrodes. (a) Single-photon approach driven by a single-junction semiconductor. (b) Two-photon approach using the Z-scheme tandem structures. (c) Multi-photon approach by integrating multiple semiconductor junctions.

It is therefore imperative to develop a semiconductor photoelectrode that can operate efficiently and stably under visible light and can be directly integrated onto Si wafers. Recently, III-nitride semiconductor nanostructures, e.g. InGaN have shown extraordinary potential for direct solar water splitting.[19, 63, 98, 104] By varying the alloy compositions, their energy bandgap can be continuously tuned from ultraviolet, through visible to the near-infrared.[45] Significantly, the energy band edge positions of InGaN can straddle water redox potentials for indium compositions up to 50%, which correspond to an energy bandgap ~1.7 eV.[45] In spite of these promises, however, the realization of a single junction InGaN photoelectrode that can drive photoelectrochemical solar water splitting stably and efficiently without any external bias has remained elusive.[19, 63, 188, 189] The underlying challenges include the corrosion/oxidation of the exposed Ga or In atoms, which, together with the presence of surface states and defects lead to surface recombination and material degradation during harsh

photocatalytic reaction. In addition, conventional InGaN materials grown on Si generally exhibit very large densities of defects and dislocations,[146, 190, 191] which makes it difficult for the efficient collection of photo-generated holes through the underlying Si wafer while simultaneously achieving efficient extraction of photo-generated electrons at the InGaN/electrolyte interface.

To overcome these challenges, we have investigated an InGaN nanowire tunnel junction photocathode epitaxially grown on Si wafer using plasma-assisted molecular beam epitaxy. The use of nanowire tunnel junction enables the direct integration of p-InGaN nanowire arrays on n-type Si wafer with few to no dislocations, due to the surface strain relaxation. Efficient charge carrier separation is facilitated by optimizing the surface band bending of InGaN nanowires through controlled p-type (Mg) dopant incorporation.[51, 57] Photo-generated electrons can readily migrate to the lateral surfaces of nanowires to drive proton reduction due to the downward band bending, whereas photo-generated holes are collected by the underlying Si wafer through the tunnel junction incorporated in each nanowire. With the use of plasma-assisted epitaxy, the surface of such nanostructures can be engineered to be N-rich, which can protect against photocorrosion and oxidation in harsh photocatalytic reaction.[24, 25]

Here, we have demonstrated that an $In_{0.25}Ga_{0.75}N$ nanowire tunnel junction photocathode grown directly on Si wafer can exhibit relatively efficient and stable unassisted solar water splitting. At zero bias vs. Pt counter electrode, InGaN tunnel junction photocathode can exhibit a true STH efficiency of 3.4%, which, to the best of our knowledge, is the highest efficiency value ever achieved in a single-photon system for unbiased photoelectrochemical water splitting. Significantly, stable operation ~300 hours has been demonstrated in two-electrode measurement under AM 1.5G one-sun illumination. Compared to previously reported photoelectrochemical water splitting devices, the InGaN nanowire tunnel junction photocathode can convert nearly two orders of magnitude more solar energy to hydrogen fuels per unit area. With further optimization of the nanowire sizes, compositions, doping, and energy bandgap, and the monolithic integration with a bottom Si, or GaAs light absorber, it may be possible to

achieve the Z-scheme structure with a potential STH efficiency over 20%.[21, 54, 114, 181]

5.2 Results and Discussions

5.2.1 Design and synthesis of $In_{0.25}Ga_{0.75}N$ nanowire tunnel junction photocathode

Schematically illustrated in Figure 5.2a is an InGaN nanowire tunnel junction photocathode, grown on a commercial Si wafer using plasma-assisted molecular beam epitaxy (see Section 5.4.1). In this simplified diagram, each nanowire consists of an n-type (Ge-doped) InGaN segment, n^{++}/p^{++}-InGaN tunnel junction, and p-type (Mg-doped) InGaN segment. The top p-InGaN severs as the light absorber. The use of n^{++}/p^{++}-InGaN tunnel junction can significantly reduce the resistivity between p-InGaN nanowires and the underlying n-Si wafer.[146, 192, 193] Significantly, InGaN tunnel junction also enhances the separation of photo-generated electrons and holes. Platinum nanoparticles were photo-deposited on InGaN nanowire surfaces (see Section 5.4.2), which provide kinetically catalytic sites for efficient water reduction reaction.[59, 194, 195] Shown in Figure 5.2b is the scanning electron microscopy (SEM) image of InGaN tunnel junction nanowires, which have lengths ~886 (±123) nm and diameters ~112 (±36) nm. Such relatively small-diameter nanowire geometry was adopted to reduce charge transfer distance to catalytic sites of photo-generated electrons in p-InGaN segment, which is often a bottleneck for conventional planar photoelectrodes.[51, 128, 196] The charge carrier generation and separation are illustrated in Supplementary Figure 5.6. Shown in Figure 5.2c is the photoluminescence (PL) spectra of such InGaN nanowires measured at room temperature (see Section 5.4.4). The PL emission wavelength is ~506 nm, corresponding to an energy gap of ~2.45 eV and an indium composition of ~25%. The small half-width at half-maximum (HWHM) of ~0.08 eV suggests excellent crystalline quality. Illustrated in Figure 5.2d, the conduction band (CB) and valence band (VB) edges of $In_{0.25}Ga_{0.75}N$ can straddle the water redox potentials with relatively large overpotentials for water splitting, which is usually a limiting factor for other single junction semiconductors to achieve unassisted solar water splitting.[4, 19, 45, 197]

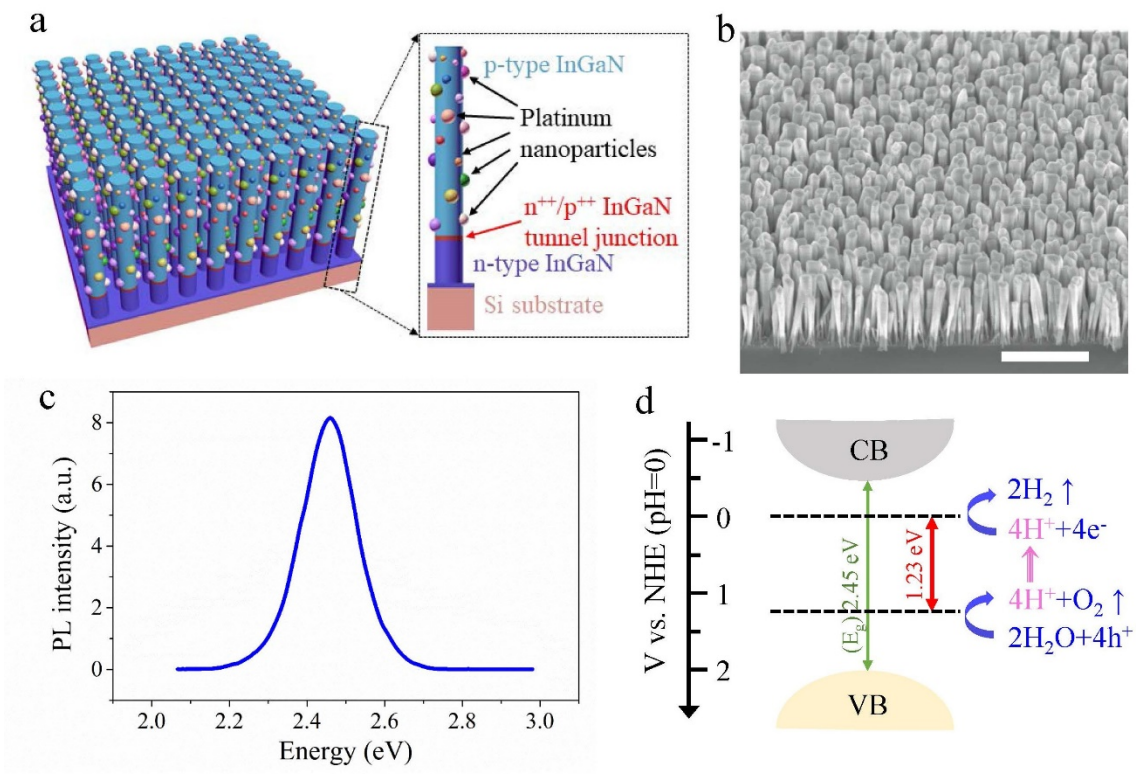

Figure 5.2 Design and properties of $In_{0.25}Ga_{0.75}N$ nanowires for unassisted solar water splitting. (a) Schematic illustration of InGaN nanowire tunnel junction structure grown directly on planar n-type Si wafer. Each nanowire includes an n-InGaN, n^{++}/p^{++}-InGaN tunnel junction, and p-InGaN segment. Pt cocatalyst nanoparticles were also deposited on the nanowire surface. (b) SEM image of InGaN nanowire tunnel junction structures grown on planar Si surface. Scale bar: 1μm. (c) Room-temperature photoluminescence spectra of InGaN nanowires with an energy gap of ~2.45 eV, corresponding to an indium composition of ~25%. (d) Schematic illustration of band edge positions of $In_{0.25}Ga_{0.75}N$ nanowires straddling water redox reaction potentials.

5.2.2 Structural characterization of $In_{0.25}Ga_{0.75}N$ nanowires

High resolution electron microscopy of the InGaN nanowires confirms many of the key features illustrated in Figure 5.2a – vertically continuous InGaN domains within highly crystalline nanowires grown across a Si substrate with Pt nanoparticles dispersed onto the surfaces – however, the actual structure deviates in uniformity, morphology, and chemical homogeneity from an ideal structure. Elemental mapping by energy dispersive X-ray (EDX) performed from the top side of InGaN nanowires (Figure 5.3a,b) confirms a continuous distribution of MBE-grown InGaN nanowires across the Si wafer. The structural details within the nanowire array are revealed in cross-sectional high angle annular dark-field scanning transmission electron microscopy (HAADF-STEM) (Figure

5.3c). The wires have a typical length of ~886 (±123) nm and a diameter that grows from an initial size of ~30 (±7) nm to ~112 (±36) nm at the top of the wire. As a result of the increasing diameter with growth (~7±2.3^{o} half angle), wires often touch or epitaxially join after ~180 nm of growth.

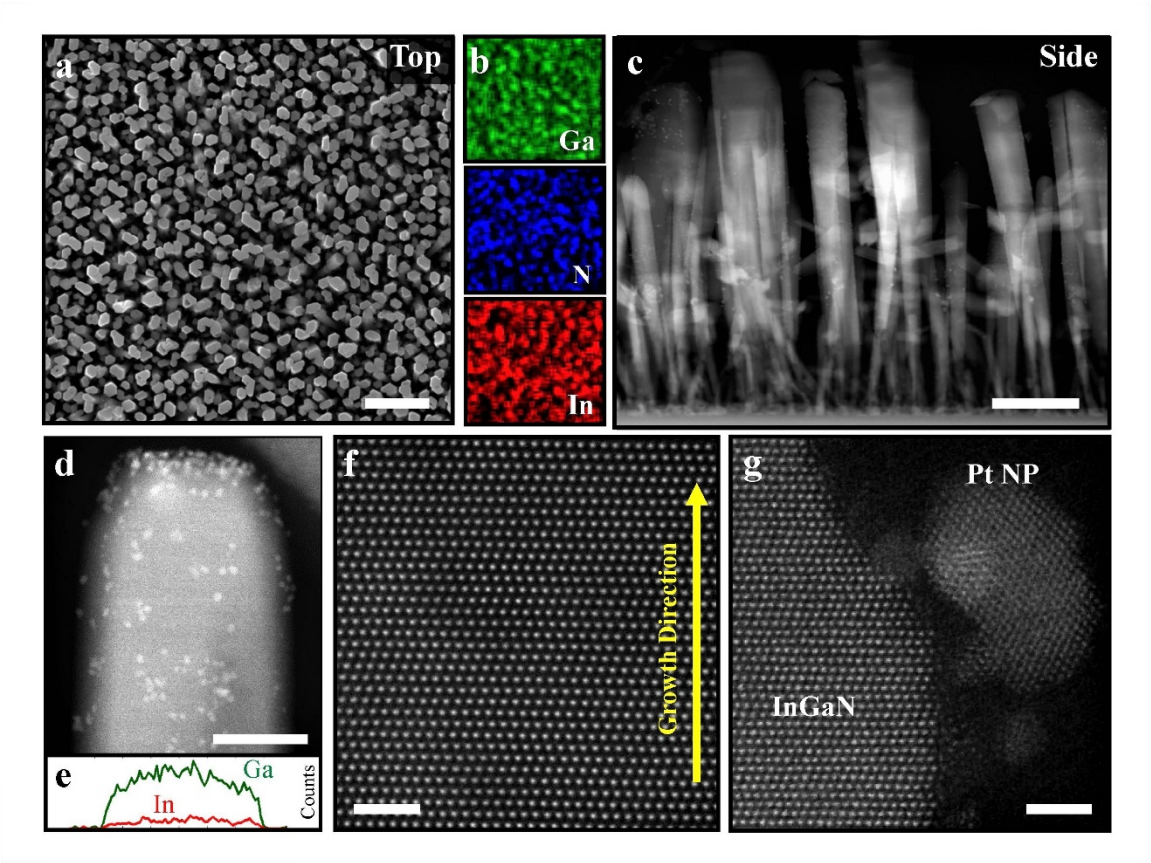

Figure 5.3 Electron microscope characterizations of MBE-grown InGaN nanowires with small size Pt cocatalyst nanoparticles. (a) Top-view secondary electron SEM image with (b) SEM-EDX maps showing Ga, In, and N presence. Scale bar: 200 nm. (c) Side-view, cross sectional HAADF STEM image of the InGaN nanowires. Scale bar: 200 nm. (d) Pt nanoparticles decorated InGaN nanowire surfaces, showing the dispersed deposition of Pt cocatalyst. Scale bar: 50 nm. (e) Ga and In concentration measured by EDX across the top section of a nanowire (acquired from similar nanowire shown in Supplementary Figure 5.10b). (f) Atomic resolution HAADF-STEM images reveal highly crystalline InGaN nanostructure preserved across the wire. Scale bar: 2 nm. (g) Highly crystalline Pt nanoparticles deposited on InGaN nanowire surface. Scale bar: 2nm.

Atomic resolution images reveal highly crystalline order that extends throughout the entirety of each nanowire and to a highly faceted surface (Figure 5.3f,g). Figure 5.3f demonstrates the atomic crystal structure of InGaN nanowires, corresponding to InGaN (0002) wurtzite lattice plane, which also confirms the <0001> growth direction of InGaN

nanowires (Supplementary Figure 5.7 and 5.8).[19] The periodic ordering of atoms further demonstrates its high-quality single-crystal structure of InGaN nanowires without significant dislocations. The flat top plane suggests an N-polar surface of InGaN nanowires expected from growth in N-rich MBE environment, which is more stable in chemical solution for solar water splitting.[24, 198, 199] Elemental mapping of vertically aligned InGaN nanowires shows growth begins with atomically registered InGaN and GaN domains that compete before the InGaN overtakes. The top of each nanowire is uniform, crystalline InGaN as confirmed by EDX (Figure 5.3e). Despite the diminishing presence of In towards the substrate, a vertically continuous InGaN domain is commonly present throughout nanowires (Supplementary Figure 5.8 and 5.9). Due to the size variations, the incorporation of indium is observed to be minimal at the nanowire bottom. Further optimization of the nanowire size and indium incorporation may lead to enhanced performance.

Pt nanoparticles as the cocatalyst for water reduction reaction have also been deposited on InGaN nanowire surface, shown in Figure 5.3d, in disperse distribution with a small size. In addition, small size Pt nanoparticles were deposited on InGaN nanowire surfaces, as shown in Figure 5.3d,g, to further accelerate water reduction reaction, wherein small-size photocatalyst performs better than bulk materials.[200-202] Moreover, its lattice spacing is determined to be ~2.3 Å along the $[1\bar{1}1]$ direction, shown in Figure 5.3g, and contains facets/edges expected to behave as an efficient catalyst for proton reduction reaction (Supplementary Figure 5.8 and 5.9).[201, 202] In summary, such highly crystalline InGaN nanowires with small size Pt nano-catalysts indicate its ability to perform efficient solar water splitting application on $In_{0.25}Ga_{0.75}N$ nanowire photocathode.

5.2.3 Photoelectrochemical performance of $In_{0.25}Ga_{0.75}N$ nanowire photocathode

Photoelectrochemical measurement of $In_{0.25}Ga_{0.75}N$ nanowire tunnel junction photocathode was performed in a dual-electrode configuration with a Pt counter electrode in 0.5 M H_2SO_4 acidic electrolyte solution under simulated AM 1.5G one-sun illumination (see Section 5.4.3). It is of importance to note that Pt electrode is not be the best for water oxidation reaction, which provides the opportunity to further improve the

overall STH efficiency by adopting better-optimized counter electrodes. Shown in Figure 5.4a is the linear sweep voltammetry (LSV) measurement of our best-performed p-$In_{0.25}Ga_{0.75}N$ nanowire photocathode. In addition, the measured dark current is negligible compared to the light current, suggesting that the measured photocurrent originates from solar energy conversion. This can be further confirmed under chopped light illumination, shown in Figure 5.4b, wherein dark/light cyclic photocurrent was continuously measured at zero bias vs. counter electrode. A short-circuit photocurrent of ~2.8 mA cm^{-2} is measured for $In_{0.25}Ga_{0.75}N$ nanowire photocathode at zero bias. Open circuit potential (OCP) measurement, shown in Figure 5.4c, further suggests the downward surface band bending of p-type InGaN nanowires in electrolyte solution, which is well suited for electron extraction to drive proton reduction reaction.[203-206] A large photoelectrochemical voltage of ~1 V was measured, which is in agreement with the onset potential shown in Figure 5.4a.

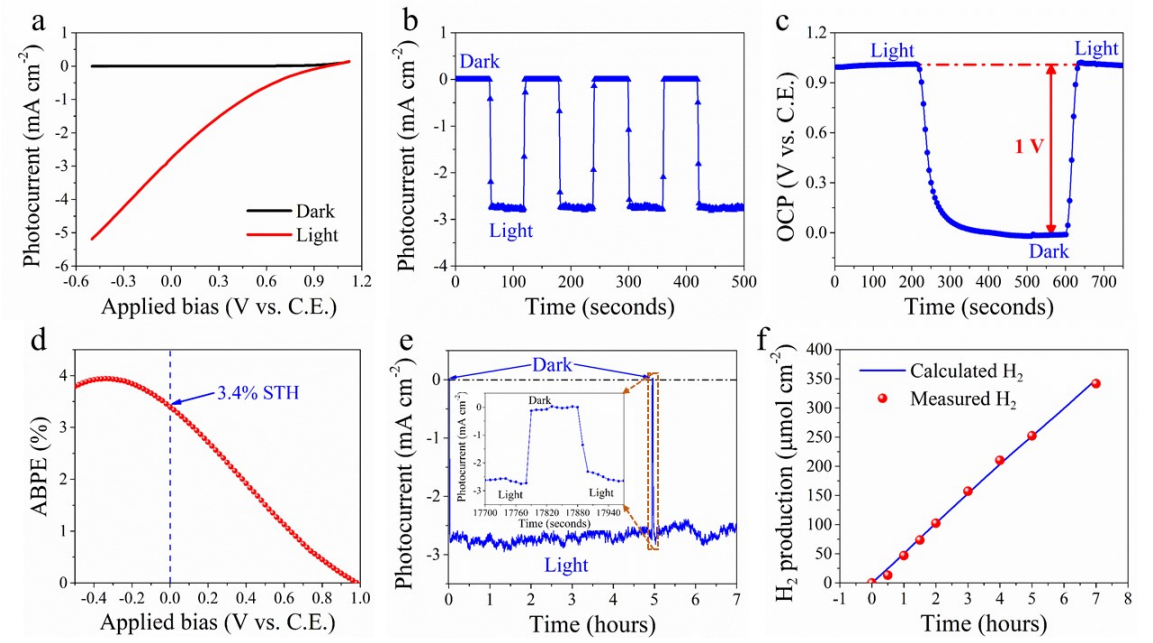

Figure 5.4 Unassisted solar water splitting performance of $In_{0.25}Ga_{0.75}N$ nanowire photocathode in two-electrode configuration vs. Pt counter electrode (C.E.) under AM 1.5G one-sun illumination. (a) Linear sweep voltammetry measurement under light and dark conditions. (b) Variation of the photocurrent under cyclic light/dark conditions measured at zero bias vs. Pt counter electrode. (c) Open circuit potential measurement of InGaN nanowire tunnel junction photocathode under chopped light illumination. (d) Solar-to-hydrogen (STH) efficiency at zero bias vs. Pt counter electrode. (e) Continuous solar water splitting experiment on $In_{0.25}Ga_{0.75}N$ nanowire tunnel junction photocathode. The spikes correspond to brief dark current measurements, confirming that the observed current

originates from light absorption of InGaN nanowires for solar hydrogen conversion. (f) H_2 gas production (red dots) collected from (e) compared to the theoretical maximum value (blue curve) calculated from the electrons flowing through the circuit with a unity Faraday efficiency.

Compared to previous work on III-nitride photoelectrodes,[19, 188, 189, 207, 208] the substantially improved onset potential and photocurrent density of InGaN tunnel junction nanowire photocathode is directly related to the efficient charge carrier separation, electron extraction, and hole collection enabled by the integration with InGaN tunnel junction. To achieve the best cathodic performance for unassisted solar water splitting, the growth conditions of $In_{0.25}Ga_{0.75}N$ nanowires were carefully optimized (see Section 5.4.1). It was identified that Mg doping incorporation played a critical role on the performance of InGaN nanowire tunnel junction photocathode (see Supplementary Figure 5.10). The best photoelectrode performance is achieved for InGaN nanowires using an Mg cell temperature of 210 ^{o}C. Our recent studies have shown that the downward surface band bending of InGaN nanowires can be precisely engineered through controlled Mg dopant incorporation, which can enable efficient separation of photo-generated charge carriers.[51, 57] It was also observed that surface treatment by HCl acid solution on InGaN nanowires can further enhance the performance significantly (see Supplementary Figure 5.11).

Applied bias photon-to-current conversion efficiency (ABPE) for p-$In_{0.25}Ga_{0.75}N$ nanowire photocathode is shown in Figure 5.4d (see Section 5.5.2.1). At zero-bias, the STH efficiency is determined to be ~3.4%. A peak energy conversion efficiency ~4% is observed at -0.3 V vs. Pt counter electrode, wherein solar energy and applied electric power are combined optimally. Compared to the conventional three-electrode configuration with a reference electrode, the presented two-electrode measurements demonstrate true solar water splitting performance.[93, 186, 187, 189, 209, 210] We have further performed continuous, unassisted solar water splitting measurements on such InGaN photocathode, shown in Figure 5.4e,f, where solar water splitting photocurrent and H_2 gas production were measured at zero bias. The spikes in Figure 5.4e correspond to a brief dark current measurement, which was conducted intentionally to confirm the observed current originates from light absorption of InGaN nanowires for solar water splitting. Figure 5.4f shows the course of H_2 gas production (red dot) vs. time, which is

further compared with the theoretical value (blue solid line) calculated from the number of photo-generated electrons flowing through the circuit (see Section 5.5.2.2). It is seen that the measured and calculated H_2 gas production, *i.e.* half of the photo-generated electron density agree well, confirming a nearly unity faradaic efficiency wherein all extracted photoexcited electrons drive solar water reduction reaction efficiently.[63, 64]

5.2.4 Long-term stability for unassisted solar water splitting

Long-term stability evaluation of such $In_{0.25}Ga_{0.75}N$ nanowire tunnel junction photocathode for unassisted solar water splitting was further performed at 0 V vs. Pt counter electrode in 0.5 M H_2SO_4 electrolyte solution under simulated one-sun illumination. Shown in Figure 5.5a is the measured photocurrent retention ratio over time. No significant performance degradation was observed for ~300 hours, demonstrating excellent photoelectrochemical stability of InGaN nanowire tunnel junction photocathode. For comparison, conventional Si and III-V photocathodes generally require the use of extra surface protection to achieve enhanced stability.[18, 93, 211] Structural properties of $In_{0.25}Ga_{0.75}N$ nanowires were characterized during the long-term stability measurements. There was no obvious degradation of InGaN nanowires after 90 hours of continuous solar water splitting (see Supplementary Figure 5.12). After 250 hours of solar water splitting, it was observed that some InGaN nanowires were removed, accompanied by some changes in the surface morphology (see Supplementary Figure 5.13). Detailed studies further reveal that a portion of Pt nanoparticles may be lost (see Supplementary Figure 5.14 and 5.15). The loss of some Pt cocatalysts reduces the efficiency of charge carrier separation and proton reduction, which ultimately leads to degraded performance for the InGaN photocathode during solar water splitting. In addition, the underlying Si wafer may not be perfectly covered by Ga(In)N, which may also be a significant issue for long-term stability during solar water splitting experiment.

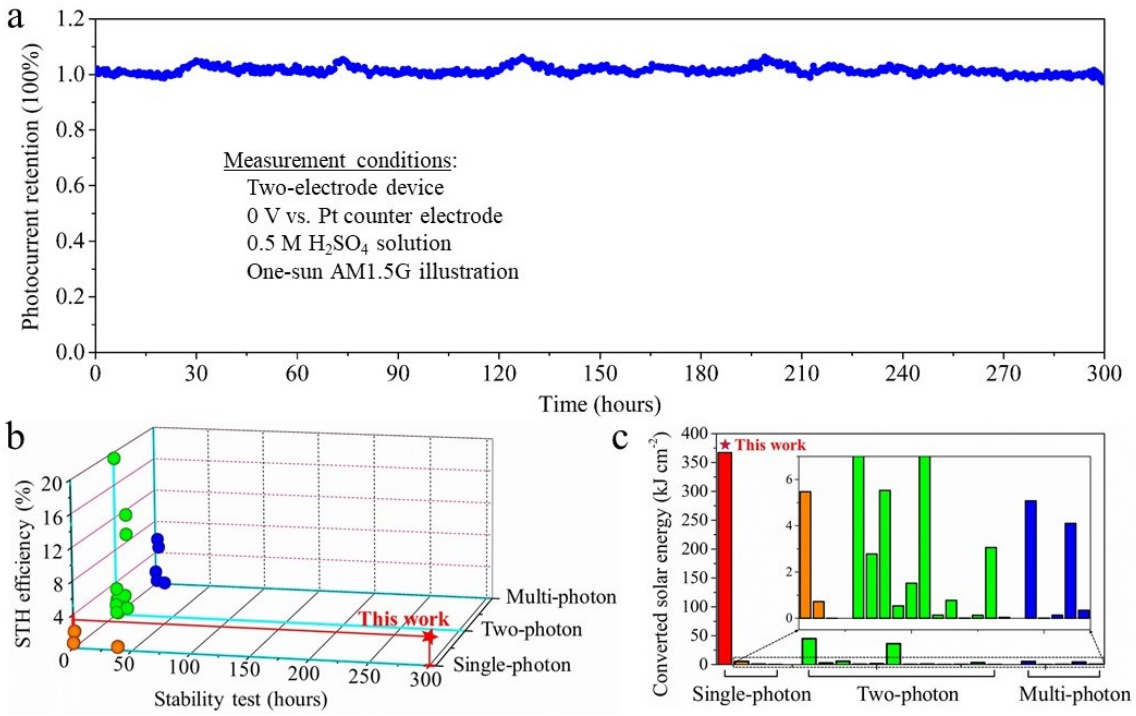

Figure 5.5 Long-term stability evaluation of p-$In_{0.25}Ga_{0.75}N$ nanowire tunnel junction photocathode for unassisted solar water splitting. (a) Photocurrent retention measured for ~300 hours of unbiased solar water splitting vs. Pt counter electrode. (b) Solar-to-hydrogen (STH) efficiency and stability of InGaN photocathode demonstrated in this work, compared to some previously reported semiconductor photoelectrodes achieving unbiased solar water splitting, as listed in Supplementary Table 5.1. (c) Comparison of converted solar energy to H_2 fuel during unbiased solar water splitting for semiconductor photoelectrodes as listed in (b) and Supplementary Table 5.1 with this work.

5.2.5 Stability discussions

Previously InGaN materials have been studied for photocatalytic water splitting and HBr splitting. [51, 57, 63, 98, 188, 208] In this work we have demonstrated, for the first time, the use of InGaN photocathode to achieve unassisted photoelectrochemical solar water splitting in a two-electrode configuration under AM 1.5G one-sun illumination. Photoelectrochemical performance of $In_{0.25}Ga_{0.75}N$ nanowire tunnel junction photocathode is further compared with that of previously reported semiconductor photoelectrodes (see Supplementary Table 5.1). Illustrated in Figure 5.5b are the STH efficiency and stability of some previously reported photoelectrochemical water splitting devices, including single-photon, two-photon, and multi-photon approaches. It is seen that high efficiency photoelectrodes are generally unstable, with stability limited to ~1 hour or less in two-electrode measurement, *i.e.* true water splitting experiments.

Relatively long-term stable operation has been reported for photoelectrodes with the use of extra surface protection,[18, 48] but these studies were generally performed in three-electrode configuration, *i.e.* not true water splitting. The measured stability ~300 hours for InGaN nanowire tunnel junction photocathode stands out to be the best reported stability for unassisted photoelectrochemical solar water splitting (Supplementary Table 5.1). The amount of solar energy converted to H_2 fuel is further summarized in Figure 5.5c. The amount of converted solar energy for previously reported photoelectrodes is extremely limited, due to the poor stability. For comparison, our InGaN nanowire tunnel junction photocathode can convert nearly one order of magnitude more solar energy to H_2 fuel per unit area.

The realization of a single junction InGaN photocathode with relatively high efficiency and long-term stability is attributed to the following factors: i) High crystallinity and significantly reduced dislocations for nanowire structures grown directly on Si; ii) Rapid separation of photo-generated charge carriers by optimizing the nanowire surface band bending through controlled Mg dopant incorporation; iii) Efficient collection of photo-generated holes with the use of tunnel junction; iv) Light trapping effect of the nanowire morphology for enhanced light absorption; And v) N-terminated surfaces that can protect against photo-corrosion[24, 212]. In addition, during epitaxy of InGaN nanowires, a thin (~20 nm) InGaN layer is also formed on Si wafer, which can protect the InGaN/Si interface from photo-corrosion (see Supplementary Figure 5.16). Further improved performance is expected by replacing the Pt counter electrode with IrO_x or RuO_x electrodes to have more efficient water oxidation [19, 31, 213-217] and by optimizing the energy bandgap of InGaN to enhance the photocurrent density. The device stability can also be improved by optimizing the deposition of co-catalysts.

5.3 Methods

5.3.1 Molecular beam epitaxial growth of InGaN tunnel junction nanowire

p-InGaN nanowire tunnel junction structures were grown on n-type Si wafer by plasma-assisted molecular beam epitaxy (MBE) in nitrogen-rich environment. The

optimized growth parameters include a substrate temperature at 675 °C, gallium (Ga) beam equivalent pressure (BEP) of 5E-8 Torr, indium (In) BEP of 6E-8 Torr, nitrogen flow rate of 1 sccm, and plasma power of 350 W. Firstly, n-type InGaN nanowire template was grown for one hour using a germanium (Ge) source as the n-type dopant with a Ge cell temperature of 1050 °C. Then n^{++}/p^{++}-InGaN tunnel junction nanostructure was integrated atop by growing 10 minutes n^{++}-InGaN doped by Ge at 1080 °C and 15 minutes p^{++}-InGaN using magnesium (Mg) with a Mg cell temperature of 290 °C. Subsequently, a p-type (Mg-doped) InGaN segment was grown to serve as the light absorber with a reduced p-type doping level using an Mg cell temperature at 210 °C for 4 hours. Both Ge and Mg doping levels are carefully optimized in the tunnel junction structure as well as in the rest of the InGaN segments to achieve the best photoelectrochemical performance. Based on secondary ion mass spectrometry (SIMS) analysis on GaN epi-layers, Ge doped at 1075 °C and Mg doped at 280 °C can give Ge and Mg estimated dopant concentration of ~5E+18 cm^{-3} and ~6E+18 cm^{-3}, respectively.

5.3.2 Platinum (Pt) co-catalyst deposition

Pt co-catalyst nanoparticles were deposited on InGaN nanowire surface by using an ultraviolet-assisted photodeposition method. In a vacuum-sealed chamber, the InGaN nanowire sample was immersed into a precursor solution including 55 mL deionized water, 11 mL methanol, and 10 µL 0.2 M H_2PtCl_6 solution. After pumping the chamber down for 10 minutes, InGaN nanowires were irradiated under 300 W Xenon lamp through a quartz lid for 30 minutes. The sample was then rinsed in deionized water and dried using N_2 gas for photoelectrochemical measurements.

5.3.3 Photoelectrochemical measurements

Photoelectrochemical measurements were conducted in a two-electrode configuration using a platinum counter electrode in 0.5 M H_2SO_4 electrolyte solution equipped with a Newport solar simulator with AM 1.5G filter and one-sun intensity. A Gamry potentiostat device was used to perform the photoelectrochemical measurements including linear sweep voltammetry, chronoamperometry, and open circuit potential tests. The production of H_2 gas from solar water splitting on InGaN nanowires was analyzed by injecting 1 mL gas sampling into a Shimazdu gas chromatograph. InGaN nanowire samples were treated

in concentrated HCl acidic solution for 5 minutes before any photoelectrochemical measurement. The tested InGaN photocathodes have areal sizes in the range of 0.05~0.1 cm^2.

5.3.4 Structural and optical characterization

Photoluminescence spectroscopy of InGaN nanowires was performed using a He-Cd 325 nm excitation laser. SEM images were taken with a secondary electron (SE) detector using a Hitachi SU8000 system (5 kV), Tescan MIRA3 system (15 kV), and a JEOL IT500 SEM (10 kV) with an EDX detector. High angle annular dark-field scanning transmission electron microscopy (HAADF-STEM) images were collected using a JEOL 3100R05 microscope with Cs aberration corrected STEM (300 keV, 22mrad) with a camera length of 15 cm. The quantitative STEM-EDS analysis was performed using a JEOL 2100 probe-corrected STEM equipped with a horizontal ultra-thin window Si-Li X-ray detector (EDAX, active area ~30 mm^2). Samples for STEM characterization were prepared using bladed exfoliation or in cross-section view by mechanical wedge polishing.

5.4 Supporting Information

5.4.1 Supplementary figures

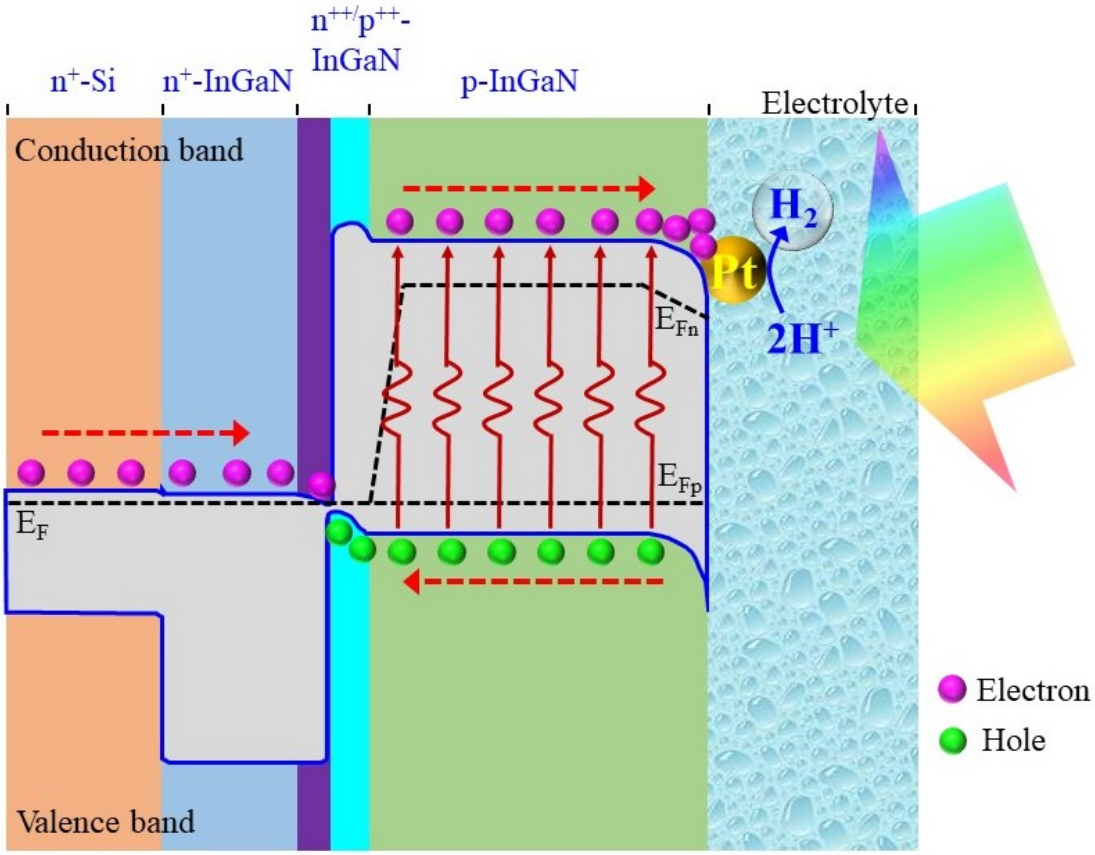

Figure 5.6 Schematic energy band diagram of InGaN nanowire tunnel junction photocathode under illumination. Photo-generated electrons in p-InGaN nanowires migrate toward the lateral surfaces, due to the downward surface band bending, and are collected by Pt co-catalyst particles to drive proton reduction reaction and H_2 evolution. Photo-generated holes are collected through the tunnel junction by n-type Si wafer and then transport to the counter electrode to drive water oxidation reaction for O_2 evolution.

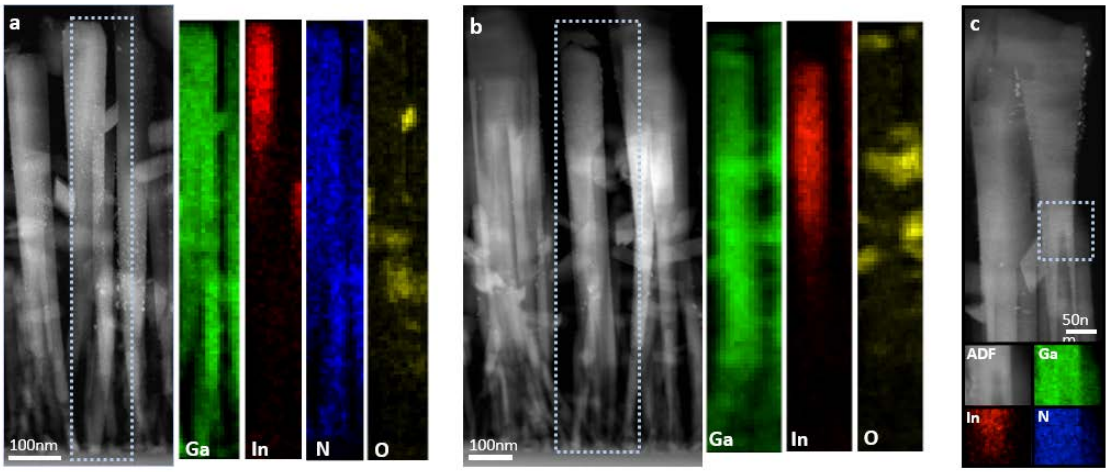

Figure 5.7 Chemical analysis of the InGaN nanowires. (a-c) STEM image and EDX elemental maps. In map reveals InGaN regions constitute the top portion of each rod. Oxide material (Ga_2O_3) occupies regions between the wires. However, it is unclear about the origination of such oxide materials, which needs further investigations. N and Ga are present throughout the wire.

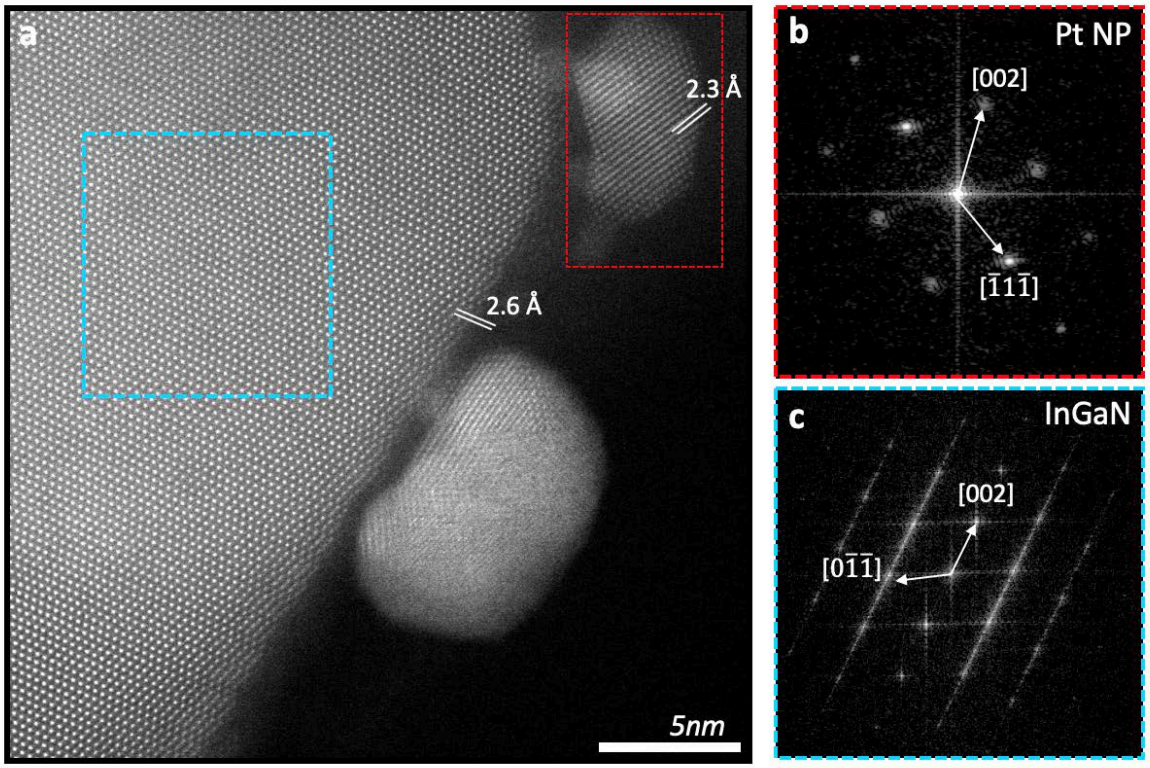

Figure 5.8 Periodic Analysis of the InGaN nanowires. (a) ADF image of an InGaN nanowire coated with Pt nanoparticles. (b-c) Fast Fourier Transform (FFT) of the Pt Nanoparticle and InGaN tip along the (110), (0002) axis, respectively.

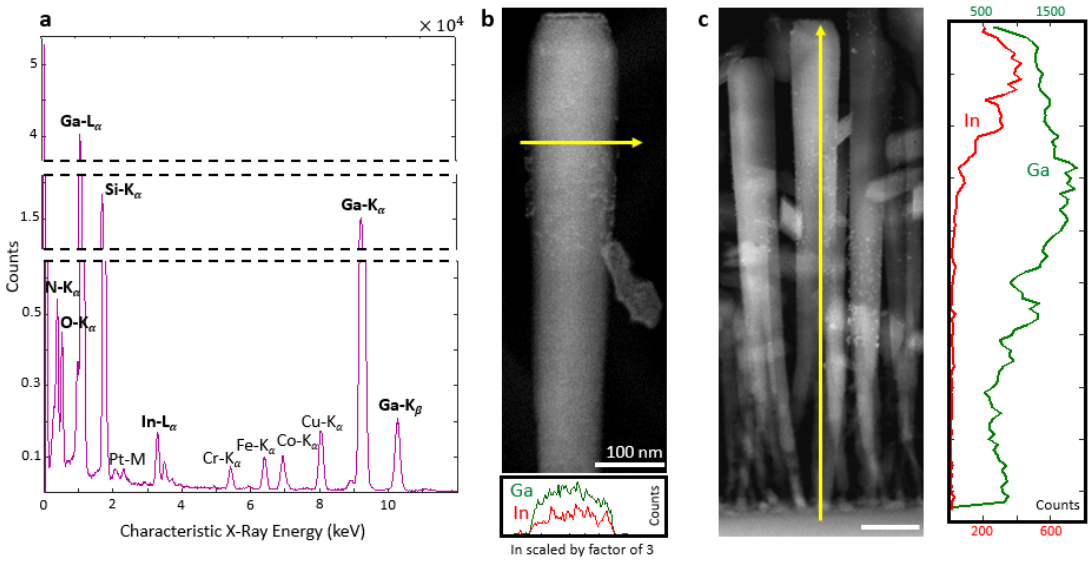

Figure 5.9 Chemical analysis of the InGaN nanowires. (a) EDX spectrum highlighting the average composition of the InGaN nanowires. Cr, Fe, Co, and Cu peaks are background signals from the sample holder. (b-c) STEM image and EDX line spectrum vertically and horizontally across the wire.

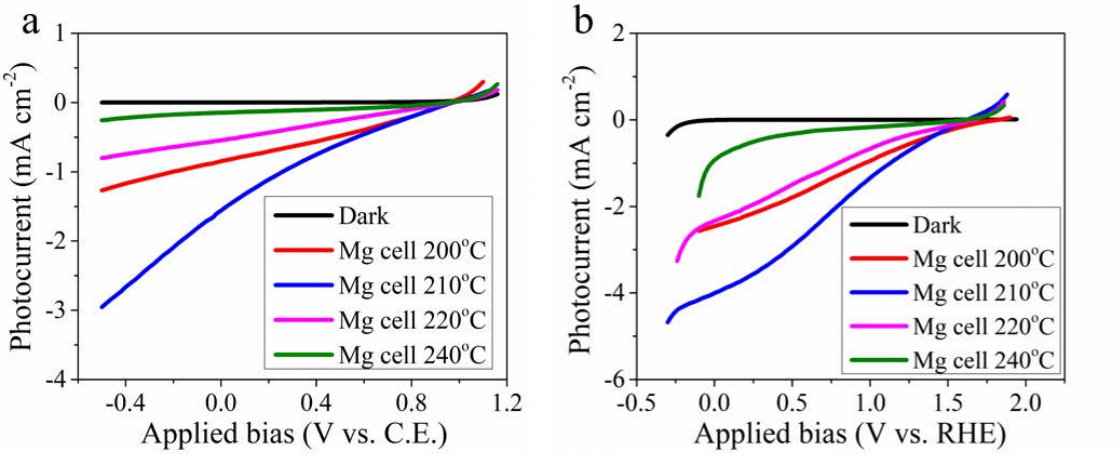

Figure 5.10 LSV performance of InGaN nanowire tunnel junction photocathodes with varied p-type (Mg) doping concentrations, which is controlled by the Mg effusion cell temperature from 200 °C to 240 °C. (a) Two-electrode measurement with a Pt counter electrode. (b) Three-electrode measurement with a Pt counter electrode and an Ag/AgCl reference electrode. All the measurements were performed in 0.5 M H_2SO_4 solution under AM1.5G one-sun illumination, at a scanning rate of 20 mV/s.

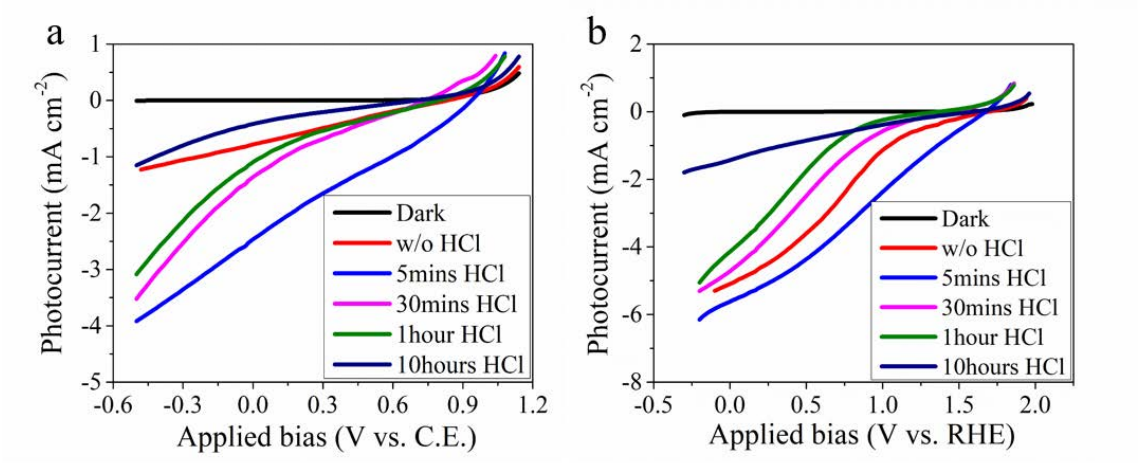

Figure 5.11 LSV performance of p-InGaN nanowire tunnel junction photocathodes after HCl surface treatment for varied soaking time, compared to the virgin sample without surface treatment. (a) Two-electrode measurement with a Pt counter electrode. (b) Three-electrode measurement with a Pt counter electrode and an Ag/AgCl reference electrode. All the measurements were performed in 0.5 M H_2SO_4 solution under AM1.5G one-sun illumination, with a scanning rate of 20 mV/s.

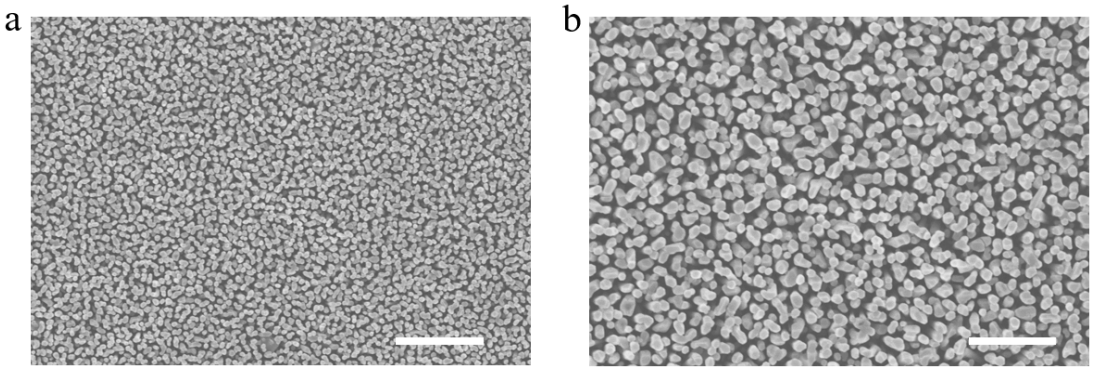

Figure 5.12 Top-view SEM imaging of $In_{0.25}Ga_{0.75}N$ nanowire tunnel junction photocathode after 90 hours unassisted solar water splitting under AM 1.5G one-sun illumination. (a) Scale bar: 2 μm. (b) Scale bar: 1 μm.

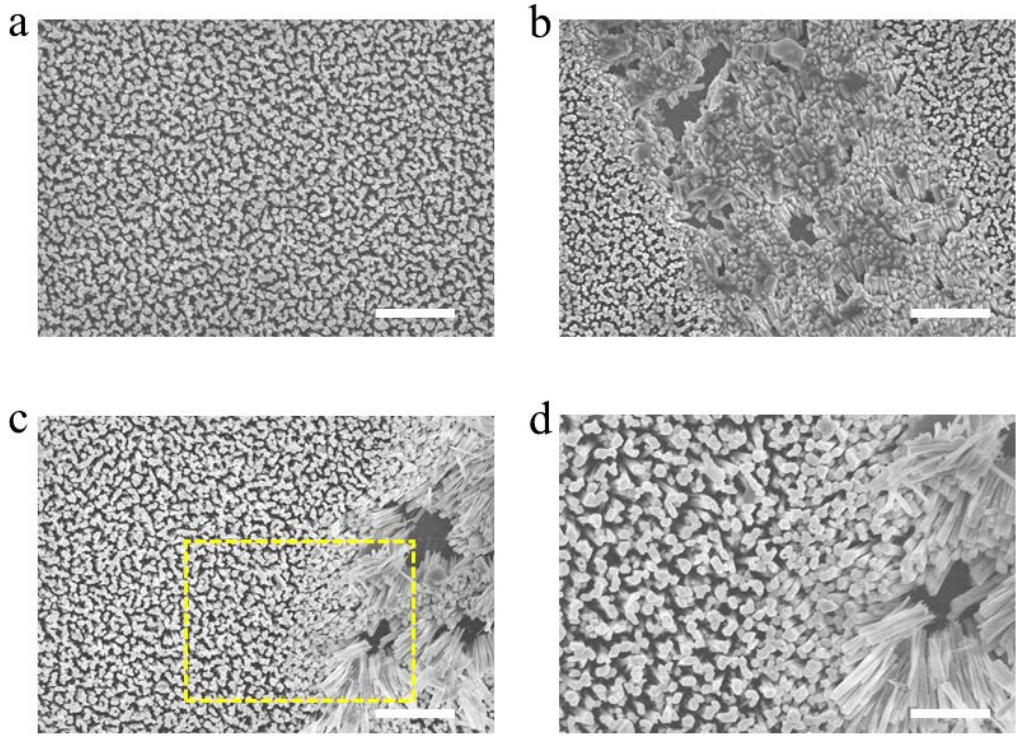

Figure 5.13 SEM characterization of InGaN nanowire tunnel junction photocathode after 250 hours unassisted solar water splitting under AM 1.5G one-sun illumination. (a-c) SEM images were taken from different regions of the sample. Scale bar: 2 μm. (d) SEM image was taken from the marked region in (c). Scale bar: 1 μm.

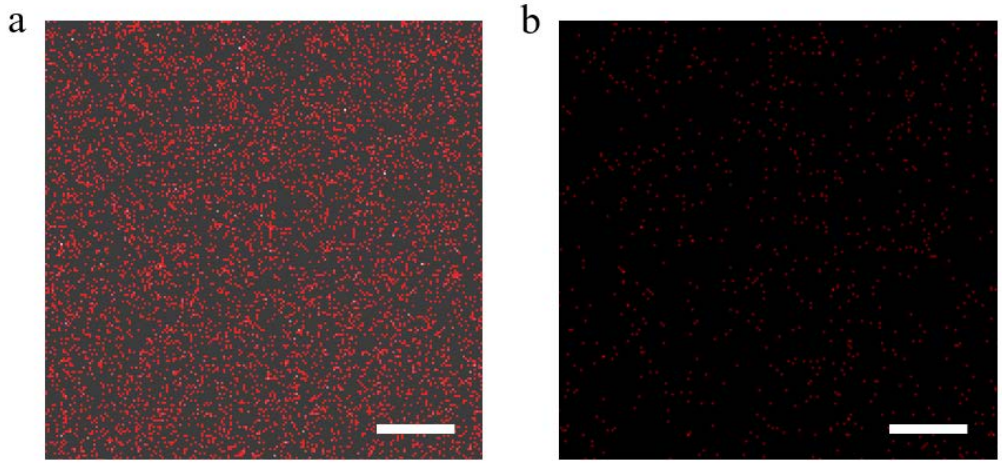

Figure 5.14 EDX elemental mapping of Pt nanoparticles deposited on InGaN nanowires (a) before and (b) after 250 hours solar water splitting experiment. Scale bar: 2 μm. Compared to the initial Pt elemental mapping, the intensity of Pt-M X-ray characteristic signal drops significantly, suggesting the loss of Pt nanoparticles on InGaN nanowires surface during water splitting experiment.

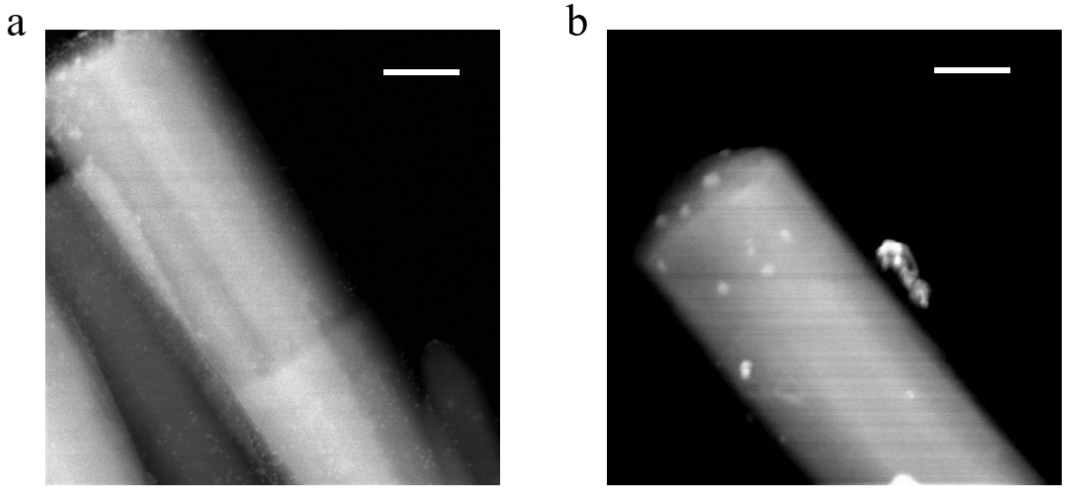

Figure 5.15 Dark-field STEM images of InGaN nanowires decorated with Pt nanoparticles. (a) Before experiment. (b) After long-term water splitting experiment. Scale bar: 50 nm. It is seen that many of the small Pt nanoparticles were lost after long term water splitting experiment.

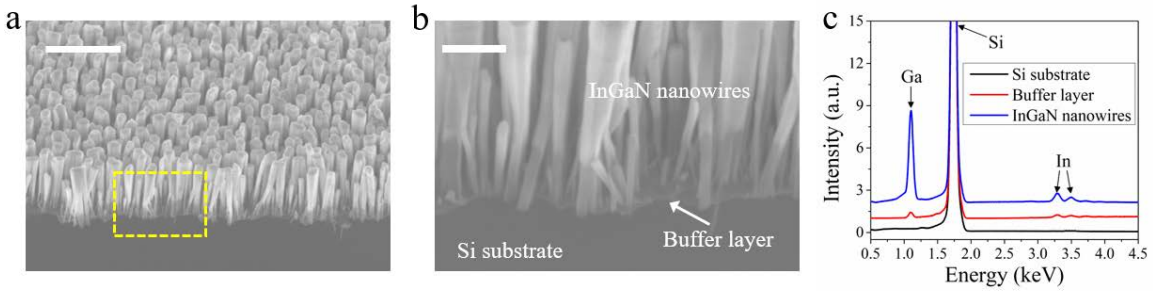

Figure 5.16 (a,b) Tilted SEM images of InGaN arrays grown on Si wafer, showing the existence of a thin InGaN buffer layer protecting the interface. Scale bar: 1 μm. (b) SEM image taken from the marked area in (a). Scale bar: 200 nm. (c) EDX point analysis showing the buffer layer consists of In and Ga.

5.4.2 Supplementary notes

5.4.2.1 Solar-to-hydrogen conversion efficiency calculation

The energy conversion efficiency for solar water splitting should be measured in the two-electrode configuration without any sacrificial reagents, by calculation the applied bias photon-to-current conversion efficiency (ABPE) using Equation (5-1) below.[21, 31] Based on the linear sweep voltammetry measurement of our best-performed p-$In_{0.25}Ga_{0.75}N$ nanowire photocathode, demonstrated in Figure 5.4a, we can plot the ABPE efficiency variation with the applied bias (V vs. Pt counter electrode) shown in Figure 5.4d. STH efficiency is the energy conversion efficiency calculated at zero bias vs. Pt

counter electrode. In addition, in using the equation below it is assumed that the Faradaic efficiency is unity, which has been demonstrated in Figure 5.4f.

$$\text{ABPE} = \left[\frac{J_{ph}\,(mA\,cm^{-2})\times(1.23+V_{app})}{P_{in}\,(mW\,cm^{-2})}\right]_{AM1.5G} \quad (5\text{-}1)$$

where J_{ph} is the measured photocurrent in a two-electrode configuration, $|V_{app}|$ represents the external electric bias (V vs. Pt counter electrode), and P_{in} is power density of the incident light (100 mW cm^{-2} in this work). Positive V_{app} demonstrates that the InGaN photocathode is generating extra photo-voltage during water splitting and negative V_{app} means that external electric voltage is required to drive water splitting reactions.

5.4.2.2 H_2 gas production by Faradaic law

H_2 gas production of the p-$In_{0.25}Ga_{0.75}N$ nanowire photocathode was measured in the two-electrode configuration for 7 hours unassisted solar water splitting by using a gas chromatograph (GC-8A, Shimadzu). In addition, the ideal gas production can be calculated using Equation (5-2) below based on the Faraday's law of water electrolysis.[63, 64] Therefore, we can calculate the theoretical H_2 gas production by assuming a unity faradaic efficiency ($\eta = 1$), shown as the solid line in Figure 5.4f. Due to the nearly perfect match between the measured H_2 production and the calculated values, shown in Figure 5.4f, it confirms the faradaic efficiency is nearly unity.

$$H_2 \text{ production} = 0.5 \times \frac{\int_0^t J_{ph}\,dt}{F} \times \eta \quad (5\text{-}2)$$

where J_{ph} is the measured photocurrent during solar water splitting experiments, t is the experiment time for solar water splitting, F represents the Faraday constant (96485 C mol^{-1}), and η is the faradaic efficiency.

5.4.3 Supplementary tables

Table 5.1 Photoelectrochemical performance of some previously reported semiconductor photoelectrodes achieving unassisted solar water splitting, compared to InGaN nanowires in this work. All the measurements were conducted under one-sun light intensity of simulated AM 1.5G solar spectrum unless noted otherwise. SP, DP and MP refer to single, double, and multiple photon approaches, respectively.

Materials	Electrode type	Approach type	STH (%)	Stability (hours)	Converted Energy (J cm^{-2})	Ref.
p-$In_{0.25}Ga_{0.75}N$	cathode	SP	3.4	300	367200	This work
N_2-treated $BiVO_4$	anode	SP	0.4	38	5472	[218]
$GaSb_{0.03}P_{0.97}$	anode	SP	2	4	2880	[183]
n-TiO_2	anode	SP	0.6[a]	0.01	2.16	[80]
p-$GaInP_2$/GaAs	cathode	DP	12.4[b]	10	44640	[184]
GaInP/GaInAs	cathode	DP	19.3	0.5	2779.2	[180]
Fe_2O_3/perovskite	anode	DP	2.4	8	5529.6	[179]
Fe_2O_3 and perovskite cell	anode	DP	1.85	0.8	532.8	[219]
CdS/CdSe/TiO_2/DSSC	anode	DP	2.1	2	1512	[220]
GaAs/InGaP/TiO_2/Ni	anode	DP	10	10	36000	[181]
p^+n-Si/W-$BiVO_4$/CoPi	anode	DP	0.37	1	133.2	[221]
n-Fe_2O_3-Au NPs/p-Si	anode	DP	3.2	0.67	771.84	[222]
p-Cu_2O vs. n-$BiVO_4$	paired	DP	1.2	0.017	7.2	[223]
CdS/TiO_2 vs CdSe/NiO	paired	DP	0.24	1.5	129.6	[224]
a-Si vs. Fe_2O_3	paired	DP	0.85	10	3060	[225]
$ZnPbO_3$/MoS_2 cathode vs. Zn_2PbO_4/CoPi anode	paired	DP	0.3	0.33	35.64	[226]
NiMoZn/3jn-a-Si	anode	MP	4.7	3	5076	[186]
n^+p-Si/InGaN vs. InGaN/GaN	paired	MP	1.5	0.01	5.4	[227]
Cu_2S/Cu_2O cathode vs. CdS/ZnO anode	paired	MP	0.38	1	108	[228]
$BiVO_4$/WO_3/DSSC/TiO_2	anode	MP	5.7	2	4104	[182]
PEDOT:PSS/P_3HT:PCBM/Pt cathode vs. ZnO anode	paired	MP	0.12	8	345.6	[229]

[a]: Measured under UV light.
[b]: Measured under Xenon lamp of ~1100 mW/cm^2 intensity.

5.5 Summary

In this chapter, we have demonstrated that an InGaN tunnel junction nanowire photocathode integrated directly on Si wafer can drive relatively efficient and stable solar water splitting. A true STH efficiency of 3.4% is measured at 0 V vs. Pt counter electrode in 0.5 M H_2SO_4 electrolyte under AM 1.5G one-sun illumination. The InGaN tunnel junction nanowire photocathode can operate efficiently for ~300 hours without any extra surface protection, with the amount of solar energy converted to H_2 per unit area being nearly order of magnitude higher than previously reported semiconductor photoelectrodes in unassisted solar water splitting. Significantly, such InGaN nanowire tunnel junction structures can be readily integrated with Si or GaAs bottom light absorbers to form a double-junction photoelectrode, which can potentially lead to STH >20% with long-term stable operation.

CHAPTER VI

High Efficiency, Stable Unassisted Solar Water Splitting on Semiconductor Photocathodes Protected by Multi-Functional GaN Nanostructures

6.1 Introduction

Unassisted solar water splitting, with high efficiency and long-term stability, is one critical step of solar fuel production by directly converting solar energy to chemical fuels without electrical bias.[15, 230, 231] The resulting hydrogen fuel can be generated directly on site, readily stored, and distributed to meet the increasing energy demand. Solar water splitting is also essential for the artificial photosynthesis conversion of CO_2 to hydrocarbon fuels, [232, 233] which have the potential to replace conventional fossil fuels while simultaneously addressing the environmental challenges we face. Recently, relatively high solar-to-hydrogen (STH) efficiency has been demonstrated on III-V semiconductor photocathodes, e.g. ~19% for TiO_2/AlInP-protected GaInP/GaInAs double-junction,[22] ~16% for inverted metamorphic GaInP/AlInP-coated GaInP/GaInAs double-junction,[17] and ~13% for metal-protected GaInP/GaInAs/Ge triple-junction.[23] However, due to the detrimental corrosion in harsh water splitting environment,[17, 22, 23] such photoelectrodes exhibit extremely poor stability, preventing any practical application. While there have been reports on semiconductor photoelectrodes with improved stability,[65, 66, 234] those devices generally exhibit extremely low efficiency. Achieving semiconductor photoelectrodes that can drive solar water splitting both *efficiently* and *stably* has remained one of the Holy Grails in solar fuels and artificial photosynthesis.[235, 236]

Stabilizing the surfaces of high efficiency III-V semiconductor photocathodes by employing an extra protection layer has been intensively studied as a potential route to address these critical challenges.[18, 103, 125] The surface protection layer should exhibit extreme chemical stability and resistance to photo-corrosion in harsh photocatalysis environment.[237] It is also critical that the protection layer can cover the semiconductor surface conformally and can be synthesized with precisely determined chemical composition and electronic properties and large scale manufacturability.[238] To maintain the high efficiency, it is essential that the surface passivation material possesses a large bandgap to have negligible absorption of solar photons,[25] while having a small, or negligible conduction band offset with the underlying semiconductor light absorber for efficient extraction of photo-generated charge carriers (electrons). To date, however, there has been no demonstration of any surface protection layer that can simultaneously meet these essential requirements for achieving high-efficiency and stable unassisted solar water splitting.[4, 239, 240] Surface protection schemes, including the use of various metal oxides,[18, 48, 65, 163, 241-244] metal contact films, [11, 245, 246] and two-dimensional (2D) transition metal dichalcogenides (TMDs), such as MoS_2 and $MoSe_2$,[66, 247, 248] have been intensively studied but with very limited success. For instance, although improved stability has been reported with the use of various surface protection schemes, e.g., 100 hours for TiO_2-protected Si,[65] 8 days for metal-passivated GaAs,[11] and 70 hours for MoS_2-protected $GaInP_2$,[66] these measurements were only performed in three-electrode configuration, which neither corresponds to, nor is relevant for the stability analysis under unbiased solar water splitting condition. When measured in two-electrode unbiased solar water splitting,[249] i.e., the conditions required for practical solar hydrogen production, high efficiency III-V semiconductor photoelectrodes can only yield stability <1 hour even with the incorporation of these extra surface protection layers (see Supplementary Table 6.1).[11, 17, 22, 23] Therefore, it is urgently required to develop novel surface protection schemes to achieve stable unassisted solar water splitting on high efficiency III-V semiconductor photocathodes.

GaN, one of the most common semiconductor materials already widely used in electronics and photonics industries,[103, 250] possesses nearly ideal attributes required for protecting the surfaces of high efficiency semiconductor photocathodes.[25] With a

large bandgap ~3.4 eV, GaN protection layer induces negligible absorption of sunlight.[19] Studies have shown that GaN nanostructures grown by molecular beam epitaxy (MBE) can exhibit N-terminated surfaces, which can protect against oxidation and photo-corrosion.[25, 26, 103] For example, stable photocatalytic solar water splitting (>500 hours) has been demonstrated on InGaN nanowire arrays without using any extra surface protection.[26] The conduction band offset between GaN and high efficiency photocathodes, e.g. Si, GaAs and InGaP semiconductors is relatively small,[25, 251-253] which enables efficient charge carrier (electron) extraction. The deep valence band of GaN, on the other hand, can effectively block photo-generated holes and suppress surface recombination.[254] Significantly, crystalline GaN, with precisely controlled structural, electronic, and optical properties can be manufactured using industry standard process, e.g., metal-organic chemical vapor deposition (MOCVD) and MBE, at scale.[255] To date, however, there has been no study on the use of GaN to protect the surfaces of conventional high efficiency III-V semiconductor photocathodes, due to the incompatibility in their processing. GaN has wurtzite crystal structure, and its synthesis often requires the use of very high temperature (~1000 °C), whereas conventional III-V materials have zinc-blende structure and can be easily damaged at such high processing temperature.[256, 257]

Here, we report the first demonstration of relatively efficient and stable solar water splitting utilizing GaN-protected $GaInP_2$/GaAs/Ge triple-junction (GaN/3J) photocathodes. We have overcome the incompatibility in GaN and conventional III-V materials processing by epitaxially growing GaN nanostructures using plasma-assisted MBE (see Section 6.3.1), which enables the conformal deposition of crystalline GaN at relatively low temperatures on foreign substrates. Detailed characterization by scanning transmission electron microscopy (STEM) showed the absence of structural defects and dislocations at the GaN/$GaInP_2$ hetero-interface. It is also found that the integration of GaN nanostructured surface protection layer can enhance light absorption due to the antireflective effect. The large surface area also leads to increased photocatalytic activity, thanks to the textured surface morphology. The monolithic GaN/3J photocathode exhibits an STH efficiency ~12.6% measured in two-electrode configuration vs. Pt dark anode at zero bias. Significantly, continuous solar water splitting has been stably performed

for >50 hours in two-electrode configuration, which is significantly better than that of previously reported high efficiency III-V photocathodes, e.g. ~0.5 hour for inverted metamorphic TiO_2-protected GaInP/GaInAs,[17] $AlInPO_x$-passivated AlInP/GaInP/GaInAs,[23] and TiO_2-protected AlInP/GaInP/GaInAs.[22] Significantly, such GaN protection layer can be controllably synthesized using industry standard processing and can be readily manufactured at scale. The newly discovered multi-functional GaN surface protection scheme, therefore, provides a viable path to achieve high efficiency artificial photosynthesis devices with long-term stable operation that was previously not possible.

6.2 Results and Discussions

6.2.1 Design of GaN-protected $GaInP_2$/GaAs/Ge triple-junction photocathode

Illustrated in Figure 6.1 is the schematic structure and energy band diagram of platinized GaN-protected $GaInP_2$/GaAs/Ge triple-junction photocathode for high efficiency and stable solar water splitting. GaN nanostructures were epitaxially grown atop of an industry available triple junction structure (see Section 6.3 and Supplementary Table 6.2), which includes the integrated $GaInP_2$ top cell, GaAs middle cell, and Ge bottom cell, respectively. Under illumination, photo-excited electrons are extracted from $GaInP_2$ surface through GaN epilayer to the semiconductor/electrolyte interface (liquid interface) driving proton reduction reaction for H_2 evolution, while photo-generated holes flow to the counter electrode through bottom Ge substrate driving O_2 evolution. The conduction barrier at n^+-GaN/n^+-$GaInP_2$ hetero-interface is insignificant due to their small conduction band offset (<0.2 eV, see Supplementary Figure 6.6),[251-253] which ensures efficient transport of photo-generated electrons from $GaInP_2$ surface. Schematically shown in Figure 6.1b is the layered structure of GaN/3J photocathode, with detailed parameters listed in Supplementary Table 6.2. GaN thin film was grown epitaxially on $GaInP_2$ surface by plasma-assisted MBE under N-rich conditions promoting the formation of N-terminated surfaces for stable operation (see Section 6.3.1).[103]

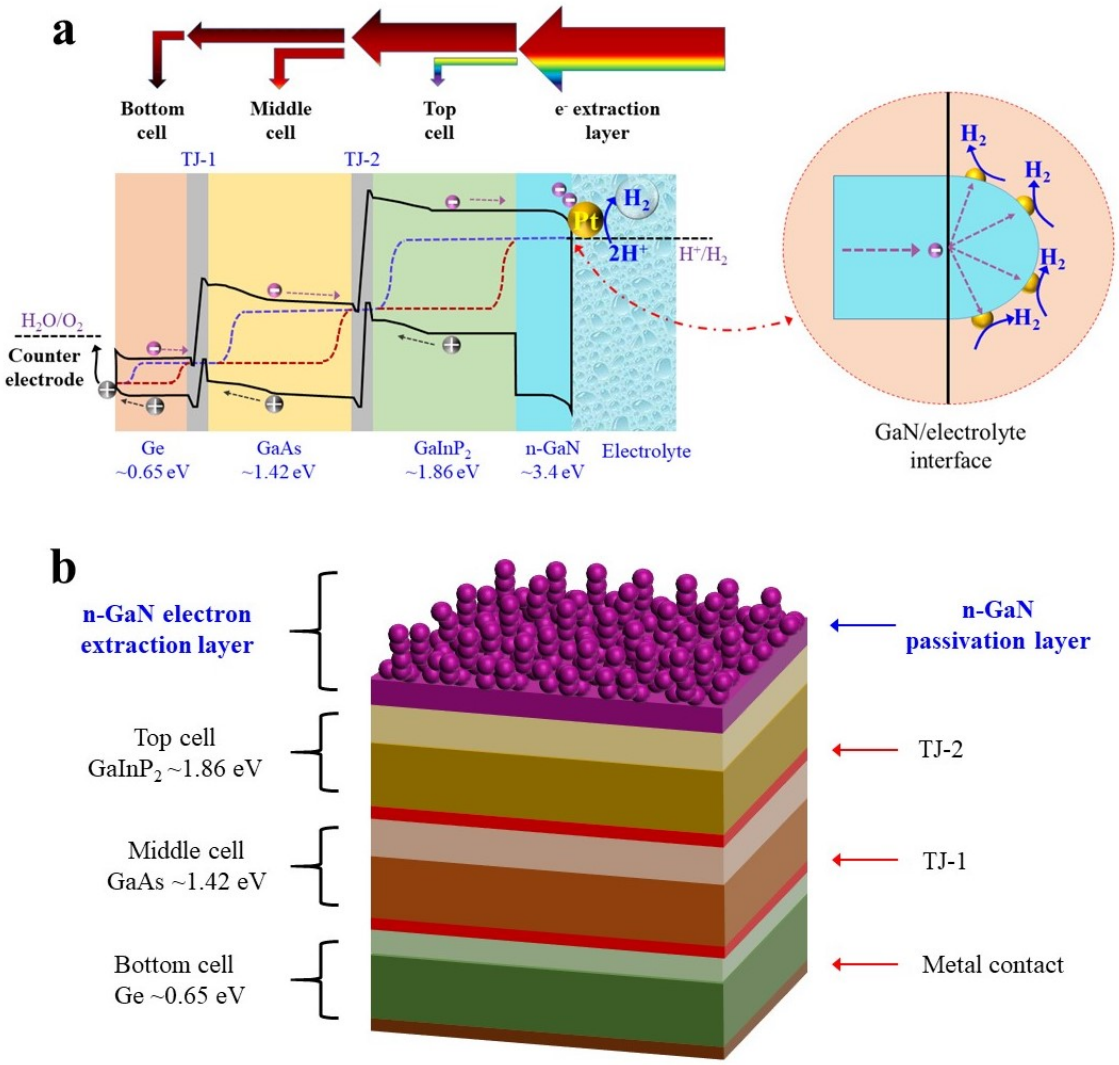

Figure 6.1 Design of GaN-protected $GaInP_2$/GaAs/Ge triple junction photocathode for stable and efficient solar water splitting. (a) Schematic energy band diagram showing the efficient extraction of photo-generated charge carriers (electrons) for proton reduction by the GaN nanostructures. (b) Schematic illustration of $GaInP_2$/GaAs/Ge triple-junction structure protected by multi-functional GaN nanostructures.

Supplementary Figure 6.7 demonstrates the current-voltage (I-V) characteristic of bare $GaInP_2$/GaAs/Ge triple-junction photovoltaic device, measured under AM 1.5G one-sun illumination without using any anti-reflective coating. A saturation photocurrent ~9.6 mA cm^{-2} is measured, which determines its maximum STH limit ~11.8% for solar water splitting if all the photo-generated electrons can drive proton reduction reaction efficiently. In addition, the optical and SEM images of such 3J structure with or without GaN growth are presented in Supplementary Figure 6.8. It is seen that GaN protection

layer can also serve as the anti-reflective coating for reduced surface light reflection, demonstrated in Supplementary Figure 6.9, which can possibly provide even higher photocurrent. In addition, the textured surface of GaN protection layer provides enormous sites for small size Pt cocatalyst deposition, thereby leading to more efficient photocatalytic proton reduction reaction. Moreover, the intensity modulated photocurrent spectroscopy (IMPS) studies revealed that GaN nanostructures could effectively suppress the detrimental surface states for charge carrier recombination of the buried photovoltaic junction.[25, 258]

6.2.2 Synthesis and structural characterization of GaN/3J heterostructure

High quality wurtzite GaN has been demonstrated on Si, SiC, and sapphire substrates using MBE and MOCVD, but it has remained difficult to achieve GaN directly on conventional III-V materials, due to the difference in crystal structure.[259-262] In this work, with the use of plasma-assisted MBE, we have demonstrated crystalline GaN nanostructures epitaxially grown on $GaInP_2$ without the formation of extensive defects and dislocation. High resolution electron microscopy imaging of the GaN/3J structure confirms the key features illustrated in Figure 6.1 - highly crystalline GaN nanostructure epitaxially grown on $GaInP_2$ surface with furcated topography decorated by Pt cocatalyst nanoparticles. Figure 6.2a shows the elemental mapping of Ga, As, In, and P by energy dispersive X-ray (EDX) characteristic signals performed from the cross-view surface of GaN/3J sample, confirming the continuous GaN epilayer growth atop $GaInP_2$ surface. The uniform growth of GaN surface protection layer is also confirmed by secondary electron SEM image, shown in Figure 6.2b, across the triple-junction wafer. Demonstrated in Figure 6.2c is the atomic-resolution scanning transmission electron microscopy (STEM) image revealing the highly crystalline order that extends throughout $GaInP_2$ surface to GaN epilayer. At the interface, crystal dislocations and boundaries generally result in serious charge carrier recombination blocking efficient charge carrier transfer, which, however, has not been observed at GaN/$GaInP_2$ hetero-interface. Such near-perfect epitaxial growth further ensures GaN to fully cover and protect $GaInP_2$ surface against corrosion in harsh electrolyte solutions. The periodic ordering of atoms further demonstrates its high-quality single-crystal structure of GaN epilayer without significant dislocations. Photoluminescence (PL) emission spectra measured at room

temperature is shown in Supplementary Figure 6.10. The relatively narrow linewidth together with strong intensity indicates the highly crystallinity of GaN material. To achieve highly efficient water reduction reaction, Pt cocatalyst nanoparticles were deposited on GaN surface (see Section 6.3.2). Compared to other planar photocathodes, the textured surface of GaN nanostructure provides more surface area, shown in Figure 6.2d, for efficient water reduction reaction with Pt deposition. Demonstrated in Figure 6.2e are the small-size Pt nanoparticles with high crystallinity anchored on GaN surface for facilitating water reduction reaction (see Supplementary Figure 6.11).

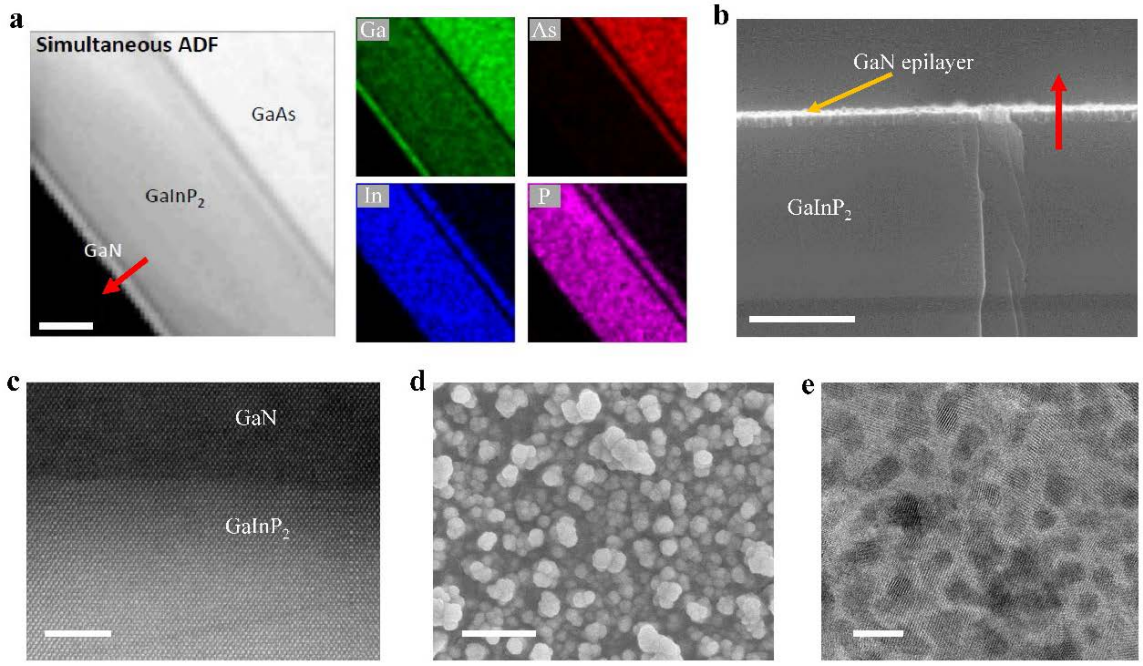

Figure 6.2 Structural characterization of the GaN/3J photocathode for solar water splitting. (a) Dark-field scanning transmission electron microscope (DF-STEM) image with EDX maps showing Ga, In, As, and P elemental distributions. The red arrow indicates the growth direction of GaN epilayer. Scale bar: 250 nm. (b) Cross-view secondary electron SEM image showing uniform GaN thickness grown atop $GaInP_2$ surface. The red arrow indicates the growth direction of GaN epilayer. Scale bar: 500 nm. (c) Atomic resolution DF-STEM image reveals highly crystalline GaN nanostructure epitaxially grown on $GaInP_2$ surface without dislocations. Scale bar: 5 nm. (d) Top-view secondary electron SEM image shows the nanostructured surface topography of GaN protection layer, which provides more surface area for water splitting reaction. Scale bar: 500 nm. (e) Dark-field STEM image demonstrates the uniform deposition of small-size Pt cocatalyst nanoparticles on GaN surface. Scale bar: 5 nm.

6.2.3 Photoelectrochemical performance measured in three-electrode configuration

Photoelectrochemical measurements of the monolithic GaN/3J photocathode were firstly performed in a three-electrode configuration with a Pt counter electrode and an Ag/AgCl reference electrode in 0.1 M H_2SO_4 electrolyte solution under simulated AM 1.5G one-sun illumination (see Section 6.3.3). Shown in Figure 6.3a is linear sweep voltammetry (LSV) measurement of the platinized GaN/3J photocathode under chopped light illumination. The measured photocurrent ~10.3 mA cm^{-2} is slightly higher than the photovoltaic current ~9.7 mA cm^{-2} in Supplementary Figure 6.7, due to the anti-reflection effect of GaN nanostructures as demonstrated in Supplementary Figure 6.8 and 6.9. The measured dark current (~18 μA cm^{-2}) is negligible compared to the light current, suggesting that photocurrent originates from solar energy conversion on GaN/3J photocathode. Furthermore, a very large onset potential, ~2.2 V vs. RHE, agrees well with the open-circuit voltage value (~2.3 V) shown in Supplementary Figure 6.7. The applied bias photon-to-current conversion efficiency (ABPE) is further plotted in Figure 3b (see Section 6.4.2.1). A maximum ABPE ~13.5% is measured at an applied bias of ~1.4 V vs. RHE.

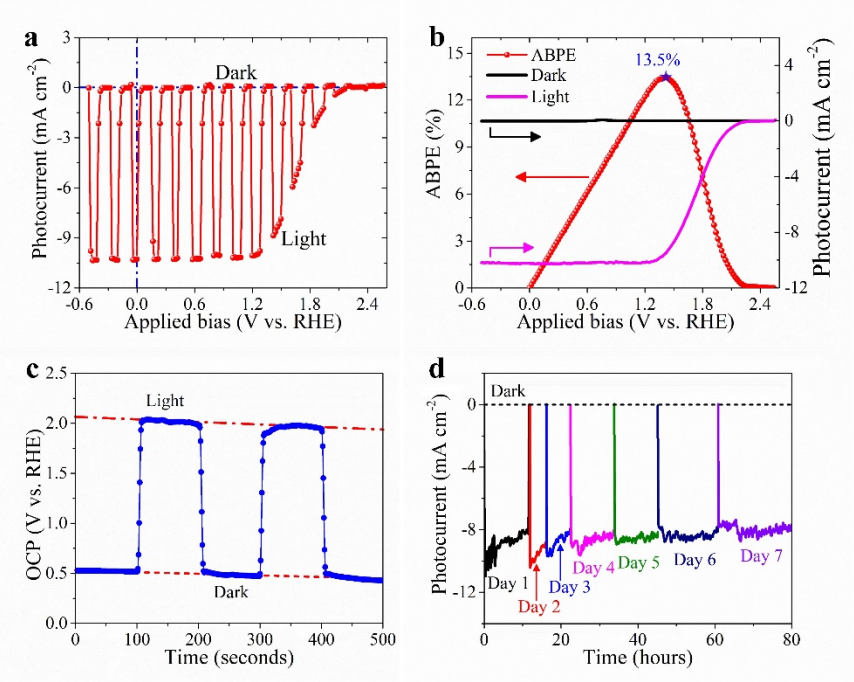

Figure 6.3 Photoelectrochemical measurements of the GaN/3J photocathode in three-electrode configuration under AM 1.5G one-sun illumination. (a) Linear sweep voltammetry (LSV) measurement of GaN/3J photocathode

under chopped light illumination. (b) Applied bias photon-to-current conversion efficiency (ABPE) of the GaN/3J photocathode vs. applied bias. Also shown in the figure are the LSV plots measured under dark and illumination. (c) Open circuit potential (OCP) measurement of GaN/3J photocathode under cyclic light or dark conditions. (d) Long-term stability test of GaN/3J photocathode for 80 hours solar water splitting.

Open circuit potential (OCP) measurement, shown in Figure 6.3c, confirms the downward surface band bending of GaN/3J photocathode under solar illumination,[170] which is suitable for electron extraction to drive water reduction reaction.[204] In addition, a large PEC voltage (~1.5 V) may indicate the onset potential of such GaN/3J photocathode measured in two-electrode configuration.[23, 263] The rapid transition between dark and light conditions demonstrates the efficient charge carrier extraction for proton reduction reaction at the liquid interface.[225, 264-266] We have further performed long-term solar water splitting measurement on the platinized GaN/3J photocathode at zero bias vs. RHE, demonstrated in Figure 6.3d, wherein stability test was conducted for continuous water splitting (see Section 6.3.3).[267] The demonstration of 80 hours solar water splitting for GaN/3J photocathode with an ABPE >13% in this work is the best reported stability for III-V semiconductor photocathodes, compared to 10 hours for inverted metamorphic TiO_2-protected GaInP/GaInAs,[17] 16 hours for $AlInPO_x$-passivated AlInP/GaInP/GaInAs,[23] and 50 hours for TiO_2-protected AlInP/GaInP/GaInAs[22] (see Supplementary Table 6.1).

6.2.4 Unassisted solar water splitting measured in two-electrode configuration

While most of the stability studies for photoelectrochemical water splitting were performed in three-electrode configuration, it is important to note that the three-electrode measurement does not represent true unbiased solar water splitting conditions. Stability measurements performed under unbiased two-electrode configuration is essentially required to evaluate the long-term stability of semiconductor photoelectrodes. In this regard, we have further performed unassisted solar water splitting on the monolithic GaN/3J photocathode in a two-electrode configuration versus a Pt counter electrode in 0.1 M H_2SO_4 electrolyte solution under simulated AM 1.5G one-sun illumination, illustrated in Figure 6.4a (see Section 6.3.3). Spontaneous H_2 and O_2 gas generation is clearly observed from the working and counter electrode, respectively. Shown in Figure 6.4b and 6.4c are the linear sweep voltammetry (LSV) measurement of GaN/3J

photocathode under chopped and constant light illumination, respectively, where the measured photocurrent originates from solar hydrogen conversion with a negligible dark current (<10 μA cm^{-2}). A large onset voltage ~1.55 V is observed, which corresponds well with the OCP measurement shown in Figure 6.3c. At ~0.7 V vs counter electrode, a saturation photocurrent (~10.3 mA cm^{-2}) is achieved, which enables the GaN/3J photocathode to reach a light-limited STH efficiency of 12.6% (see Section 6.4.2.2). Important factors that contribute to the relatively high STH efficiency include efficient electron transport through GaN film and enormous small-size Pt cocatalyst nanoparticles on textured GaN surface. Shown in Supplementary Figure 6.12 is the effect of using different Pt deposition methods, wherein electroplating method demonstrates the best photoelectrochemical performance with large onset potential and fill factor, achieving the light-limiting photocurrent at zero bias (see Section 6.3). Considering the small photovoltage ~0.3 V provided by bottom Ge junction,[268-270] compared to the large saturation voltage ~0.7 V vs. counter electrode in two electrode configuration, we can reasonably conclude that GaN-protected $GaInP_2$/GaAs double-junction tandem structure can drive unassisted solar water splitting with significantly improved (light-limited) efficiency. In addition, the use of RuO_x, IrO_x or other high performance counter electrode for more efficient water oxidation reaction will lead to further improved performance.[19, 234, 271-273]

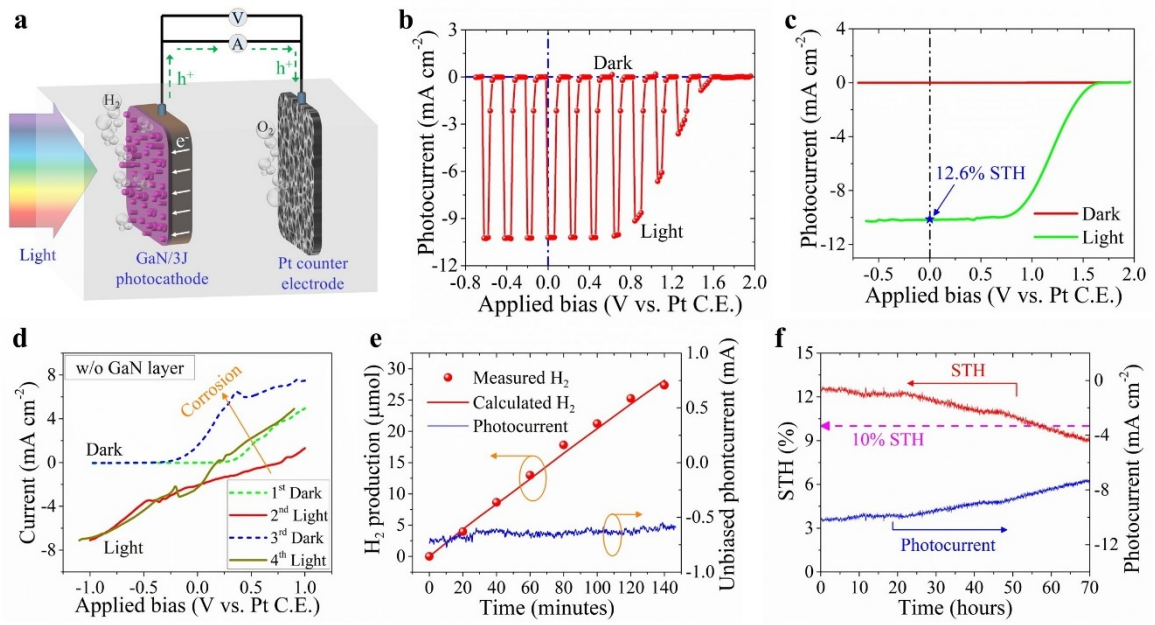

Figure 6.4 Photoelectrochemical measurements of the GaN/3J photocathode in two-electrode configuration under AM 1.5G one-sun illumination. (a) Schematic illustration of the two-electrode measurement of GaN/3J photocathode versus a Pt counter electrode (Pt C.E.). (b-c) Linear sweep voltammetry measurement of GaN/3J photocathode under chopped illumination (b) and under constant light illumination (c). The current measured under dark is also shown. (d) The first four LSV measurements of a platinized 3J photocathode without using GaN surface protection, showing significant corrosion and performance degradation from the 1st scan under dark, 2nd scan under illumination, 3rd scan under dark, to 4th scan under illumination. (e) H_2 gas production (red dots) for ~2.5 hours continuous solar water splitting, which agrees well with the theoretical value (red solid curve) calculated from the photocurrent (blue solid curve) with a unity Faraday efficiency. (f) Stability evaluation of GaN/3J photocathode, showing that a relatively high STH >10% is measured for >50 hours unassisted solar water splitting.

The most important function of such epitaxial GaN nanostructure is to protect buried 3J structure against corrosion for stabilizing operation, which has been elusive for high efficiency III-V photoelectrodes.[22] Previous reports have demonstrated that MBE-grown GaN nanostructure is stable in harsh solar water splitting environment, due to the formation of N-terminated surfaces.[25, 103] Figure 6.4d shows that, without GaN passivation layer, significant corrosion easily happened to bare III-V triple-junction structure in very short time. Moreover, the measured fill factor and onset potential are much worse than that using GaN passivation layer, which further demonstrates its multi-functional properties of GaN nanostructures, including achieving efficient electron transport and enhancing catalytic proton reduction. We have also investigated the effect of GaN thickness on the performance of GaN/3J photocathode (Supplementary Figure

6.13). It is observed that a very thin GaN layer may not effectively protect $GaInP_2$ surface, whereas a too thick GaN layer leads to worse fill factor.

H_2 production through unassisted solar water splitting on the GaN/3J photocathode is evaluated at zero bias in the two-electrode configuration. Shown in Figure 6.4e is the course of H_2 gas production (red dot) vs. time, compared to its theoretical value (solid red line) calculated from the number of photo-generated electrons flowing through the circuit (see Section 6.4.3). It is seen that the measured and calculated hydrogen gas production agree well with a nearly unity faradaic efficiency. Long-term stability evaluation of the GaN/3J photocathode for unassisted solar water splitting was further performed in two-electrode configuration, demonstrated in Figure 6.4f. GaN/3J photocathode can operate stably for unassisted solar water splitting at >10% STH efficiency for >50 hours. Such a long-term stability for true unassisted solar water splitting, i.e., measured at zero bias in two-electrode configuration, has not been reported previously (see Supplementary Table 6.1 and 6.3). The 10% STH efficiency was suggested to be commercially viable,[274] if long-term stability can be maintained. For comparison, for the recently reported ~19% achieved on $GaInP_2$/GaAs in 2018,[22] continuous unassisted solar water splitting has been demonstrated for only 30 minutes, even when protected by extra TiO_2 layer.

6.2.5 Discussions

Summarized in Figure 6.5 is the performance comparison of STH efficiency, device efficiency, and stability of previously reported photocathodes, mainly $GaInP_2$/GaAs tandem structures, compared to GaN/3J photocathode in this work for unassisted solar water splitting (see Supplementary Table 6.3). By using multi-functional GaN nanostructures, the device efficiency of GaN/3J photocathode reaches >90% of its maximum limit, with an electron extraction efficiency ~100%, compared to an 85% device efficiency of the previously best reported $GaInP_2$/GaAs photocathode with a TiO_2 protection layer.[22] To date, there have been many demonstrations of TiO_2 protected photoelectrodes for enhanced stability. However, the electron extraction efficiency of TiO_2 films is still below 85%,[22, 275] which significantly limits the device efficiency (see Supplementary Table 6.3). Furthermore, there has been no demonstration of semiconductor photocathodes with an STH efficiency >10% and stability >50 hours, even by depositing extra surface protection layer,[62] for unassisted solar water splitting

(see Supplementary Figure 6.14). TiO_2 thin film can protect photoelectrodes for >100 hours in three-electrode measurements,[18, 48, 276] but not for unassisted photoelectrochemical solar water splitting devices operated in two-electrode configuration, which is essentially required for practical application. The important advantages of using GaN nanostructures as a surface protection layer include: 1) large bandgap ~3.4 eV to have negligible light absorption, 2) negligible conduction band offset between GaN and $GaInP_2$ surface for smooth electron transfer, 3) large surface area for Pt cocatalyst deposition driving efficient proton reduction reaction, 4) extreme chemical stability due to N-terminated surface[26], 5) nontoxic, 6) controlled and reproducible molecular beam epitaxial growth, and 7) earth abundant and large scale manufacturability.

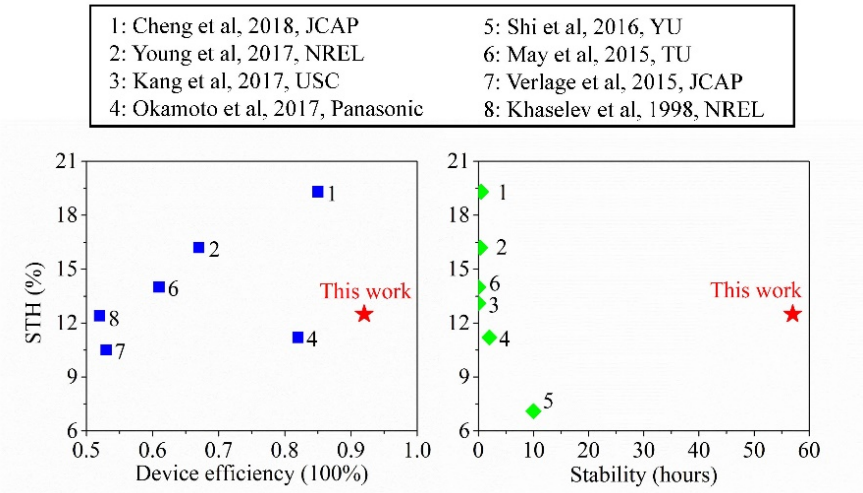

Figure 6.5 Performance comparison of previously reported high efficiency photocathodes with this work. (Left) Solar-to-hydrogen (STH) efficiency plotted vs. the device efficiency. (Right) STH efficiency vs. the reported stability.

In summary, we report on the demonstration of GaN/3J photocathode for high efficiency, stable solar water splitting by using multi-functional GaN nanostructures as novel surface protection layer. When measured in two-electrode configuration, the GaN/3J photocathode can exhibit a true STH efficiency of ~12.6% at zero bias. Moreover, long term stability has been demonstrated on GaN protected 3J photocathode for >50 hours in two-electrode configuration at an STH efficiency >10%. Such multi-functional GaN nanostructures can be monolithically integrated on $GaInP_2$/GaInAs tandem structure, to potentially achieve semiconductor photocathode with STH efficiency >20% for stable unassisted water splitting.

6.3 Experimental Section

6.3.1 GaN/3J photocathode fabrication

The commercially available $GaInP_2$/GaAs/Ge triple-junction wafer (purchased from IQE Ltd.) was used in this study, with details in Supplementary Table 6.2. GaN nanostructures were grown atop the wafer by plasma-assisted molecular beam epitaxy (MBE) under nitrogen-rich conditions to promote the formation of N-terminated surfaces. Growth parameters used in this study include a substrate temperature at ~500 °C, gallium (Ga) beam equivalent pressure (BEP) of 9E-8 Torr, germanium (Ge) cell temperature at 1050 °C, nitrogen flow rate of 1 sccm, and nitrogen plasma power of 350 W. The growth duration was varied from 15 to 60 mins, which leads to GaN protection layers with different thicknesses.

6.3.2 Platinum nanoparticles deposition

Platinum (Pt) nanoparticles were deposited on textured GaN nanostructure surfaces as the cocatalyst nanoparticles for efficient proton reduction reaction by using an electroplating deposition method. Prepared in a three-electrode configuration versus Pt counter electrode and Ag/AgCl reference electrode, the GaN/3J photocathode was kept at ~0 V vs. RHE for 165 seconds in 1 mmol H_2PtCl_6 precursor solution under AM 1.5G one-sun illumination. The platinized GaN/3J photocathode was rinsed by pure water and then dried under argon ambient for subsequent photoelectrochemical measurements. Other deposition methods were also investigated, including ultraviolet-assisted photodeposition and electron-beam evaporation. However, their performance was not comparable to the electroplating deposition.

6.3.3 Photoelectrochemical measurements

Photoelectrochemical (PEC) measurements were conducted in both three-electrode and two-electrode configurations in 0.1 M H_2SO_4 electrolyte solution (pH ~1) equipped with a Newport solar simulator with AM 1.5G filter and one-sun intensity. The Ag/AgCl reference electrode was only used for three electrode measurements. Gamry potentiostat device was used to perform all the PEC measurements including linear sweep voltammetry, chronoamperometry, and open circuit potential tests. H_2 gas production

from solar water splitting on GaN/3J photocathode was analyzed by injecting 1 mL gas sampling into a Shimazdu gas chromatograph machine (GC-8A). The active area of GaN/3J photocathode is in the range of 0.05~0.2 cm^2. For long-term experiment in three-electrode configuration, the electrolyte was periodically refreshed to avoid accumulated heating effect.

6.3.4 Structural and optical characterization

Room-temperature photoluminescence properties of MBE-grown GaN nanostructures were measured using a He-Cd 325 nm excitation laser. SEM images were recorded with a secondary electron detector using a Hitachi SU8000 system (5 kV) and a Tescan MIRA3 system (15 kV) with an EDX detector. High angle annular dark-field scanning transmission electron microscopy (HAADF-STEM) images were collected using a JEOL 3100R05 microscope with Cs aberration corrected STEM (300 keV). Sample for STEM characterization was prepared using bladed exfoliation or in cross-section view by mechanical wedge polishing.

6.4 Supporting Information

6.4.1 Supplementary figures

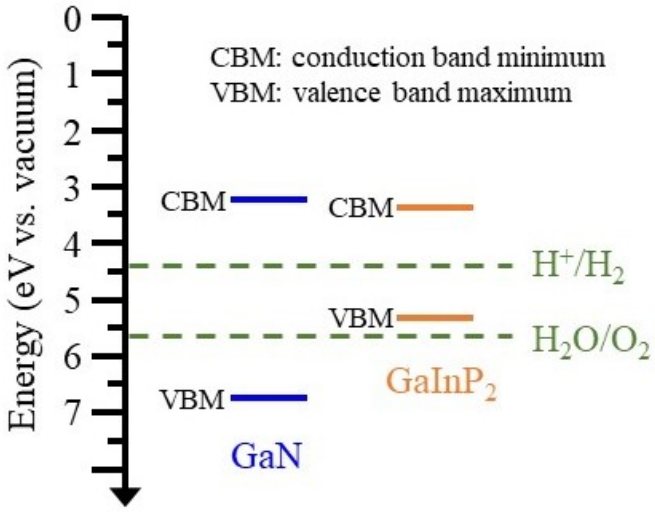

Figure 6.6 Flat band diagram of $GaInP_2$ and GaN semiconductors.[252] Water redox potentials are listed as in pH ~1 acidic electrolyte solutions. The small conduction band offset (<0.2 eV) ensures smooth charge carrier transfer of photo-excited electrons from $GaInP_2$ surface to GaN protection layer.

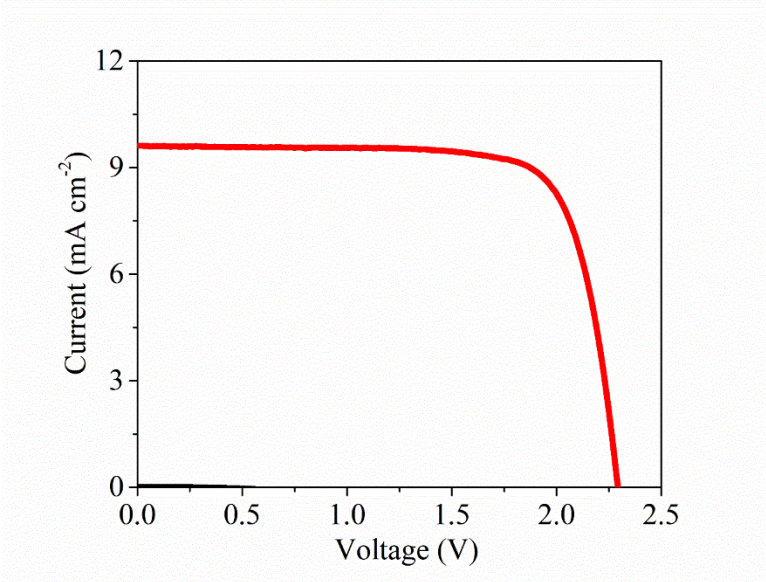

Figure 6.7 Measured current-voltage characteristics of $GaInP_2$/GaAs/Ge triple junction photovoltaic device under AM 1.5G one sun illumination.

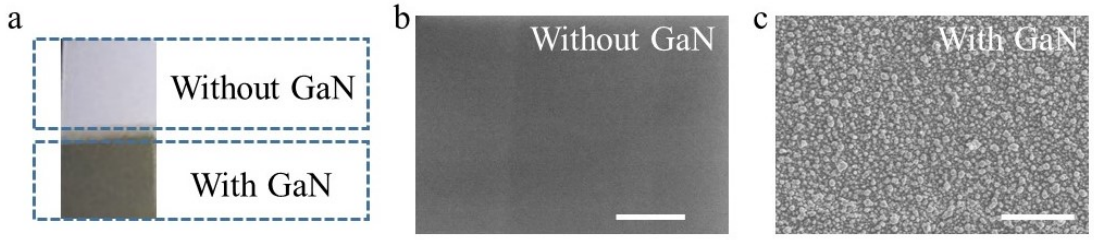

Figure 6.8 Optical and SEM images of $GaInP_2$/GaAs/Ge triple-junction samples with or without GaN nanostructures. Scale bar: 5 μm.

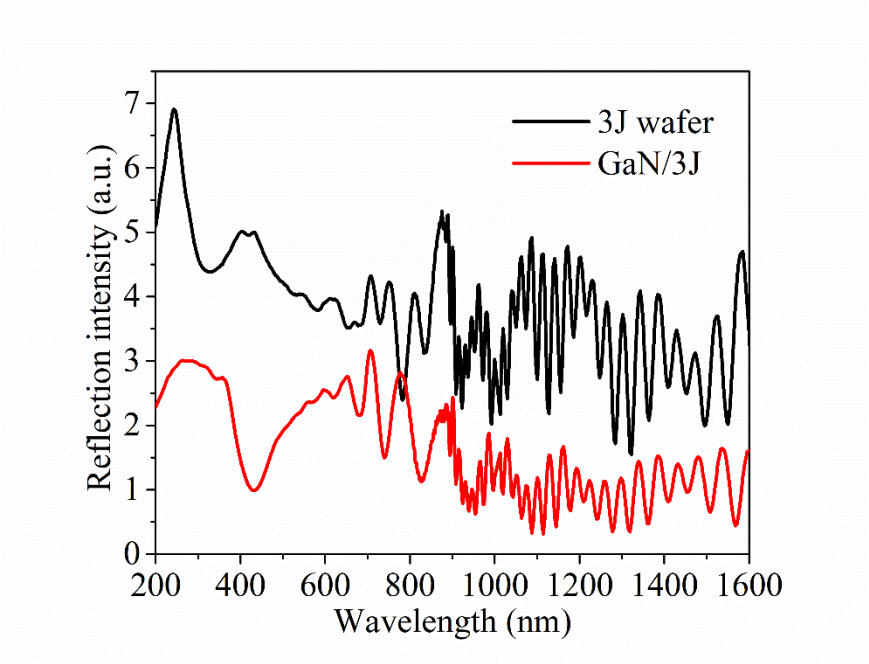

Figure 6.9 Ellipsometric spectrum measured for surface light reflection of GaN protected 3J wafer and bare 3J wafer, showing the reduced reflection for GaN/3J.

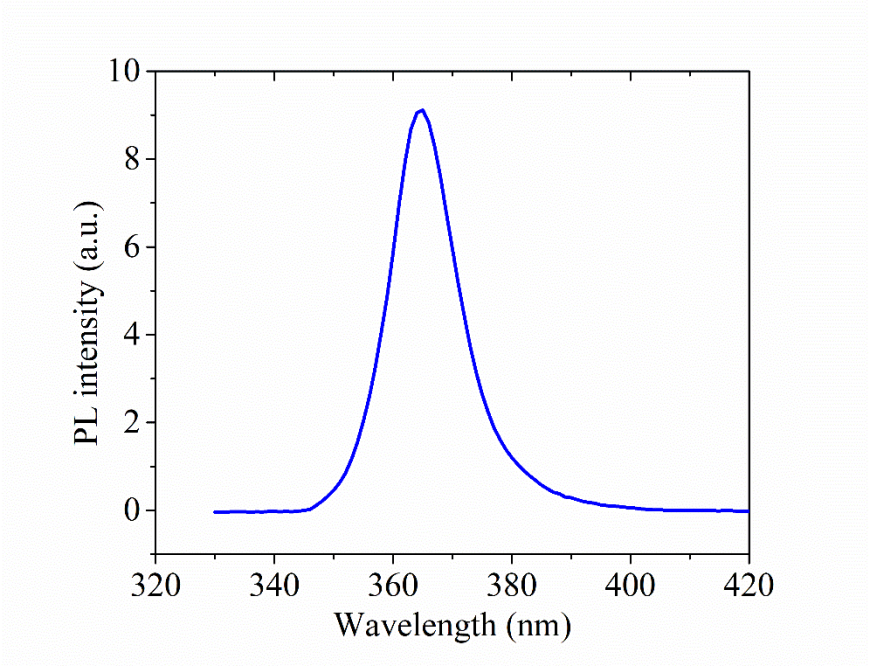

Figure 6.10 Photoluminescence emission spectrum of the multifunctional GaN nanofilm measured at room temperature.

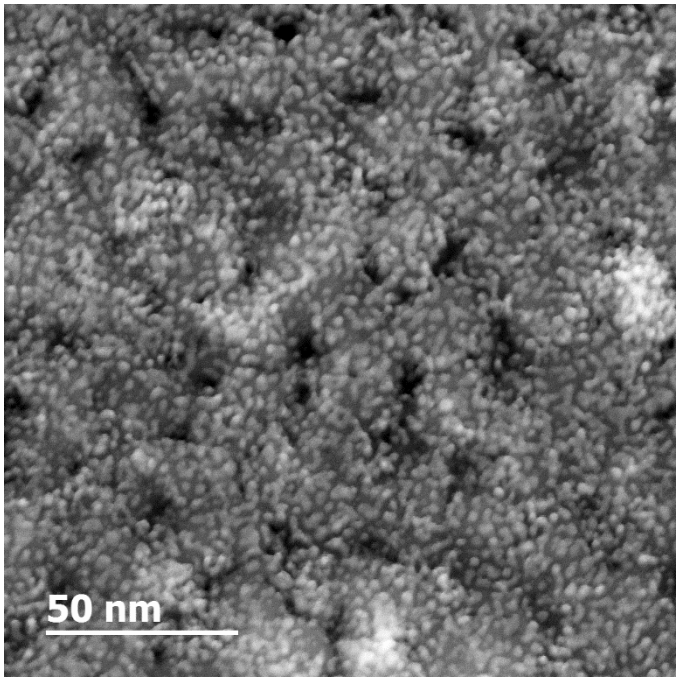

Figure 6.11 Dark-field STEM image revealing the uniform deposition of Pt cocatalyst nanoparticles on GaN nanostructure surfaces.

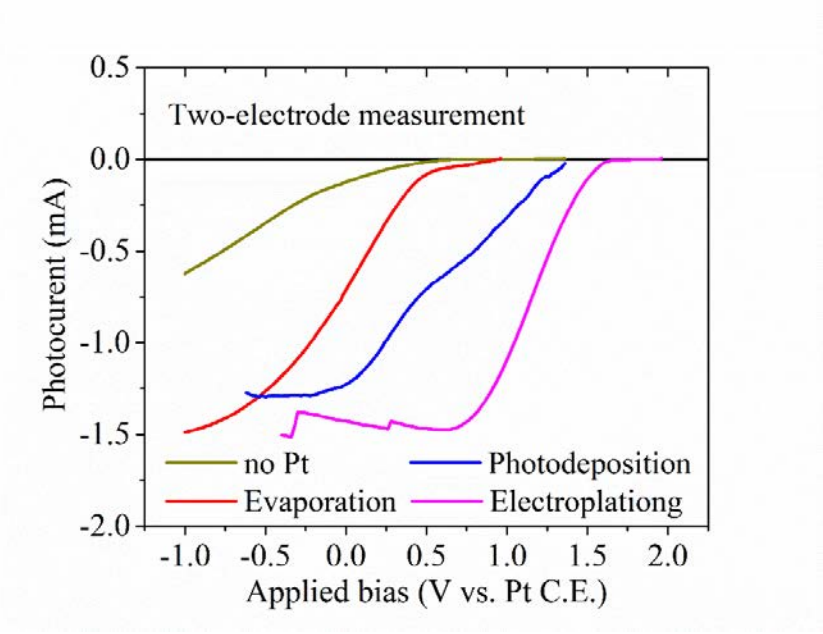

Figure 6.12 Photoelectrochemical performance of the multi-functional GaN/3J photocathodes using different platinum deposition methods. The LSV measurements were performed in two-electrode configuration under AM 1.5G one-sun illumination.

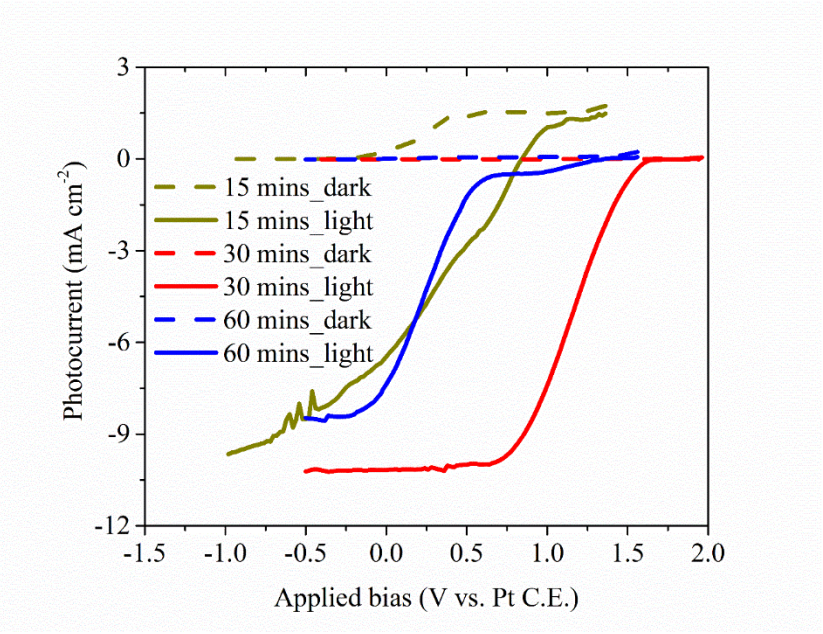

Figure 6.13 Linear sweep voltammetry measurement of GaN/3J photocathode with varied GaN film thicknesses, represented by the growth duration time of 15 mins, 30 mins, and 60 mins, respectively. The measurement for 30 mins is the same as that shown in Figure 6.4c.

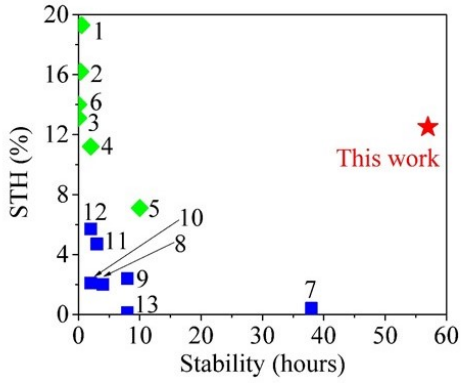

1: GaInP/GaInAs, *ACS Energy Lett.*, 3, 1795, 2018.
2: GaInP/GaInAs, *Nat. Energy*, 2, 17028, 2017.
3: n^+p-GaAs/p^+n-GaAs, *Nat. Energy*, 2, 17043, 2017.
4: $GaInP_2$/GaAs/Ge, *J. Phys. Chem. C*, 121, 1393, 2017.
5: $BiVO_4/WO_3$, *Nat. Commun.*, 7, 11943, 2016.
6: GaInP/GaInAs, *Nat. Commun.*, 6, 8286, 2015.
7: $BiVO_4$, *Nat. Commun.*, 6, 8769, 2015.
8: GaSbP, *Adv. Energy Mater.*, 8, 1703247, 2018.
9: Fe_2O_3/perovskite, *Nano Lett.*, 15, 3833-3839, 2015.
10: CdS/CdSe/DSSC, *Appl. Mater. Interfaces*, 7, 18429, 2015.
11: 3jn-a-Si, *Science*, 334, 645, 2011.
12: $BiVO_4/WO_3$/DSSC/TiO_2, *Nano Energy*, 13, 182, 2015.
13: PEDOT/P_3HT vs. ZnO anode, *ACS Catal.*, 7, 5308, 2017.

Figure 6.14 STH efficiency and stability of previously reported photoelectrodes achieving unassisted solar water splitting measured in two-electrode configuration, compared to the GaN/3J photocathode demonstrated in this work.

6.4.2 Supplementary notes

6.4.2.1 Applied-bias photon-to-current conversion efficiency

As measured in three-electrode configuration, there is external electrical bias applied to the working electrode, wherein STH conversion efficiency cannot be derived. On the other side, applied-bias photon-to-current efficiency (ABPE) is defined to evaluate the performance for solar water half reactions, so-called water reduction reaction. For the GaN/3J photocathode demonstrated in Figure 6.3, ABPE values can be calculated using Equation (6-1).[25]

$$\text{ABPE}\ (\%) = \frac{J_{ph}\ (mA{\cdot}cm^{-2}) \times V_{app}\ (V\ vs.\ RHE)}{P_{in}\ (mW{\cdot}cm^{-2})} \times 100\% \qquad (6\text{-}1)$$

where J_{ph} is the measured photocurrent of a photocathode in a three-electrode configuration (Figure 6.3b), V_{app} represents the external electric bias (V vs. RHE), and P_{in} is power density of the incident light (100 mW cm^{-2} in this work).

6.4.2.2 Solar-to-hydrogen conversion efficiency

For overall water splitting measured in two-electrode configuration, the solar-to-hydrogen (STH) conversion efficiency is defined as the chemical energy of generated H_2 gas divided by the solar energy of incident light, which can be simplified to the output power divided by incident solar power. The energy conversion efficiency for solar water

splitting is measured in two-electrode configuration without any sacrificial reagents. We can calculate the STH efficiency using Equation (6-2) below,[277] based on the LSV measurement under light in Figure 6.4c.

$$\text{STH} = \left[\frac{J_{ph}\,(mA\,cm^{-2})\times 1.23V}{P_{in}\,(mW\,cm^{-2})}\right]_{AM1.5G} \quad (6\text{-}2)$$

where J_{ph} is the measured photocurrent at zero bias a two-electrode configuration, and P_{in} is power density of the incident light (100 mW cm^{-2} in this work).

6.4.2.3 H_2 gas production by Faradaic law

H_2 gas production of GaN/3J photocathode was measured in two-electrode configuration for ~2.5 hours unassisted solar water splitting using a gas chromatograph (GC-8A, Shimadzu). In addition, the ideal gas production can be calculated using Equation (6-3) below based on the Faraday's law of water electrolysis.[63, 64] Therefore, we can calculate the theoretical H_2 gas production by assuming a unity faradaic efficiency ($\eta = 1$), shown as the solid line in Figure 6.4e. Due to the nearly perfect match between the measured H_2 production and the calculated values, shown in Figure 6.4e, the faradaic efficiency is demonstrated to be nearly unity.

$$H_2 \text{ production} = 0.5 \times \frac{\int_0^t J_{ph}dt}{F} \times \eta \quad (6\text{-}3)$$

where J_{ph} is the measured photocurrent during solar water splitting experiments, t is the experiment time for solar water splitting, F represents the Faraday constant (96485 C mol^{-1}), and η is the faradaic efficiency.

6.4.3 Supplementary tables

Table 6.1 Summary of stability of some previously reported high-efficiency photocathodes measured in three-electrode (3E) configuration for half-cell water reduction reaction and in two-electrode (2E) configuration for unassisted solar water splitting, and the comparison with the GaN/3J photocathode presented in this work. All measurements were performed under AM 1.5G one-sun illumination.

Materials	STH efficiency	Electrolyte	3E stability	2E stability	Surface protection	Ref.
Platinized Multi-functional GaN/3J	12.6%	H_2SO_4	80 hours	57 hours	GaN	This work
Inverted metamorphic PtRu-GaInP/GaInAs	16.2%	H_2SO_4	10 hours	0.5 hour	TiO_2	[17]
Pt-$AlInPO_x$/AlInP/ GaInP/GaInAs	14%	$HClO_4$	16 hours	<0.5 hour	Rh film/ $AlInPO_x$	[23]
Pt-metal/n^+p-GaAs cathode & IrO_x/metal/p^+n-GaAs anode	13.1%	H_2SO_4	10 hours	<0.5 hour	Metal film	[11]
Ru-TiO_2/oxide/AlInP/GaInP/ GaInAs/GaAs	19.3%	KH_2PO_4 /K_2HPO_4	50 hours	0.5 hour	TiO_2	[22]

Table 6.2 $GaInP_2$/GaAs/Ge triple-junction (3J) structure used in this work for preparing GaN/3J photocathode.

Layer	Materials	Thickness (μm)	Dopant	Doping type	Dopant concentration (cm^{-3})
11	$Ga_{0.44}In_{0.56}P$	0.1	Silicon	N	5E+17
10	$Ga_{0.44}In_{0.56}P$	0.5	Zinc	P	1.2E+17
9	$Al_{0.11}Ga_{0.33}In_{0.56}P$	0.03	Zinc	P	1E+18
8	$Al_{0.45}Ga_{0.55}As$	0.06	Carbon	P	2E+20
7	$Ga_{0.44}In_{0.56}P$	0.06	Tellurium	N	1E+20
6	$Ga_{0.98}In_{0.02}As$	0.1	Silicon	N	5E+18
5	$Ga_{0.98}In_{0.02}As$	3.4	Zinc	P	1.2E+17
4	$Ga_{0.44}In_{0.56}P$	0.1	Zinc	P	1E+18
3	GaAs	0.08	Carbon	P	1E+20
2	GaAs	0.03	Tellurium	N	6E+19
1	$Ga_{0.98}In_{0.02}As$	0.8	Silicon	N	5E+18
0	Ge wafer	170	Gallium	P	N/A

Table 6.3 Summary of the photoelectrochemical performance of previously reported high-efficiency photocathodes achieving unassisted solar water splitting, and the comparison with the GaN/3J photocathode presented in this work. All measurements were performed under AM 1.5G one-sun illumination unless noted.

Materials	STH efficiency (%)	Theoretic limit (%)	Device efficiency (%)	Unbiased stability (h)	Extra Protection layer	Year [Ref.]
Platinized Multi-functional GaN/3J	12.5	13.6	92	57	N/A	This work
Rh-TiO_2-AlInP/GaInP-/GaInAs/GaAs-RuO_x	19.3	22.8	85	0.5	TiO_2	2018 [22]
PtRu-GaInP/AlInP/GaInP-GaInP/GaInAs	16.2	24.2	67	0.4	n-GaInP	2017 [17]
Pt-metal/n^+pGaAs & IrO_x-metal/p^+nGaAs	13.1	N/A	N/A	N/A	ohmic metal layer	2017 [11]
Pt-TiO_2-3J-SUS-IrO_2[a]	11.2	13.6	82	2	TiO_2	2017 [61]
Pt-TiO_2-Dye |cDBR/ITO| Pt-$BiVO_4$/WO_3	7.1	N/A	N/A	10	TiO_2	2016 [62]
Rh/AlInP-GaInP/GaInAs-RuO_2	14	22.8	61	0.04	N/A	2015 [23]
Ni-TiO_2/GaInP/GaAs[b]	10.5	19.7	53	40	Thick TiO_2	2015 [278]
Pt/$GaInP_2$/GaAs[c]	12.4	24	52	10	N/A	1998 [15]

[a] Wireless device
[b] Photoanode structure.
[c] Measured under 1190 mW/cm^2 tungsten-halogen white light illumination.

6.5 Summary

In this chapter, we report the GaN/3J photocathode for high efficiency, stable solar water splitting by using a multi-functional GaN surface protection layer. When measured in the two-electrode configuration, the monolithic GaN/3J photocathode can exhibit a true STH efficiency of ~12.6% at zero bias. Moreover, long term stability has been demonstrated on GaN protected 3J photocathode for 80 hours in three-electrode configuration and 57 hours in two-electrode measurement at zero bias with an efficiency >10%, which is the best reported stability for high efficiency multi-junction semiconductor photocathodes. The multifunctional GaN nanostructure not only

significantly reduces the charge transfer resistance at semiconductor/electrolyte interface but also protects buried III-V materials against corrosion. Such multi-functional GaN photocatalytic nanostructure provides a new pathway to protect conventionally efficient, but unstable photoelectrodes to achieve both efficient and stable operation for unassisted solar water splitting at scale.

CHAPTER VII

Wafer-Scale Synthesis of Monolayer WSe_2: A Multi-Functional Photocatalyst for Efficient Overall Pure Water Splitting

7.1 Introduction

Solar water splitting, through the dissociation of water molecules to H_2 and O_2, is one significant step of artificial photosynthesis to solve future energy and environmental issues.[128, 279] Critical to the development of an efficient solar water splitting cell is the integration of catalysts, for water oxidation and/or proton reduction, with the semiconductor light absorber. For practical applications, it is also essential that the catalysts are of low cost and are earth-abundant. Si and III-V semiconductor materials[4, 15, 18, 186, 280] have been extensively studied for solar-to-fuel conversion due to the efficient light absorption. However, their operation often requires the use of expensive noble metal catalysts and their performance suffers from serious photo-corrosion.[15, 18] Moreover, the substrates to grow III-V semiconductors are prohibitively expensive, and it is extremely difficult to integrate III-V semiconductor light absorbers on low cost foreign substrates, due to the lattice mismatch related issues.[11, 257, 281] Additionally, previously reported photocatalysts, such as CoO_x, IrO_x, Pt, MoS_2, and RuO_x are only capable of either oxidizing water[11, 34, 224] or proton reduction[10, 37, 282, 283]. To efficiently catalyze overall water splitting, the integration of dual catalysts with light absorbers is required. In such systems, charge carrier transport from the semiconductor light absorber to the catalyst is often hindered by the presence of impurities and/or potential barriers related to imperfect band alignment.[21, 284] It has been envisioned that a multi-functional photocatalyst, that exhibit both catalytic and light harvesting

capacities, can potentially address the challenges and performance bottlenecks of solar water splitting by minimizing the over-potential requirement, enhancing charge carrier transport and collection efficiency, and reducing the fabrication cost.[11, 279]

Recently, two-dimensional (2D) transitional metal dichalcogenides (TMDCs) have been intensively studied for electronic, optoelectronic, and solar energy device applications.[285-289] Among various TMDCs, monolayer WSe_2 has a direct bandgap of ~1.65 eV and can absorb visible light efficiently while promising a relatively large photovoltage. Even for a single monolayer, 1~5% light[290, 291] can be absorbed for photons with energy above the bandgap. Significantly, the energy band edges of monolayer WSe_2 can straddle water redox reactions:[67, 292-294] its conduction band edge is positioned slightly more negative than the water reduction potential, while its valence band edge is located more positive than water oxidation potential and can therefore drive oxygen evolution which is normally a bottleneck for water splitting. Previously, WSe_2 was used as a photoanode in iodate electrolytes.[295-297] Recent studies have shown that monolayer TMDC provides catalytic sites[282, 298-300] at edges for water redox reaction, which was not significant in bulk TMDC materials, and hydrogen evolution reaction through TMDC 2D materials has been intensively studied.[283, 298, 301] To date, however, there have been no reports on overall water splitting on monolayer or few layers WSe_2, and their capacity for water oxidation has remained largely unknown.[299] This has been limited, in part, by the lack of controlled synthesis of large area TMDC atomic crystals. Recently, significant efforts have been devoted toward the large area growth of TMDC monolayers using chemical vapor deposition (CVD) and physical vapor deposition (PVD),[285, 289, 302-304] but with limited success.

To achieve scalable, low cost solar water splitting devices and systems, it is highly desired to integrate TMDC catalysts on nonconventional substrates, such as amorphous SiO_x or metal substrates. In this work, by exploiting two-dimensional van der Waals (vdW) growth,[67, 287] we have investigated the molecular beam epitaxial (MBE) growth and structural, optical and photocatalytic characteristics of monolayer and multi-layer WSe_2 directly on amorphous SiO_x templates. This is in direct contrast to previous

MBE attempts of isolated TMDC flakes on crystalline substrates.[67, 305-308] The vdW epitaxy of large area, uniform, and crystalline WSe_2 on amorphous substrates is unambiguously supported by the streaky reflection high-energy electron diffraction (RHEED) pattern, a widely used technique to distinguish single crystalline, polycrystalline, and amorphous structures during epitaxy, and by detailed transmission electron microscopy (TEM) studies. The formation of uniform, continuous WSe_2 monolayer on 2" SiO_x templates is further confirmed by detailed optical studies, including photoluminescence (PL) and Raman mapping. We have further demonstrated that, through the seamless integration of catalytic properties with light harvesting capacity, monolayer WSe_2 can serve as a multi-functional photocatalyst and offer distinct advantages for solar water splitting, including significantly reduced over-potential, high efficiency, and stability.

7.2 Results and Discussions

7.2.1 Molecular beam epitaxial growth

2D WSe_2 layers were grown on amorphous SiO_x substrates using a Veeco GENxplor MBE system (see Section 7.4.1). The observation of streaky RHEED feature during vdW growth of monolayer WSe_2 film is shown in Figure 7.1a, which provides unambiguous evidence for the achievement of crystalline WSe_2 directly on amorphous substrates with atomically smooth surface. Similar streaky RHEED feature was reported for WSe_2 epitaxy previously, but the growth took place on crystalline GaAs and graphite substrates. [67, 305-308] Moreover, with the vdW interaction between WSe_2 layers,[67, 289] multilayer WSe_2 films can be directly synthesized on a wafer scale. Optical images of WSe_2 grown on SiO_x are shown in Supplementary Figure 7.4 and 7.5 and RHEED observation of WSe_2 grown on sapphire is displayed in Supplementary Figure 7.6. Stoichiometric analysis of epitaxial WSe_2 was performed using high-resolution X-ray photoelectron spectroscopy (XPS), shown in Figure 7.1b. The atomic percentage ratio of W and Se was measured to be ~1:2, suggesting the formation of nearly stoichiometric WSe_2. The absence of W and Se oxidation peaks confirms the high purity of epitaxial WSe_2. Elemental analysis of monolayer WSe_2 was further analyzed by energy dispersive

X-ray spectroscopy (EDX) as shown in Supplementary Figure 7.7. A typical optical microscope image of monolayer WSe_2 grown on SiO_x is shown in Figure 7.1c, and its thickness was measured to be ~0.8 nm by atomic force microscopy (AFM).

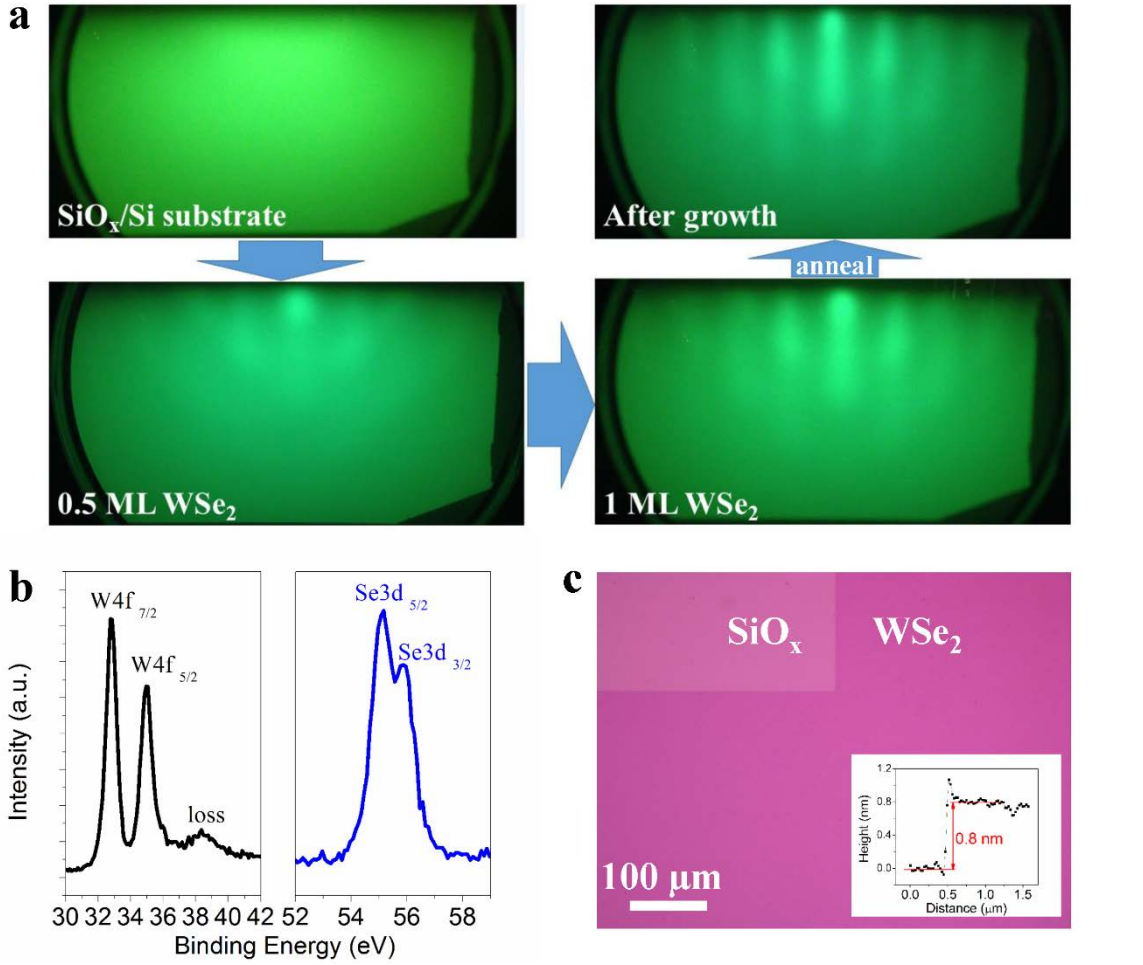

Figure 7.1 Growth and characterization of monolayer WSe_2 directly on SiO_x templates. (a) *In-situ* observation of RHEED patterns during MBE growth of WSe_2 monolayer on SiO_x/Si substrates. (b) XPS spectra of W and Se core-level peaks. The atomic percentage ratio of W and Se was determined to be ~1:2. (c) Optical microscope image of bare SiO_x/Si substrate and as-grown WSe_2 monolayer sample; partial WSe_2 film was intentionally removed to expose SiO_x surface. The insert is an AFM height measurement revealing its thickness of ~0.8 nm corresponding to monolayer WSe_2 film.

7.2.2 Optical properties

PL and Raman footprint of 1-3ML WSe_2 films are investigated to elucidate their optical properties. Figure 7.2a compares the PL spectra of 1-3ML WSe_2 samples measured at room temperature (R.T.). With increasing thickness, the energy bandgap,

evidenced by the PL peak position,[280, 290, 291, 309] is reduced gradually. The relatively large full-width-at-half-maximum (FWHM, ~45 nm) is attributed to the inhomogeneous broadening associated with the presence of defects and grain boundaries. Shown in Figure 7.2b are the Raman scattering spectra for WSe_2 samples with different thicknesses. One in-plane vibration mode E_{2g} at ~250.8 cm^{-1} is observed for identifying WSe_2 nanostructures; the shoulder peak A_{1g}, representing out-of-plane vibration, at ~260.2 cm^{-1} is undetected in monolayer sample but is present in thicker layers.[307, 310] There are also several weak modes at 350~400 cm^{-1} representing second-order vibration[304] for WSe_2 crystals. A typical Raman mapping of E_{2g} scattering at ~250.8 cm^{-1} is shown in Figure 7.2c. Some WSe_2 material was intentionally removed to expose SiO_x surface for better observation under optical microscope.

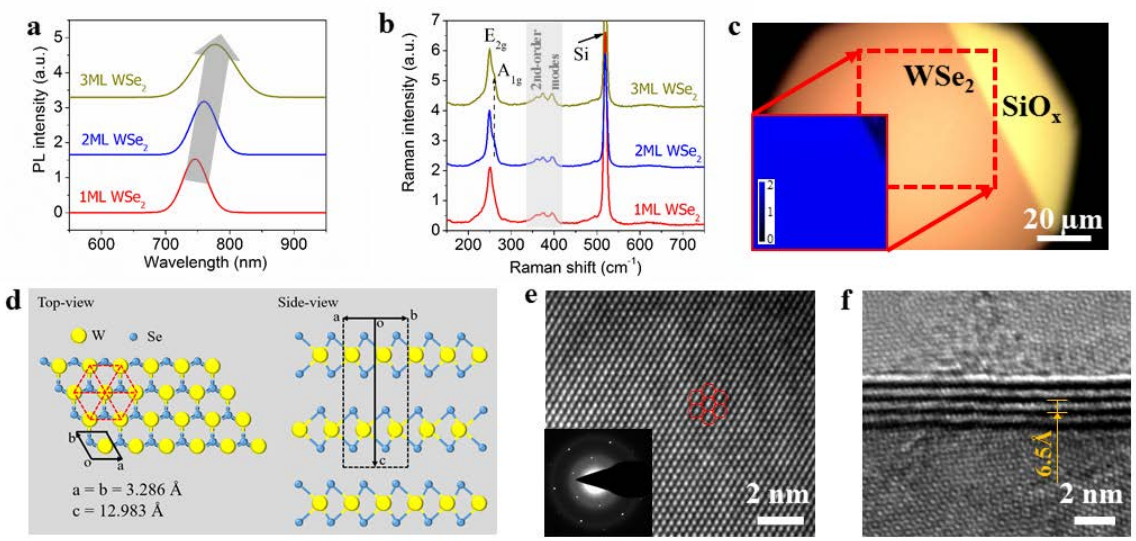

Figure 7.2 Optical properties and crystal structures of 1-3ML WSe_2 nanostructures. (a) Micro-photoluminescence spectra of 1-3ML WSe_2; the gray arrow indicates the reduced energy gap of WSe_2 with increased thickness. (b) Micro-Raman spectra of 1-3ML WSe_2 samples at room temperature; E_{2g} peak at ~250.8 cm^{-1} is the identification of WSe_2 crystals. (c) Raman mapping of E_{2g} peak, in 50 μm × 50 μm region as labeled under optical microscope, where some material was deliberately removed to expose SiO_x surface. (d) Schematic atomic configuration of 2H-WSe_2 crystal with layered structure. The dashed hexagon represents the distribution of tungsten atoms. (e) High-resolution plane-view TEM image of WSe_2 monolayer film and the insert corresponds to selected area electron diffraction pattern. The suspended solid hexagons in Figure 7.2e represent W atomic distribution of 2H-WSe_2 crystal. (f) Lateral view of multilayer WSe_2 revealing its layer-by-layer stacking structure.

7.2.3 Crystal structure

Monolayer WSe_2 consists of three atom layers where W atom layer is sandwiched between two equivalent Se layers by forming interatomic covalent bonding.[288, 311] The atomic structure[293, 312] of 2H-phase WSe_2 crystal is schematically depicted in Figure 7.2d. Tungsten atoms form face-centered hexagonal pattern[313] and only van der Waals force exists between layers. High-resolution transmission electron microscopy (HR-TEM) was utilized to observe its hexagonal symmetry and layer structure of WSe_2 sample, shown in Figure 7.2e,f. The corresponding selected area electron diffraction (SAED) pattern within six-fold symmetry demonstrates that it is monolayer crystal structure with a hexagonal lattice.[288] Red solid hexagons in Figure 7.2e represent the atomic distribution of tungsten in WSe_2 crystal, which reflects a three-fold rotational symmetry in 2H phase. Recent studies have shown that the edge sites of 2H-phase TMDC are catalytically active.[282, 298] In this study, during the MBE growth of WSe_2, a large number of edge sites are spontaneously formed, as shown in Supplementary Figure 7.8, which can provide catalytic functions.[298-300] Figure 7.2f reveals the layer-by-layer growth of WSe_2 films. The interlayer spacing is determined to be ~0.65 nm for one WSe_2 layer, which is consistent with theoretical calculation and other experimental reports.[67, 289, 291, 302] The atomically smooth layer structure further confirms the vdW epitaxy of WSe_2 grown on amorphous SiO_x substrates by MBE. Light absorption property of WSe_2, as presented in Supplementary Figure 7.9 and 7.10, was examined by ultraviolet-visible spectrophotometry (UV-Vis).

7.2.4 Photocatalytic overall pure water splitting

Previous studies have suggested that the band edges of monolayer WSe_2 straddles water redox reactions,[67, 292-294] schematically illustrated in Figure 7.3a. However, it has remained unknown if monolayer WSe_2 possesses the capacity to spontaneously drive proton reduction and water oxidation under sunlight illumination. In this regard, we first performed H_2 and O_2 evolution half-reactions using sacrificial reagents CH_3OH and $AgNO_3$, respectively, shown in Figure 7.3b,c. For the H_2 evolution half-reaction, CH_3OH is sacrificially oxidized by photo-generated holes in the valence band, and photo-generated electrons can reduce H^+ to H_2 at the catalytic edge sites of monolayer WSe_2.

The continuous H_2 evolution under light illumination demonstrates the catalytic capability of proton reduction for monolayer WSe_2 without any other co-catalysts. For O_2 evolution half-reaction, H_2O molecule is oxidized to produce O_2 gas while the photo-excited electrons reduce Ag^+ to Ag. The continuous O_2 generation shown in Figure 7.3c confirms the catalytic ability of water oxidation for monolayer WSe_2. In these studies, we have performed detailed control experiments on SiO_x/Si wafer without the presence of monolayer WSe_2, no H_2 or O_2 production was measured within the experimental error. The continuous evolution of H_2 and O_2, shown in Figure 7.3b,c, therefore suggests that the conduction and valence band edges of monolayer WSe_2 meet the thermodynamic and kinetic requirements for solar water splitting. This is somewhat surprising, given the relatively narrow energy bandgap (~1.65 eV) of monolayer WSe_2 and small overpotential for proton reduction (~0.1 eV) and water oxidation (~0.3 eV), shown in Figure 7.3a. However, in monolayer WSe_2 photocatalyst, charge carrier generation via photoexcitation and catalytic reaction take place approximately at the same location. As such, photoexcited high-energy electrons and holes can possibly drive proton reduction and water oxidation before cooling to excitons. The resulting hot carrier effect can significantly enhance the photocatalytic activity, which has been reported previously.[313-316] In addition, being in close proximity for the key steps in water splitting reaction, including photoexcitation, charge carrier generation and extraction, and catalytic reaction may enhance the thermodynamic and kinetic coupling of sequential reactions at the nanoscale, which has been a topic being intensively investigated.[317-319]

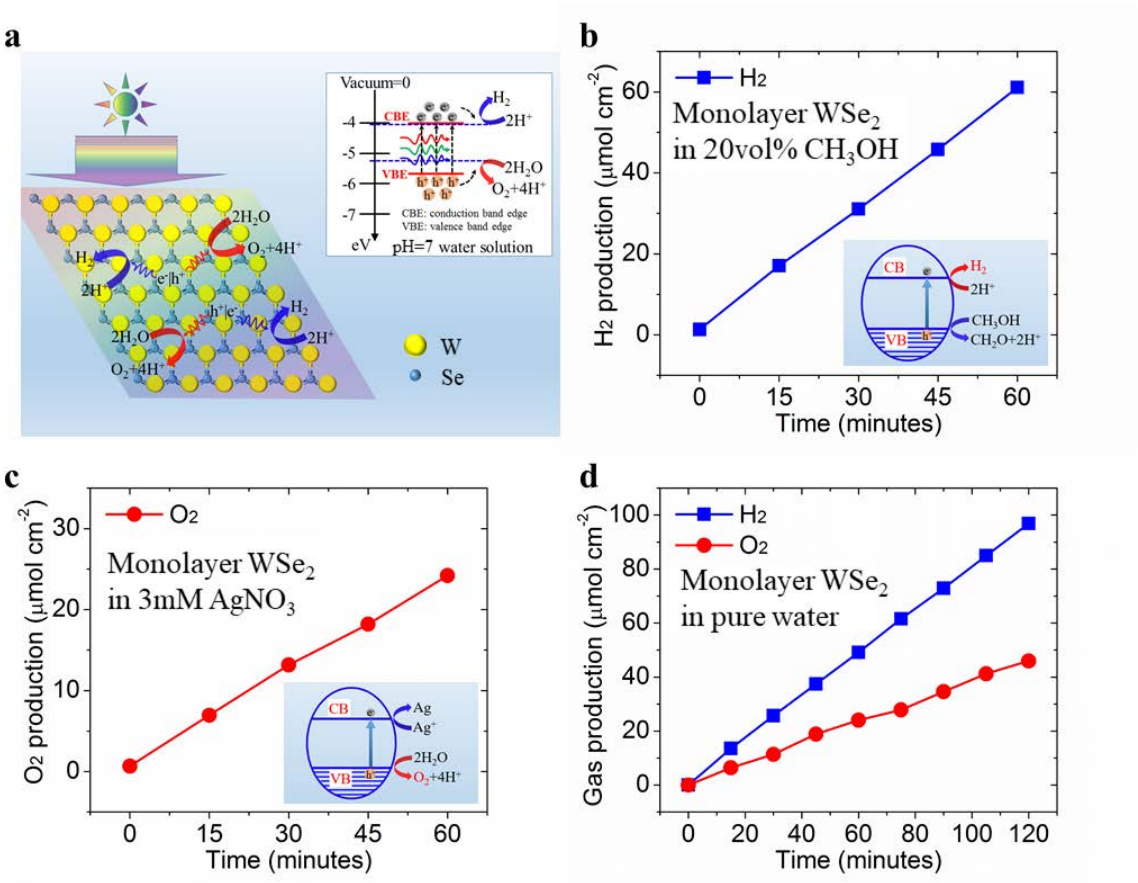

Figure 7.3 Solar water splitting measurements of MBE-grown multi-functional monolayer WSe_2 photocatalyst. (a) Schematic illustration of overall water splitting reaction on monolayer WSe_2 without incorporating any co-catalyst. Inset: conduction and valence band edge positions vs. water reduction and water oxidation reactions in pH=7 water solution. (b) H_2 and (c) O_2 evolution half reactions in the presence of sacrificial reagents, methanol and silver nitrate solutions, respectively, over monolayer WSe_2 under a 300 W full arc xenon lamp illumination. (d) Overall photocatalytic water splitting on monolayer WSe_2 under a 300 W xenon lamp irradiation with an AM 1.5G optical filter. No degradation of the photocatalytic activity was observed during the course of the reaction.

We have subsequently investigated overall solar water splitting on monolayer WSe_2 in pure water (see Section 7.4.3). Shown in Figure 7.3d, the H_2/O_2 evolution ratio is nearly stoichiometric, in the range of 1.95-2.1, confirming the reaction is direct water splitting. H_2 generation rate is measured to be ~48.4 μmol h^{-1} cm^{-2} corresponding to ~0.145% solar-to-hydrogen (STH) conversion efficiency and ~12.3% absorbed photon conversion efficiency (APCE). Detailed calculations are shown in Section 7.5.2. It is noticed that the photon-to-electron conversion efficiency may be limited by non-radiative recombination, due to the presence of defects.[320, 321] The reported solar-to-hydrogen conversion efficiency of ~0.145% on monolayer WSe_2 is compared favorably with the

maximum power conversion efficiency (~0.2%) of WSe_2-$MoSe_2$ and WSe_2-WSe_2 p-n junctions reported previously.[302, 311] The turnover number, defined as the ratio of the total amount of gas evolved (143 μmol cm^{-2} for H_2 and O_2) to the amount of WSe_2 photocatalyst material (1.75×10^{-3} μmol cm^{-2}), exceeded 80,000 during the course of ~2 h of pure water splitting. We have further investigated the variation of STH efficiency for overall pure water splitting on monolayer WSe_2 as a function of light intensity. Shown in Supplementary Figure 7.11, STH efficiency showed an increasing trend with increasing light intensity, possibly due to the reduced nonradiative recombination at high carrier densities. Similar trends have also been observed in overall pure water splitting on nanowire structures.[128] Finally, when normalized by the volume and mass of the WSe_2 photocatalyst material, the H_2 production rates are estimated to be ~18,370 L h^{-1} cm^{-3} and 1,972 L h^{-1} g^{-1}, respectively, shown in Supplementary Figure 7.12, which are more than 50 times higher compared to previously best reported photocatalyst (1.6 L h^{-1} g^{-1} under 100 mW cm^{-2} light) for CoO nanoparticles.[7] As shown in Supplementary Figure 7.13, similar photocatalytic results were observed for monolayer WSe_2 grown on sapphire substrate. In these studies, careful control experiments were performed on both SiO_x/Si and sapphire without the presence of monolayer WSe_2, which did not show any H_2 or O_2 evolution. In addition, Rh/Cr_2O_3/CoO_x nanoparticles as cocatalysts did not significantly improve the photocatalytic performance of monolayer WSe_2, which could be partly due to the light blocking effect of the co-catalysts. Illustrated in Supplementary Figure 7.13, we have also performed overall water splitting experiments on 2ML and 3ML WSe_2 samples, which, however, exhibit negligible photocatalytic activity, possibly due unsuited energy band alignment for overall water splitting with increasing thicknesses. Photocatalytic stability of 1ML WSe_2 samples for overall pure water splitting was further studied. There is no significant change of both H_2 and O_2 gas production over 8 hours, shown in Supplementary Figure 7.14, which suggests that monolayer WSe_2 exhibit a high level of stability. In addition, Raman spectra of 1ML WSe_2 sample before and after pure water splitting experiments were conducted, as shown in Supplementary Figure 7.15, which are nearly identical, indicating monolayer WSe_2 was stable during pure water splitting experiments. As listed in Supplementary Table 7.1, the photocatalytic performance of 1ML WSe_2 was further compared to some previously reported

semiconductors for pure water splitting experiments. It is seen that the normalized H_2 evolution rate (L h^{-1} g^{-1}) is orders of magnitude higher than previously reported values, showing the extraordinary potential of monolayer materials for solar fuel production.

7.3 Materials and Methods

7.3.1 Molecular beam epitaxial growth

WSe_2 monolayer, bilayer, and trilayer samples were grown on 250 nm SiO_x/Si substrates using a Veeco GENxplor MBE system. Prior to loading into the MBE chamber, SiO_x/Si substrates were first cleaned using acetone, methanol, and deionized water. During the growth of WSe_2, the substrate temperature was kept at ~400 ºC. A PBN effusion cell and an e-bean evaporator are used for the thermal evaporation of Se and W sources, respectively. Se flux beam equivalent pressure was measured to be ~3.5×10^{-7} Torr; and W deposition rate was ~0.16 Å min^{-1}. The growth rate was estimated to be ~0.7 Å min^{-1} and it took ~11 minutes to synthesize one monolayer. Low substrate temperature and high selenium flux are chosen to ensure that tungsten atoms can be selenidized thoroughly. After growth with a desired thickness, substrate temperature was raised to 650 ºC for 10-minute annealing with continuous Se flux.

7.3.2 Characterization techniques

Reflection high-energy electron diffraction (RHEED, Staib Instruments) was used to monitor the layer-by-layer growth of WSe_2 nanostructures in situ. Beam energy and filament heating current was set to 13.5 keV and 1.5 A, respectively. Micro-PL and micro-Raman studies were conducted using Renishaw inVia confocal Raman microscope with a 514 nm argon laser. The stoichiometric analysis was performed by X-ray photoelectron spectroscope (XPS, Thermo Scientific K-Alpha) with Al- Al-Kα monochromatic source (hν = 1,486.6 eV) with a spot size of 400 µm. The microstructure and morphology were characterized by optical microscope (Olympus MX40), atomic force microscope (AFM, Bruker Multimode), and transmission electron microscope (TEM, FEI Tecnai G^2 F20). TEM operated at 200 kV with a point resolution of 0.25 nm with a built-in EDX equipment (Oxford Instruments).

PMMA-assisted transfer method was used to prepare samples for TEM imaging. PMMA supporting layer for handling WSe_2 film was first spin-coated on top of WSe_2 sample on SiO_x/Si substrates at 3000 rpm for 30 seconds, followed by a curing process at 160 ^oC for 10 minutes. PMMA-coated WSe_2 sample was then diced into small pieces and immersed into 1 M KOH solution. After one hour, KOH solution etched SiO_x sublayer away making PMMA/WSe_2 film peel off from substrate and float on etchant surface. Subsequently, the detached PMMA/WSe_2 film was transferred into deionized water to remove etchant residues for several times. A TEM grid, or other substrates, was used to scoop it out from water surface. Then PMMA/WSe_2 film on new substrate was baked at 65 ^oC for two hours to enhance the adhesion. Finally, PMMA supporting layer was removed in acetone solution.

7.3.3 Solar water splitting measurements

WSe_2 monolayer samples were placed in a quartz chamber using polytetrafluoroethylene holders. 65 ml DI-water was added as reactant that had been pre-purged with argon gas for 30 minutes to remove the dissolved gases. Afterwards, the chamber was sealed with a transparent quartz cover by pumping down for 10 minutes. Ahead of water splitting reaction, 1 ml inside gas was injected into a gas chromatograph machine (GC, Shimazdu GC-8A) for vacuum configuration. Then solar spectra (~2200 mW cm^{-2}) from Xenon lamp with AM 1.5G filter was irradiated onto WSe_2 sample through the quartz lid, driving solar water splitting reactions on the surface of WSe_2 monolayer. After every 15 minutes, gas production from water splitting was analyzed by injecting 1 ml gas sampling into GC using an SGE syringe with valves. For half reaction experiments with sacrificial reagents, 13 ml CH_3OH with 52 ml DI-water and 65 ml 3 mM $AgNO_3$ solutions were added, respectively, for water reduction reaction with H_2 generation and water oxidation reaction with O_2 evolution.

7.4 Supporting Information

7.4.1 Supplementary figures

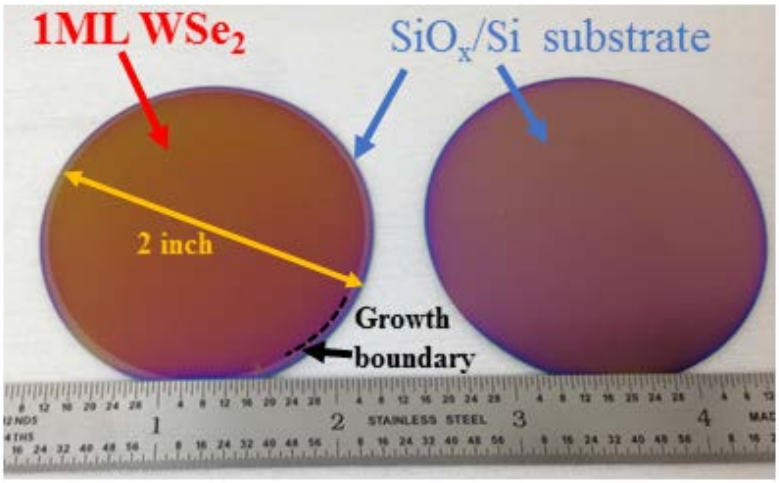

Figure 7.4 Optical image of bare SiO_x/Si substrate and as-grown monolayer WSe_2 sample which covers the two-inch substrate continuously.

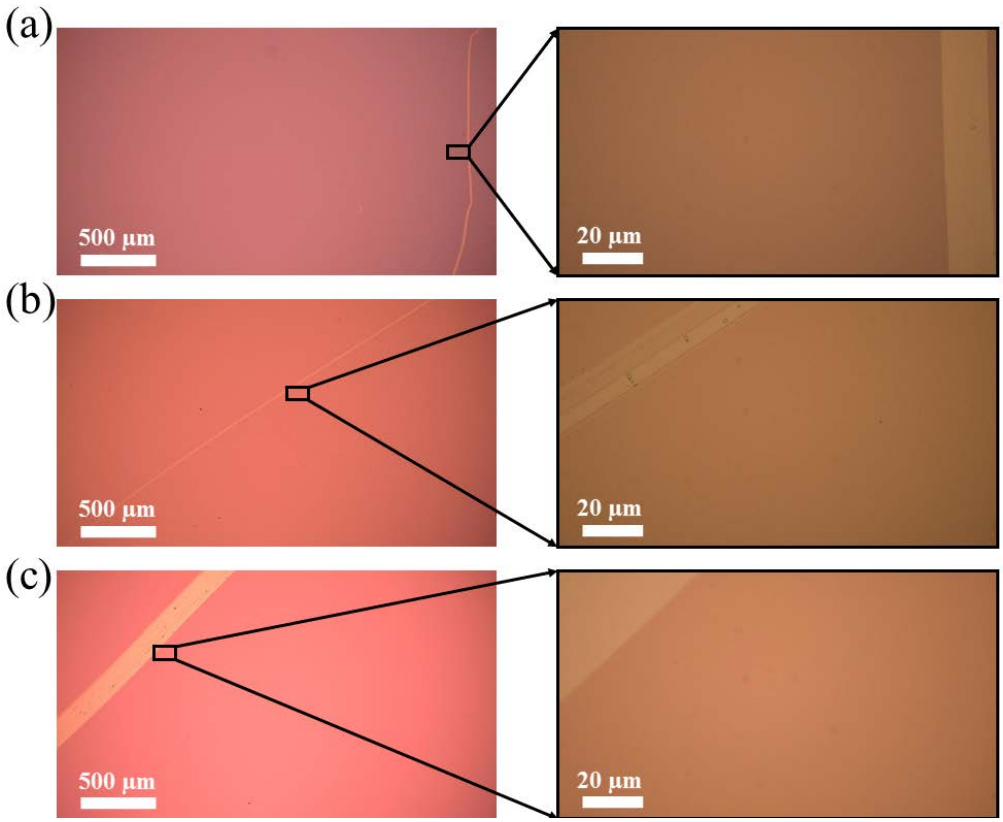

Figure 7.5 Optical microscopy images of WSe_2 films on SiO_x/Si substrates. (a) 3 ML WSe_2, (b) 2 ML WSe_2, and (c) 1 ML WSe_2. Part of the WSe_2 material was removed intentionally to expose SiO_x surface. Optical microscopy images of

WSe_2 2D films grown on SiO_x templates are shown in Figure 7.5. Note that some WSe_2 materials were removed intentionally to expose SiO_x surface for easy focus and better contrast. Except the intentionally exposed SiO_x surfaces, there is no discontinuity observed in WSe_2 samples, demonstrating large-area WSe_2 growth across the entire wafer. Moreover, the uniform color shown in the optical microscopy images also indicates the excellent uniformity of WSe_2 samples.

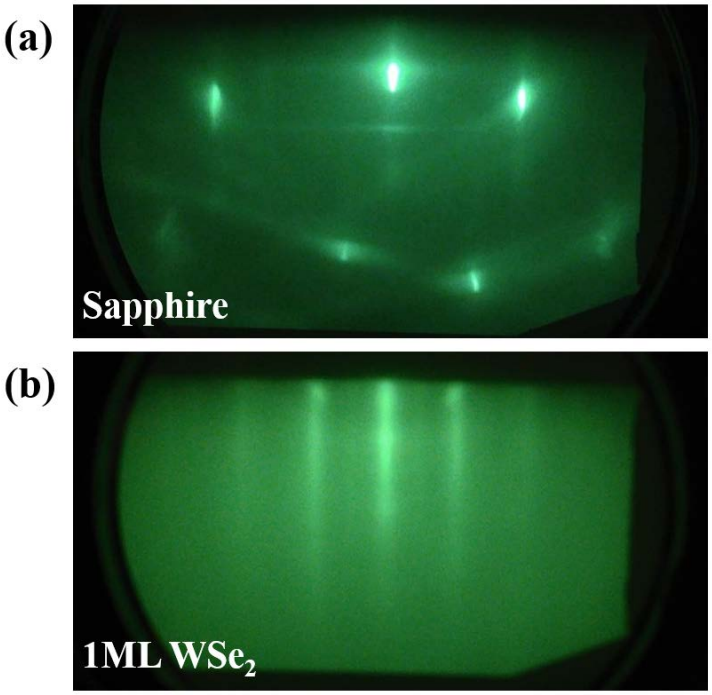

Figure 7.6 RHEED patterns of (a) sapphire substrate and (b) monolayer WSe_2.

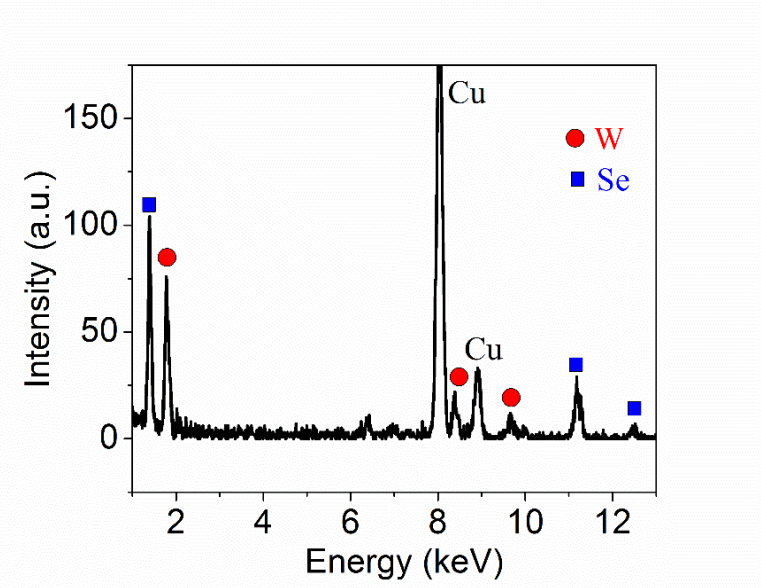

Figure 7.7 EDX spectrum of monolayer WSe_2 transferred onto copper grid.

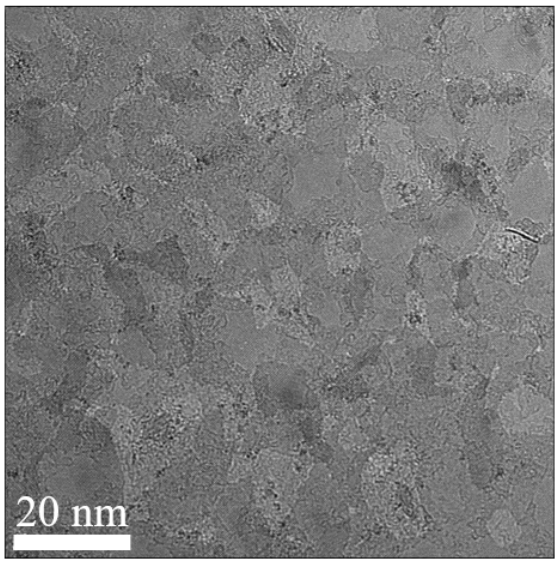

Figure 7.8 Low-magnification TEM imaging of WSe_2.

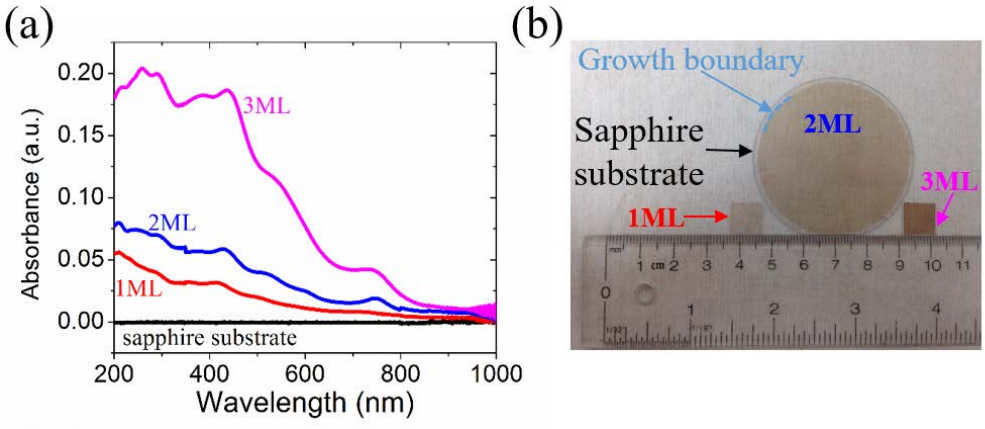

Figure 7.9 (a) UV-Vis transmission measurements of 1-3 ML WSe_2 samples. (b) Transparency comparison of 1-3 ML WSe_2 samples besides a regular ruler.

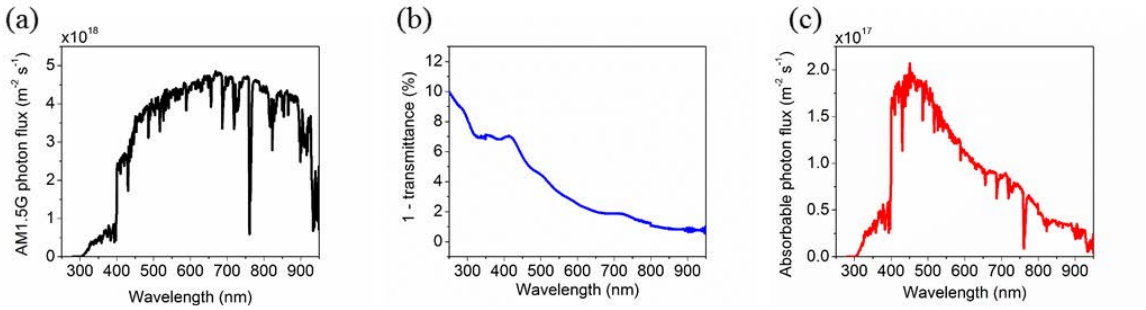

Figure 7.10 Absorption property of monolayer WSe_2 under standard AM 1.5G irradiation. (a) Photon flux distribution of AM 1.5G spectra. (b) The absorption properties of monolayer WSe_2 sample for photons of different wavelengths. (c) Photon absorption property of monolayer WSe_2 sample for AM 1.5G spectrum.

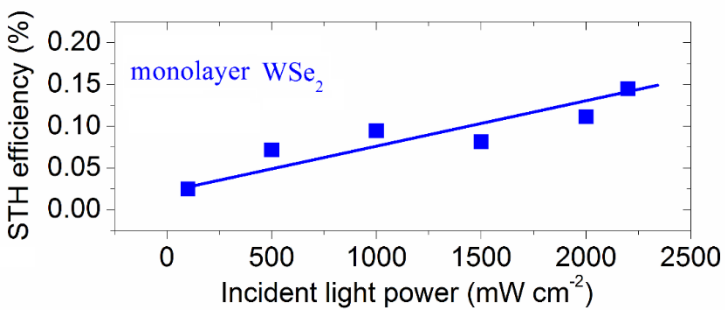

Figure 7.11 Solar-to-hydrogen conversion efficiency of pure water splitting on monolayer WSe_2 under AM 1.5G illumination of varied incident intensity. (The solid line is a guide to the eye.)

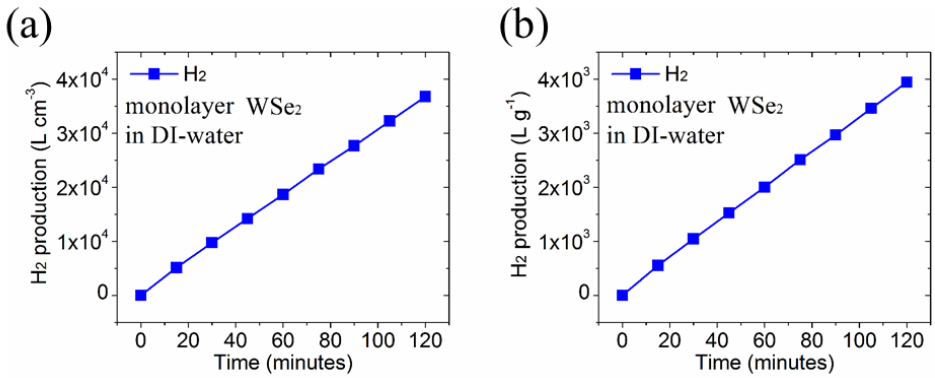

Figure 7.12 Normalized hydrogen production of water splitting on monolayer WSe_2 sample by the volume (a) and mass (b) of WSe_2 photocatalyst, based on the results shown in Figure 7.3d.

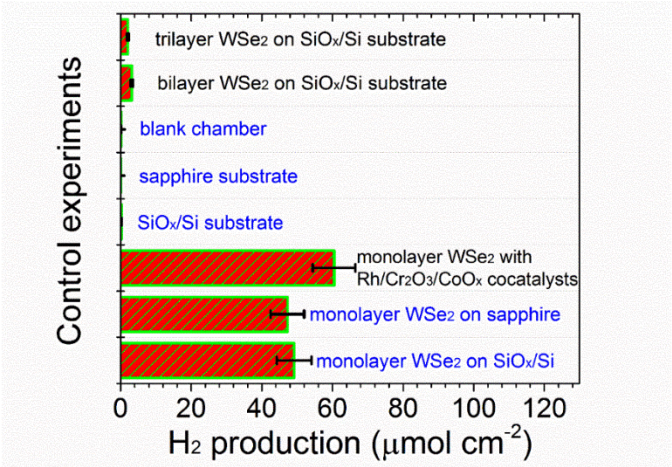

Figure 7.13 Summary of the amount of hydrogen produced after one hour solar water splitting measured under identical condition for different samples, including monolayer WSe_2 on SiO_x/Si substrate, monolayer WSe_2 on sapphire substrate, monolayer WSe_2 with $Rh/Cr_2O_3/CoO_x$ cocatalysts on SiO_x/Si substrate, bare SiO_x/Si substrate, bare sapphire substrate, blank chamber without WSe_2 or substrate, bilayer WSe_2 on SiO_x/Si substrate, and trilayer WSe_2 on SiO_x/Si substrate.

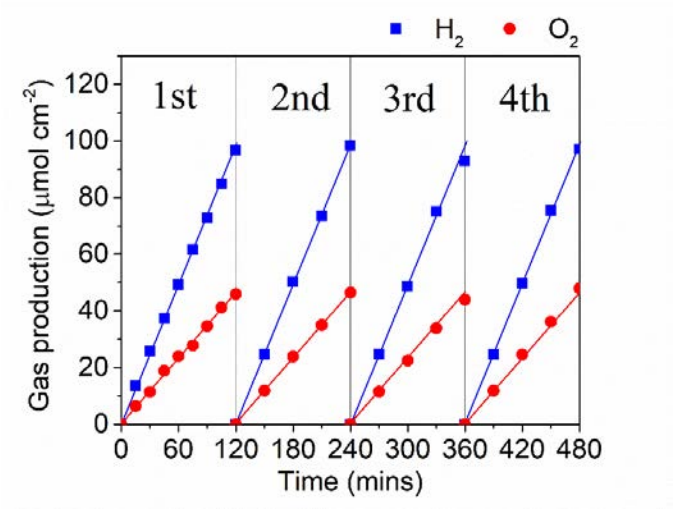

Figure 7.14 H_2 and O_2 evolution measured during repeated cycles of overall pure water splitting on monolayer WSe_2 samples.

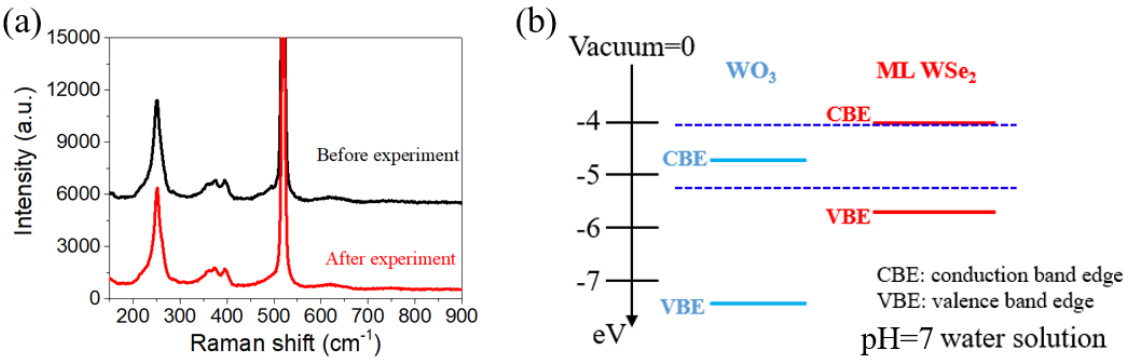

Figure 7.15 (a) Raman spectra of monolayer WSe_2 sample before (black) and after (red) solar water splitting experiment. There is no additional peak introduced after the experiment indicating WSe_2 was not oxidized to WO_3. (b) Illustration of the conduction band edge (CBE) and valence band edge (VBE) of WO_3 and monolayer WSe_2 together with water redox reactions (dash lines) in pH=7 water solution.

7.4.2 Supplementary notes

7.4.2.1 Light absorption of monolayer WSe_2

Light absorption properties of 1-3 ML WSe_2, as presented in Figure 7.9a, were examined by ultraviolet-visible (UV-Vis, Agilent Cary 5000) spectrophotometry with an incident light of 200~1000 nm wavelength. Absorption peaks in 600-800 nm range represent band edge excitons while others at higher energy correspond to interband absorption to higher unoccupied orbitals. The ~97% transparency (see the calculation in

Section 7.5.2.1) of monolayer WSe_2 makes it attractive for semi-transparent photovoltaic applications.[311, 322] Due to strong exciton binding energy of WSe_2 monolayer, however, electron-hole pairs are difficult to separate which results in low photon-to-power conversion efficiency.[14, 286, 290, 323] Optical images of 1-3ML WSe_2 samples on polished sapphire substrates are presented in Figure 7.9b.

Light absorption property of monolayer WSe_2 was analyzed for AM1.5G irradiation, shown in Figure 7.10, in order to estimate the maximum hydrogen production and quantum efficiency of solar water splitting. Figure 7.10a provides the standard photon flux distribution of AM 1.5G spectrum.[324] Fig. S7b shows the absorption of photons with different wavelengths for monolayer WSe_2, which was derived from UV-Vis data of Figure 7.9a using Equation (7-1) following Beer-Lambert law.[50] Then the absorption property of WSe_2 monolayer under AM 1.5G spectrum is determined by multiplying them together, as shown in Figure 7.10c, where the overall absorption percentage is estimated to be ~2.51% using Equation (7-2).

$$\text{Absorption } (100\%) = 1 - transmittance = 1 - \ 10^{-absorbance} \tag{7-1}$$

$$\text{Absorption of AM1.5G} = \frac{\int photon\ flux\ absorbed\ by\ WSe_2\ monolayer}{\int incident\ photon\ flux} \tag{7-2}$$

7.4.2.2 Solar-to-hydrogen conversion efficiency

Solar-to-hydrogen (STH) conversion efficiency is calculated by Equation (7-3) using the Gibbs free energy (237 kJ mol^{-1}) of H_2.

$$\text{STH} = \left[\frac{H_2\ generation\ rate\ (\mu mol\ h^{-1}\ cm^{-2}) \times 237\ kJ\ mol^{-1}}{incident\ solar\ power\ (mW\ cm^{-2}) \times time\ (3600\ s\ h^{-1})}\right]_{AM1.5G} \tag{7-3}$$

Using Equation (7-4) and Equation (7-5), absorbed photon conversion efficiency (APCE) and apparent quantum efficiency (AQE) were determined to be ~12.3% and ~0.31%, respectively.

$$\text{APCE} = \left[\frac{\#\ of\ produced\ H_2\ molecules \times 2}{\#\ of\ absorbed\ incident\ photons}\right]_{AM1.5G} \tag{7-4}$$

$$\text{AQE} = \left[\frac{\#\ of\ produced\ H_2\ molecules \times 2}{\#\ of\ total\ incident\ photons}\right]_{AM1.5G} \tag{7-5}$$

Solar water splitting performance of monolayer WSe_2 photocatalytic cell was further investigated, shown in Supplementary Figure 7.11, with varied illumination intensity from 100 to 2200 mW cm^{-2}. STH efficiency increases with higher incident light power density, possibly due to saturation of recombination sites at high carrier densities.

7.4.2.3 Raman study after experiments

Raman scattering spectra were conducted before and after the experiment, as shown in Supplementary Figure 7.15a. Previous studies[325] reported that the oxidation of WSe_2 to WO_3 would eliminate the main Raman peak at ~250 cm^{-1} of WSe_2 and introduce a new Raman peak at ~805 cm^{-1} for WO_3. However, in our work, we did not observe any Raman peak of WO_3 after the experiments. In addition, the band edge position [10,11] of WO_3,[326, 327] Supplementary Figure 7.15b, makes itself unsuitable for pure water splitting in pH=7 solution since it cannot straddle the water reduction reaction. This will also eliminate the possibility of overall water splitting occurring on WO_3 under light. If WSe_2 was oxidized to WO_3, the photocatalytic capability would be rapidly degraded and the H_2/O_2 production rate would be significantly reduced. Our studies suggest that the oxidation of WSe_2 to WO_3 is negligible during the reaction.

7.4.3 Supplementary table

Table 7.1 Photocatalytic performance of 1ML WSe_2 sample used in this work compared with some typical semiconductors for overall pure water splitting.

Materials	APCE %	AQE %	Turn over number	H_2 evolution rate $L\ h^{-1}\ g^{-1}$	STH %	Reference
1ML WSe_2	**12.3**	**0.31**	**>80,000**	**1,972**	**0.145**	**This work**
CoO nanoparticles	N/A	N/A	N/A	1.6	5	Nat. Nanotechnol., 2014, 9, 69-73.
TiO_2/Si nanowires	N/A	N/A	N/A	0.021	0.12	Nano Lett., 2013, 13, 2989-2992.
Rh/Cr_2O_3 loaded GaN nanowires	N/A	N/A	10,000	96	N/A	Nat. Commun., 2014, 5, 3825.
Rh/Cr_2O_3 loaded GaN/$In_{0.2}Ga_{0.8}N$ nanowires	68.5	12.3	N/A	124	1.8	Nat. Commun., 2015, 6, 7797.
Rh/Cr_2O_3 loaded GaN/$In_{0.22}Ga_{0.78}N$ nanosheet	N/A	19.93	N/A	195	3.3	Nat. Commun., 2018, 9, 1707.
Rh/Cr_2O_3 loaded $SrTiO_3$	N/A	30 at 360nm	7.7	0.67	N/A	J. Mater. Chem. A, 2016, 4, 3027-3033.

Rh/Cr_2O_3 loaded $SrTiO_3$:La,Rh/C/$BiVO_4$: Mo sheet	N/A	19 at 419nm	N/A	N/A	1.2	J. Am. Chem. Soc., 2017, 139, 1675-1683.
NRGO-MoS_2	N/A	N/A	N/A	3.17	N/A	Angew. Chem. Int. Ed., 2013, 52, 13057-13061.
MoS_2/G-CdS	N/A	28.1 at 420nm	N/A	0.04	N/A	ACS Nano, 2014, 8, 7078-7087.
Cu_2O/WSe_2/carbon foam	N/A	6.8 at 365nm	N/A	1.46	N/A	Adv. Energy Mater. 2016, 6, 1600510.
$ZnIn_2S_4$/2 %$MoSe_2$	N/A	21.39 at 420nm	N/A	0.06	N/A	ChemSusChem, 2017, 10, 4624-4631.
CdS/m-TiO_2/graphene	N/A	N/A	N/A	0.9	N/A	Nano Energy, 2018, 47, 8-17.
Al-doped $SrTiO_3$	N/A	5 at 380nm	N/A	0.94	0.4	Joule, 2018, 2, 509-520.
Ru–$SrTiO_3$:Rh/$BiVO_4$	N/A	1.29 at 435nm	N/A	N/A	0.028	Nano Lett. 2018, 18, 805-810.
2D Black Phosphorus/$BiVO_4$	N/A	0.89 at 420nm	N/A	3.6E-3	N/A	Angew. Chem. Int. Ed., 2018, 57, 2160-2164.
TiO_2 single crystal	N/A	N/A	N/A	1.36	N/A	Energy Environ. Sci. 2018, Advance Article,

7.5 Summary

In this chapter, we have demonstrated the multifunctionality of monolayer WSe_2 in solar water splitting, including extraordinary capacities for efficient light harvesting, water oxidation, and proton reduction. The absorbed photon conversion efficiency exceeds 12% for a single monolayer WSe_2. We have shown that wafer-scale WSe_2 monolayer sample could be directly grow on amorphous substrates by MBE with precise layer control and can exhibit superb optical properties and catalytic performance. This work provides a viable strategy for wafer-scale synthesis of multi-functional photocatalysts for the development of efficient, low cost, and scalable solar fuel devices and systems.

Chapter VIII

Conclusion and Future Work

8.1 Summary of Present Work

The dissertation presented here focuses on the demonstration of high efficiency and stable solar water splitting on low-dimensional III-nitride and TMDC nanostructures grown by molecular beam epitaxial (MBE) method. Reaction mechanisms of solar water splitting on semiconductors are first described, including the fundamental requirements on energy band structures for photocatalytic and photoelectrochemical water splitting. The ideal attributes of semiconductor photocatalysts and photoelectrodes are further discussed, which include relatively large energy gaps straddling water redox reaction potentials, strong light absorption, rapid carrier extraction, reduced surface recombination, efficient catalytic property, and chemical stability. In this work, we demonstrate high efficiency photocatalytic overall water splitting on monolithic multi-band InGaN nanowires, stable water reduction reaction and unassisted solar water splitting on p-InGaN nanowire tunnel junction photocathode, multi-functional GaN protection nanostructure for high efficiency and stable unassisted solar water splitting on $GaInP_2$/GaAs/Ge triple-junction structure, and wafer-scale synthesis of monolayer WSe_2 on amorphous SiO_x/Si substrates as a multifunctional photocatalyst for overall solar water splitting.

Described in Chapter III, we have investigated monolithically integrated quadruple-band InGaN nanowire arrays for photocatalytic overall water splitting, which achieves a record STH efficiency of ~5.2%. To our best knowledge, it is the first time for metal nitride nanostructures demonstrating such high efficiency for one-step solar water

splitting. The quadruple-band arrays of $In_{0.35}Ga_{0.65}N/In_{0.27}Ga_{0.73}N/In_{0.20}Ga_{0.80}N/GaN$ are integrated on a nonplanar silicon wafer for enhanced light absorption. Moreover, doping effects on photocatalytic performance by varying the Mg doping cell temperature have been investigated and, simultaneously, a polarized doping gradient leads to the presence of lateral built-in electric field for metal nitride nanowires, which promotes efficient charge carrier separation and extraction for water redox reactions. Several important factors are also discussed to further improve the STH efficiency >10%: (1) optimization of the design by placing large energy gap materials on top, (2) optimization of the deposition of co-catalyst particles, (3) integration of such nanowire photocatalysts on reflective substrate surface to further enhance light absorption, and (4) minimization of surface recombination by surface treatment or passivation layers.

In Chapter IV we report on the fabrication and photoelectrochemical performance of a monolithically integrated p-InGaN tunnel junction nanowire photocathode on a nonplanar Si wafer with relatively high indium composition (up to ~51%), which can drive relatively efficient and stable solar-to-hydrogen conversion. The nanowire photocathode exhibits a photocurrent density of 12.3 mA cm^{-2} at 0 V vs. RHE and an onset potential of 0.79 V vs. RHE under AM 1.5G one-sun illumination. The maximum applied bias photon-to-current efficiency reaches 4% at ~0.52 V vs. RHE, which is one order of magnitude higher than the previously reported values for III-nitride photocathodes. Significantly, no performance degradation was measured for over 30 hours solar water splitting with a steady photocurrent density ~12 mA cm^{-2} without using any extra surface protection, which may be attributed to the spontaneous formation of N-terminated surfaces of InGaN nanowires to protect against photocorrosion. The improved performance of p-InGaN tunnel junction nanowire photocathode, compared to previously reported InGaN photocathodes, is attributed to following factors: i) strongly enhanced light absorption for nanowire arrays grown on non-planar Si wafer; ii) crystalline nanowires with efficient p-type dopant incorporation; and iii) nanowire tunnel junctions that facilitate efficient collection of photo-excited holes and serve as an electron blocking layer to enhance the extraction of photo-excited electrons.

In Chapter V we have demonstrated a single junction $In_{0.25}Ga_{0.75}N$ nanowire photocathode that can drive relatively efficient and stable unassisted water splitting. A true STH efficiency of 3.4% is measured at 0 V vs. Pt counter electrode in 0.5 M H_2SO_4 electrolyte under AM 1.5G one-sun illumination. The InGaN nanowire tunnel junction photocathode can operate efficiently for ~300 hours without any extra surface protection, with the amount of solar energy converted to H_2 per unit area being nearly 10-fold higher than previously reported semiconductor photoelectrodes in unassisted solar water splitting. Beyond this demonstration, such InGaN nanowire tunnel junction photocathode can be integrated with a narrow bandgap junction, *e.g.* Si or GaAs, to form a double-junction tandem photoelectrode to achieve further improved efficiency for long-term stable solar water splitting. The realization of a single junction InGaN photocathode with relatively high efficiency and long-term stability is attributed to the following factors: i) High crystallinity and significantly reduced dislocations for nanowire structures grown directly on Si; ii) Rapid separation of photo-generated charge carriers by optimizing the nanowire surface band bending through controlled Mg dopant incorporation; iii) Efficient collection of photo-generated holes with the use of tunnel junction; iv) Light trapping effect of the nanowire morphology for enhanced light absorption; And v) N-terminated surfaces that can protect against photo-corrosion.

In Chapter VI we report the GaN/3J photocathode for high efficiency, stable solar water splitting by using a multi-functional GaN surface protection nanostructure. Measured in the two-electrode configuration, such monolithic GaN/3J photocathodes can exhibit a true STH efficiency of ~12.6% at zero bias. Moreover, long term stability has been demonstrated on GaN protected 3J photocathode for 80 hours in three-electrode configuration and 57 hours in two-electrode configuration at zero bias with an STH efficiency >10%, which is the best reported stability for high efficiency multi-junction semiconductor photocathodes. The multifunctional GaN nanostructure not only significantly reduces the charge transfer resistance at semiconductor/electrolyte interface but also protects buried III-V materials against corrosion. Such multi-functional GaN nanostructure provides a new pathway to protect conventionally efficient, but unstable photoelectrodes to achieve both efficient and stable operation for unassisted solar water splitting at scale.

In Chapter VII we have demonstrated the multi-functionality of monolayer WSe_2 in solar water splitting, including extraordinary capacities for efficient light harvesting, water oxidation, and proton reduction. Wafer-scale monolayer WSe_2 can be synthesized by van de Waals epitaxial growth on large area amorphous SiO_x substrates using MBE. We have demonstrated, for the first time, the bi-facial catalytic property of monolayer WSe_2 in overall solar water splitting, for efficient water reduction reaction and water oxidation reaction. The absorbed-photon-conversion-efficiency exceeds 12% for a single monolayer WSe_2. This work provides a viable strategy for wafer-scale synthesis of multi-functional photocatalysts for the development of efficient, low cost, and scalable solar fuel devices and systems.

8.2 Future Work

8.2.1 Monolithic InGaN/Si tandem structure for unassisted solar water splitting with an STH efficiency >15%

As described in Chapter IV and Chapter V, we have demonstrated a relatively efficient InGaN nanowire photocathode for solar water reduction and unassisted solar water splitting, which is monolithically integrated on industry available Si wafers through a tunnel junction nanostructure. However, the overall efficiency of such single-junction InGaN photocathode is still below 5%. Z-scheme using double-junction structure has been proposed and intensively studied to achieve high-efficiency unassisted solar water splitting.[62, 185, 186] A theoretical solar-to-hydrogen conversion efficiency ~27% has been predicted for a double-junction photoelectrode consisting of a 1.70 eV top junction and a 1.05 eV bottom junction under AM 1.5G one-sun illumination.[17] While Si, given its narrow energy bandgap (~1.1 eV), scalable manufacturing, and mature fabrication process, is ideally suited for the bottom light absorber, it has remained extremely challenging to identify a practical top light absorber that is stable in photoelectrochemical reaction and can be monolithically integrated with Si. This dissertation demonstrates the stable performance of InGaN nanowires, which can be integrated on the bottom Si p-n junction to form nearly ideal, current matching 1.8 eV/1.1 eV tandem structure for further improved efficiency (>15%), schematically demonstrated in Figure 8.1.

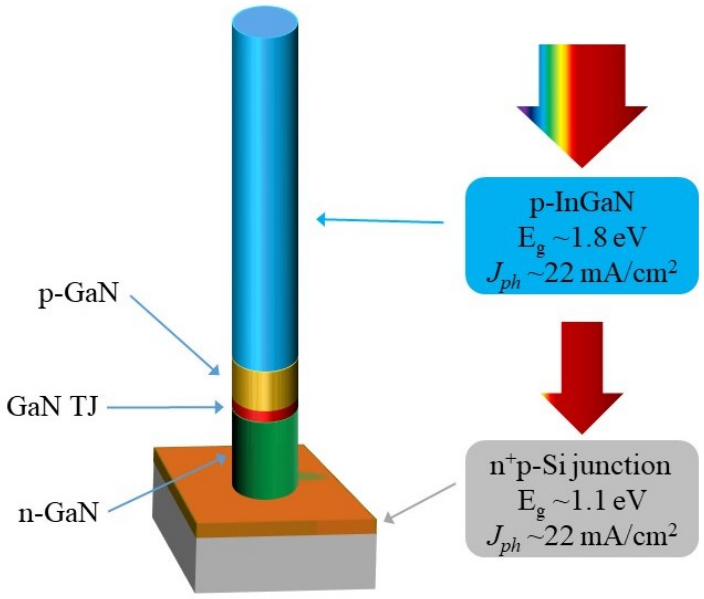

Figure 8.1 Schematic structure of the proposed p-InGaN/n$^+$p-Si tandem photocathode, which promises a solar-to-hydrogen conversion efficiency up to 30%.

8.2.2 Multifunctional GaN nanostructure protected GaInP/GaInAs double-junction photocathode for high efficiency and stable unassisted solar water splitting

Demonstrated in Chapter VI, the multi-functional GaN nanostructure is a novel surface passivation layer for protecting high efficiency III-V photocathode structures against corrosion. GaN passivated $GaInP_2$/GaAs/Ge triple-junction structure already demonstrates a zero-biased operation >50 hours with an STH efficiency >10% in two-electrode configuration, which is relatively stable compared to previously reported high efficiency III-V photocathodes with a limited stability <1 hour.[11, 17, 22] Therefore, it is possibly practical to utilize such GaN protection nanostructure to protect the previously-demonstrated GaInP/GaInAs double-junction photocathode showing an STH efficiency ~19%, schematically illustrated in Figure 8.2 and 8.3, for achieving relatively stable and high efficiency unassisted solar water splitting, with a potential STH efficiency >20%, which has been elusive for solar fuel conversion systems.

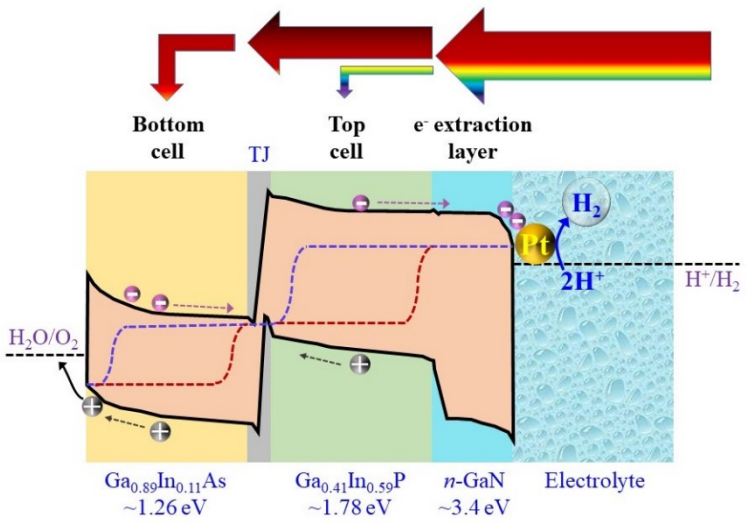

Figure 8.2 Schematic band diagram of GaN protected GaInP/GaInAs double-junction tandem structure as a high efficiency and stable photocathode for unassisted solar water splitting.

n^+-GaN	Protection	GaN protection
n-GaInP	Emitter	Top cell $Ga_{0.41}In_{0.59}P$ ~1.78 eV
p-GaInP	Base	
p^+-AlGaInP	BSF	
p^+-AlGaInP	TJ	Tunnel junction
n^+-GaInP	TJ	
n^+-GaInP	Window	Bottom cell $Ga_{0.89}In_{0.11}As$ ~1.26 eV
n-GaInAs	Emitter	
p-GaInAs	Base	
p^+-GaInP	BSF	
p^+-GaAs	Substrate	

Figure 8.3 Schematic layer structure of GaN protected GaInP/GaInAs double-junction tandem structure.

8.2.3 InGaN nanowire photocathode for carbon dioxide reduction

Recently, greenhouse effect has been an urgent crisis as the result of heavy fossil fuel consumption, with increased carbon dioxide (CO_2) emission and accumulation.[1, 2, 4] H_2 fuel converted from solar water splitting, as presented in this dissertation, is one method to reduce the consumption of fossil fuels; and another proposed strategy for solar fuel conversion is to convert CO_2 waste directly to some hydrocarbon chemical fuels, such as syngas (CO and H_2), methane (CH_4), formic acid (HCOOH), and methanol

(CH_3OH).[232, 328, 329] Since photo-excited electrons are simultaneously required to drive water reduction reaction and CO_2 reduction reaction, it is feasible to adopt the InGaN nanowire photocathode demonstrated in solar water splitting to perform the CO_2 reduction reaction, by simply providing CO_2 source into the experiment chamber. In addition, compared to the photocatalytic experiments, photoelectrochemical configuration offers the advantages of separated reactions on two electrodes, avoiding the reverse reaction to oxidize hydrocarbon fuels back to CO_2. Compared to conventional metal oxides for CO_2 reduction, InGaN has the tunable electronic band structure to produce various hydrocarbon fuels and to absorb nearly the entire solar spectrum. In addition, N-terminated InGaN nanowires have been demonstrated to be stable in harsh electrolyte environment, which will be critical for practical solar fuel conversion devices and systems. Schematically illustrated in Figure 8.4, we can propose the photoelectrochemical CO_2 reduction on InGaN nanowire photocathode, in electrolyte solutions saturated with CO_2 gas.

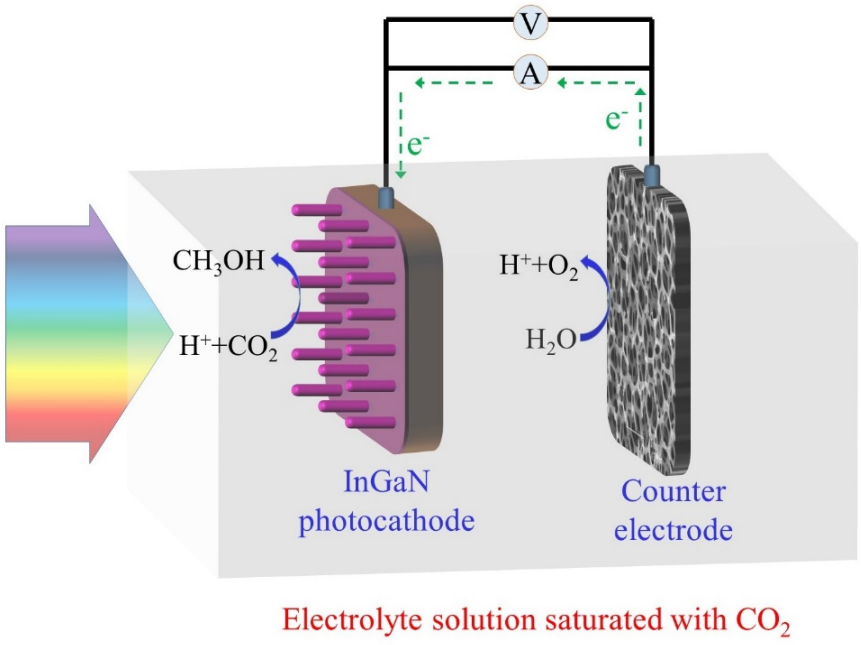

Figure 8.4 Schematic design for photoelectrochemical CO_2 reduction on InGaN nanowire photocathode.

BIBLIOGRAPHY

BIBLIOGRAPHY

[1] N. Armaroli, V. Balzani, The future of energy supply: Challenges and opportunities, *Angew. Chem. Int. Ed.*, 46 (2006) 52-66.

[2] F. Perera, Pollution from fossil-fuel combustion is the leading environmental threat to global pediatric health and equity: solutions exist, *Int. J. Environ. Res. Public Health*, 15 (2017) 16.

[3] M.G. Kibria, F.A. Chowdhury, S. Zhao, B. AlOtaibi, M.L. Trudeau, H. Guo, Z. Mi, Visible light-driven efficient overall water splitting using p-type metal-nitride nanowire arrays, *Nat. Commun.*, 6 (2015) 6797.

[4] M.G. Kibria, Z. Mi, Artificial photosynthesis using metal/nonmetal-nitride semiconductors: current status, prospects, and challenges, *J. Mater. Chem. A*, 4 (2016) 2801-2820.

[5] J. Juodkazytė, G. Seniutinas, B. Šebeka, I. Savickaja, T. Malinauskas, K. Badokas, K. Juodkazis, S. Juodkazis, Solar water splitting: Efficiency discussion, *Int. J. Hydrog. Energy*, 41 (2016) 11941-11948.

[6] A. Hussain, S.M. Arif, M. Aslam, Emerging renewable and sustainable energy technologies: State of the art, *Renew Sust. Energy Rev.*, 71 (2017) 12-28.

[7] L. Liao, Q. Zhang, Z. Su, Z. Zhao, Y. Wang, Y. Li, X. Lu, D. Wei, G. Feng, Q. Yu, X. Cai, J. Zhao, Z. Ren, H. Fang, F. Robles-Hernandez, S. Baldelli, J. Bao, Efficient solar water-splitting using a nanocrystalline CoO photocatalyst, *Nat. Nanotechnol.*, 9 (2014) 69-73.

[8] T. Hisatomi, H. Dotan, M. Stefik, K. Sivula, A. Rothschild, M. Grätzel, N. Mathews, Enhancement in the performance of ultrathin hematite photoanode for water splitting by an oxide underlayer, *Adv. Mater.*, 24 (2012) 2699-2702.

[9] S.U.M. Khan, M. Al-Shahry, W.B. Ingler, Efficient photochemical water splitting by a chemically modified n-TiO_2, *Science*, 297 (2002) 2243.

[10] J. Luo, L. Steier, M.-K. Son, M. Schreier, M.T. Mayer, M. Grätzel, Cu_2O nanowire photocathodes for efficient and durable solar water splitting, *Nano Lett.*, 16 (2016) 1848-1857.

[11] D. Kang, J.L. Young, H. Lim, W.E. Klein, H. Chen, Y. Xi, B. Gai, T.G. Deutsch, J. Yoon, Printed assemblies of GaAs photoelectrodes with decoupled optical and reactive interfaces for unassisted solar water splitting, *Nat. Energy*, 2 (2017) 17043.

[12] F. Ishizaka, Y. Hiraya, K. Tomioka, J. Motohisa, T. Fukui, Growth of all-wurtzite InP/AlInP core–multishell nanowire array, *Nano Lett.*, 17 (2017) 1350-1355.

[13] A. Standing, S. Assali, L. Gao, M.A. Verheijen, D. van Dam, Y. Cui, P.H.L. Notten, J.E.M. Haverkort, E.P.A.M. Bakkers, Efficient water reduction with gallium phosphide nanowires, Nature Communications, 6 (2015) 7824.
[14] L. Gao, Y. Cui, J. Wang, A. Cavalli, A. Standing, T.T.T. Vu, M.A. Verheijen, J.E.M. Haverkort, E.P.A.M. Bakkers, P.H.L. Notten, Photoelectrochemical hydrogen production on InP nanowire arrays with molybdenum sulfide electrocatalysts, *Nano Lett.*, 14 (2014) 3715-3719.
[15] O. Khaselev, J.A. Turner, A monolithic photovoltaic-photoelectrochemical device for hydrogen production via water splitting, *Science*, 280 (1998) 425.
[16] A. Kudo, Y. Miseki, Heterogeneous photocatalyst materials for water splitting, *Chem. Soc. Rev.*, 38 (2009) 253-278.
[17] J.L. Young, M.A. Steiner, H. Döscher, R.M. France, J.A. Turner, Todd G. Deutsch, Direct solar-to-hydrogen conversion via inverted metamorphic multi-junction semiconductor architectures, *Nat. Energy*, 2 (2017) 17028.
[18] S. Hu, M.R. Shaner, J.A. Beardslee, M. Lichterman, B.S. Brunschwig, N.S. Lewis, Amorphous TiO_2 coatings stabilize Si, GaAs, and GaP photoanodes for efficient water oxidation, *Science*, 344 (2014) 1005.
[19] S. Chu, S. Vanka, Y. Wang, J. Gim, Y. Wang, Y.-H. Ra, R. Hovden, H. Guo, I. Shih, Z. Mi, Solar water oxidation by an InGaN nanowire photoanode with a bandgap of 1.7 eV, *ACS Energy Lett.*, 3 (2018) 307-314.
[20] M. Gopalakrishnan, S. Gopalakrishnan, G.M. Bhalerao, K. Jeganathan, Multiband InGaN nanowires with enhanced visible photon absorption for efficient photoelectrochemical water splitting, *J. Power Sources*, 337 (2017) 130-136.
[21] M.G. Walter, E.L. Warren, J.R. McKone, S.W. Boettcher, Q. Mi, E.A. Santori, N.S. Lewis, Solar water splitting cells, *Chem. Rev.*, 110 (2010) 6446-6473.
[22] W.-H. Cheng, M.H. Richter, M.M. May, J. Ohlmann, D. Lackner, F. Dimroth, T. Hannappel, H.A. Atwater, H.-J. Lewerenz, Monolithic photoelectrochemical device for direct water splitting with 19% efficiency, *ACS Energy Lett.*, 3 (2018) 1795-1800.
[23] M.M. May, H.-J. Lewerenz, D. Lackner, F. Dimroth, T. Hannappel, Efficient direct solar-to-hydrogen conversion by in situ interface transformation of a tandem structure, *Nat. Commun.*, 6 (2015) 8286.
[24] M.G. Kibria, R. Qiao, W. Yang, I. Boukahil, X. Kong, F.A. Chowdhury, M.L. Trudeau, W. Ji, H. Guo, F.J. Himpsel, L. Vayssieres, Z. Mi, Atomic-scale origin of long-term stability and high performance of p-GaN nanowire arrays for photocatalytic overall pure water splitting, *Adv. Mater.*, 28 (2016) 8388-8397.
[25] S. Vanka, E. Arca, S. Cheng, K. Sun, G.A. Botton, G. Teeter, Z. Mi, High efficiency Si photocathode protected by multifunctional GaN nanostructures, *Nano Lett.*, 18 (2018) 6530-6537.
[26] X. Guan, F.A. Chowdhury, Y. Wang, N. Pant, S. Vanka, M.L. Trudeau, L. Guo, L. Vayssieres, Z. Mi, Making of an industry-friendly artificial photosynthesis device, *ACS Energy Lett.*, 3 (2018) 2230-2231.
[27] K. Takanabe, Photocatalytic water splitting: quantitative approaches toward photocatalyst by design, *ACS Catal.*, 7 (2017) 8006-8022.
[28] T. Su, Q. Shao, Z. Qin, Z. Guo, Z. Wu, Role of interfaces in two-dimensional photocatalyst for water splitting, *ACS Catal.*, 8 (2018) 2253-2276.

[29] Y. Li, Y.-L. Li, B. Sa, R. Ahuja, Review of two-dimensional materials for photocatalytic water splitting from a theoretical perspective, *Catal. Sci. Technol.*, 7 (2017) 545-559.
[30] M. Samadi, N. Sarikhani, M. Zirak, H. Zhang, H.-L. Zhang, A.Z. Moshfegh, Group 6 transition metal dichalcogenide nanomaterials: Synthesis, applications and future perspectives, *Nanoscale Horiz.*, 3 (2018) 90-204.
[31] Y. Wang, S. Zhao, Y. Wang, D.A. Laleyan, Y. Wu, B. Ouyang, P. Ou, J. Song, Z. Mi, Wafer-scale synthesis of monolayer WSe_2: A multi-functional photocatalyst for efficient overall pure water splitting, *Nano Energy*, 51 (2018) 54-60.
[32] Y. Inoue, Photocatalytic water splitting by RuO_2-loaded metal oxides and nitrides with d^0- and d^{10}- related electronic configurations, *Energy Environ. Sci.*, 2 (2009) 364-386.
[33] H. Ahmad, S.K. Kamarudin, L.J. Minggu, M. Kassim, Hydrogen from photo-catalytic water splitting process: A review, *Renew. Sust. Energy Rev.*, 43 (2015) 599-610.
[34] M.G. Kibria, H.P.T. Nguyen, K. Cui, S. Zhao, D. Liu, H. Guo, M.L. Trudeau, S. Paradis, A.-R. Hakima, Z. Mi, One-step overall water splitting under visible light using multiband InGaN/GaN nanowire heterostructures, *ACS Nano*, 7 (2013) 7886-7893.
[35] C. Sheng, L. Wei, Y. Yanfa, H. Thomas, S. Ishiang, W. Dunwei, M. Zetian, Roadmap on solar water splitting: Current status and future prospects, *Nano Futures*, 1 (2017) 022001.
[36] T. Hisatomi, J. Kubota, K. Domen, Recent advances in semiconductors for photocatalytic and photoelectrochemical water splitting, *Chem. Soc. Rev.*, 43 (2014) 7520-7535.
[37] S. Fan, B. AlOtaibi, S.Y. Woo, Y. Wang, G.A. Botton, Z. Mi, High efficiency solar-to-hydrogen conversion on a monolithically integrated InGaN/GaN/Si adaptive tunnel junction photocathode, *Nano Lett.*, 15 (2015) 2721-2726.
[38] B. AlOtaibi, H.P.T. Nguyen, S. Zhao, M.G. Kibria, S. Fan, Z. Mi, Highly Stable Photoelectrochemical Water Splitting and Hydrogen Generation Using a Double-Band InGaN/GaN Core/Shell Nanowire Photoanode, Nano Letters, 13 (2013) 4356-4361.
[39] E. Kemppainen, A. Bodin, B. Sebok, T. Pedersen, B. Seger, B. Mei, D. Bae, P.C.K. Vesborg, J. Halme, O. Hansen, P.D. Lund, I. Chorkendorff, Scalability and feasibility of photoelectrochemical H_2 evolution: the ultimate limit of Pt nanoparticle as an HER catalyst, *Energy Environ. Sci.*, 8 (2015) 2991-2999.
[40] Y. Yan, B.Y. Xia, B. Zhao, X. Wang, A review on noble-metal-free bifunctional heterogeneous catalysts for overall electrochemical water splitting, *J. Mater. Chem. A*, 4 (2016) 17587-17603.
[41] C.C.L. McCrory, S. Jung, I.M. Ferrer, S.M. Chatman, J.C. Peters, T.F. Jaramillo, Benchmarking hydrogen evolving reaction and oxygen evolving reaction electrocatalysts for solar water splitting devices, *J. Am. Chem. Soc.*, 137 (2015) 4347-4357.
[42] M. Gong, H. Dai, A mini review of NiFe-based materials as highly active oxygen evolution reaction electrocatalysts, *Nano Res.*, 8 (2015) 23-39.

[43] S. Anantharaj, S.R. Ede, K. Sakthikumar, K. Karthick, S. Mishra, S. Kundu, Recent trends and perspectives in electrochemical water splitting with an emphasis on sulfide, selenide, and phosphide catalysts of Fe, Co, and Ni: A review, *ACS Catal.*, 6 (2016) 8069-8097.
[44] S.G. Ullattil, S.B. Narendranath, S.C. Pillai, P. Periyat, Black TiO_2 nanomaterials: A review of recent advances, *Chem. Eng. J.*, 343 (2018) 708-736.
[45] P.G. Moses, C.G. Van de Walle, Band bowing and band alignment in InGaN alloys, *Appl. Phys. Lett.*, 96 (2010) 021908.
[46] P.G. Moses, M. Miao, Q. Yan, C.G. Van de Walle, Hybrid functional investigations of band gaps and band alignments for AlN, GaN, InN, and InGaN, *J. Chem. Phys.*, 134 (2011) 084703.
[47] F. Qiu, Z. Han, J.J. Peterson, M.Y. Odoi, K.L. Sowers, T.D. Krauss, Photocatalytic hydrogen generation by CdSe/CdS nanoparticles, *Nano Lett.*, 16 (2016) 5347-5352.
[48] M.R. Shaner, S. Hu, K. Sun, N.S. Lewis, Stabilization of Si microwire arrays for solar-driven H_2O oxidation to O_2(g) in 1.0 M KOH(aq) using conformal coatings of amorphous TiO_2, *Energy Environ. Sci.*, 8 (2015) 203-207.
[49] K. Sun, Y. Kuang, E. Verlage, S. Brunschwig Bruce, W. Tu Charles, S. Lewis Nathan, Sputtered NiO_x films for stabilization of p^+n-InP photoanodes for solar-driven water oxidation, *Adv. Energy Mater.*, 5 (2015) 1402276.
[50] Z. Chen, H.N. Dinh, E. Miller, Photoelectrochemical water splitting: Standards, experimental methods, and protocols, 1 ed., Springer-Verlag New York, New York, 2013.
[51] F.A. Chowdhury, M.L. Trudeau, H. Guo, Z. Mi, A photochemical diode artificial photosynthesis system for unassisted high efficiency overall pure water splitting, *Nat. Commun.*, 9 (2018) 1707.
[52] Y. Goto, T. Hisatomi, Q. Wang, T. Higashi, K. Ishikiriyama, T. Maeda, Y. Sakata, S. Okunaka, H. Tokudome, M. Katayama, S. Akiyama, H. Nishiyama, Y. Inoue, T. Takewaki, T. Setoyama, T. Minegishi, T. Takata, T. Yamada, K. Domen, A particulate photocatalyst water-splitting panel for large-scale solar hydrogen generation, *Joule*, 2 (2018) 509-520.
[53] A. Nakada, S. Nishioka, J.J.M. Vequizo, K. Muraoka, T. Kanazawa, A. Yamakata, S. Nozawa, H. Kumagai, S.-i. Adachi, O. Ishitani, K. Maeda, Solar-driven Z-scheme water splitting using tantalum/nitrogen co-doped rutile titania nanorod as an oxygen evolution photocatalyst, *J. Mater. Chem. A*, 5 (2017) 11710-11719.
[54] Q. Wang, T. Hisatomi, Y. Suzuki, Z. Pan, J. Seo, M. Katayama, T. Minegishi, H. Nishiyama, T. Takata, K. Seki, A. Kudo, T. Yamada, K. Domen, Particulate photocatalyst sheets based on carbon conductor layer for efficient Z-scheme pure-water splitting at ambient pressure, *J. Am. Chem. Soc.*, 139 (2017) 1675-1683.
[55] H. Fujito, H. Kunioku, D. Kato, H. Suzuki, M. Higashi, H. Kageyama, R. Abe, Layered perovskite oxychloride Bi_4NbO_8Cl: A stable visible light responsive photocatalyst for water splitting, *J. Am. Chem. Soc.*, 138 (2016) 2082-2085.
[56] Q. Wang, T. Hisatomi, Q. Jia, H. Tokudome, M. Zhong, C. Wang, Z. Pan, T. Takata, M. Nakabayashi, N. Shibata, Y. Li, I.D. Sharp, A. Kudo, T. Yamada, K. Domen, Scalable water splitting on particulate photocatalyst sheets with a solar-

to-hydrogen energy conversion efficiency exceeding 1%, *Nat. Mater.*, 15 (2016) 611.

[57] M.G. Kibria, S. Zhao, F.A. Chowdhury, Q. Wang, H.P.T. Nguyen, M.L. Trudeau, H. Guo, Z. Mi, Tuning the surface Fermi level on p-type gallium nitride nanowires for efficient overall water splitting, *Nat. Commun.*, 5 (2014) 3825.

[58] R. Asai, H. Nemoto, Q. Jia, K. Saito, A. Iwase, A. Kudo, A visible light responsive rhodium and antimony-codoped $SrTiO_3$ powdered photocatalyst loaded with an IrO_2 cocatalyst for solar water splitting, *Chem. Commun.*, 50 (2014) 2543-2546.

[59] C. Liu, J. Tang, H.M. Chen, B. Liu, P. Yang, A fully integrated nanosystem of semiconductor nanowires for direct solar water splitting, *Nano Lett.*, 13 (2013) 2989-2992.

[60] X. Chen, S. Shen, L. Guo, S.S. Mao, Semiconductor-based photocatalytic hydrogen generation, *Chem. Rev.*, 110 (2010) 6503-6570.

[61] S. Okamoto, M. Deguchi, S. Yotsuhashi, Modulated III–V triple-junction solar cell wireless device for efficient water splitting, *J. Phys. Chem. C*, 121 (2017) 1393-1398.

[62] X. Shi, H. Jeong, S.J. Oh, M. Ma, K. Zhang, J. Kwon, I.T. Choi, I.Y. Choi, H.K. Kim, J.K. Kim, J.H. Park, Unassisted photoelectrochemical water splitting exceeding 7% solar-to-hydrogen conversion efficiency using photon recycling, *Nat. Commun.*, 7 (2016) 11943.

[63] B. AlOtaibi, H.P.T. Nguyen, S. Zhao, M.G. Kibria, S. Fan, Z. Mi, Highly stable photoelectrochemical water splitting and hydrogen generation using a double-band InGaN/GaN core/shell nanowire photoanode, *Nano Lett.*, 13 (2013) 4356-4361.

[64] H. Svengren, M. Chamoun, J. Grins, M. Johnsson, Water splitting catalysis studied by using real-time Faradaic efficiency obtained through coupled electrolysis and mass spectrometry, *ChemElectroChem*, 5 (2017) 44-50.

[65] J. Zheng, Y. Lyu, R. Wang, C. Xie, H. Zhou, S.P. Jiang, S. Wang, Crystalline TiO_2 protective layer with graded oxygen defects for efficient and stable silicon-based photocathode, *Nat. Commun.*, 9 (2018) 3572.

[66] R.J. Britto, J.D. Benck, J.L. Young, C. Hahn, T.G. Deutsch, T.F. Jaramillo, Molybdenum disulfide as a protection layer and catalyst for gallium indium phosphide solar water splitting photocathodes, *J. Phys. Chem. Lett.*, 7 (2016) 2044-2049.

[67] S. Vishwanath, X. Liu, S. Rouvimov, L. Basile, N. Lu, A. Azcatl, K. Magno, R.M. Wallace, M. Kim, J.-C. Idrobo, J.K. Furdyna, D. Jena, H.G. Xing, Controllable growth of layered selenide and telluride heterostructures and superlattices using molecular beam epitaxy, *J. Mater. Res.*, 31 (2016) 900-910.

[68] E.C. Larkins, J.S. Harris, 2 - Molecular beam epitaxy of high-quality GaAs and AlGaAs, in: R.F.C. Farrow (Ed.) Molecular Beam Epitaxy, William Andrew Publishing, Park Ridge, NJ, 1995, pp. 114-274.

[69] S. Bai, J. Jiang, Q. Zhang, Y. Xiong, Steering charge kinetics in photocatalysis: intersection of materials syntheses, characterization techniques and theoretical simulations, *Chem. Soc. Rev.*, 44 (2015) 2893-2939.

[70] T. Kuykendall, P. Ulrich, S. Aloni, P. Yang, Complete composition tunability of InGaN nanowires using a combinatorial approach, *Nat. Mater.*, 6 (2007) 951.
[71] R.R. Pelá, C. Caetano, M. Marques, L.G. Ferreira, J. Furthmüller, L.K. Teles, Accurate band gaps of AlGaN, InGaN, and AlInN alloys calculations based on LDA-1/2 approach, *Appl. Phys. Lett.*, 98 (2011) 151907.
[72] I. Vurgaftman, J.R. Meyer, Band parameters for nitrogen-containing semiconductors, *J. Appl. Phys.*, 94 (2003) 3675-3696.
[73] H. R.T., X-ray photoelectron spectroscopy (XPS) and auger electron spectroscopy (AES), Springer, New York, NY2014.
[74] Q. Wang, X. Liu, M.G. Kibria, S. Zhao, H.P.T. Nguyen, K.H. Li, Z. Mi, T. Gonzalez, M.P. Andrews, p-Type dopant incorporation and surface charge properties of catalyst-free GaN nanowires revealed by micro-Raman scattering and X-ray photoelectron spectroscopy, *Nanoscale*, 6 (2014) 9970-9976.
[75] D. Graf, F. Molitor, K. Ensslin, C. Stampfer, A. Jungen, C. Hierold, L. Wirtz, Spatially resolved raman spectroscopy of single- and few-layer graphene, *Nano Lett.*, 7 (2007) 238-242.
[76] K. Eberhardt, C. Stiebing, C. Matthäus, M. Schmitt, J. Popp, Advantages and limitations of Raman spectroscopy for molecular diagnostics: an update, *Expert Rev. Mol. Diagn.*, 15 (2015) 773-787.
[77] A. Bogner, P.H. Jouneau, G. Thollet, D. Basset, C. Gauthier, A history of scanning electron microscopy developments: Towards "wet-STEM" imaging, *Micron*, 38 (2007) 390-401.
[78] N.D. Browning, M.F. Chisholm, S.J. Pennycook, Atomic-resolution chemical analysis using a scanning transmission electron microscope, *Nature*, 366 (1993) 143.
[79] B.A. Pinaud, J.D. Benck, L.C. Seitz, A.J. Forman, Z. Chen, T.G. Deutsch, B.D. James, K.N. Baum, G.N. Baum, S. Ardo, H. Wang, E. Miller, T.F. Jaramillo, Technical and economic feasibility of centralized facilities for solar hydrogen production via photocatalysis and photoelectrochemistry, *Energy Environ. Sci.*, 6 (2013) 1983-2002.
[80] A. Fujishima, K. Honda, Electrochemical photolysis of water at a semiconductor electrode, *Nature*, 238 (1972) 37.
[81] C.F. Shih, T. Zhang, J. Li, C. Bai, Powering the future with liquid sunshine, *Joule*, (2018).
[82] L. Liao, Q. Zhang, Z. Su, Z. Zhao, Y. Wang, Y. Li, X. Lu, D. Wei, G. Feng, Q. Yu, X. Cai, J. Zhao, Z. Ren, H. Fang, F. Robles-Hernandez, S. Baldelli, J. Bao, Efficient solar water-splitting using a nanocrystalline CoO photocatalyst, *Nat. Nanotechnol.*, 9 (2013) 69.
[83] Z. Wang, Y. Inoue, T. Hisatomi, R. Ishikawa, Q. Wang, T. Takata, S. Chen, N. Shibata, Y. Ikuhara, K. Domen, Overall water splitting by Ta_3N_5 nanorod single crystals grown on the edges of $KTaO_3$ particles, *Nat. Catal.*, (2018).
[84] M. Grätzel, Photoelectrochemical cells, *Nature*, 414 (2001) 338.
[85] J. Liu, Y. Liu, N. Liu, Y. Han, X. Zhang, H. Huang, Y. Lifshitz, S.-T. Lee, J. Zhong, Z. Kang, Metal-free efficient photocatalyst for stable visible water splitting via a two-electron pathway, *Science*, 347 (2015) 970.

[86] K. Maeda, K. Teramura, D. Lu, T. Takata, N. Saito, Y. Inoue, K. Domen, Photocatalyst releasing hydrogen from water, *Nature*, 440 (2006) 295.
[87] Z. Zou, J. Ye, K. Sayama, H. Arakawa, Direct splitting of water under visible light irradiation with an oxide semiconductor photocatalyst, *Nature*, 414 (2001) 625.
[88] S.Y. Tee, K.Y. Win, W.S. Teo, L.-D. Koh, S. Liu, C.P. Teng, M.-Y. Han, Recent progress in energy-driven water splitting, *Adv. Sci.*, 4 (2017) 1600337.
[89] M. Ge, Q. Li, C. Cao, J. Huang, S. Li, S. Zhang, Z. Chen, K. Zhang, S.S. Al-Deyab, Y. Lai, One-dimensional TiO_2 nanotube photocatalysts for solar water splitting, *Adv. Sci.*, 4 (2016) 1600152.
[90] S.P. Phivilay, C.A. Roberts, A.D. Gamalski, E.A. Stach, S. Zhang, L. Nguyen, Y. Tang, A. Xiong, A.A. Puretzky, F.F. Tao, K. Domen, I.E. Wachs, Anatomy of a visible light activated photocatalyst for water splitting, *ACS Catal.*, 8 (2018) 6650-6658.
[91] Z. Pan, T. Hisatomi, Q. Wang, S. Chen, A. Iwase, M. Nakabayashi, N. Shibata, T. Takata, M. Katayama, T. Minegishi, A. Kudo, K. Domen, Photoreduced graphene oxide as a conductive binder to improve the water splitting activity of photocatalyst sheets, *Adv. Func. Mater.*, 26 (2016) 7011-7019.
[92] Y.H. Lee, J. Kim, J. Oh, Wafer-scale ultrathin, single-crystal Si and GaAs photocathodes for photoelectrochemical hydrogen production, *ACS Appl. Mater. Interfaces*, 10 (2018) 33230-33237.
[93] R. Fan, G. Huang, Y. Wang, Z. Mi, M. Shen, Efficient n^+p-Si photocathodes for solar H_2 production catalyzed by Co-W-S and stabilized by Ti buffer layer, *Appl. Catal. B*, 237 (2018) 158-165.
[94] M.H. Lee, K. Takei, J. Zhang, R. Kapadia, M. Zheng, Y.-Z. Chen, J. Nah, T.S. Matthews, Y.-L. Chueh, J.W. Ager, A. Javey, p-Type InP nanopillar photocathodes for efficient solar-driven hydrogen production, *Angew. Chem. Int. Ed.*, 51 (2012) 10760-10764.
[95] R. Chen, S. Pang, H. An, J. Zhu, S. Ye, Y. Gao, F. Fan, C. Li, Charge separation via asymmetric illumination in photocatalytic Cu_2O particles, *Nat. Energy*, 3 (2018) 655-663.
[96] B. Wang, S. Shen, S.S. Mao, Black TiO_2 for solar hydrogen conversion, *J. Materiomics*, 3 (2017) 96-111.
[97] C. Pan, T. Takata, M. Nakabayashi, T. Matsumoto, N. Shibata, Y. Ikuhara, K. Domen, A complex perovskite-type oxynitride: the first photocatalyst for water splitting operable at up to 600 nm, *Angew. Chem. Int. Ed.*, 54 (2015) 2955-2959.
[98] X. Guan, F.A. Chowdhury, N. Pant, L. Guo, L. Vayssieres, Z. Mi, Efficient unassisted overall photocatalytic seawater splitting on GaN-based nanowire arrays, *J. Phys. Chem. C*, 122 (2018) 13797-13802.
[99] Y.L. Wang, T. Nie, Y.H. Li, X.L. Wang, L.R. Zheng, A.P. Chen, X.Q. Gong, H.G. Yang, Black tungsten nitride as a metallic photocatalyst for overall water splitting operable at up to 765 nm, *Angew. Chem. Int. Ed.*, 56 (2017) 7430-7434.
[100] E. Nurlaela, A. Ziani, K. Takanabe, Tantalum nitride for photocatalytic water splitting: concept and applications, *Mater. Renew. Sustain. Energy*, 5 (2016) 18.
[101] X. Jia, Y. Zhao, G. Chen, L. Shang, R. Shi, X. Kang, G.I.N. Waterhouse, L.-Z. Wu, C.-H. Tung, T. Zhang, Ni_3FeN nanoparticles derived from ultrathin NiFe-

layered double hydroxide nanosheets: An efficient overall water splitting electrocatalyst, *Adv. Energy Mater.*, 6 (2016) 1502585.
[102] T. Ohno, L. Bai, T. Hisatomi, K. Maeda, K. Domen, Photocatalytic water splitting using modified GaN:ZnO solid solution under visible light: Long-time operation and regeneration of activity, *J. Am. Chem. Soc.*, 134 (2012) 8254-8259.
[103] Y. Wang, S. Vanka, J. Gim, Y. Wu, R. Fan, Y. Zhang, J. Shi, M. Shen, R. Hovden, Z. Mi, An $In_{0.42}Ga_{0.58}N$ tunnel junction nanowire photocathode monolithically integrated on a nonplanar Si wafer, *Nano Energy*, 57 (2019) 405-413.
[104] D. Wang, A. Pierre, M.G. Kibria, K. Cui, X. Han, K.H. Bevan, H. Guo, S. Paradis, A.-R. Hakima, Z. Mi, Wafer-level photocatalytic water splitting on GaN nanowire arrays grown by molecular beam epitaxy, *Nano Lett.*, 11 (2011) 2353-2357.
[105] M.G. Kibria, F.A. Chowdhury, M.L. Trudeau, H. Guo, Z. Mi, Dye-sensitized InGaN nanowire arrays for efficient hydrogen production under visible light irradiation, *Nanotechnology*, 26 (2015) 285401.
[106] S. Rajaambal, M. Mapa, C.S. Gopinath, $In_{1-x}Ga_xN$@ZnO: A rationally designed and quantum dot integrated material for water splitting and solar harvesting applications, *Dalton Trans.*, 43 (2014) 12546-12554.
[107] Y. Cui, L. Peng, L. Sun, Q. Qian, Y. Huang, Two-dimensional few-layer group-III metal monochalcogenides as effective photocatalysts for overall water splitting in the visible range, *J. Mater. Chem. A*, 6 (2018) 22768-22777.
[108] F.A. Chowdhury, Z. Mi, M.G. Kibria, M.L. Trudeau, Group III-nitride nanowire structures for photocatalytic hydrogen evolution under visible light irradiation, *APL Mater.*, 3 (2015) 104408.
[109] S. Chen, T. Takata, K. Domen, Particulate photocatalysts for overall water splitting, *Nat. Rev. Mater.*, 2 (2017) 17050.
[110] D.-H. Tu, H.-C. Wang, P.-S. Wang, W.-C. Cheng, K.-H. Chen, C.-I. Wu, S. Chattopadhyay, L.-C. Chen, Improved corrosion resistance of GaN electrodes in NaCl electrolyte for photoelectrochemical hydrogen generation, *Int. J. Hydrog. Energy*, 38 (2013) 14433-14439.
[111] E. Garnett, P. Yang, Light trapping in silicon nanowire solar cells, *Nano Lett.*, 10 (2010) 1082-1087.
[112] L. Meng, Y. Zhang, C. Yam, Multiscale study of plasmonic scattering and light trapping effect in silicon nanowire array solar cells, *J. Phys. Chem. Lett.*, 8 (2017) 571-575.
[113] Y. Wang, F. Silveri, M.K. Bayazit, Q. Ruan, Y. Li, J. Xie, C.R.A. Catlow, J. Tang, Bandgap engineering of organic semiconductors for highly efficient photocatalytic water splitting, *Adv. Energy Mater.*, 8 (2018) 1801084.
[114] K.T. Fountaine, H.J. Lewerenz, H.A. Atwater, Efficiency limits for photoelectrochemical water-splitting, *Nat. Commun.*, 7 (2016) 13706.
[115] Z. Chen, H. Dinh, E. Miller, Photoelectrochemical water splitting: Standards, experimental methods, and protocols, Springer-Verlag New York2013.
[116] C. Zhu, C.a. Liu, Y. Fu, J. Gao, H. Huang, Y. Liu, Z. Kang, Construction of CDs/CdS photocatalysts for stable and efficient hydrogen production in water and seawater, *Appl. Catal. B*, 242 (2019) 178-185.

[117] L. Guo, Z. Yang, K. Marcus, Z. Li, B. Luo, L. Zhou, X. Wang, Y. Du, Y. Yang, MoS_2/TiO_2 heterostructures as nonmetal plasmonic photocatalysts for highly efficient hydrogen evolution, *Energy Environ. Sci.*, 11 (2018) 106-114.
[118] K.T. Fountaine, H.J. Lewerenz, H.A. Atwater, Efficiency limits for photoelectrochemical water-splitting, Nature Communications, 7 (2016) 13706.
[119] W. Yang, J. Ahn, Y. Oh, J. Tan, H. Lee, J. Park, H.-C. Kwon, J. Kim, W. Jo, J. Kim, J. Moon, Adjusting the anisotropy of 1D Sb_2Se_3 nanostructures for highly efficient photoelectrochemical water splitting, *Adv. Energy Mater.*, (2018) 1702888.
[120] J. Su, T. Minegishi, K. Domen, Efficient hydrogen evolution from water using CdTe photocathodes under simulated sunlight, *J. Mater. Chem. A*, 5 (2017) 13154-13160.
[121] G. Wang, Y. Ling, H. Wang, L. Xihong, Y. Li, Chemically modified nanostructures for photoelectrochemical water splitting, *J. Photochem. Photobiol. C*, 19 (2014) 35-51.
[122] D. Jing, L. Guo, L. Zhao, X. Zhang, H. Liu, M. Li, S. Shen, G. Liu, X. Hu, X. Zhang, K. Zhang, L. Ma, P. Guo, Efficient solar hydrogen production by photocatalytic water splitting: From fundamental study to pilot demonstration, *Int. J. Hydrog. Energy*, 35 (2010) 7087-7097.
[123] Y. Lin, R. Kapadia, J. Yang, M. Zheng, K. Chen, M. Hettick, X. Yin, C. Battaglia, I.D. Sharp, J.W. Ager, A. Javey, Role of TiO_2 surface passivation on improving the performance of p-InP photocathodes, *J. Phys. Chem. C*, 119 (2015) 2308-2313.
[124] R. Fan, W. Dong, L. Fang, F. Zheng, M. Shen, More than 10% efficiency and one-week stability of Si photocathodes for water splitting by manipulating the loading of the Pt catalyst and TiO2 protective layer, *J. Mater. Chem. A*, 5 (2017) 18744-18751.
[125] J. Gu, Y. Yan, J.L. Young, K.X. Steirer, N.R. Neale, J.A. Turner, Water reduction by a p-$GaInP_2$ photoelectrode stabilized by an amorphous TiO_2 coating and a molecular cobalt catalyst, *Nat. Mater.*, 15 (2015) 456.
[126] S. Fan, I. Shih, Z. Mi, A monolithically integrated InGaN nanowire/Si tandem photoanode approaching the ideal bandgap configuration of 1.75/1.13 eV, *Adv. Energy Mater.*, 7 (2017) 1600952.
[127] A.B. Laursen, S. Kegnaes, S. Dahl, I. Chorkendorff, Molybdenum sulfides-efficient and viable materials for electro - and photoelectrocatalytic hydrogen evolution, *Energy Environ. Sci.*, 5 (2012) 5577-5591.
[128] S. Zhao, H.P.T. Nguyen, M.G. Kibria, Z. Mi, III-Nitride nanowire optoelectronics, *Prog. Quantum Electron.*, 44 (2015) 14-68.
[129] Y. Dong, B. Tian, T.J. Kempa, C.M. Lieber, Coaxial group III−nitride nanowire photovoltaics, *Nano Lett.*, 9 (2009) 2183-2187.
[130] J. Kamimura, P. Bogdanoff, J. Lähnemann, C. Hauswald, L. Geelhaar, S. Fiechter, H. Riechert, Photoelectrochemical properties of (In,Ga)N nanowires for water splitting investigated by in situ electrochemical mass spectroscopy, *J. Am. Chem. Soc.*, 135 (2013) 10242-10245.
[131] C. Hahn, A.A. Cordones, S.C. Andrews, H. Gao, A. Fu, S.R. Leone, P. Yang, Effect of thermal annealing in ammonia on the properties of InGaN nanowires with different indium concentrations, *J. Phys. Chem. C*, 117 (2013) 3627-3634.

[132] S. Zhao, O. Salehzadeh, S. Alagha, K.L. Kavanagh, S.P. Watkins, Z. Mi, Probing the electrical transport properties of intrinsic InN nanowires, *Appl. Phys. Lett.*, 102 (2013) 073102.
[133] M. Sun, Y. Zhang, X. Gao, T. Palacios, High-performance GaN vertical fin power transistors on bulk GaN substrates, *IEEE Electron Device Lett.*, 38 (2017) 509-512.
[134] A. Stockman, M. Uren, A. Tajalli, M. Meneghini, B. Bakeroot, P. Moens, Temperature dependent substrate trapping in AlGaN/GaN power devices and the impact on dynamic ron, 47th European Solid-State Device Research Conference (ESSDERC), 2017, pp. 130-133.
[135] N. Ikeda, Y. Niiyama, H. Kambayashi, Y. Sato, T. Nomura, S. Kato, S. Yoshida, GaN power transistors on Si substrates for switching applications, *Proc. IEEE*, 98 (2010) 1151-1161.
[136] A. Nakamura, M. Suzuki, K. Fujii, Y. Nakano, M. Sugiyama, Low-temperature growth of AlN and GaN by metal organic vapor phase epitaxy for polarization engineered water splitting photocathode, *J. Cryst. Growth*, 464 (2017) 180-184.
[137] V. Ganesh, M. Alizadeh, A. Shuhaimi, A. Adreen, A. Pandikumar, M. Jayakumar, N.M. Huang, R. Ramesh, K. Baskar, S.A. Rahman, Correlation between indium content in monolithic InGaN/GaN multi quantum well structures on photoelectrochemical activity for water splitting, *J. Alloys Compd.*, 706 (2017) 629-636.
[138] V. Parameshwaran, C. Gallinat, R.W. Enck, A.V. Sampath, P.H. Shen, T. Kuykendall, S. Aloni, M. Wraback, B.M. Clemens, III-V nitride semiconductors for solar hydrogen production, SPIE Defense, Security, and Sensing, SPIE, 2012, pp. 7.
[139] S. Zhao, Z. Mi, Recent advances on p-type III-nitride nanowires by molecular beam epitaxy, *Crystals*, 7 (2017) 268.
[140] K. Sasamoto, T. Hotta, K. Sugita, A.G. Bhuiyan, A. Hashimoto, A. Yamamoto, K. Kinoshita, Y. Kohji, MOVPE growth of high quality p-type InGaN with intermediate In compositions, *J. Cryst. Growth*, 318 (2011) 492-495.
[141] P.-C. Chen, C.-H. Chen, S.-J. Chang, Y.-K. Su, P.-C. Chang, B.-R. Huang, High hole concentration of p-type InGaN epitaxial layers grown by MOCVD, *Thin Solid Films*, 498 (2006) 113-117.
[142] C.J. Eiting, P.A. Grudowski, R.D. Dupuis, P- and N-type doping of GaN and AlGaN epitaxial layers grown by metalorganic chemical vapor deposition, *J. Electron. Mater.*, 27 (1998) 206-209.
[143] H. Kaneko, T. Minegishi, K. Domen, Recent Progress in the Surface Modification of Photoelectrodes toward Efficient and Stable Overall Water Splitting, Chemistry – A European Journal, 23 (2017) n/a-n/a.
[144] M. Ebaid, D. Priante, G. Liu, C. Zhao, M. Sharizal Alias, U. Buttner, T. Khee Ng, T. Taylor Isimjan, H. Idriss, B.S. Ooi, Unbiased photocatalytic hydrogen generation from pure water on stable Ir-treated $In_{0.33}Ga_{0.67}N$ nanorods, *Nano Energy*, 37 (2017) 158-167.
[145] S. Zhao, S.M. Sadaf, S. Vanka, Y. Wang, R. Rashid, Z. Mi, Sub-milliwatt AlGaN nanowire tunnel junction deep ultraviolet light emitting diodes on silicon operating at 242 nm, *Appl. Phys. Lett.*, 109 (2016) 201106.

[146] S.M. Sadaf, Y.H. Ra, H.P.T. Nguyen, M. Djavid, Z. Mi, Alternating-current InGaN/GaN tunnel junction nanowire white-light emitting diodes, *Nano Lett.*, 15 (2015) 6696-6701.
[147] C.X. Ren, Polarisation fields in III-nitrides: Effects and control, *Mater. Sci. Technol.*, 32 (2016) 418-433.
[148] P. Bhattacharya, Semiconductor optoelectronic devices, Second Edition ed., Pearson Education Inc., New Jersey, 1996.
[149] R. Belghouthi, M.H. Gazzah, H. Mejri, Effect of III-nitride polarization on photo-current in N-polar GaN/InGaN p-n, 2017 International Conference on Green Energy Conversion Systems (GECS), 2017, pp. 1-6.
[150] S. Krishnamoorthy, F. Akyol, P.S. Park, S. Rajan, Low resistance GaN/InGaN/GaN tunnel junctions, *Appl. Phys. Lett.*, 102 (2013) 113503.
[151] C. Liu, N.P. Dasgupta, P. Yang, Semiconductor nanowires for artificial photosynthesis, *Chem. Mater.*, 26 (2014) 415-422.
[152] M.D. Kelzenberg, S.W. Boettcher, J.A. Petykiewicz, D.B. Turner-Evans, M.C. Putnam, E.L. Warren, J.M. Spurgeon, R.M. Briggs, N.S. Lewis, H.A. Atwater, Enhanced absorption and carrier collection in Si wire arrays for photovoltaic applications, *Nat. Mater.*, 9 (2010) 239.
[153] J. Kang, Q. Huang, A broad photoluminescence band in heavily Ge‐doped GaAs grown by the liquid‐encapsulated Czochralski technique, *J. Appl. Phys.*, 76 (1994) 5927-5930.
[154] S.Y. Woo, M. Bugnet, H.P.T. Nguyen, Z. Mi, G.A. Botton, Atomic ordering in InGaN alloys within nanowire heterostructures, *Nano Lett.*, 15 (2015) 6413-6418.
[155] R.T. ElAfandy, M. Ebaid, J.-W. Min, C. Zhao, T.K. Ng, B.S. Ooi, Flexible InGaN nanowire membranes for enhanced solar water splitting, Opt. Express, 26 (2018) A640-A650.
[156] S. Eftychis, J. Kruse, T. Koukoula, T. Kehagias, P. Komninou, A. Adikimenakis, K. Tsagaraki, M. Androulidaki, P. Tzanetakis, E. Iliopoulos, A. Georgakilas, Understanding the effects of Si (111) nitridation on the spontaneous growth and properties of GaN nanowires, Journal of Crystal Growth, 442 (2016) 8-13.
[157] H. Bazrafshan, R. Shajareh Touba, Z. Alipour Tesieh, S. Dabirnia, B. Nasernejad, Hydrothermal synthesis of Co_3O_4 nanosheets and its application in photoelectrochemical water splitting, *Chem. Eng. Commun.*, 204 (2017) 1105-1112.
[158] T. Wang, Y. Wei, X. Chang, C. Li, A. Li, S. Liu, J. Zhang, J. Gong, Homogeneous Cu_2O p-n junction photocathodes for solar water splitting, *Appl. Catal. B*, 226 (2018) 31-37.
[159] M. Patel, M. Kumar, J. Kim, Y.K. Kim, Photocurrent enhancement by a rapid thermal treatment of nanodisk-shaped SnS photocathodes, *J. Phys. Chem. Lett.*, (2017) 6099-6105.
[160] W. Vijselaar, P. Westerik, J. Veerbeek, R.M. Tiggelaar, E. Berenschot, N.R. Tas, H. Gardeniers, J. Huskens, Spatial decoupling of light absorption and catalytic activity of Ni–Mo-loaded high-aspect-ratio silicon microwire photocathodes, *Nat. Energy*, 3 (2018) 185-192.
[161] M. Gong, W. Zhou, M.J. Kenney, R. Kapusta, S. Cowley, Y. Wu, B. Lu, M.-C. Lin, D.-Y. Wang, J. Yang, B.-J. Hwang, H. Dai, Blending Cr_2O_3 into a NiO–Ni

electrocatalyst for sustained water splitting, *Angew. Chem. Int. Ed.*, 127 (2015) 12157-12161.
[162] M.J. Kenney, M. Gong, Y. Li, J.Z. Wu, J. Feng, M. Lanza, H. Dai, High-performance silicon photoanodes passivated with ultrathin nickel films for water oxidation, *Science*, 342 (2013) 836.
[163] J. Gu, J.A. Aguiar, S. Ferrere, K.X. Steirer, Y. Yan, C. Xiao, James L. Young, M. Al-Jassim, N.R. Neale, J.A. Turner, A graded catalytic–protective layer for an efficient and stable water-splitting photocathode, *Nat. Energy*, 2 (2017) 16192.
[164] J.-H. Park, A. Mandal, S. Kang, U. Chatterjee, J.S. Kim, B.-G. Park, M.-D. Kim, K.-U. Jeong, C.-R. Lee, Hydrogen generation using non-polar coaxial InGaN/GaN multiple quantum well structure formed on hollow n-GaN nanowires, *Sci. Rep.*, 6 (2016) 31996.
[165] P. Varadhan, H.-C. Fu, D. Priante, J.R.D. Retamal, C. Zhao, M. Ebaid, T.K. Ng, I. Ajia, S. Mitra, I.S. Roqan, B.S. Ooi, J.-H. He, Surface passivation of GaN nanowires for enhanced photoelectrochemical water-splitting, *Nano Lett.*, 17 (2017) 1520-1528.
[166] P. Zhang, T. Wang, J. Gong, Current mechanistic understanding of surface reactions over water-splitting photocatalysts, *Chem*, 4 (2018) 223-245.
[167] W. Cheng, N. Singh, W. Elliott, J. Lee, A. Rassoolkhani, X. Jin, E.W. McFarland, S. Mubeen, Earth-abundant tin sulfide-based photocathodes for solar hydrogen production, *Adv. Sci.*, 5 (2018) 1700362.
[168] B.K. Patra, S. Khilari, D. Pradhan, N. Pradhan, Hybrid dot–disk Au-$CuInS_2$ nanostructures as active photocathode for efficient evolution of hydrogen from water, *Chem. Mater.*, 28 (2016) 4358-4366.
[169] Y. Wang, S. Fan, B. AlOtaibi, Y. Wang, L. Li, Z. Mi, A monolithically integrated gallium nitride nanowire/silicon solar cell photocathode for selective carbon dioxide reduction to methane, *Chemistry – A European Journal*, 22 (2016) 8809-8813.
[170] N. Kornienko, N.A. Gibson, H. Zhang, S.W. Eaton, Y. Yu, S. Aloni, S.R. Leone, P. Yang, Growth and photoelectrochemical energy conversion of wurtzite indium phosphide nanowire arrays, *ACS Nano*, 10 (2016) 5525-5535.
[171] D.M. Andoshe, S. Choi, Y.-S. Shim, S.H. Lee, Y. Kim, C.W. Moon, D.H. Kim, S.Y. Lee, T. Kim, H.K. Park, M.G. Lee, J.-M. Jeon, K.T. Nam, M. Kim, J.K. Kim, J. Oh, H.W. Jang, A wafer-scale antireflective protection layer of solution-processed TiO_2 nanorods for high performance silicon-based water splitting photocathodes, *J. Mater. Chem. A*, 4 (2016) 9477-9485.
[172] A. Standing, S. Assali, L. Gao, M.A. Verheijen, D. van Dam, Y. Cui, P.H.L. Notten, J.E.M. Haverkort, E.P.A.M. Bakkers, Efficient water reduction with gallium phosphide nanowires, *Nat. Commun.*, 6 (2015) 7824.
[173] M. Hettick, M. Zheng, Y. Lin, C.M. Sutter-Fella, J.W. Ager, A. Javey, Nonepitaxial thin-film InP for scalable and efficient photocathodes, *J. Phys. Chem. Lett.*, 6 (2015) 2177-2182.
[174] M. Basu, Z.-W. Zhang, C.-J. Chen, P.-T. Chen, K.-C. Yang, C.-G. Ma, C.C. Lin, S.-F. Hu, R.-S. Liu, Heterostructure of Si and $CoSe_2$: A promising photocathode based on a non-noble metal catalyst for photoelectrochemical hydrogen evolution, *Angew. Chem. Int. Ed.*, 54 (2015) 6211-6216.

[175] S.D. Tilley, M. Schreier, J. Azevedo, M. Stefik, M. Graetzel, Ruthenium oxide hydrogen evolution catalysis on composite cuprous oxide water-splitting photocathodes, *Adv. Func. Mater.*, 24 (2014) 303-311.
[176] M. Malizia, B. Seger, I. Chorkendorff, P.C.K. Vesborg, Formation of a p-n heterojunction on GaP photocathodes for H_2 production providing an open-circuit voltage of 710 mV, *J. Mater. Chem. A*, 2 (2014) 6847-6853.
[177] Y. Lin, C. Battaglia, M. Boccard, M. Hettick, Z. Yu, C. Ballif, J.W. Ager, A. Javey, Amorphous Si thin film based photocathodes with high photovoltage for efficient hydrogen production, *Nano Lett.*, 13 (2013) 5615-5618.
[178] B. Koo, S.-W. Nam, R. Haight, S. Kim, S. Oh, M. Cho, J. Oh, J.Y. Lee, B.T. Ahn, B. Shin, Tailoring photoelectrochemical performance and stability of $Cu(In,Ga)Se_2$ photocathode via TiO_2-coupled buffer layers, *ACS Appl. Mater. Interfaces*, 9 (2017) 5279-5287.
[179] Gurudayal, D. Sabba, M.H. Kumar, L.H. Wong, J. Barber, M. Grätzel, N. Mathews, Perovskite–hematite tandem cells for efficient overall solar driven water splitting, *Nano Lett.*, 15 (2015) 3833-3839.
[180] W.-H. Cheng, M.H. Richter, M.M. May, J. Ohlmann, D. Lackner, F. Dimroth, T. Hannappel, H.A. Atwater, H.-J. Lewerenz, Monolithic photoelectrochemical device for direct water splitting with 19% efficiency, *ACS Energy Lett.*, (2018) 1795-1800.
[181] E. Verlage, S. Hu, R. Liu, R.J.R. Jones, K. Sun, C. Xiang, N.S. Lewis, H.A. Atwater, A monolithically integrated, intrinsically safe, 10% efficient, solar-driven water-splitting system based on active, stable earth-abundant electrocatalysts in conjunction with tandem III-V light absorbers protected by amorphous TiO_2 films, *Energy Environ. Sci.*, 8 (2015) 3166-3172.
[182] X. Shi, K. Zhang, K. Shin, M. Ma, J. Kwon, I.T. Choi, J.K. Kim, H.K. Kim, D.H. Wang, J.H. Park, Unassisted photoelectrochemical water splitting beyond 5.7% solar-to-hydrogen conversion efficiency by a wireless monolithic photoanode/dye-sensitised solar cell tandem device, *Nano Energy*, 13 (2015) 182-191.
[183] A. Martinez-Garcia, B. Russell Harry, W. Paxton, S. Ravipati, S. Calero-Barney, M. Menon, E. Richter, J. Young, T. Deutsch, K. Sunkara Mahendra, Unassisted water splitting using a $GaSb_xP_{(1-x)}$ photoanode, *Adv. Energy Mater.*, 8 (2018) 1703247.
[184] O. Khaselev, J.A. Turner, A monolithic photovoltaic-photoelectrochemical device for dydrogen production via water splitting, *Science*, 280 (1998) 425.
[185] B. Seger, I.E. Castelli, P.C.K. Vesborg, K.W. Jacobsen, O. Hansen, I. Chorkendorff, 2-Photon tandem device for water splitting: comparing photocathode first versus photoanode first designs, *Energy Environ. Sci.*, 7 (2014) 2397-2413.
[186] S.Y. Reece, J.A. Hamel, K. Sung, T.D. Jarvi, A.J. Esswein, J.J.H. Pijpers, D.G. Nocera, Wireless solar water splitting using silicon-based semiconductors and earth-abundant catalysts, *Science*, 334 (2011) 645.
[187] M. Li, W. Luo, D. Cao, X. Zhao, Z. Li, T. Yu, Z. Zou, A Co-catalyst-loaded Ta_3N_5 photoanode with a high solar photocurrent for water splitting upon facile removal of the surface layer, *Angew. Chem. Int. Ed.*, 52 (2013) 11016-11020.

[188] K. Aryal, B.N. Pantha, J. Li, J.Y. Lin, H.X. Jiang, Hydrogen generation by solar water splitting using p-InGaN photoelectrochemical cells, *Appl. Phys. Lett.*, 96 (2010) 052110.
[189] N.u.H. Alvi, P.E.D. Soto Rodriguez, P. Aseev, V.J. Gómez, A.u.H. Alvi, W.u. Hassan, M. Willander, R. Nötzel, InN/InGaN quantum dot photoelectrode: Efficient hydrogen generation by water splitting at zero voltage, *Nano Energy*, 13 (2015) 291-297.
[190] H.P.T. Nguyen, K. Cui, S. Zhang, M. Djavid, A. Korinek, G.A. Botton, Z. Mi, Controlling electron overflow in phosphor-free InGaN/GaN nanowire white light-emitting diodes, *Nano Lett.*, 12 (2012) 1317-1323.
[191] W. Guo, M. Zhang, A. Banerjee, P. Bhattacharya, Catalyst-free InGaN/GaN nanowire light emitting diodes grown on (001) silicon by molecular beam epitaxy, *Nano Lett.*, 10 (2010) 3355-3359.
[192] S.M. Sadaf, S. Zhao, Y. Wu, Y.H. Ra, X. Liu, S. Vanka, Z. Mi, An AlGaN core–shell tunnel junction nanowire light-emitting diode operating in the ultraviolet-C band, *Nano Lett.*, 17 (2017) 1212-1218.
[193] M. Ebaid, J.-W. Min, C. Zhao, T.K. Ng, H. Idriss, B.S. Ooi, Water splitting to hydrogen over epitaxially grown InGaN nanowires on a metallic titanium/silicon template: reduced interfacial transfer resistance and improved stability to hydrogen, *J. Mater. Chem. A*, 6 (2018) 6922-6930.
[194] Z. Jiang, Z. Zhang, W. Shangguan, M.A. Isaacs, L.J. Durndell, C.M.A. Parlett, A.F. Lee, Photodeposition as a facile route to tunable Pt photocatalysts for hydrogen production: on the role of methanol, *Catal. Sci. Technol.*, 6 (2016) 81-88.
[195] N. Cheng, S. Stambula, D. Wang, M.N. Banis, J. Liu, A. Riese, B. Xiao, R. Li, T.-K. Sham, L.-M. Liu, G.A. Botton, X. Sun, Platinum single-atom and cluster catalysis of the hydrogen evolution reaction, *Nat. Commun.*, 7 (2016) 13638.
[196] J. Benton, J. Bai, T. Wang, Utilisation of GaN and InGaN/GaN with nanoporous structures for water splitting, *Appl. Phys. Lett.*, 105 (2014) 223902.
[197] S.K. Tc, G. Gupta, Band alignment and Schottky behaviour of InN/GaN heterostructure grown by low-temperature low-energy nitrogen ion bombardment, *RSC Adv.*, 4 (2014) 27308-27314.
[198] H. Komaki, R. Katayama, K. Onabe, M. Ozeki, T. Ikari, Nitrogen supply rate dependence of InGaN growth properties, by RF-MBE, *J. Cryst. Growth*, 305 (2007) 12-18.
[199] A.I. Duff, L. Lymperakis, J. Neugebauer, Ab initio-based bulk and surface thermodynamics of InGaN alloys: Investigating the effects of strain and surface polarity, *Phys. Status Solidi B*, 252 (2015) 855-865.
[200] T.L. Tan, L.-L. Wang, J. Zhang, D.D. Johnson, K. Bai, Platinum nanoparticle during electrochemical hydrogen evolution: Adsorbate distribution, active reaction species, and size effect, *ACS Catal.*, 5 (2015) 2376-2383.
[201] G.-F. Wei, Z.-P. Liu, Restructuring and hydrogen evolution on Pt nanoparticle, *Chem. Sci.*, 6 (2015) 1485-1490.
[202] C.M. Zalitis, A.R. Kucernak, J. Sharman, E. Wright, Design principles for platinum nanoparticles catalysing electrochemical hydrogen evolution and

oxidation reactions: edges are much more active than facets, *J. Mater. Chem. A*, 5 (2017) 23328-23338.
[203] S.P. Berglund, F.F. Abdi, P. Bogdanoff, A. Chemseddine, D. Friedrich, R. van de Krol, Comprehensive evaluation of $CuBi_2O_4$ as a photocathode material for photoelectrochemical water splitting, *Chem. Mater.*, 28 (2016) 4231-4242.
[204] C. Das, M. Tallarida, D. Schmeisser, Si microstructures laminated with a nanolayer of TiO_2 as long-term stable and effective photocathodes in PEC devices, *Nanoscale*, 7 (2015) 7726-7733.
[205] J.-Y. Jung, J.-Y. Yu, J.-H. Lee, Dynamic photoelectrochemical device using an electrolyte-permeable $NiO_x/SiO_2/Si$ photocathode with an open-circuit potential of 0.75 V, *ACS Appl. Mater. Interfaces*, 10 (2018) 7955-7962.
[206] R.T. ElAfandy, M. Ebaid, J.-W. Min, C. Zhao, T.K. Ng, B.S. Ooi, Flexible InGaN nanowire membranes for enhanced solar water splitting, Opt. Express, 26 (2018) A640-A650.
[207] W. Luo, B. Liu, Z. Li, Z. Xie, D. Chen, Z. Zou, R. Zhang, Stable response to visible light of InGaN photoelectrodes, *Appl. Phys. Lett.*, 92 (2008) 262110.
[208] Y.J. Hwang, C.H. Wu, C. Hahn, H.E. Jeong, P. Yang, Si/InGaN core/shell hierarchical nanowire arrays and their photoelectrochemical properties, *Nano Lett.*, 12 (2012) 1678-1682.
[209] B. Weng, C.R. Grice, J. Ge, T. Poudel, X. Deng, Y. Yan, Barium bismuth niobate double perovskite/tungsten oxide nanosheet photoanode for high-performance photoelectrochemical water splitting, *Adv. Energy Mater.*, 8 (2017) 1701655.
[210] Y. Zhao, K.R. Yang, Z. Wang, X. Yan, S. Cao, Y. Ye, Q. Dong, X. Zhang, J.E. Thorne, L. Jin, K.L. Materna, A. Trimpalis, H. Bai, S.C. Fakra, X. Zhong, P. Wang, X. Pan, J. Guo, M. Flytzani-Stephanopoulos, G.W. Brudvig, V.S. Batista, D. Wang, Stable iridium dinuclear heterogeneous catalysts supported on metal-oxide substrate for solar water oxidation, *Proc. Natl. Acad. Sci. U.S.A.*, (2018) doi.org/10.1073/pnas.1722137115.
[211] R. Liu, Z. Zheng, J. Spurgeon, X. Yang, Enhanced photoelectrochemical water-splitting performance of semiconductors by surface passivation layers, *Energy Environ. Sci.*, 7 (2014) 2504-2517.
[212] B. Zhou, X. Kong, S. Vanka, S. Chu, P. Ghamari, Y. Wang, N. Pant, I. Shih, H. Guo, Z. Mi, Gallium nitride nanowire as a linker of molybdenum sulfides and silicon for photoelectrocatalytic water splitting, *Nat. Commun.*, 9 (2018) 3856.
[213] I. Roger, M.A. Shipman, M.D. Symes, Earth-abundant catalysts for electrochemical and photoelectrochemical water splitting, *Nat. Rev. Chem.*, 1 (2017) 0003.
[214] X. Shi, S. Siahrostami, G.-L. Li, Y. Zhang, P. Chakthranont, F. Studt, T.F. Jaramillo, X. Zheng, J.K. Nørskov, Understanding activity trends in electrochemical water oxidation to form hydrogen peroxide, *Nat. Commun.*, 8 (2017) 701.
[215] K. Rui, G. Zhao, Y. Chen, Y. Lin, Q. Zhou, J. Chen, J. Zhu, W. Sun, W. Huang, S.X. Dou, Hybrid 2D dual-metal–organic frameworks for enhanced water oxidation catalysis, *Adv. Func. Mater.*, 28 (2018) 1801554.

[216] P. Zhang, L. Li, D. Nordlund, H. Chen, L. Fan, B. Zhang, X. Sheng, Q. Daniel, L. Sun, Dendritic core-shell nickel-iron-copper metal/metal oxide electrode for efficient electrocatalytic water oxidation, *Nat. Commun.*, 9 (2018) 381.
[217] M. Zheng, Y. Ding, X. Cao, T. Tian, J. Lin, Homogeneous and heterogeneous photocatalytic water oxidation by polyoxometalates containing the most earth-abundant transition metal, iron, *Appl. Catal. B*, 237 (2018) 1091-1100.
[218] T.W. Kim, Y. Ping, G.A. Galli, K.-S. Choi, Simultaneous enhancements in photon absorption and charge transport of bismuth vanadate photoanodes for solar water splitting, *Nat. Commun.*, 6 (2015) 8769.
[219] C.G. Morales-Guio, M.T. Mayer, A. Yella, S.D. Tilley, M. Grätzel, X. Hu, An optically transparent iron nickel oxide catalyst for solar water splitting, *J. Am. Chem. Soc.*, 137 (2015) 9927-9936.
[220] K. Shin, J.H. Park, Highly transparent dual-sensitized titanium dioxide nanotube arrays for spontaneous solar water splitting tandem configuration, *ACS Appl. Mater. Interfaces*, 7 (2015) 18429-18434.
[221] P. Chakthranont, R. Hellstern Thomas, M. McEnaney Joshua, F. Jaramillo Thomas, Design and fabrication of a precious metal-free tandem core–shell p^+n Si/W-doped $BiVO_4$ photoanode for unassisted water splitting, *Adv. Energy Mater.*, 7 (2017) 1701515.
[222] X. Wang, K.-Q. Peng, Y. Hu, F.-Q. Zhang, B. Hu, L. Li, M. Wang, X.-M. Meng, S.-T. Lee, Silicon/hematite core/shell nanowire array decorated with gold nanoparticles for unbiased solar water oxidation, *Nano Lett.*, 14 (2014) 18-23.
[223] P. Bornoz, F.F. Abdi, S.D. Tilley, B. Dam, R. van de Krol, M. Graetzel, K. Sivula, A bismuth vanadate–cuprous oxide tandem cell for overall solar water splitting, *J. Phys. Chem. C*, 118 (2014) 16959-16966.
[224] H.B. Yang, J. Miao, S.-F. Hung, F. Huo, H.M. Chen, B. Liu, Stable quantum dot photoelectrolysis cell for unassisted visible light solar water splitting, *ACS Nano*, 8 (2014) 10403-10413.
[225] J.-W. Jang, C. Du, Y. Ye, Y. Lin, X. Yao, J. Thorne, E. Liu, G. McMahon, J. Zhu, A. Javey, J. Guo, D. Wang, Enabling unassisted solar water splitting by iron oxide and silicon, *Nat. Commun.*, 6 (2015) 7447.
[226] H. Lin, X. Long, J. Hu, Y. Qiu, Z. Wang, M. Ma, Y. An, S. Yang, Exploratory study of Zn_xPbO_y photoelectrodes for unassisted overall solar water splitting, *ACS Appl. Mater. Interfaces*, 10 (2018) 10918-10926.
[227] B. AlOtaibi, S. Fan, S. Vanka, M.G. Kibria, Z. Mi, A metal-nitride nanowire dual-photoelectrode device for unassisted solar-to-hydrogen conversion under parallel illumination, *Nano Lett.*, 15 (2015) 6821-6828.
[228] Z. Bai, Y. Zhang, A Cu_2O/Cu_2S-ZnO/CdS tandem photoelectrochemical cell for self-driven solar water splitting, *J. Alloys Compd.*, 698 (2017) 133-140.
[229] D. Shao, Y. Cheng, J. He, D. Feng, L. Zheng, L. Zheng, X. Zhang, J. Xu, W. Wang, W. Wang, F. Lu, H. Dong, L. Li, H. Liu, R. Zheng, H. Liu, A spatially separated organic–inorganic hybrid photoelectrochemical cell for unassisted overall water splitting, *ACS Catal.*, 7 (2017) 5308-5315.
[230] Y. Tachibana, L. Vayssieres, J.R. Durrant, Artificial photosynthesis for solar water-splitting, *Nat. Photon.*, 6 (2012) 511.

[231] A. Heller, B. Miller, H.J. Lewerenz, K.J. Bachmann, An efficient photocathode for semiconductor liquid junction cells: 9.4% solar conversion efficiency with p-InP/VCl_3-VCl_2-HCl/C, *J. Am. Chem. Soc.*, 102 (1980) 6555-6556.
[232] S. Chu, P. Ou, P. Ghamari, S. Vanka, B. Zhou, I. Shih, J. Song, Z. Mi, Photoelectrochemical CO_2 reduction into syngas with the metal/oxide interface, *J. Am. Chem. Soc.*, 140 (2018) 7869-7877.
[233] Y. Wang, S. Fan, B. AlOtaibi, Y. Wang, L. Li, Z. Mi, A monolithically integrated gallium nitride nanowire/silicon solar cell photocathode for selective carbon dioxide reduction to methane, *Chem. A Eur. J.*, 22 (2016) 8809-8813.
[234] X. Zhou, R. Liu, K. Sun, K.M. Papadantonakis, B.S. Brunschwig, N.S. Lewis, 570 mV photovoltage, stabilized n-Si/CoO_x heterojunction photoanodes fabricated using atomic layer deposition, *Energy Environ. Sci.*, 9 (2016) 892-897.
[235] Z. Wang, C. Li, K. Domen, Recent developments in heterogeneous photocatalysts for solar-driven overall water splitting, *Chem. Soc. Rev.*, (2019).
[236] Z. Luo, T. Wang, J. Gong, Single-crystal silicon-based electrodes for unbiased solar water splitting: current status and prospects, *Chem. Soc. Rev.*, (2019).
[237] D. Bae, B. Seger, P.C.K. Vesborg, O. Hansen, I. Chorkendorff, Strategies for stable water splitting via protected photoelectrodes, Chemical Society Reviews, 46 (2017) 1933-1954.
[238] S.D. Tilley, Recent advances and emerging trends in photo-electrochemical solar energy conversion, *Adv. Energy Mater.*, 9 (2019) 1802877.
[239] H. Kaneko, T. Minegishi, K. Domen, Recent progress in the surface modification of photoelectrodes toward efficient and stable overall water splitting, *Chem. Eur. J.*, 24 (2017) 5697-5706.
[240] C. Jiang, S.J.A. Moniz, A. Wang, T. Zhang, J. Tang, Photoelectrochemical devices for solar water splitting – materials and challenges, *Chem. Soc. Rev.*, 46 (2017) 4645-4660.
[241] R. Matheu, I.A. Moreno-Hernandez, X. Sala, H.B. Gray, B.S. Brunschwig, A. Llobet, N.S. Lewis, Photoelectrochemical behavior of a molecular Ru-based water-oxidation catalyst bound to TiO_2-protected Si photoanodes, *J. Am. Chem. Soc.*, 139 (2017) 11345-11348.
[242] M. Malizia, B. Seger, I. Chorkendorff, P.C.K. Vesborg, Formation of a p–n heterojunction on GaP photocathodes for H_2 production providing an open-circuit voltage of 710 mV, *J. Mater. Chem. A*, 2 (2014) 6847-6853.
[243] J. Azevedo, S.D. Tilley, M. Schreier, M. Stefik, C. Sousa, J.P. Araújo, A. Mendes, M. Grätzel, M.T. Mayer, Tin oxide as stable protective layer for composite cuprous oxide water-splitting photocathodes, *Nano Energy*, 24 (2016) 10-16.
[244] C. Li, T. Wang, Z. Luo, D. Zhang, J. Gong, Transparent ALD-grown Ta_2O_5 protective layer for highly stable ZnO photoelectrode in solar water splitting, *Chem. Commun.*, 51 (2015) 7290-7293.
[245] C.U. Maier, M. Specht, G. Bilger, Hydrogen evolution on platinum-coated p-silicon photocathodes, *Int. J. Hydrog. Energy*, 21 (1996) 859-864.
[246] M.G. Kast, L.J. Enman, N.J. Gurnon, A. Nadarajah, S.W. Boettcher, Solution-deposited F:SnO_2/TiO_2 as a base-stable protective layer and antireflective coating for microtextured buried-junction H_2-evolving Si photocathodes, *ACS Appl. Mater. Interfaces*, 6 (2014) 22830-22837.

[247] S. Vanka, Y. Wang, P. Ghamari, S. Chu, A. Pandey, P. Bhattacharya, I. Shih, Z. Mi, A high efficiency Si photoanode protected by few-layer $MoSe_2$, *Solar RRL*, 2 (2018) 1800113.
[248] A.B. Laursen, T. Pedersen, P. Malacrida, B. Seger, O. Hansen, P.C.K. Vesborg, I. Chorkendorff, MoS_2—an integrated protective and active layer on n^+p-Si for solar H_2 evolution, *Phys. Chem. Chem. Phys.*, 15 (2013) 20000-20004.
[249] L. Pan, J.H. Kim, M.T. Mayer, M.-K. Son, A. Ummadisingu, J.S. Lee, A. Hagfeldt, J. Luo, M. Grätzel, Boosting the performance of Cu_2O photocathodes for unassisted solar water splitting devices, *Nat. Catal.*, 1 (2018) 412-420.
[250] T.J. Flack, B.N. Pushpakaran, S.B. Bayne, GaN technology for power electronic applications: A review, *J. Electron. Mater.*, 45 (2016) 2673-2682.
[251] W. Walukiewicz, Intrinsic limitations to the doping of wide-gap semiconductors, *Phys. B Condens. Matter*, 302-303 (2001) 123-134.
[252] C.G. Van de Walle, J. Neugebauer, Universal alignment of hydrogen levels in semiconductors, insulators and solutions, *Nature*, 423 (2003) 626.
[253] J.W. Ager, J. Wu, K.M. Yu, R.E. Jones, S.X. Li, W. Walukiewicz, E.E. Haller, H. Lu, W.J. Schaff, Group III-nitride alloys as photovoltaic materials, Optical Science and Technology, the SPIE 49th Annual Meeting, SPIE, 2004, pp. 8.
[254] J. Kamimura, P. Bogdanoff, F.F. Abdi, J. Lähnemann, R. van de Krol, H. Riechert, L. Geelhaar, Photoelectrochemical properties of GaN photoanodes with cobalt phosphate catalyst for solar water splitting in neutral electrolyte, *J. Phys. Chem. C*, 121 (2017) 12540-12545.
[255] A.M. Dabiran, F. Machuca, I. De, R. Weiss, Epitaxial growth of high quality GaN films on lattice matched metallic layers, *ECS Trans.*, 66 (2015) 113-117.
[256] S. Zhao, M.G. Kibria, Q. Wang, H.P.T. Nguyen, Z. Mi, Growth of large-scale vertically aligned GaN nanowires and their heterostructures with high uniformity on SiO_x by catalyst-free molecular beam epitaxy, *Nanoscale*, 5 (2013) 5283-5287.
[257] K. Chen, R. Kapadia, A. Harker, S. Desai, J. Seuk Kang, S. Chuang, M. Tosun, C.M. Sutter-Fella, M. Tsang, Y. Zeng, D. Kiriya, J. Hazra, S.R. Madhvapathy, M. Hettick, Y.-Z. Chen, J. Mastandrea, M. Amani, S. Cabrini, Y.-L. Chueh, J.W. Ager Iii, D.C. Chrzan, A. Javey, Direct growth of single-crystalline III–V semiconductors on amorphous substrates, *Nat. Commun.*, 7 (2016) 10502.
[258] J.E. Thorne, Y. Zhao, D. He, S. Fan, S. Vanka, Z. Mi, D. Wang, Understanding the role of co-catalysts on silicon photocathodes using intensity modulated photocurrent spectroscopy, *Phys. Chem. Chem. Phys.*, 19 (2017) 29653-29659.
[259] A. Isamu, A. Hiroshi, Crystal growth and conductivity control of group III nitride semiconductors and their application to short wavelength light emitters, *Jpn. J. Appl. Phys.*, 36 (1997) 5393.
[260] S.C. Jain, M. Willander, J. Narayan, R.V. Overstraeten, III–nitrides: Growth, characterization, and properties, *J. Appl. Phys.*, 87 (2000) 965-1006.
[261] J. Laifi, N. Chaaben, H. Bouazizi, N. Fourati, C. Zerrouki, Y. El Gmili, A. Bchetnia, J.P. Salvestrini, B. El Jani, Effect of GaAs substrate orientation on the growth kinetic of GaN layer grown by MOVPE, *Superlattices Microstruct.*, 94 (2016) 30-38.
[262] Y.L. Casallas-Moreno, S. Gallardo-Hernández, F. Ruiz-Zepeda, B.M. Monroy, A. Hernández-Hernández, A. Herrera-Gómez, A. Escobosa-Echavarría, G. Santana,

A. Ponce, M. López-López, As4 overpressure effects on the phase purity of cubic GaN layers grown on GaAs substrates by RF-MBE, *Appl. Surf. Sci.*, 353 (2015) 588-593.

[263] Y. Imazeki, Y. Iwai, A. Nakamura, K. Koike, S.-i. Sato, T. Ohshima, K. Fujii, M. Sugiyama, Y. Nakano, Band alignment at n-GaN/electrolyte interface explored by photo-induced offset of open-circuit potential for efficient water splitting, *ECS Trans.*, 77 (2017) 25-30.

[264] J.E. Thorne, J.-W. Jang, E.Y. Liu, D. Wang, Understanding the origin of photoelectrode performance enhancement by probing surface kinetics, *Chem. Sci.*, 7 (2016) 3347-3354.

[265] F. Karnbach, X. Yang, G. Mutschke, J. Fröhlich, J. Eckert, A. Gebert, K. Tschulik, K. Eckert, M. Uhlemann, Interplay of the open circuit potential-relaxation and the dissolution behavior of a single H_2 bubble generated at a Pt microelectrode, *J. Phys. Chem. C*, 120 (2016) 15137-15146.

[266] J. Krysa, M. Zlamal, S. Kment, M. Brunclikova, Z. Hubicka, TiO_2 and Fe_2O_3 films for photoelectrochemical water splitting, *Molecules*, 20 (2015).

[267] M.R. Shaner, M.T. McDowell, A. Pien, H.A. Atwater, N.S. Lewis, Si/TiO_2 tandem-junction microwire arrays for unassisted solar-driven water splitting, *J. Electrochem. Soc.*, 163 (2016) H261-H264.

[268] M. Korun, T.S. Navruz, Comparison of Ge, InGaAs p-n junction solar cell, *J Phys. Conf. Ser.*, 707 (2016) 012035.

[269] Y. Kim, N.D. Lam, K. Kim, W.-K. Park, J. Lee, Ge nanopillar solar cells epitaxially grown by metalorganic chemical vapor deposition, *Sci. Rep.*, 7 (2017) 42693.

[270] L. Zhang, P. Niu, Y. Li, M. Song, J. Zhang, P. Ning, P. Chen, Investigation on high-efficiency $Ga_{0.51}In_{0.49}P/In_{0.01}Ga_{0.99}As$/Ge triple-junction solar cells for space applications, *AIP Adv.*, 7 (2017) 125217.

[271] D.E. Polyansky, J.T. Muckerman, J. Rochford, R. Zong, R.P. Thummel, E. Fujita, Water oxidation by a mononuclear ruthenium catalyst: Characterization of the intermediates, *J. Am. Chem. Soc.*, 133 (2011) 14649-14665.

[272] J. Yang, D. Wang, H. Han, C. Li, Roles of cocatalysts in photocatalysis and photoelectrocatalysis, *Acc. Chem. Res.*, 46 (2013) 1900-1909.

[273] K. Sun, Y. Kuang, E. Verlage, B.S. Brunschwig, C.W. Tu, N.S. Lewis, Sputtered NiO_x films for stabilization of p^+n-InP photoanodes for solar-driven water oxidation, *Adv. Energy Mater.*, 5 (2015) 1402276.

[274] R. Sathre, C.D. Scown, W.R. Morrow, J.C. Stevens, I.D. Sharp, J.W. Ager, K. Walczak, F.A. Houle, J.B. Greenblatt, Life-cycle net energy assessment of large-scale hydrogen production via photoelectrochemical water splitting, *Energy Environ. Sci.*, 7 (2014) 3264-3278.

[275] N. Loew, S. Komatsu, H. Akita, K. Funayama, T. Yuge, T. Fujiwara, M. Ihara, TiO_2 as electron-extraction-layer in reverse type P_3HT/ICBA organic solar cells, *ECS Trans.*, 58 (2014) 77-88.

[276] M.F. Lichterman, A.I. Carim, M.T. McDowell, S. Hu, H.B. Gray, B.S. Brunschwig, N.S. Lewis, Stabilization of n-cadmium telluride photoanodes for water oxidation to O_2(g) in aqueous alkaline electrolytes using amorphous TiO_2

films formed by atomic-layer deposition, *Energy Environ. Sci.*, 7 (2014) 3334-3337.
[277] J.W. Ager, M.R. Shaner, K.A. Walczak, I.D. Sharp, S. Ardo, Experimental demonstrations of spontaneous, solar-driven photoelectrochemical water splitting, *Energy Environ. Sci.*, 8 (2015) 2811-2824.
[278] E. Verlage, S. Hu, R. Liu, R.J.R. Jones, K. Sun, C. Xiang, N.S. Lewis, H.A. Atwater, A monolithically integrated, intrinsically safe, 10% efficient, solar-driven water-splitting system based on active, stable earth-abundant electrocatalysts in conjunction with tandem III–V light absorbers protected by amorphous TiO_2 films, *Energy Environ. Sci.*, 8 (2015) 3166-3172.
[279] J. Yang, J.K. Cooper, F.M. Toma, K.A. Walczak, M. Favaro, J.W. Beeman, L.H. Hess, C. Wang, C. Zhu, S. Gul, J. Yano, C. Kisielowski, A. Schwartzberg, I.D. Sharp, A multifunctional biphasic water splitting catalyst tailored for integration with high-performance semiconductor photoanodes, *Nat. Mater.*, 16 (2017) 335-341.
[280] D. Liu, L. Li, Y. Gao, C. Wang, J. Jiang, Y. Xiong, The nature of photocatalytic "water splitting" on silicon nanowires, *Angew. Chem. Int. Ed.*, 54 (2015) 2980-2985.
[281] M. Yamaguchi, T. Takamoto, K. Araki, N. Ekins-Daukes, Multi-junction III–V solar cells: Current status and future potential, *Solar Energy*, 79 (2005) 78-85.
[282] G. Ye, Y. Gong, J. Lin, B. Li, Y. He, S.T. Pantelides, W. Zhou, R. Vajtai, P.M. Ajayan, Defects engineered monolayer MoS_2 for improved hydrogen evolution reaction, *Nano Lett.*, 16 (2016) 1097-1103.
[283] J.R. McKone, A.P. Pieterick, H.B. Gray, N.S. Lewis, Hydrogen evolution from Pt/Ru-coated p-type WSe_2 photocathodes, *J. Am. Chem. Soc.*, 135 (2013) 223-231.
[284] R.M. Navarro Yerga, M.C. Álvarez Galván, F. del Valle, J.A. Villoria de la Mano, J.L.G. Fierro, Water splitting on semiconductor catalysts under visible-light irradiation, *ChemSusChem*, 2 (2009) 471-485.
[285] X. Duan, C. Wang, J.C. Shaw, R. Cheng, Y. Chen, H. Li, X. Wu, Y. Tang, Q. Zhang, A. Pan, J. Jiang, R. Yu, Y. Huang, X. Duan, Lateral epitaxial growth of two-dimensional layered semiconductor heterojunctions, *Nat. Nanotechnol.*, 9 (2014) 1024-1030.
[286] J. Feng, X. Qian, C.-W. Huang, J. Li, Strain-engineered artificial atom as a broad-spectrum solar energy funnel, *Nat. Photon.*, 6 (2012) 866-872.
[287] K.S. Novoselov, A. Mishchenko, A. Carvalho, A.H. Castro Neto, 2D materials and van der Waals heterostructures, *Science*, 353 (2016) aac9439.
[288] C. Huang, S. Wu, A.M. Sanchez, J.J.P. Peters, R. Beanland, J.S. Ross, P. Rivera, W. Yao, D.H. Cobden, X. Xu, Lateral heterojunctions within monolayer $MoSe_2$–WSe_2 semiconductors, *Nat. Mater.*, 13 (2014) 1096-1101.
[289] K. Chen, X. Wan, J. Xu, Epitaxial stitching and stacking growth of atomically thin transition-metal dichalcogenides (TMDCs) heterojunctions, *Adv. Func. Mater.*, 27 (2017) 1603884.
[290] J.S. Ross, P. Klement, A.M. Jones, N.J. Ghimire, J. Yan, D.G. Mandrus, T. Taniguchi, K. Watanabe, K. Kitamura, W. Yao, D.H. Cobden, X. Xu, Electrically tunable excitonic light-emitting diodes based on monolayer WSe_2 p-n junctions, *Nat. Nanotechnol.*, 9 (2014) 268-272.

[291] A. Pospischil, M.M. Furchi, T. Mueller, Solar-energy conversion and light emission in an atomic monolayer p-n diode, *Nat. Nanotechnol.*, 9 (2014) 257-261.
[292] S. McDonnell, A. Azcatl, R. Addou, C. Gong, C. Battaglia, S. Chuang, K. Cho, A. Javey, R.M. Wallace, Hole contacts on transition metal dichalcogenides: Interface chemistry and band alignments, *ACS Nano*, 8 (2014) 6265-6272.
[293] W. Liu, J. Kang, D. Sarkar, Y. Khatami, D. Jena, K. Banerjee, Role of metal contacts in designing high-performance monolayer n-type WSe_2 field effect transistors, *Nano Lett.*, 13 (2013) 1983-1990.
[294] M.S. Christopher, A. Rafik, M. Stephen, L.H. Christopher, M.W. Robert, WSe_2-contact metal interface chemistry and band alignment under high vacuum and ultra high vacuum deposition conditions, *2D Mater.*, 4 (2017) 025084.
[295] G. Kline, K. Kam, D. Canfield, B.A. Parkinson, Efficient and stable photoelectrochemical cells constructed with WSe_2 and $MoSe_2$ photoanodes, *Solar Energy Mater.*, 4 (1981) 301-308.
[296] R. Tenne, A. Wold, Passivation of recombination centers in n-WSe_2 yields high efficiency (>14%) photoelectrochemical cell, *Appl. Phys. Lett.*, 47 (1985) 707-709.
[297] R. Bourezg, G. Couturier, J. Salardenne, F. Lévy, Interface of n-type WSe_2 photoanodes in aqueous solution. I. Electrical properties, *Phys. Rev. B*, 46 (1992) 15404-15410.
[298] X. Yu, M.S. Prevot, N. Guijarro, K. Sivula, Self-assembled 2D WSe_2 thin films for photoelectrochemical hydrogen production, *Nat. Commun.*, 6 (2015) 7596.
[299] P. Karfa, R. Madhuri, P.K. Sharma, Multifunctional fluorescent chalcogenide hybrid nanodots ($MoSe_2$:CdS and WSe_2:CdS) as electro catalyst (for oxygen reduction/oxygen evolution reactions) and sensing probe for lead, *J. Mater. Chem. A*, 5 (2017) 1495-1508.
[300] Y. Ouyang, C. Ling, Q. Chen, Z. Wang, L. Shi, J. Wang, Activating inert basal planes of MoS_2 for hydrogen evolution reaction through the formation of different intrinsic defects, *Chem. Mater.*, 28 (2016) 4390-4396.
[301] H. Wang, D. Kong, P. Johanes, J.J. Cha, G. Zheng, K. Yan, N. Liu, Y. Cui, $MoSe_2$ and WSe_2 nanofilms with vertically aligned molecular layers on curved and rough surfaces, *Nano Lett.*, 13 (2013) 3426-3433.
[302] M.-Y. Li, Y. Shi, C.-C. Cheng, L.-S. Lu, Y.-C. Lin, H.-L. Tang, M.-L. Tsai, C.-W. Chu, K.-H. Wei, J.-H. He, W.-H. Chang, K. Suenaga, L.-J. Li, Epitaxial growth of a monolayer WSe_2-MoS_2 lateral p-n junction with an atomically sharp interface, *Science*, 349 (2015) 524-528.
[303] A. Neumann, J. Lindlau, L. Colombier, M. Nutz, S. Najmaei, J. Lou, A.D. Mohite, H. Yamaguchi, A. Högele, Opto-valleytronic imaging of atomically thin semiconductors, *Nat. Nanotechnol.*, 12 (2017) 329-334.
[304] B. Liu, M. Fathi, L. Chen, A. Abbas, Y. Ma, C. Zhou, Chemical vapor deposition growth of monolayer WSe_2 with tunable device characteristics and growth mechanism study, *ACS Nano*, 9 (2015) 6119-6127.
[305] S.M. Poh, S.J.R. Tan, X. Zhao, Z. Chen, I. Abdelwahab, D. Fu, H. Xu, Y. Bao, W. Zhou, K.P. Loh, Large area synthesis of 1D-$MoSe_2$ using molecular beam epitaxy, *Adv. Mater.*, 12 (2017) 1605641.

[306] O. Koji, K. Aleksandra, A.E.N. Ryan, M. Fumihiko, K. Kazuhide, Y. Hideki, Epitaxial growth of monolayer $MoSe_2$ on GaAs, *Appl. Phys. Express*, 9 (2016) 115501.
[307] K.E. Aretouli, D. Tsoutsou, P. Tsipas, J. Marquez-Velasco, S. Aminalragia Giamini, N. Kelaidis, V. Psycharis, A. Dimoulas, Epitaxial 2D $SnSe_2$/2D WSe_2 van der Waals heterostructures, *ACS Appl. Mater. Interfaces*, 8 (2016) 23222-23229.
[308] V. Suresh, L. Xinyu, R. Sergei, C.M. Patrick, A. Angelica, M. Stephen, M.W. Robert, M.F. Randall, K.F. Jacek, J. Debdeep, X. Huili Grace, Comprehensive structural and optical characterization of MBE grown $MoSe_2$ on graphite, CaF_2 and graphene, *2D Mater.*, 2 (2015) 024007.
[309] D.-H. Lien, J.S. Kang, M. Amani, K. Chen, M. Tosun, H.-P. Wang, T. Roy, M.S. Eggleston, M.C. Wu, M. Dubey, S.-C. Lee, J.-H. He, A. Javey, Engineering light outcoupling in 2D materials, *Nano Lett.*, 15 (2015) 1356-1361.
[310] J. Lu, A. Carvalho, H. Liu, S.X. Lim, A.H. Castro Neto, C.H. Sow, Hybrid bilayer WSe_2–$CH_3NH_3PbI_3$ organolead halide perovskite as a high-performance photodetector, *Angew. Chem. Int. Ed.*, 55 (2016) 11945-11949.
[311] B.W.H. Baugher, H.O.H. Churchill, Y. Yang, P. Jarillo-Herrero, Optoelectronic devices based on electrically tunable p-n diodes in a monolayer dichalcogenide, *Nat. Nanotechnol.*, 9 (2014) 262-267.
[312] W. Wong-Ng, H.F. McMurdie, B. Paretzkin, Y. Zhang, K.L. Davis, C.R. Hubbard, A.L. Dragoo, J.M. Stewart, Reference X-ray diffraction powder patterns of fifteen ceramic phases, *Powder Diffr.*, 2 (2013) 257-265.
[313] K. Tennakone, J. Bandara, Photocatalytic activity of dye-sensitized tin(IV) oxide nanocrystalline particles attached to zinc oxide particles: long distance electron transfer via ballistic transport of electrons across nanocrystallites, *Appl. Catal. A*, 208 (2001) 335-341.
[314] Y. Dong, J. Choi, H.-K. Jeong, D.H. Son, Hot electrons generated from doped quantum dots via upconversion of excitons to hot charge carriers for enhanced photocatalysis, *J. Am. Chem. Soc.*, 137 (2015) 5549-5554.
[315] P. Sippel, W. Albrecht, D. Mitoraj, R. Eichberger, T. Hannappel, D. Vanmaekelbergh, Two-photon photoemission study of competing auger and surface-mediated relaxation of hot electrons in CdSe quantum dot solids, *Nano Lett.*, 13 (2013) 1655-1661.
[316] X. Fu, M. Xie, P. Luan, L. Jing, Effective visible-excited charge separation in silicate-bridged ZnO/$BiVO_4$ nanocomposite and its contribution to enhanced photocatalytic activity, *ACS Appl. Mater. Interfaces*, 6 (2014) 18550-18557.
[317] C. Li, S. Wang, T. Wang, Y. Wei, P. Zhang, J. Gong, Monoclinic porous $BiVO_4$ networks decorated by discrete g-C_3N_4 nano-islands with tunable coverage for highly efficient photocatalysis, *Small*, 10 (2014) 2783-2790.
[318] F.E. Osterloh, Inorganic nanostructures for photoelectrochemical and photocatalytic water splitting, *Chem. Soc. Rev.*, 42 (2013) 2294-2320.
[319] B. Wu, N. Zheng, Surface and interface control of noble metal nanocrystals for catalytic and electrocatalytic applications, *Nano Today*, 8 (2013) 168-197.
[320] D. Mark, Z. Viktor, I.F.k. Vladimir, L.A. Igor, Auger recombination of dark excitons in WS_2 and WSe_2 monolayers, *2D Mater.*, 3 (2016) 035011.

[321] W.-T. Hsu, Y.-L. Chen, C.-H. Chen, P.-S. Liu, T.-H. Hou, L.-J. Li, W.-H. Chang, Optically initialized robust valley-polarized holes in monolayer WSe_2, *Nat. Commun.*, 6 (2015) 8963.
[322] W. Yang, J. Shang, J. Wang, X. Shen, B. Cao, N. Peimyoo, C. Zou, Y. Chen, Y. Wang, C. Cong, W. Huang, T. Yu, Electrically tunable valley-light emitting diode (vLED) based on CVD-grown monolayer WS_2, *Nano Lett.*, 16 (2016) 1560-1567.
[323] K.L. Seyler, J.R. Schaibley, P. Gong, P. Rivera, A.M. Jones, S. Wu, J. Yan, D.G. Mandrus, W. Yao, X. Xu, Electrical control of second-harmonic generation in a WSe_2 monolayer transistor, *Nat. Nanotechnol.*, 10 (2015) 407-411.
[324] N.R.E. Laboratory, Reference solar spectral irradiance: ASTM G-173, 2017 (2010).
[325] Y. Liu, C. Tan, H. Chou, A. Nayak, D. Wu, R. Ghosh, H.-Y. Chang, Y. Hao, X. Wang, J.-S. Kim, R. Piner, R.S. Ruoff, D. Akinwande, K. Lai, Thermal oxidation of WSe_2 nanosheets adhered on SiO_2/Si substrates, *Nano Lett.*, 15 (2015) 4979-4984.
[326] C. Liu, Y. Yang, W. Li, J. Li, Y. Li, Q. Chen, In situ synthesis of Bi_2S_3 sensitized WO_3 nanoplate arrays with less interfacial defects and enhanced photoelectrochemical performance, *Sci. Rep.*, 6 (2016) 23451.
[327] M.V. Dozzi, S. Marzorati, M. Longhi, M. Coduri, L. Artiglia, E. Selli, Photocatalytic activity of TiO_2-WO_3 mixed oxides in relation to electron transfer efficiency, *Appl. Catal. B*, 186 (2016) 157-165.
[328] S. Chu, S. Fan, Y. Wang, D. Rossouw, Y. Wang, G.A. Botton, Z. Mi, Tunable syngas production from CO_2 and H_2O in an aqueous photoelectrochemical cell, *Angew. Chem. Int. Ed.*, 55 (2016) 14262-14266.
[329] Y. Wang, S. Fan, B. AlOtaibi, Y. Wang, L. Li, Z. Mi, A monolithically integrated gallium nitride nanowire/silicon solar cell photocathode for selective carbon dioxide reduction to methane, *Chem. Eur. J.*, 22 (2016) 8809-8813.